AN INVESTIGATION OF GROUND-BASED OBSERVATIONS OF SOLAR OSCILLATIONS AT STANFORD

Harald M.J. Henning

Center for Space Science and Astrophysics
Stanford University
Stanford, CA 94305

CSSA-ASTRO-87-21

December 1987

This work was supported in part by the Atmospheric Sciences Division of the National Science Foundation under Grant ATM 86-18263, by the Office of Naval Research under Contract NOOO14-86-K-0085, and by the National Aeronautics and Space Administration under Grant NGR 05-020-559.

AN INVESTIGATION OF GROUND-BASED OBSERVATIONS OF SOLAR OSCILLATIONS AT STANFORD

A DISSERTATION

SUBMITTED TO THE DEPARTMENT OF APPLIED PHYSICS

AND THE COMMITTEE ON GRADUATE STUDIES

OF STANFORD UNIVERSITY

IN PARTIAL FULFILLMENT OF THE REQUIREMENTS

FOR THE DEGREE OF

DOCTOR OF PHILOSOPHY

By

Harald Martin Jakob Henning

December 1987

Acknowledgements

The author would like to thank Professor Philip H. Scherrer for his excellent guidance into the field of helioseismology. His abilities as a scientist and adviser have provided much inspiration and support for this work. Dr. J. Todd Hoeksema and Dr. Richard S. Bogart are thanked for many fruitful discussions in general and for their constructive criticism during this work's progress in particular. The late Professor John M. Wilcox is remembered with appreciation as the person who first introduced the author to solar research, and whose name the Solar Observatory at Stanford, built under his guidance, now carries.

Gratitude is expressed to Dr. Douglas O. Gough and Dr. Jørgen Christensen-Dalsgaard whose shared insights and model results provided valuable assistance to this study. Dr. J. Gethyn Timothy and Dr. Arthur B. C. Walker are thanked for being readers of this dissertation. Financial support for this investigation has been provided by the National Aeronautics and Space Administration through Grant NGR 05-020-559 and Grant NAG 5-944, by the National Science Foundation through Grant ATM 86-18263, and by the Office of Naval Research through Contract N00014-86-K-0085.

Last, but not least, many thanks go to Inger and Nicholas, whose unswerving support and love always provided a safe haven for recuperation after the battle with machine and number.

Table of Contents

List of Tables

List of Illustrations

Chapter 1

Introduction

The sun, while being one member of a rather common and simple class of stars, is unique in its proximity to the earth. It presents unequaled opportunities for investigations of the physical processes which govern most other stellar objects. As a plasma laboratory and nuclear accelerator it provides information on conditions which are hard to duplicate in a man-made laboratory. However, the processes in this astrophysical laboratory are to a large part cloaked from the direct observation of scientists.

The surface of the sun displays the signatures of many complex magneto-hydrodynamical interactions, whose study has long held the fascination of researchers. The most popularly known of these phenomena are sunspots, concentrations of magnetic field bundles which can be easily seen as darker areas on the bright solar disk. Other intricate configurations of the magnetic field on the solar surface are involved in the eruption of flares, the formation of the structure of the solar wind, the ejection of energetic particles, and numerous other processes which can be observed from the earth. The 11-year sunspot cycle has been recognized to be one signature of a large scale reversal of the magnetic field structure on the solar surface. It is thought that the non-uniform solar rotation combined with the turbulence of the convection in the outer envelope of the sun combine to form these intricate patterns of magnetic activity. Yet the complexities of the surface phenomena are not considered to affect the basic structure of the sun. The sun is understood and modelled to be one of the simpler stars when considering its large scale structure.

The sun's interior is generally modelled as a perfect sphere with solely a radial variation of the physical parameters. Magnetic fields are usually not considered in the stellar evolution calculations which can reproduce most of the known properties of the large scale sun very accurately. However, experiments have provided clues that there are some uncertainties or flaws in these models. The discrepancy between the measured value of the neutrino production and the model result is well established as one of the major problems in solar and nuclear physics. The understanding of the dynamics of the convection zone is another problem which has occupied many scientists.

The measurements of solar quantities which can be made are constrained to the information which can be obtained by a distant observer. This information is carried in the form of light and energetic particles. Of these carriers, only neutrinos originate from the deep interior of the sun. All other carriers originate no lower down in the sun than the solar photosphere. This limitation has until fairly recently prevented any direct measurement of conditions under the surface of our star. The development and growth of helioseismology has in the past decade provided solar physicists with a powerful new tool to probe the interior of the sun. Helioseismology is the measurement and analysis of global oscillations of the sun. These oscillations manifest themselves as wave-like motions of the photosphere which can be measured through the Doppler shift which they introduce in solar absorption lines. Contrary to photons, which take on the order of 100,000 years to traverse the sun, these waves take only on the order of an hour to pass through the sun. The waves carry information on the structure of the regions through which they pass. Analogous to the discipline of seismology on earth, the measurements can then be deciphered to extract this information. Helioseismology thus has the ability of directly probing layers of the sun which have never before been observationally examined.

The presence of oscillations on the surface of the sun was discovered by Leighton, Noyes, and Simon (Leighton, 1960; Leighton et al., 1962). These authors observed that large patches of the sun, with a size scale of 30,000 km or about 2% of the solar radius, exhibited oscillatory motions with about a 5 minute period. The motions persist for several cycles of oscillation and then subside into the general background of motion which is visible. It wasn't until 10 years later that theoretical proposals were published (Leibacher and Stein, 1971; Ulrich, 1970) which suggested that the observed 5 minute oscillations were actually the result of a superposition of many globally coherent acoustic wave modes. This insight has since led to the very fruitful development of the new discipline of helioseismology.

The restoring forces which drive the waves comprising the oscillations are primarily pressure, as in acoustic waves, and gravity, resulting in buoyancy oscillations. The relative contribution of these two forces to any one wave can be used to separate the modes into two groups which are separated in spatial distribution in the sun as well as frequency. Waves which are primarily acoustic waves have frequencies ranging from several hundred μHz to over 5000 μHz. The largest amplitude modes at the solar surface have periods around 5 minutes, or about 3000 μHz in frequency. These are the 5 minute p-modes which had been seen in the sixties but not understood and confirmed as global oscillations until the observations by Deubner (1975) which marked the first success in measuring the dispersion relation of high-degree p-modes. Their region of propagation extends from the photosphere to the core of the sun, and depends on the horizontal wavelength and frequency of a mode. Buoyancy waves, on the other hand, cannot propagate in the convective envelope, and are thus generally trapped in the deeper interior. The frequencies of buoyancy waves lie below a few hundred μHz, with the vast majority of modes existing below 100 μHz. Other modes of oscillation can exist in the atmosphere of the sun above

the photosphere, but these play no role in this study and will therefore not be considered further.

1.1. Theory of Solar Oscillations

A quick survey through the mathematical description of the modes will help put the work undertaken in this study in perspective. A global mode of oscillation exists through the combination of two conditions. Firstly, a wave must be trapped in a cavity of propagation. Secondly, the wave must have a wavelength which fits inside this cavity such that it can constructively interfere and form a standing wave. If these conditions are met a mode of oscillation can exist at the appropriate frequency and wavelength.

The interference pattern which is a mode of oscillation can be described in spherical coordinates (r,θ,ϕ):

$$\xi(r,\theta,\phi,t) = \mathrm{Re}[\Xi(r)P_l^m(\cos\theta)\cos m\phi\ e^{i\omega t}] \tag{1.1}$$

Based on work by Lamb (1908) Gough has obtained a general differential equation governing the modes, assuming adiabatic oscillations and ignoring the local effects of spherical geometry (Deubner and Gough, 1984). Note that one must be careful when considering the oscillations measured in this study, since their wavelengths are relatively large and thus a complete theoretical analysis would likely need to include the effects of spherical geometry, as well as perturbations to the gravitational potential introduced by the oscillation. However, the simplifying assumptions are valid for most of the conditions encountered in the sun, and suffice for illustrating the properties of the modes. If one defines a dependent variable

$$\Psi = \rho^{1/2}c^2\nabla\cdot\xi$$

where c is the sound speed and ρ the density, then the differential equation describing the

oscillations is

$$\Psi'' + K^2\Psi = 0 \tag{1.2}$$

The vertical component of the local wave number K is

$$K^2 = \frac{\omega^2-\omega_c^2}{c^2} + \frac{l(l+1)}{r^2}\left[\frac{N^2}{w^2}-1\right]$$

where ω_c is a generalized acoustic cutoff frequency

$$\omega_c^2 = \frac{c^2}{4H^2}\,(1-2\frac{dH}{dr})$$

with H the density scale height, and

$$N^2 = g(\frac{1}{H}-\frac{g}{c^2})$$

is the square of the buoyancy frequency, also known as the Brunt-Väisälä frequency. For a propagating wave, one requires that $K^2 > 0$. A convenient way to rewrite the equation is

$$K^2 = \frac{\omega^2}{c^2}\left[1-\frac{\omega_+^2}{\omega^2}\right]\left[1-\frac{\omega_-^2}{\omega^2}\right] \tag{1.3}$$

where $\omega_\pm^2$ is defined as

$$\omega_\pm^2 = \frac{1}{2}(S_l^2+\omega_c^2) \pm [\frac{1}{4}(S_l^2+\omega_c^2)^2-N^2S_l^2]^{1/2}$$

and the Lamb frequency S_l

$$S_l = \frac{\sqrt{l(l+1)}\,c}{r}$$

Equation (1.3) makes it clear that for K^2 to be larger than 0, it is necessary that the critical frequencies $\omega_\pm$ are either both larger or both less than the wave frequency.

In the solar interior, it is generally true that the magnitude of S_l is much larger than both the generalized acoustic cutoff frequency and the Brunt-Väisälä buoyancy frequency. This simplifies the expression for $\omega_\pm$ so that $\omega_+ \approx S_l$ and $\omega_- \approx N$. The behavior of ω_+ and ω_-, combined with the requirement that the wave frequency is either larger than both or less than both, divides the modes into two groups.

If the wave frequency ω is greater than both ω_+ and ω_-, then the wave's propagation region is determined by $\omega_+ \approx S_l$. These modes can be identified as acoustic waves, also known as pressure modes or p-modes. Their region of propagation is bounded just underneath the solar photosphere by the steep gradient in density which causes a reflection of the mode when the acoustic cutoff frequency becomes equal to the mode's frequency. In the solar interior the mode's direction of propagation is slowly refracted away from the vertical by the increasing sound speed as the temperature increases. The mode is completely refracted when the horizontal phase speed, given by $\omega r/\sqrt{l(l+1)}$, equals the sound speed c. Figure 1.1, adapted from Gough (1983), shows two sample ray paths of acoustic modes, illustrating that modes with a smaller horizontal scale, as indicated by a larger spherical harmonic degree l, penetrate less deeply into the solar interior. It is the low-degree modes, which provide information about the deep interior of the sun, which the observations used in this study are sensitive to.

If, on the other hand, the wave frequency ω is less than both ω_+ and ω_-, then the wave's propagation region is determined by $\omega_- \approx N$. The buoyancy frequency N which governs these modes identifies them as gravity modes, or g-modes. Over most of the interior ω_- is fairly constant. However, N declines rapidly near the center of the sun due to the decrease in the gravity force, as well as at the boundary of the convective envelope, where the material becomes unstable to buoyancy fluctuations. G-modes are thus trapped

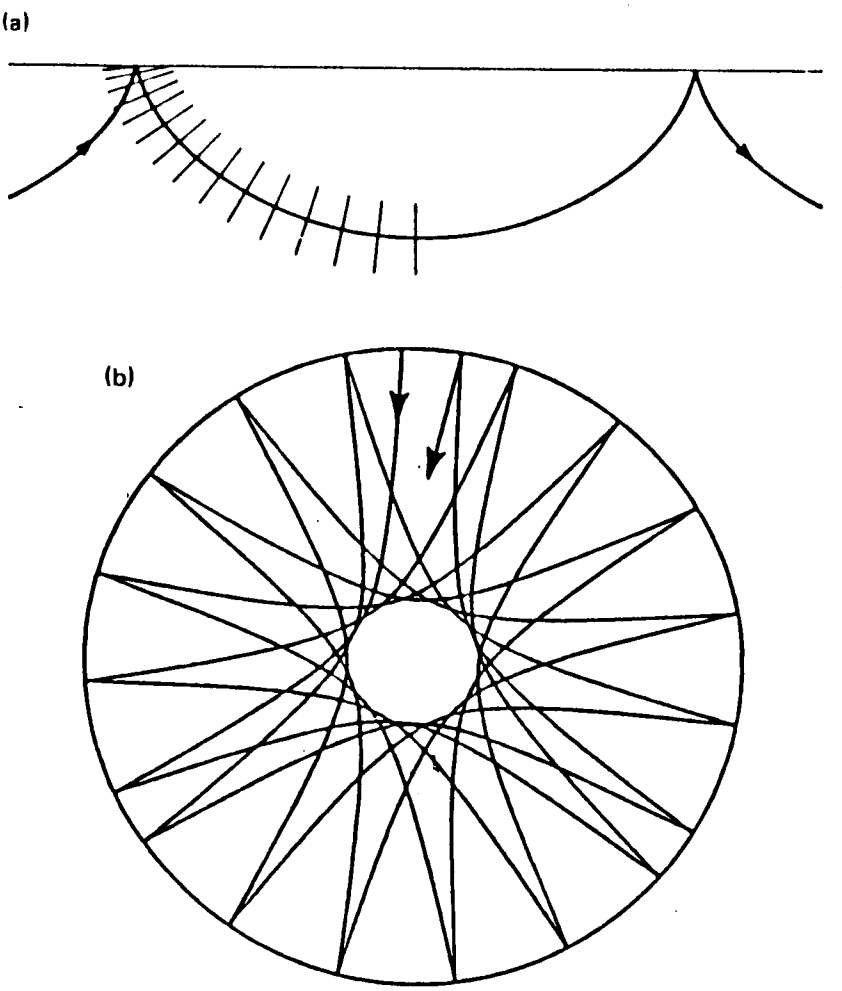

Figure 1.1 - Ray Paths. Typical ray paths of acoustic modes within the sun. a) shows a high-degree mode confined to a shallow region just below the solar surface. b) shows a high-order, low-degree mode with $n/l \approx 5$, which propagates throughout the solar interior. Adapted from Gough (1983).

in the deep interior of the sun. They decay exponentially through the convection zone, so that the amplitude of the oscillations at the surface of the sun is small. The relative amplitude at the photosphere is smallest for modes with higher degree l, so that it is likely that only the lowest degree modes are observable. However, their detection and identification can provide information on the solar core which nicely complements the information from p-modes whose frequencies are determined by conditions in the whole sun.

Figure 1.2, based on computations with a solar model (Model 1) (Christensen-Dalsgaard, 1982), is an illustration of the sensitivity of the modes to conditions in the solar interior. The period of the illustrated modes is about 5 minutes for p-modes, and 165 minutes for g-modes. Thus the change in penetration is solely attributable to the changing degree l of the modes. All p-modes have a strong and complicated contribution from the solar envelope. As l increases though, the p-mode becomes confined to a shallower region of the sun. The decreased depth of the turning radius with increasing degree l for the p-modes is easily apparent.

In the left panels of figure 1.2 is visible the decay of the g-modes through the convective envelope, increasing in severity with increasing l. While the g-mode structure gets complicated near in the core of the sun, its high amplitude emphasizes the fact that g-modes are a very sensitive probe of the energy-generating region in the sun.

An asymptotic expression for the mode frequency ω of p-modes can be found in an analysis by Tassoul (1980):

$$\nu_{n,l} \approx (n+\tfrac{1}{2}l+\varepsilon_p)\nu_0 + \delta_{n,l} + \nu_R m\left[1 - \frac{1}{l(l+1)}\right]$$

where

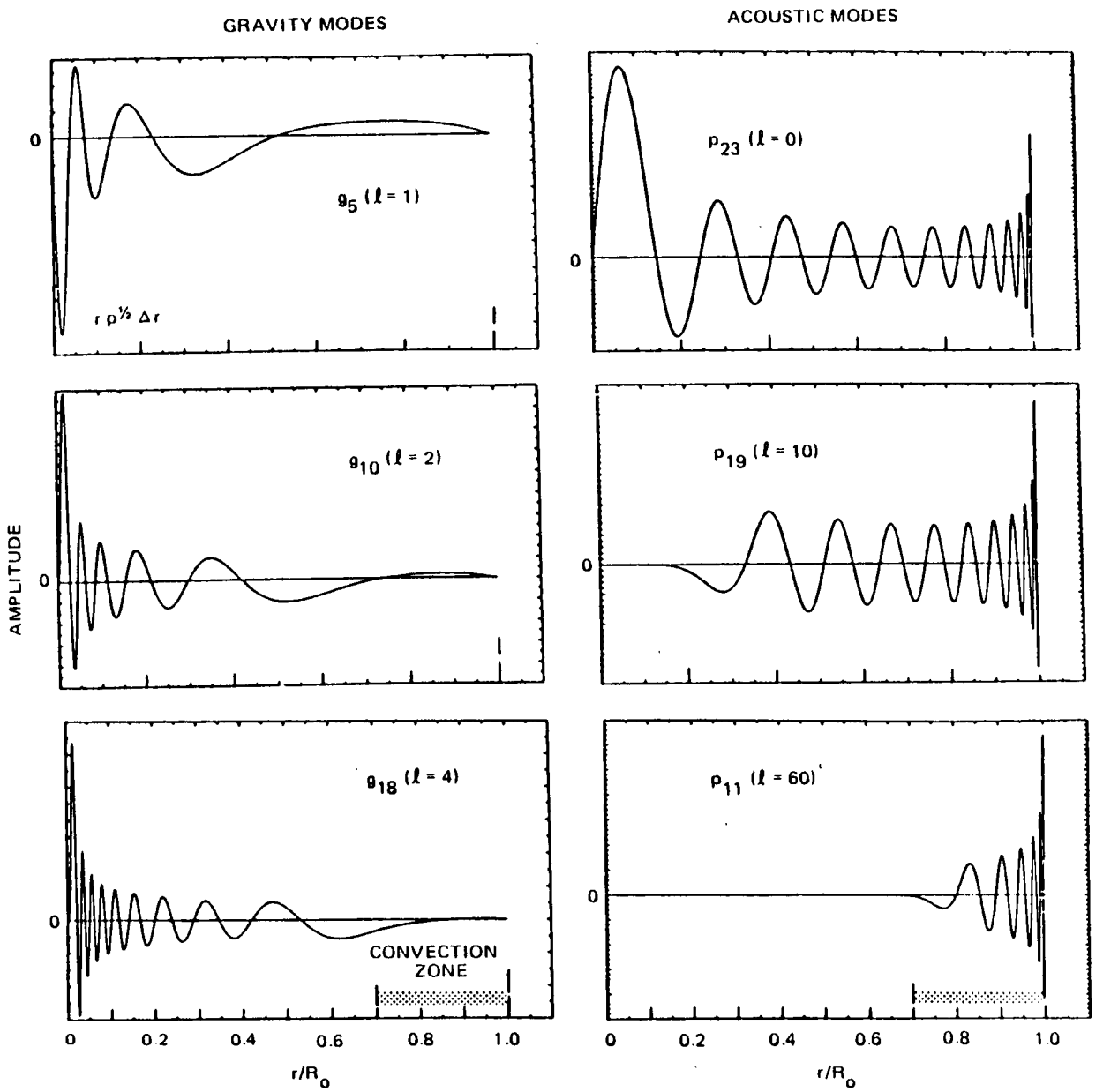

Figure 1.2 - Mode Sensitivity. The panels show the variation with radius of displacement amplitudes of acoustic modes and gravity modes. The subscript denotes the radial order n. The p-modes in the right-hand panels all have periods of about 5 minutes, while the g-modes in the left-hand panels have frequencies of about 100 μHz. Derived from a model described in Christensen-Dalsgaard (1982).

$$\nu_0 = \left[2\int_0^R \frac{dr}{c}\right]^{-1}$$

Here R is the solar radius, and $\delta_{n,l}$ is a small correction depending on solar parameters, n, and l. This expression is only valid when $n \gg l$, which disqualifies it for use on the p-modes found in this analysis, but it illustrates the distinctive behavior of p-modes that different n values are asymptotically equally spaced in frequency. This separation ν_0, the inverse of the integral of the sound travel time through the sun, is about 136 μHz. The separation is clearly visible in the nearly vertical ridges of modes in the echelle diagrams in chapter 4.

A similar asymptotic expression can be derived for g-modes (Fröhlich, 1986; Tassoul, 1980):

$$\nu_{n,l} \approx \frac{\sqrt{l(l+1)}}{T_0(n+\frac{1}{2}l+\varepsilon_g)} + \nu_R m\left[1 - \frac{1}{l(l+1)}\right]$$

In this equation T_0 is an asymptotic constant spacing in period between g-modes. This contrasts with the p-modes which are equally spaced in frequency with increasing radial order n. Again, although it provides guidance for the g-mode search, the asymptotic equation is only valid for very large n, as will be demonstrated in chapter 5.

1.2. Observations of Solar Oscillations

The first results, signalling the birth of helioseismology as an observational tool for probing the sun, were published in 1975 by Deubner (1975). They indicated that the theoretical frequencies calculated for the observed high-degree p-modes were too high. To fix this discrepancy required an increase of the depth of the convection zone to about 30% of the solar radius. Standard solar model calculations then determined the initial helium abundance Y_0 to be about 25% by mass.

Observations of low-degree degree modes (Claverie et al., 1979; Claverie et al., 1980; Claverie et al., 1981; Grec et al., 1980; Grec et al., 1983; Scherrer et al., 1982; Scherrer et al., 1983) provided the next stage for identification of p-modes. The observations consist of full disk measurements in the case of the Birmingham and Nice groups, sensitive only to modes with degrees l less than or equal to about 3. In the case of the observations by the Crimean and Stanford groups, being differential measurements the observations are sensitive to somewhat higher degrees, about l=2 to l=5. At these low degrees it was possible to identify individual modes of oscillation, not just ridges of power corresponding to many l-values of a given order n as was the case for the high-degree modes. The values of the frequencies enabled further comparisons with theory which tend to corroborate the determination of Y_0 indicated by the high-degree modes and also imply that no substantial mixing of core material with material outside the energy-generating region has occurred. However, the frequencies determined by the best-fitting solar models still do not match the measured frequencies to within the accuracy that these are known, indicating problems with the models.

The observation and identification of intermediate-degree modes (Duvall and Harvey, 1983) tied the two previous groups of observations together by bridging the gap in l values. For high-degree modes the order n of the modes is exactly determined by counting the ridges of power starting with the clearly visible f mode. For the low-degree modes the order n was not observationally determinable. Careful matching of the intermediate-degree modes between the two sets allowed unique identification of the order n for the low-degree modes, corroborating their previous identifications which had been made on a theoretical basis.

The identification of p-modes ranging over such a broad scale of degrees has

permitted the determination of the sound speed through a large part of the solar interior (Christensen-Dalsgaard et al, 1985a). The lack of measurements of low-degree modes of very low order n, and the complete lack of g-modes, has prevented an accurate inversion below .3 R. The modes identified in this study take a step towards filling this gap.

Further measurements have provided information on the angular velocity in the interior of the sun by determining the rotational splitting which is manifest in the frequency difference between peaks in the power spectrum corresponding to different values of the azimuthal order m for identical l and n (Brown, 1985; Brown and Morrow, 1987; Duvall and Harvey, 1984; Duvall et al., 1984). Carefully constructed kernel functions which utilize the frequencies from many different modal peaks can provide a value of the rotation averaged over a small range of the solar interior. The results indicate an almost constant angular velocity, decreasing slightly with decreasing radius, until the deep interior of the sun is reached, where the velocity sharply increases. This increase, however, is based upon only one point with very large error bars, due to the incompleteness of the measurements of frequencies of modes which penetrate this deep. This investigation will provide the frequencies of p-modes of lower order n, and thus greater sensitivity to the structure of the solar interior, than have been identified previously. Their addition to the known modes could eventually result in the construction of better kernels which improve the accuracy of the rotation curve.

The history of the detection and identification of g-modes has provided far less occasion for triumph than p-modes. The g-modes lie in a frequency range which poses difficult problems for the analysis of most observations. The periods where there appears to be power corresponding to g-modes are so long, on the order of several hours, that the restriction of day-long observations and instrumental systematic errors, combined with the relatively low amplitude of the modes, has so far prevented a consensus on the detection or

identification of any modes. The most famous candidate has been the 160.01 minute oscillation, which had exhibited phase coherence over time and between different observatories which would confirm its solar origin (Scherrer et al., 1979; Scherrer et al., 1980). However, recent evidence has called even this long-standing result into question (Henning and Scherrer, 1987). Other g-mode detections have been made by several groups (Delache and Scherrer, 1983; Fröhlich, 1986; Isaak et al., 1983; Scherrer, 1984), but no agreement between the identified modes or even the value of the asymptotic period separation T_0 has been reached. This analysis identifies g-modes in the Stanford differential observations based on a systematic statistical search which provides a high level of confidence in the solar origin and g-mode identity of the observed peaks in the power spectrum.

Chapter 2

Data

All the data analyzed in this investigation were obtained at the Wilcox Solar Observatory at Stanford. This Observatory is located in the foothills near Stanford University, within a few miles of the campus. The proximity to the offices and computational facilities on campus is convenient in terms of ensuring a rapid response to either instrumental problems or observational opportunities. This situation has resulted in a highly successful program of photospheric large-scale magnetic field observations extending back to 1976 (Hoeksema and Scherrer, 1986). The other major dedication of the telescope has been to the observation of solar oscillations. This program extends back to 1975, with the vast majority of the data being collected in the summers of the years. The reasons for this data distribution basically rest on the quantity of useful data. The main reason is that the quality of the power spectra which can be obtained by analysis of the oscillation observations is highly sensitive to the completeness of data coverage within a given time period. Thus a completely cloudless sky is desirable for these measurements. Stanford is blessed with Northern California weather which provides many nearly perfect days for observations in the summer months from May through September. However, experience has demonstrated that it is only the period from June through early August which has reasonably consistently rendered long stretches of day-long observations. Another reason why summers provide the best data is the length of each day's observation. The Stanford instrument is a coelostat, which requires an interruption of the observations around noon during most of the year, excepting summer, due to shadowing of the coelostat mirror. The instrumental description section of this chapter will describe this in more

detail.

Only the best years, in terms of coverage, have been used in this analysis since the others hold little additional useful new information. It should be noted that despite the selection of only the periods with the most complete coverage the filling factor of the data is still only around a quarter. That is, the times with no data outweigh the times when there is oscillation data by a ratio of about 3 to 1. The majority of this dark time consists of nights, but there are also scattered cloudy days and times with instrumental problems, as well as the periodic magnetic observations which occupy a few hours every two or three days.

The first part of this chapter will briefly describe the telescope, the observational method, and the data taking procedure, as well as discuss the systematic errors which can be expected in the data. The second part of this chapter then describes the observations used in this study, including the first steps in the reduction and analysis process.

2.1. Instrumental Description

The Wilcox Solar Observatory is described in great detail elsewhere (Dittmer 1977). This section will provide a brief and specific tour of the telescope as it applies to the oscillation data. The telescope can be visualized by referring to the diagram in figure 2.1 as the path of light is traced through the optics.

Sunlight passes through a shuttered window in the dome whose opening and pointing direction is controlled by computer. The light is reflected from the coelostat mirror onto the second flat mirror. The coelostat mirror rotates around an axis parallel to the earth's axis of rotation with a 48 hour period, while the second flat is fixed so that the light is directed down through the observing and guiding lenses. The coelostat arrangement, as opposed to a heliostat arrangement, has the advantage that it produces an image which

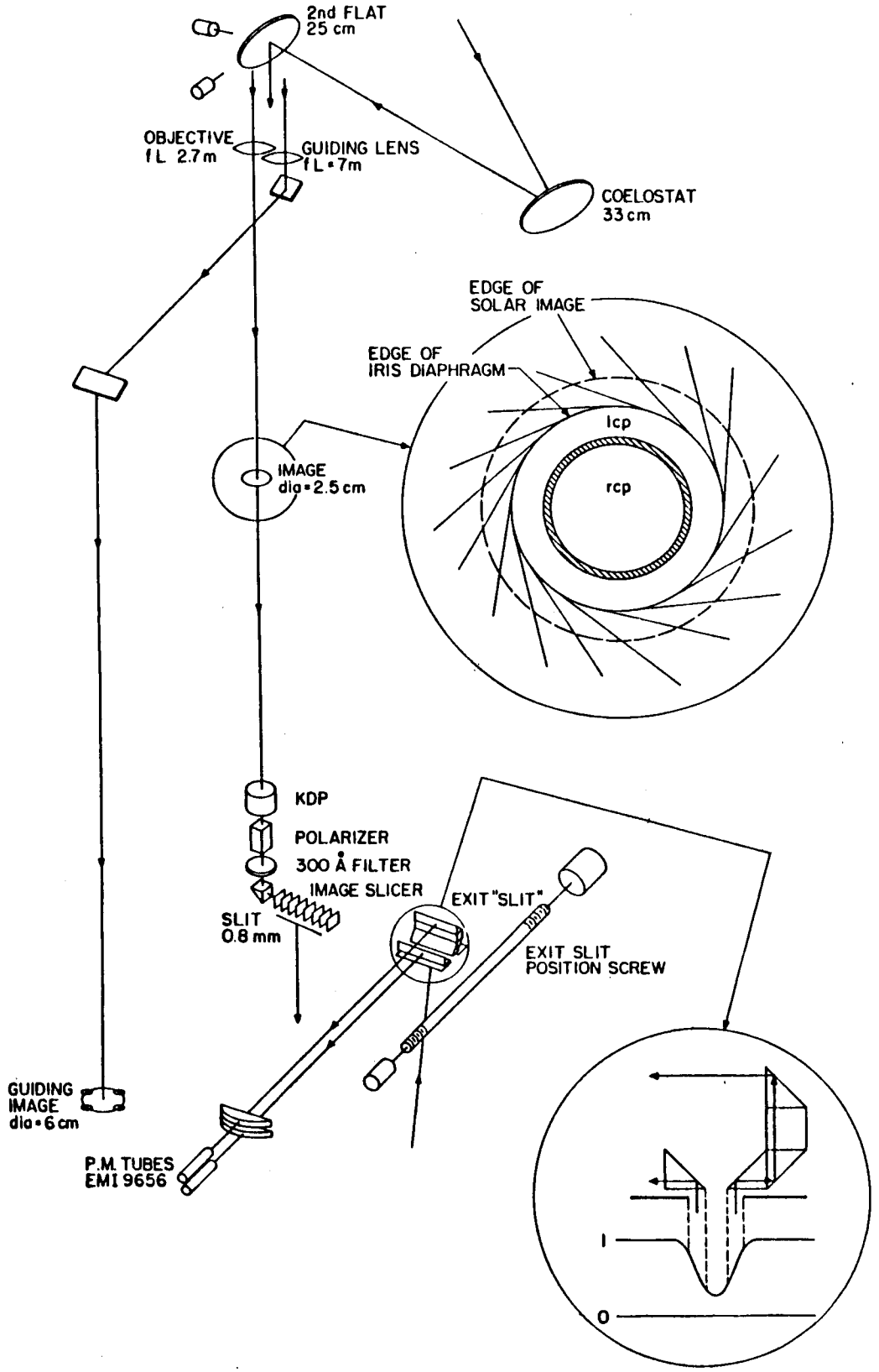

Figure 2.1 - Telescope Diagram. Schematic drawing of the optical path for the differential doppler measurements at the Wilcox Solar Observatory.

does not rotate with the earth's rotation. This turns out to be rather important for these measurements, as it avoids a possible diurnal signal contribution due to light from different parts of the sun passing through different sections of the optical components throughout the day. Any variation in the transparency function of the optics with rotation would produce a signal, as is explained later in the discussion of the effects of brightness variations on the measurement.

The disadvantage of the coelostat system is that the second flat assembly can cast its shadow directly onto the coelostat mirror if the sun isn't high enough above the horizon. To avoid this problem the coelostat mirror must be moved to the east (in the morning) or the west (in the afternoon) of the second flat assembly for much of the year. This change of configuration is performed near noon of each observing day. This motion not only rotates the images of the sun, introducing potential systematic errors as discussed above, but forces interruption of the observations, causing an undesirable data gap. For these reasons the best oscillation observations are constrained to lie in the period from about April 28th to August 10th, the dates when the coelostat is not shadowed at any time during the day by the second flat, and can thus be kept centered directly north of it. Combined with the time of very good weather at Stanford, where the probability of many-day stretches of clear sky is high, this effectively puts the observing season for solar oscillations at Stanford between the beginning of June and early August.

The light which passes through the guiding lens is directed by two mirrors down into the observing room, where the image is focused. Four photodiodes are located at the cardinal points on the edges of this image. The differences of the signals from each of the two pairs of opposing diodes are used to drive a servo system which adjusts the second flat so that the guiding image, and thus ideally also the observing image, stays fixed. This corrective motion is necessary since the positioning of the image with just the coelostat

clock drive is not accurate or stable to the degree desired, mostly due to the changing speed of the sun across the sky. This guiding method is susceptible to error if there is any relative motion in the support structure between the two beams. Since the beams are parallel, vertical or horizontal motion of the support structure as a whole, especially the whole building, has no adverse effect on the guiding system. Thus the daily expansion and contraction of the building walls, which are heated slightly by the sun, does not affect the guiding system in such a way as to move the data beam.

The observing beam forms a 2.52 cm image at the circular polarization assembly which is detailed in figure 2.2. The light first passes through a linear polarizer, then through a quarter-wave plate. These are aligned in such a way that the light is left circularly polarized. Finally the light from the central portion of the image passes through a half-wave plate which gives it right circular polarization. This central portion has a diameter of 0.5 inches which is half the size of the solar image. The last part of this assembly is an iris diaphragm which is adjusted at the beginning of each observing season such that the light coming from the central portion is equal to the light from the annulus around it. The inner diameter of this annulus lies at about 0.55 inches due to the edge of the half-wave plate. An analytical calculation including limb darkening determines the outer edge of the annulus to have a diameter of about 0.77 inches. The light which has passed through this assembly now consists of right circularly polarized light from a central disk of the image and left circularly polarized light from an annular ring centered on the image around the central disk.

The beam next encounters a component consisting of a KD^*P (KD_2PO_4) crystal and a linear polarizer, hereafter referred to simply as the KDP assembly. The KD^*P crystal is subjected to a 110 Hz square wave of a voltage such that it alternately becomes a positive

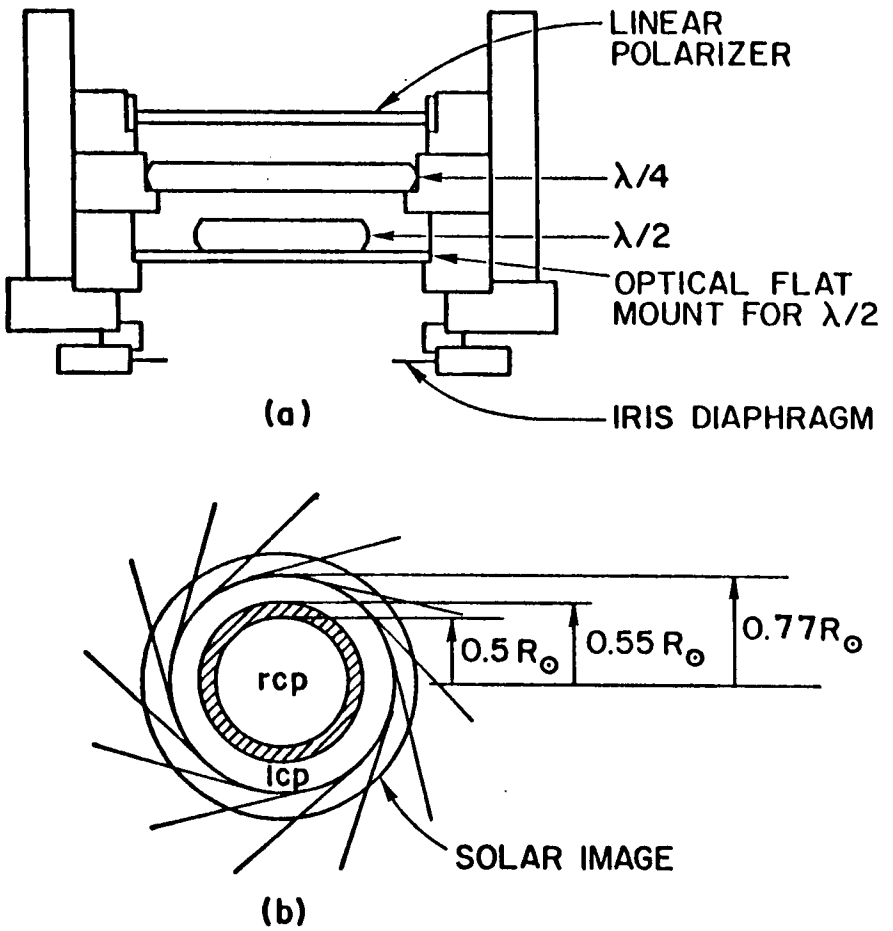

Figure 2.2 - Circular Polarization Assembly. Light from the center of the image becomes right circularly polarized, while light from the annulus around it is left circularly polarized.

or negative quarter-wave retarder. The polarizer is oriented such that in combination with the modulated KD^*P crystal the assembly acts as a circular analyzer, passing either right or left circularly polarized light, depending on the direction of the voltage. This component thus alternately passes the light from the center of the solar image and the annulus, with a 110 Hz frequency of modulation.

A 300 Å filter is necessary because the observations are carried out by looking at the FeI 5123.73 Å line in fifth order. Thus the filter, centered at 5200 Å, prevents sixth order blue and fourth order red light from overlapping with the region of interest. Although the location of the filter in the light path is shown in figure 2.1 to be below the KDP assembly where it is usually mounted, for the oscillation observations beginning in the 1984 season it was actually moved to be located above the circular polarization assembly in an effort to protect a new polarizer from the full impact of the sun's heat. This was done after it was discovered that the old polarizer had literally darkened in its center during the previous season.

Upon passing through the image slicer the beam's shape is converted into a long, thin rectangle to match the entrance slit of the spectrograph, a vertical Littrow spectrograph with 22.8 m focal length. The ruled grating measures 12 inches by 6 inches with 633 lines per mm. The light is focused by the Littrow lens and an image of the spectrum forms at the top of the spectrograph at the height of the entrance and exit slits. The exit slits take the form of a mobile assembly of two prisms, 75 mÅ wide and separated by 18 mÅ, which direct the light from the portion of the spectrum where they are located onto two EMI 9656 RM photomultiplier tubes which measure the intensity in each respective exit slit. These measurements of intensity are combined electronically to produce three different signals:

The first signal is a time average of the average of the two phototube measurements. In other words, the two signals are electronically added and divided by 2, then integrated over a period of 0.1 seconds, which corresponds to 11 KDP cycles. This signal will be referred to as the intensity signal.

The second signal is a KDP modulated time average of the difference between the two phototube measurements. To clarify, the two signals from the phototubes are electronically subtracted, then multiplied by either plus or minus one, depending on whether the KDP is passing right or left circularly polarized light. The resulting signal is then integrated for 0.1 seconds. This signal will be referred to as the difference signal.

The third signal is the difference between the two phototube signals, but not modulated by the KDP cycle. In this case, the two phototube signals are again electronically subtracted, and then fed directly into a servo system controlling the position of the exit slit assembly. This signal will be referred to as the exit slit servo signal.

Another piece of information which is recorded is the actual position of the exit slit assembly. This quantity is determined by an encoder with one encoder unit corresponding to 6.2 microns of lateral motion. The dispersion of the spectrum at the observing wavelength of 5124 Å is 12.24 mm/Å. With this information one quickly calculates that a displacement of the exit slits by one encoder unit corresponds to 5.07×10^{-5} Å in wavelength, which equates to 2.96 m/s for a doppler shift. This signal will be referred to as the exit slit encoder signal or the exit slit position.

2.2. Differential Measurement

The great sensitivity and relative stability of the solar oscillation measurements made at the Wilcox Solar Observatory depend to a great extent on the differential method of observation which was originally developed by Valeri A. Kotov of the Crimean

Astrophysical Observatory. This method avoids the very large and uncalibratable wavelength shifts of instrumental origin which are difficult to separate from the rather smaller solar oscillation signal. For example, it was recognized long ago that changes in temperature, barometric pressure, or relative humidity could produce large apparent wavelength shifts in the instrument. These quantities are not recorded on a regular basis at the Wilcox Solar Observatory. Another major source of wavelength drift is the relative gain change of the two phototubes. Appendix B contains the calculation of the sensitivity of the exit slit position to this effect. It is known that the relative gain of the phototubes does change by a few percent throughout the day, probably as a function of the history of illumination of the phototube, but the exact shape of this function is not known. As shown in Appendix B, this small gain change can cause an apparent wavelength shift corresponding to 140 m/s.

The differential method of observation is designed to circumvent these problems and systematic errors by avoiding the use of an absolute wavelength measurement. Instead, the quantity measured corresponds to the difference in velocity between one part of the sun and another. The velocity difference measured for solar oscillations with the Stanford instrument corresponds to only a very small difference in wavelength, no more than a fraction of a mÅ. To a large extent the much larger wavelength drifts which can plague an absolute measurement of the line position cancel out exactly in the differential measurement. A later section discusses in detail the systematic errors that nonetheless do exist in this measurement.

The differential measurement is obtained by rapidly alternating between light coming from the central portion of the sun and light originating in an annulus around this central disc. This is accomplished by the KDP which passes either right circularly polarized light (from the central portion of the solar disc) or left circularly polarized light (from the

annulus), switching between the two at a rate of 110 Hz. In the following description of the output signals it is helpful to consult figure 2.3, which diagrams the exit slit's position relative to the FeI 5123.730 Å line used for the observations.

The two absorption lines drawn in the figure represent the two positions of the observed line. The separation in wavelength between them corresponds to the difference of average velocities between the center and annulus. The exit slit position is centered on the two lines at all times, tracking any drift which the lines may be undergoing together. This is done by using the exit slit servo signal to drive a servo system which has a response time much slower than the 110 Hz KDP cycle. Thus the exit slit assembly essentially straddles the peaks, adjusting itself such that the difference between its two slits remains on the average zero over a 0.1 second integration cycle. This behavior can be described mathematically by the relation

$$(I_c^B - I_c^R) + (I_a^B - I_a^R) = 0 \tag{2.1}$$

where the subscripts to the intensity I denote the central disk (c) or annulus (a), and the superscripts denote the slit located on the red (R) or blue (B) wing of the line. The intensity signal can be written as

$$I = \tfrac{1}{2} \times \left[\frac{I_c^B + I_c^R}{2} + \frac{I_a^B + I_a^R}{2} \right] \tag{2.2}$$

And the difference signal is correspondingly

$$D = \tfrac{1}{2} \times [(I_c^B - I_c^R) - (I_a^B - I_a^R)] \tag{2.3}$$

Since the intensity in the wing of the line changes nearly linearly with position of the slit for the wavelength shifts being measured, the difference signal D is a measure of the separation of the lines, weighted by the intensity. Experimental testing has been done to

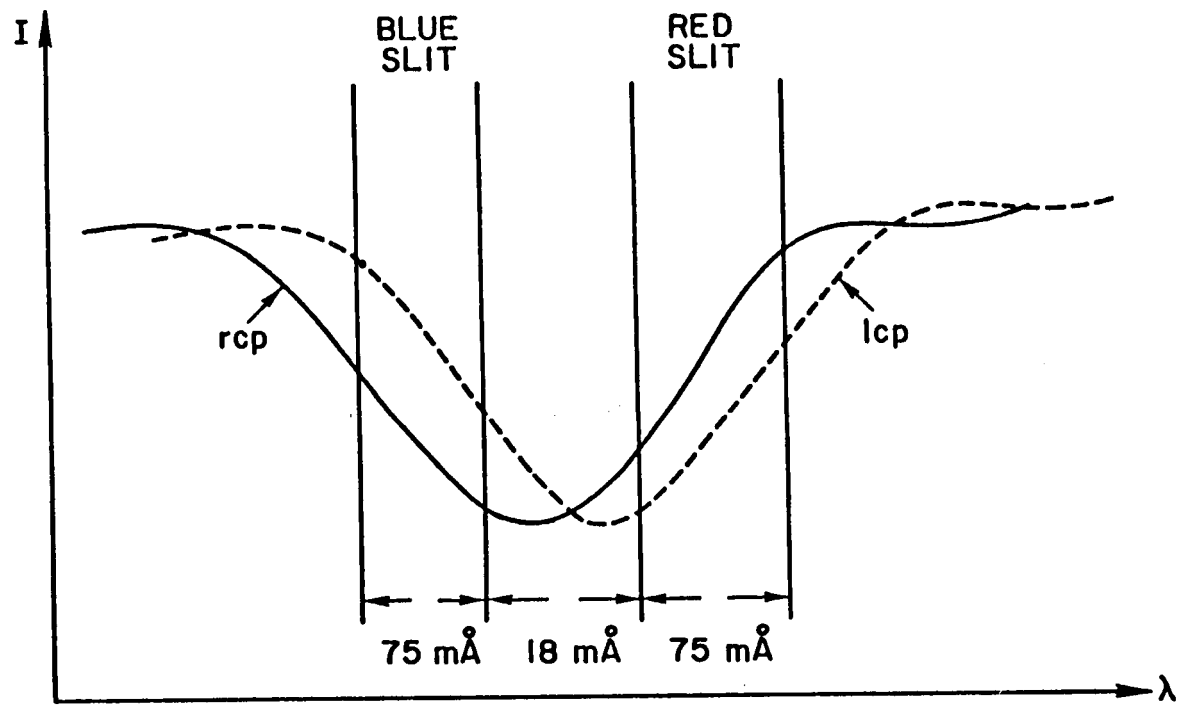

Figure 2.3 - Differential Measurement. The diagram depicts the location of the exit slit assembly with respect to the two lines. The splitting of the lines is exagerated in the illustration.

accurately determine the phase of the sign change (see Appendix A), so that the equation above is correct in its implication that the value for the center is subtracted from the annulus, and that the blue slit is subtracted from the red slit. These minus signs are important since they influence the phase of the D signal.

The observed signal which is used in this analysis is obtained by dividing D by the intensity signal I. In Appendix A these relations are used to calculate the theoretical calibration of the instrument

$$\frac{D}{I} = G_D I_c I_a \left[\frac{-\Delta m_c m_a - \frac{1-g}{1+g}(m_c f_a - m_a f_c)}{(I_c m_c + I_a m_a)\frac{g}{(1+g)^2}(I_c f_c + I_a f_a + (I_c m_c + I_a m_a)d)} \right] \tag{2.4}$$

In this equation G_D is an electronic gain factor in the difference signal circuit with a value of 100, I is the brightness of the respective line, m is the slope in the wing of the respective line, g is the ratio of gains between the two phototubes, f corresponds to the depth of the respective line, and Δ is the line separation. The phototube gain ratio g is very close to 1, making the second term in the numerator close to 0. If this is considered it is immediately obvious that the D/I signal is directly proportional to the line separation.

The brightness of the lines is set to be identical for the central portion and annulus in the yearly calibration before each observing season. However, the changing size of the solar image, as well as transparency variations in the earth's atmosphere, cause slight variations in these values. For purposes of calculating a calibration value for D/I, however, they are taken to be equal. A measurement of the line profiles, described in Appendix A, provides values for the slopes and line depths of

$$m_c = 0.00011 \text{ (m/s)}^{-1} \qquad f_c = 0.27$$

$$m_a = 0.00010 \text{ (m/s)}^{-1} \qquad f_a = 0.31$$

resulting in an idealized calibration factor of 55 m/s per unit *D/I*.

A more direct calibration procedure would perhaps be more aesthetically satisfying, as it would involve the direct measurement of a known separation. Given the dependence of the relation for *D/I* on the exact line profile it is important to use the FeI 5123.73 Å line used in the observations for the calibration. Thus the known input signal must somehow derive from the sun. Even this constraint proves to be too relaxed, as several attempts at a direct calibration reveal. Several additional calibration measurements were undertaken in this study to determine the value of the constant. The details of each calibration measurement and determination are given in Appendix A. The results are summarized here.

In the first measurement half of the sun's image at the circular polarization assembly is blocked off by a mask, with the dividing line lying along the solar rotation axis. Thus the input light either comes only from the West half or East half of the sun. The solar rotation, which is about 2 km/s at the solar limb, dominates the signal since it isn't canceled any more by the opposite rotation on the other half of the sun. A computational model described in chapter 3 was used to calculate the expected velocity difference. Detailed examination of the signal reveals that there are problems which prevent its use as a calibration tool. The problems derive from two main sources. Firstly, the line profile is changed heavily by the fact that half of the sun is blocked off in such a way as to eliminate one sign of solar rotation. The line becomes skewed to one side, throwing off the exit slit position, and the *D/I* signal. The other reason, which also will play a role in the inability to exactly model each day's error signal, is the fact that the image of the spectrum made by the Littrow lens is slightly defocused for the purpose of sharpening the line profile. This sharpening is accomplished through the defocusing by moving the lens such

that light from either limb of the sun, as approximated by the East - West direction in the observing room, actually falls closer to the line center in the defocused image. This of course reduces the perceived velocity shift due to solar rotation, especially the large limb velocities. A calculation reveals that the 3.5 cm shift of the 22.8 m focal length lens, given a solar image on the grating of size 15 cm, produces a shift of the position of the light from the limb of up to about 500 m/s. This value depends on the position angle of the solar rotation axis. During the regular observations this effect will largely cancel since both limbs are affected, and thus the slit remains in the same position. The oscillation velocities themselves are too small to be affected by the defocusing. For this calibration measurement, however, this sharpening thus causes the exit slit position to be less shifted than expected. The combination of a skewed line profile with a solar position dependent line shape adjustment prevent this method of calibration from working to a satisfactory degree. The calibration constant calculated from the measurement is 99 m/s per unit D/I, implying that the changed line profile caused the D/I signal to be about half of the expected value.

The second measurement was done by letting the solar image drift across the circular polarization assembly. The resulting average velocity is a combination of averaged velocities dominated by the solar rotation. Again a model was used to calculate the expected signal. The problem sources discussed for the previous method of calibration also come into play for this measurement, although to a lesser degree if only the middle section of the drift scan is considered, when the sun is close to centered on the circular polarization assembly. However, the uncertainty is still too large to make this a good calibration measurement. The calibration factor resulting from this measurement is 100 m/s $\pm$ 10 m/s, showing that it was also adversely affected by the line profile change.

The calibration factor was originally determined by Dittmer (1977) to be 54 m/s per unit of *D/I* by measuring the value of *D/I* as the exit slit is driven manually across a line from only the center or limb. This method has the advantage that it uses exactly the same line profile as the actual observations. It has the drawback that it measures the line separation calibration not directly, but by inference from the varying *D/I* signal as the position of the exit slit varies. This calibration was repeated for this study, and resulted in a calibration value of 53 m/s.

The value of the calibration actually used in the reduction of the data used in this study is 54 m/s, so that this study is compatible with previous analyses performed on Stanford data. Since the solar mode amplitudes are relatively small, this value is probably good to within 10%. This value is certainly exact enough, since the amplitudes of individual peaks are affected much more strongly, and unpredictably, by the particular structure of the data window, i.e. the times when there are data gaps. Much more discussion of the effect of the data window can be found in relevant sections of subsequent chapters.

2.3. Systematic Errors

Although the differential method of observation greatly reduces systematic errors due to shifts of the absolute position of the observing line, there are still a multitude of effects which contribute to a sizable drift in the data throughout the day which is demonstrably not of solar origin. This drift causes severe problems for the analysis of long period modes of oscillations.

The most obvious and pervasive effect is due to the dependence of the data signal on the intensity. A variation in intensity propagates into the data signal in two places. The most obvious can be seen in equation (2.4) which, for purposes of investigating the effect

of changing intensity the equation, can be simplified to

$$\frac{D}{I} = G_D \left[\frac{I_c I_a}{(I_c + I_a)^2} \right] \left[\frac{-\Delta m}{\frac{g}{(1+g)^2} (f + md)} \right] \tag{2.5}$$

since the slopes m and depths f are almost identical for the two lines. The multiplicative factor due to intensity is

$$\frac{I_c I_a}{(I_c + I_a)^2} = \frac{i}{(1+i)^2}$$

where i is the ratio between the line intensities. The behavior of this factor is such that it is maximal for equal intensities, and decreases as the ratio becomes different from 1. If either intensity drops to zero, the data signal also goes to zero. This is easily visualized in figure 2.3. If one line disappears, the exit slit assembly is driven to the center of the sole remaining line by the requirement that the exit slit servo signal is zero (equation 2.1). Then the difference signal D is also zero.

Since the intensities are balanced in the calibration and adjustment of the instrument at the beginning of each observing season, and any change is very small and gradual over the whole season, this sensitivity change does not play much of a role in a systematic daily error signal. Moreover, the seasonal change, as measured in October after the end of the 1987 observing season, was only 3%. This is larger than the expected ratio change of 0.6% from the seasonal variation of solar disk size, implying some additional change in the optics of the circular polarization assembly. This is not surprising, as the combination of accumulated dust, mechanical shifts of the optical elements, and possible heat-associated transparency changes to the filter or polarizer can easily account for the total. In any case, applying equation 2.5, a 3% difference in brightness corresponds to only a .02% change in the sensitivity of the instrument, a negligible factor.

The more troublesome effect of intensity variations appears in the line separation Δ. The position of each line is strongly affected by small variations in intensity across the solar disc. Since the line is a superposition of light from different parts of the solar disc, its position is actually a weighted average of the velocities at those parts of the disc. The weight of each velocity is just the intensity which is seen in the spectrum. Thus the position of the line, the average velocity, is obtained by essentially summing velocity times intensity over the whole area on the disk contributing to that line and dividing by the summed intensity. Δ is the difference between the average line positions of the center and the annulus. Equation (2.4) shows that the data signal is directly proportional to Δ if the gain is balanced correctly to 1 (which it is before every observation). The solar oscillation velocity is small compared to other velocities which can shift the line, but the instrument is designed so that those large velocities cancel in the optical integration. However, a small brightness gradient can prevent the correct and complete cancellation of large velocities, and thus appear as a velocity difference between the line positions.

The velocity signals which cause the greatest problems are the solar rotation and the earth's orbital motion and rotation. In the ideal case these signals all cancel in the differential measurement. The solar rotation cancels because the central disk and the annulus are circularly symmetric and the solar image is centered on them. The earth's rotation and orbital motion cancel because the gradient of these velocities across the solar disc, being close to linear, is nearly antisymmetric around the center of the disc. Thus the circular symmetry of the center and annulus result in the same line shift, again giving $\Delta = 0$ as for the solar rotation.

However, we don't live in a perfect world, and it doesn't take much to introduce some portion of these large velocity signals into the data signal. Any gradient in the sky transparency, such as that caused by airmass or clouds, or any position or size change

involving the circular polarization assembly, such as inexact positioning of the image or the seasonal variation in solar disk size, results in a direct contribution to the data signal *D/I*, as Δ will then be different from 0.

Another velocity contribution comes from the solar limbshift. This quantity takes the shape of a small relative red shift in the center of the disc, a small relative blue shift further out, turning over to a large relative red shift as one approaches the limb. The integrated average velocity difference between the center and an annulus is usually non-zero. Thus the limbshift introduces a fixed value of Δ into the measurement, a zero-level offset. This has little effect on the analysis, since the zero-level is removed for each day, but the uncertainty of the exact value and shape of the limbshift for the 5123.73 Å observing line could introduce a slightly different velocity signal than expected. However, the analysis in chapter 3 shows that any effect due to the limbshift is small compared to other possible systematic errors, so that its uncertainty is negligible for purposes of this analysis.

Chapter 3 is devoted to the exploration of the effects of different transparency gradients and configuration changes on the data signal. This analysis reveals that many of the systematic errors introduced by the sky gradient could be modelled or at least fit to the data. Some attempts have actually been made to completely remove the modelled systematic errors from the data signal, but have not been notably successful in improving the data. The fault lies partially with the difficulty in exactly modelling the effect of the changing sky transparency, the uncertainty of the calibration constant, and the effect of the Littrow lens defocusing on the weighted velocity average, but mostly with the other large systematic errors which are present in the data but cannot be modelled.

Probably the most problematic of these other systematic errors is the relative gain

change of the photomultiplier tubes. The two exit slits send their light to two different phototubes, and thus the output signal is sensitive to the gain ratio of these two phototubes. This ratio is set to 1 by the balancing adjustment at the beginning of each day's observation, but it varies during the observation, each phototube apparently changing in its own unique pattern depending on the history of light falling on it. The ratio is close to 1.0, and varies by no more than a few percent, but this is enough to introduce a sizable drift into the signals. In Appendix B is calculated the response of both the exit slit servo signal (causing an apparent absolute drift of the line as measured by the exit slit encoder signal) and the data signal D/I to a change in the gain ratio. For a 5% gain change, the exit slit moves a distance corresponding to 140 m/s, which is nearly half as large as the expected daily line shift due to earth's rotation. The data signal is much less sensitive to the gain change, receiving about a 16 m/s contribution, but the relative size of this drift is still large - about half of the average peak-to-peak signal on a typical day. Moreover, the drift is large throughout the day, whereas the transparency signal is large only in the morning and evening. Thus for most of the observing period, the gain change drift appears to dominate the error signal. Examples of this can be seen in figure 3.12.

Another source of error which has had a large impact on the data was discovered before the 1987 observing season. The circular polarization assembly is swung into the light beam at the beginning of each observation and out again at the end of each observation. This is necessary to allow the execution of the magnetic field observation programs which are continued during the whole year. It appears that the construction of the assembly was loosened enough by the daily motions of the supporting arm that the linear polarizer was able to move slightly but systematically. Each time the servo motor swung the assembly in and out, the linear polarizer was apparently jiggled in such a manner as to slowly rotate with respect to the quarter-wave plate. This of course translates directly into a

lessening of the sensitivity of the data signal, as light from both the center and the annulus then contributes to both the right and left circular polarization cycle of the KDP. The effect on the data analysis is severe - essentially all amplitude information is put in question. Furthermore, the consequent normalization required for the analysis has a deleterious effect on the detection of any solar oscillation mode, by splitting it into several closely spaced smaller peaks in the power spectrum. It is reassuring that part of the initial recalibration before each observing season includes a realignment of the assembly. The problem was fixed before the 1987 observing season by securing the polarizer to the rest of the assembly, so that the amplitude information provided by 1987 is valid and correct, as well as superior in quality to the other seasons for the detection of modes.

Another purely mechanical source of error which has been recognized for a long time is due to the "settling" of the spectrograph grating. This motion occurs only for a short period of time after the initial setup, but is easily visible in the exit slit encoder signal. The data signal also often displays a short period of steep drift at the very beginning of the observation, indicating that a small portion of this fast line position shift apparently is reflected even in that signal.

Temperature and barometric pressure can and do also cause erroneous contributions to the data signal, although they are not nearly as severe as for a non-differential measurement. One example which has been discovered but not resolved is the air conditioner cycle. The temperature in the observing room is kept fairly constant, but does vary slightly and periodically. After the 1984 observing season it was first noticed that a region of the spectrum of the data displayed power around 1000 μHz, a range where there had been very little in previous years. This frequency was eventually discovered to be just the frequency of a periodic 1 °C temperature variation in the observatory. Considering that this had not been seen before, it was assumed that a change installed that year had to be

the cause of this sensitivity. The only reasonable candidate was a new 300 Å bandpass filter, installed above the circular polarization assembly, which might have interference fringes which change with a temperature variation. However, replacement of that filter has not proven effective in removing that power from the spectrum.

As mentioned before, other instrumental imperfections can easily cause an error signal by coupling with the large velocities of the sun's or earth's rotation, and the earth's orbital motion. At one time the polarizer in the circular polarization assembly was found to be darkened in the center, apparently by solar heating. Such a transparency gradient produces a sensitivity change in the signal due to the changed intensity ratio, but if there is any asymmetry it also produces a drift in the signal. Presumably this change in the polarizer transparency was gradual, producing only a perceived zero-level change over a period of many days, which would not greatly affect the analysis. Other imperfections in the transparency of the circular polarization assembly are always present - running from simple dust to misalignment of the solar image and the assembly. Most of these change on a long time scale, though, and thus only produce a zero offset in the data which is easily removed in the analysis.

It is clear that all of these effects must somehow be removed from the data in the analysis, or at least reduced to a level where a solar signal can be identified. Chapters 4 and 5 describe the methods developed and employed for removing the signal drift so that the detection and identification of the two groups of solar oscillations becomes possible.

2.4. Description of the Observations

This section is devoted to describing the actual data which have been used in this analysis. Although the final treatment of the data differs for the two different groups of solar oscillations (see chapters 4 and 5), the first steps in the acquisition and reduction of

the data are identical and described below.

A brief summary of the observing procedure is appropriate as the first part of this section. Each oscillation observation is started with an adjustment of the phototube output. The exit slit assembly is driven to the continuum near the observing line, so that the light gathered in each slit and falling onto the respective phototube is of equal intensity. Then a manual voltage adjustment is made which changes the gain ratio between the two phototubes. The instrument is balanced so that the gain is equal in both phototubes by setting the difference of the output of the two phototubes to zero. Next the light is completely blocked from the phototubes by a cover, and the output of both the intensity signal and the difference signal is checked to make sure it is zero. If this is not the case an electronic offset is introduced into the respective circuit to zero out this dark current. After these fine tunings, and insertion of the appropriate optics so that the telescope looks as described in the previous section, the observation is started.

The observation runs until manually stopped or the sun is totally obscured by clouds or the horizon. The average of the measured values is calculated numerically from 0.1 second (11 KDP cycles) electronic averages of the phototube output. Every 15 seconds the average of the three measured signals - intensity I, difference D, and exit slit encoder - as well as the value of the data signal D/I is recorded.

Observations of the solar oscillations have been carried out each summer since 1977. However, in this analysis only 4 observing seasons are examined in detail. These are the summers of 1981, 1984, 1986, and 1987. The primary reasons for choosing only these particular years are simply the larger quantity and the superior quality of data in these seasons.

Regarding the quantity of data, for any attempt of detection to be successful,

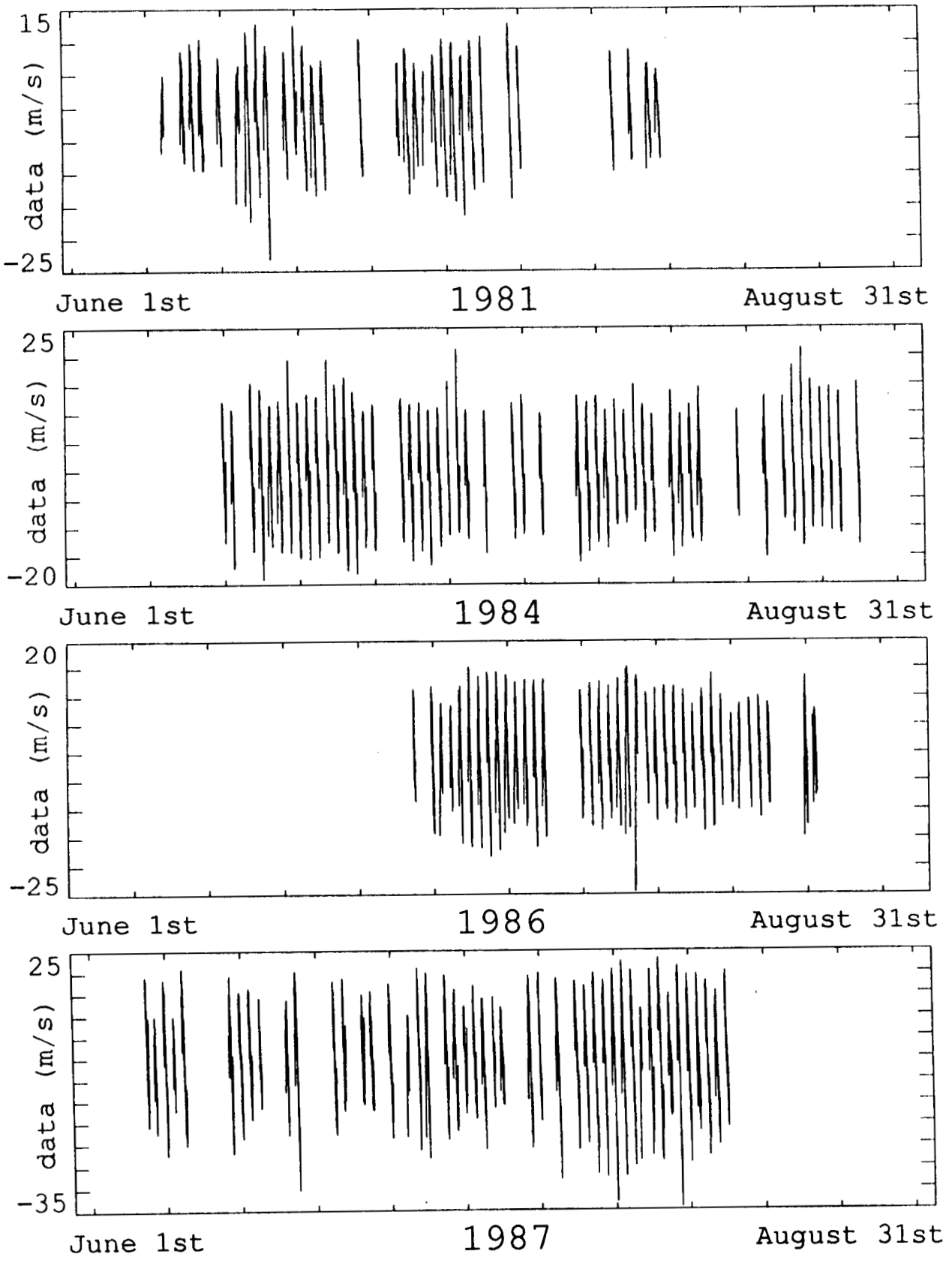

Figures 2.4a-d - Observations in 1981, 1984, 1986, 1987. The actual data with only the zero-level removed is shown for the 4 seasons analyzed in this study. One can see the data gaps as well as the daily drift.

especially in the case of the long period g-modes, it is desirable to have a record of observations which is as long as possible, but also as complete as possible. As can be seen by the analyses in chapter 5, the structure of the data window can effectively bury any modal signature in the spectrum. Since the night time data gaps are unavoidable, it is important to avoid as many whole day gaps (due to clouds or instrumental problems) as possible. However, it is only the theoretically long lifetime of the g-modes and low frequency p-modes which enables one to potentially separate them from the noise. This requires long periods of observations, at least a month long. Combining these two somewhat conflicting criteria one is constrained to use only data where there are month-long stretches of nearly perfect days of observations. Even in the best of years there are a few days in the analysis period where clouds prevented observations. Figures 2.4a-d show the data in a highly compressed form so that the whole period which is used in the analysis can be seen. Only the zero level has been removed from the data in these figures, leaving the daily drift. The data for the first three seasons has also been renormalized to remove the sensitivity change. One can see that the magnitude of the unnormalized 1987 signal is still 50% larger than for the other seasons. The regular daily error signal is easily visible as an inverted V-shape, or a rotated S, depending on the length of the observation. One also notices that the time series are dominated by gaps - there are more times when there is no data than when there is data. The ratio of the amount of data points to the total number of possible data points in the time period is defined as the filling factor. For the p-mode analysis in chapter 4 only the best, most complete portions of the data shown in figure 2.4 are used. Thus the filling factor lies at 37.3% for 1987, 32.8% for 1986, 31.1% for 1984, and 28.6% for 1981. The g-mode analysis in chapter 5 requires the full resolution provided by the length of the time series, and thus forces inclusion of larger data gaps. Moreover, the necessary filtering of the data cuts off about 1 hour from each day's

observations, and thus causes a further increase of gap time. The combination results in a filling factor for the g-mode analysis of only 23.6% for 1987, 22.0% for 1986, 22.6% for 1984, and 20.1% for 1981.

The quality of the data also influenced the choice of which season and which days to utilize for analysis. In the summer of 1980 the sensitivity of the instrument seemed abnormally low, resulting in very poor data. It is now thought that this was the result of a complete misalignment of the polarizer whose inadvertent motion was discovered in 1987. Subsequent years are also plagued by this problem, but not to the extent of 1980. The years of 1982 and 1983 were disqualified on the basis of a combination of reasons ranging from the primary reason - quantity of useful observations - to the questionable quality of the data due to the polarizer motion and discoloration. 1985 was not used because of a particularly cloudy observing season.

Previous analyses of the data from years before 1980 (Delache and Scherrer, 1983; Scherrer et al., 1982; Scherrer et al., 1983; Scherrer, 1984) played a major role in the decision not to analyze these years again. It should also be pointed out, however, that the filling factor in those years was very low, below a value that would be desired for this analysis in any case.

Having chosen the data for this study, it next needs to be put into a form which is useful for the analysis. The first step in this process is to examine each day individually and select the times of "good" data. On most days this only involves trimming the data at the beginning of the observation, where the grating drift causes a steep change in the data signal, and at the end of the observation, where the setting sun enters a region of steep atmospheric gradient. On some days it is also necessary to clip out time periods where clouds have obscured the sun. Figure 2.5 shows a record of the observations for a typical

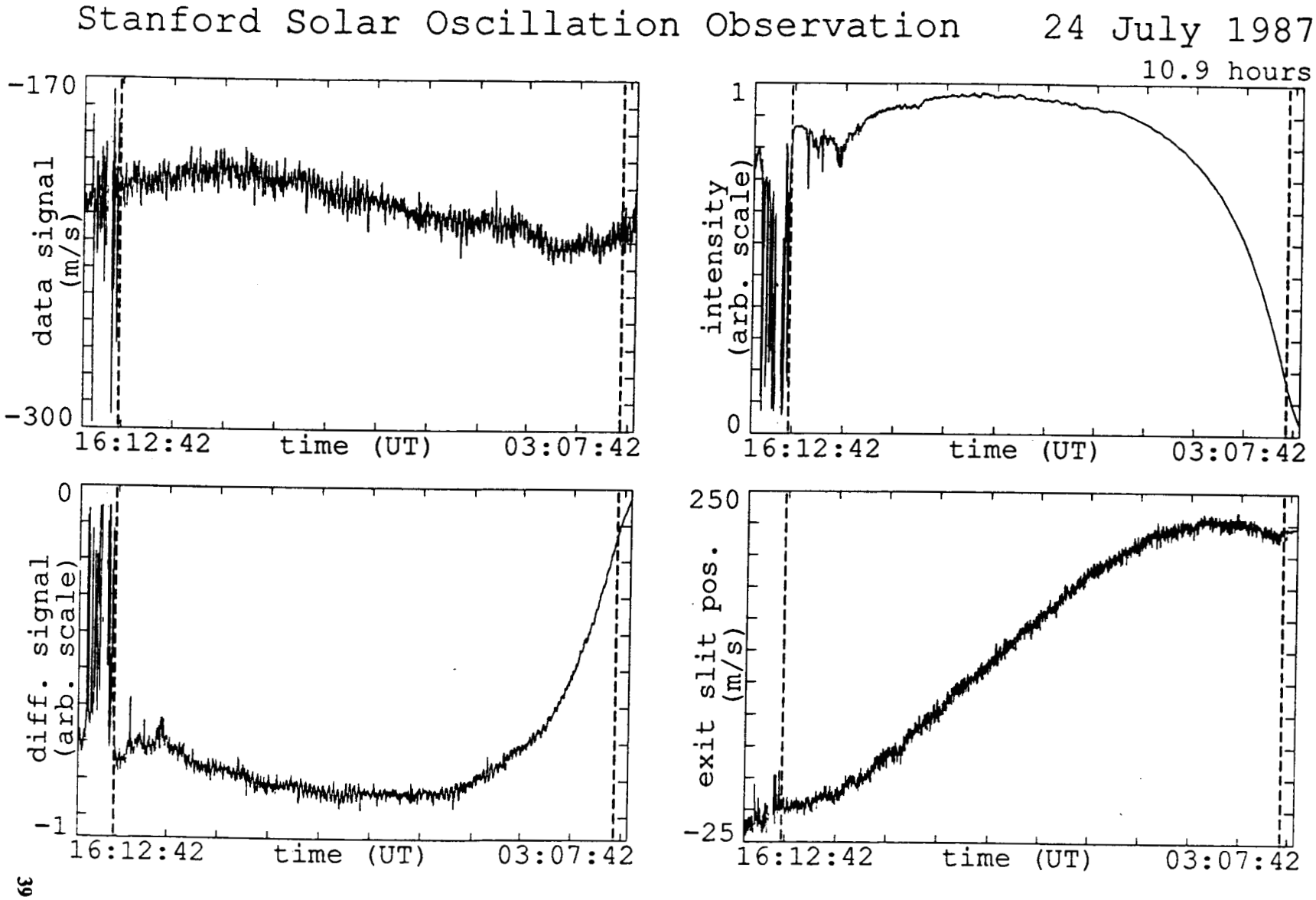

Figure 2.5 - Data on July 24th, 1987. The plot shows the four values which are recorded during the observation. The dashed lines indicate the times where the data was cut for use in the analysis.

day with some cloudyness. The upper right hand panel shows the intensity signal I. The shape of the curve clearly follows the atmospheric transparency law of

$$I = I_0 \, e^{-k A} \tag{2.5}$$

where I_0 is the brightness if there were no atmospheric extinction, A is the airmass, and the constant k depends on the transparency of the air. At Stanford an average value for this constant is 0.24. However, this average hides the fact that there is actually a small but systematic change of this "constant" throughout the day as the line-of-sight between the sun and the observatory passes from the smoggy and hazy, heavily populated Silicon Valley area to the clear air over the western foothills. The intensity signal is thus not symmetric about local noon even on cloudless days. This doesn't affect the part of the data signal coming from solar oscillations, but does affect the data signal through the error signal introduced by the transparency gradient integrated with solar rotation.

The lower right hand panel shows the exit slit encoder signal. Earth's rotation can be seen easily, but an additional drift is apparent as the shape deviates slightly from the expected shape of a sine wave and the peak-to-peak variation is less than can be expected from earth's rotation. On many days the drift is large enough to noticeably change the shape of the sine curve. The major contribution to this drift derives from the change of phototube gain ratio throughout the day. The drifts at the beginning of the observation and at sunset are also visible. The variance in the signal, corresponding to about 15 m/s, is due mainly to light path variations - seeing - in the spectrograph pit itself.

The lower left hand panel shows the difference signal. The most striking property of this curve is that its large scale shape is an almost exact mirror image of the intensity signal, clearly emphasizing the direct effect that a change of intensity has on the difference signal. Superimposed on the shape of the inverted intensity curve is the actual velocity

signal.

Finally, the upper left hand panel shows the data signal, *D/I*. The quality of the data can be estimated from this graph by noticing the clear presence of an oscillatory motion with a period of about 5 minutes and peak-to-peak amplitude of about 15 m/s. It should be noted that the noise in the spectrograph pit alone would be enough to seriously degrade this signal if it were affected by it. Thanks to the differential technique, however, this is not the case. The oscillatory signal is the signature of a superposition of dozens of low-degree p-modes. At times of poor quality, such as in all of 1980, this oscillation is not so clearly visible to the naked eye in the data signal, rather high-frequency noise dominates and the signal magnitude is much lower.

The vertical, dashed lines are the points where this data was cut to exclude the periods with poor quality signal. In this case that is a short period in the afternoon near sunset, and a larger period in the morning where the sun was obscured by clouds. Figure 2.6 shows the power spectrum of that particular day's data as calculated by an FFT (Fast Fourier Transform). The spectrum shows a large, clearly defined bump in power around 3000 μHz. This power is due to the well-known 5 minute p-mode solar oscillations which could be seen in the data signal even without needing the FFT. Another increase in power can be seen around 700 μHz to 1000 μHz before the steep rise at lower frequencies. This signal is, however, not of solar origin, but as discussed earlier, is due to the temperature variation in the observing room. Finally, the power gets very large as the frequency decreases below 300 μHz. This increase is due mainly to the long-term transparency and gain ratio related drift discussed previously.

The new modes which are detected and identified in this analysis lie in two different regions of the spectrum. The p-modes of low frequency lie between 1000 μHz and 1800

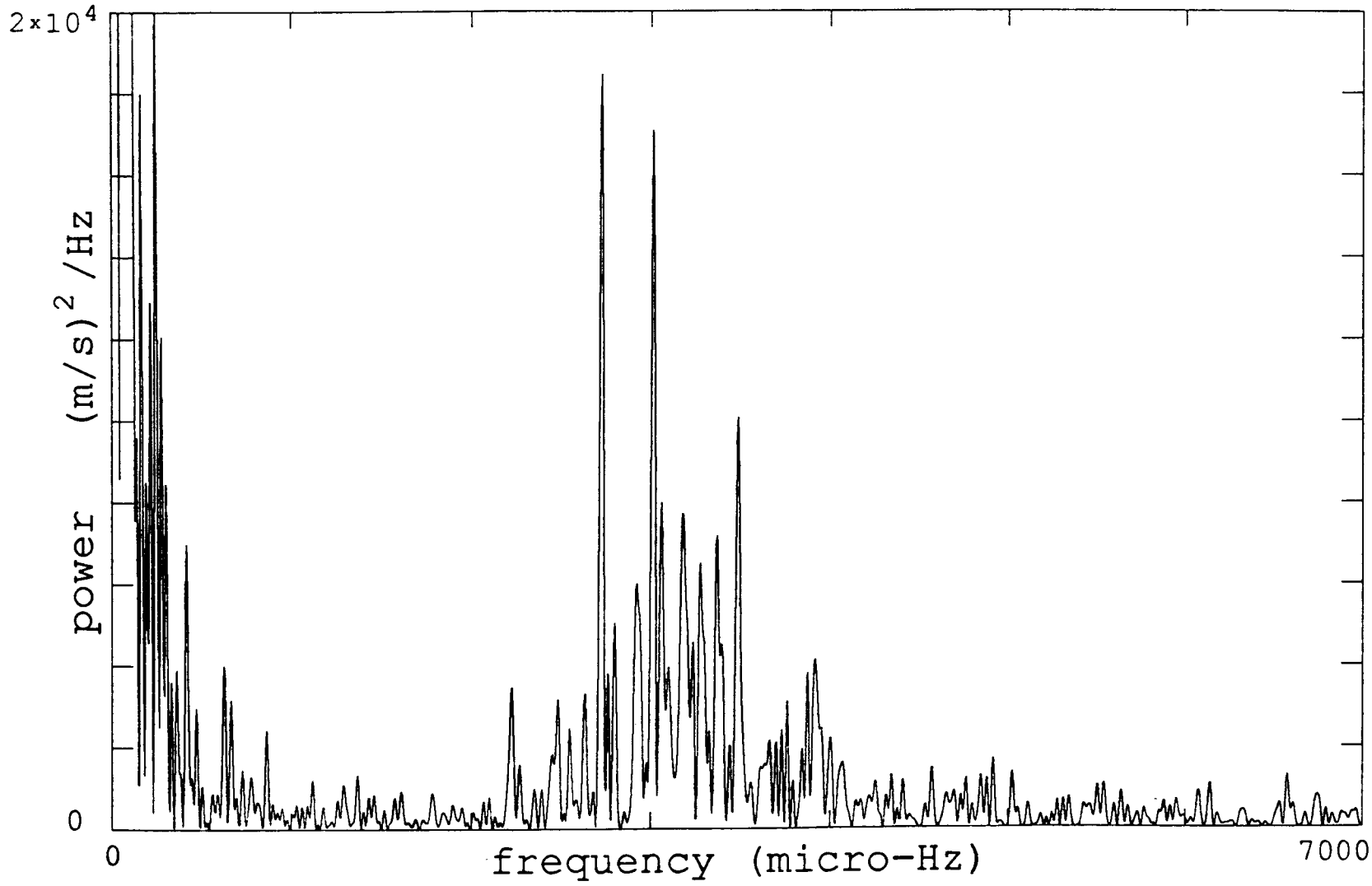

Figure 2.6 - Power Spectrum of July 24th, 1987. The power around 3000 μHz is due to p-modes. The steep rise at low frequencies is a result of the daily drift. The level of power above 5000 μHz gives a good estimate of the noise level at all frequencies above about 1000 μHz.

μHz, while the g-modes lie between 50 μHz and 100 μHz. Both of these regions are dominated by noise in this single day spectrum. The part of the data signal which is of solar origin is buried in the noise power. Clearly any detection of modes requires a longer stretch of data which will allow the modes, which have long theoretical lifetimes in both of the regions of interests, to rise above the noise as the resolution of the spectrum increases and the mode's power becomes concentrated in a smaller frequency bin. For the p-modes only a few days can suffice, while for the g-modes a period exceeding a month is necessary. This is a reflection of the difference in noise power between the two regions.

Thus the individual days of data must be strung together into a single time series. To do so requires some initial processing which is virtually identical for both the p-mode and g-mode analyses. For the years of 1981, 1984, and 1986 each day's data must be normalized since the sensitivity of the instrument changed markedly throughout the observing season. This is accomplished by assuming that the integrated power above the noise power in the 5 minute range, taken from 2500 μHz to 3500 μHz, is constant every day. For the g-modes each day's data is multiplied by a factor equal to the inverse of the power in that range. For the p-modes the variance of the data is simply set to 1.0. These treatments of course wreck the amplitude information which the data may have contained. They also affect the mode determination adversely. When the normalization is performed, it is unlikely that it is exactly the correct relative value, since the integrated power which determines the normalization factor is affected by the varying quality of the particular day. Thus a day with a noisier signal due to hazy sky conditions will have a larger integrated power than a very clear day, even if the modal power remains the same. The true solar amplitude of a particular mode is fairly constant for the long-lifetime modes, resulting in a sharp peak. An error in the normalization factor will result in the true solar signal becoming a signal varying in amplitude in the normalized time series of concatenated days.

The effect on the spectrum will be to spread the power of the solar mode into multiple smaller peaks around the original mode frequency. Therefore the solar oscillation peaks will be smaller and harder to detect in the spectrum. This problem is especially noticeable in the g-mode analysis, where 1987 proves to be by far the best year for modal detection. It is fortunate that the sensitivity change problem was avoided in the 1987 observing season, so that no normalization was necessary for the 1987 data, preserving the amplitude information contained in it, and concentrating the power of each mode in a smaller frequency range.

In both the p-mode and g-mode analyses the mean of the data signal is removed for all days before they are combined into one time series. Figures 2.7a-d show the power spectrum of each year. Compared to figure 2.6, the noise level, estimated by the power at frequencies from 5000 μHz to 7000 μHz, has been decreased by a factor of up to 4 relative to the signal level, the best year being 1987. The resolution is of course also greatly increased.

The disadvantage of these combined time series is also visible, although difficult to distinguish in figure 2.7. One can see the effect of the data window, as many peaks separated by 11.574 μHz appear. This value corresponds to 1/day, and each peak which exists in the data signal appears in the power spectrum accompanied by sidelobe peaks which are at a distance of 11.574 μHz from the original peak. The power from the original peak is distributed among itself and these sidelobes. Figures 2.8a-d show the window function of each observing season. To obtain this function an artificial signal with a frequency of 3000 μHz was put into the data window. That is, at those times where there exists real data, the artificial signal is calculated and put into the time series of the season. Then an FFT is performed on this artificial data. The whole power spectrum is not shown in figure 2.8, since there is virtually no power outside of the plotted range.

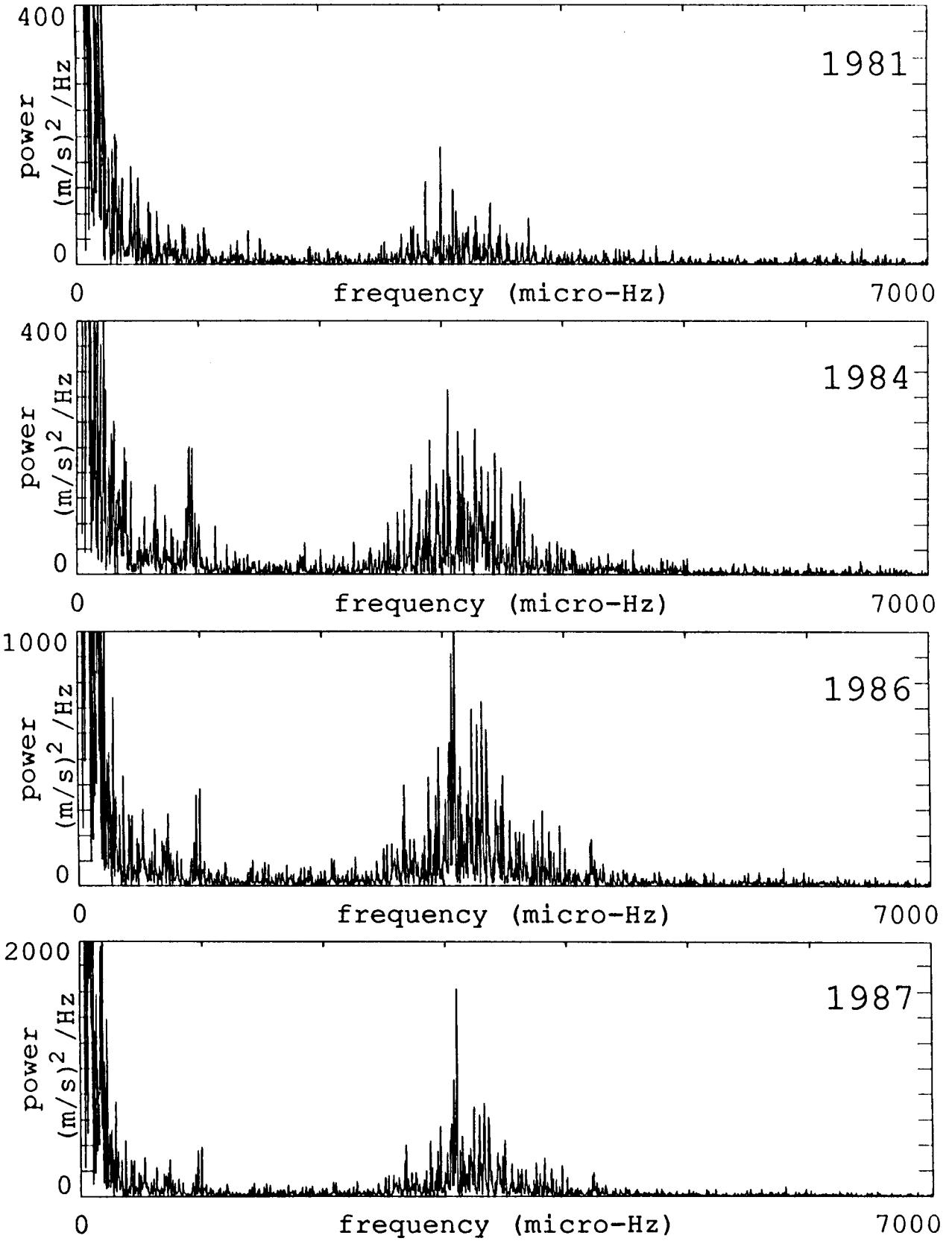

Figures 2.7a-d - Power Spectra of Data. The spectra are calculated using the whole season of data.

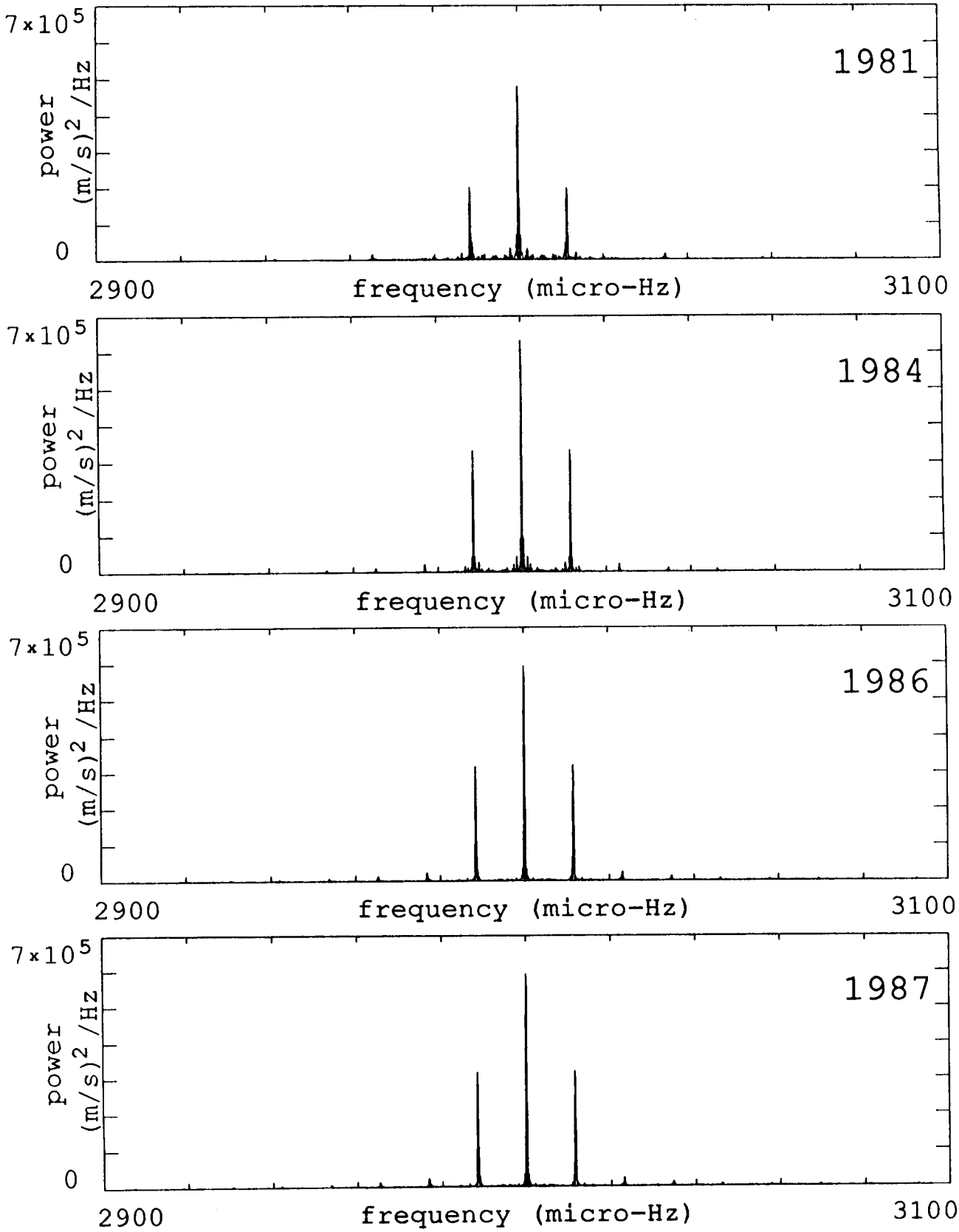

Figures 2.8a-d - Window Functions. The main contribution of the data window in each of these 4 seasons is a pair of peaks, separated by 11.574 μHz from the main peak, with an amplitude of about half the main peak's.

The further methods of data reduction developed for extracting the solar signal from the data are described in detail in chapters 4 and 5, since they are particular to the modes being searched for.

Chapter 3

Transparency Effects on the Data Signal

In the previous chapter it was described how the data signal (the differential velocity measurement) can be affected by a variation in transparency over the observed solar disk. Briefly summarizing, the data signal in effect derives from the difference between the positions of the FeI 5123.73Å line integrated from a central circular section of the solar disk and an annulus around that central area. The position of a line is essentially determined by a summation over the area of optical integration of the velocity multiplied by intensity, then divided by the integral of that intensity. Thus any velocity difference seen by the instrument depends on both the true average velocity difference of the areas and the intensities weighting that velocity.

This chapter is devoted to examining the exact form of the transparency error signal, with the goal of obtaining a power spectrum of this contribution to the data signal. The amplitude of the power in different regions of that power spectrum will give a good estimation of the noise level which will be a determining factor in the analysis. To attain that goal, the power spectrum will be combined from two different sources. The low frequency range of the spectrum, below about 500 μHz, can be obtained by calculating a model for the static transparency gradient due to airmass. The higher frequency contribution, due mostly to haze and clouds, is determined using actual measured intensity variations in the sky and calculating the signal produced by them.

3.1. Static Structure - Airmass

One of the largest, most persistent, and most troublesome error signals in the data has proven to be the contribution of the static transparency gradient of the earth's atmosphere. The gradient is largest close to the horizon, but causes a marked signal in the data throughout the whole day. The gradient acts directly upon the line separation, shifting the lines from the center and the annulus differently and producing an apparent velocity difference. A simplified example will serve to illustrate the effect. Figure 3.1a is a diagram of the solar image with the circular polarization assembly superimposed in it. Solar rotation is indicated by the equally spaced dashed and solid lines on the solar disk. Solid lines represent velocity away from the observer (defined as positive), while dashed lines represent velocity toward the observer (defined as negative). Let's assume a transparency gradient in the sky with a change of 1% per solar radius, i.e. 1% per 1000 seconds of arc, perpendicular to the solar axis of rotation. This is a reasonable number for the mid-morning or mid-afternoon transparency gradient due to airmass. Furthermore, for simplicity let us approximate the integrated velocity by only considering the four marked points on the disk. The solar rotation is about 2 km/s at the limb at the solar equator. Thus, its value at the marked points is about 1300 m/s, 500 m/s, -500 m/s, and -1300 m/s respectively, going from the West limb to the East limb. Assuming the direction of the gradient is as in the afternoon, so that the East limb is brighter, the average relative line position of light coming from the annulus, measured in m/s, is

$$\frac{1300 \times 1 + (-1300) \times 1.015}{1+1.015} \approx -10 \qquad (3.1)$$

Correspondingly, for the center one calculates

$$\frac{500 \times 1.005 + (-500) \times 1.01}{1.005+1.01} \approx -1 \qquad (3.2)$$

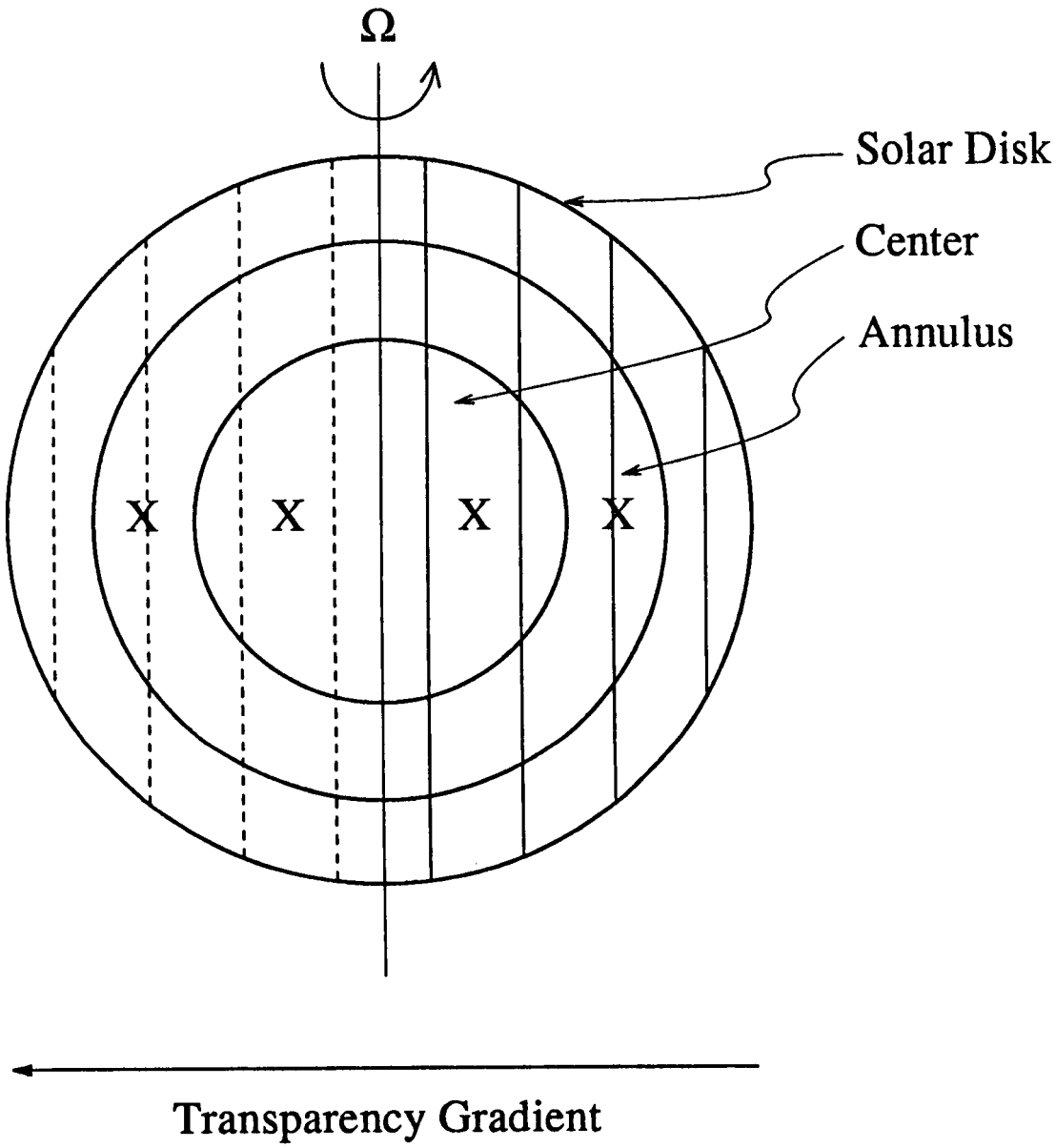

Figure 3.1a - Transparency Diagram. The solar image is shown superimposed on the circular polarization assembly. The vertical lines represent solar rotation.

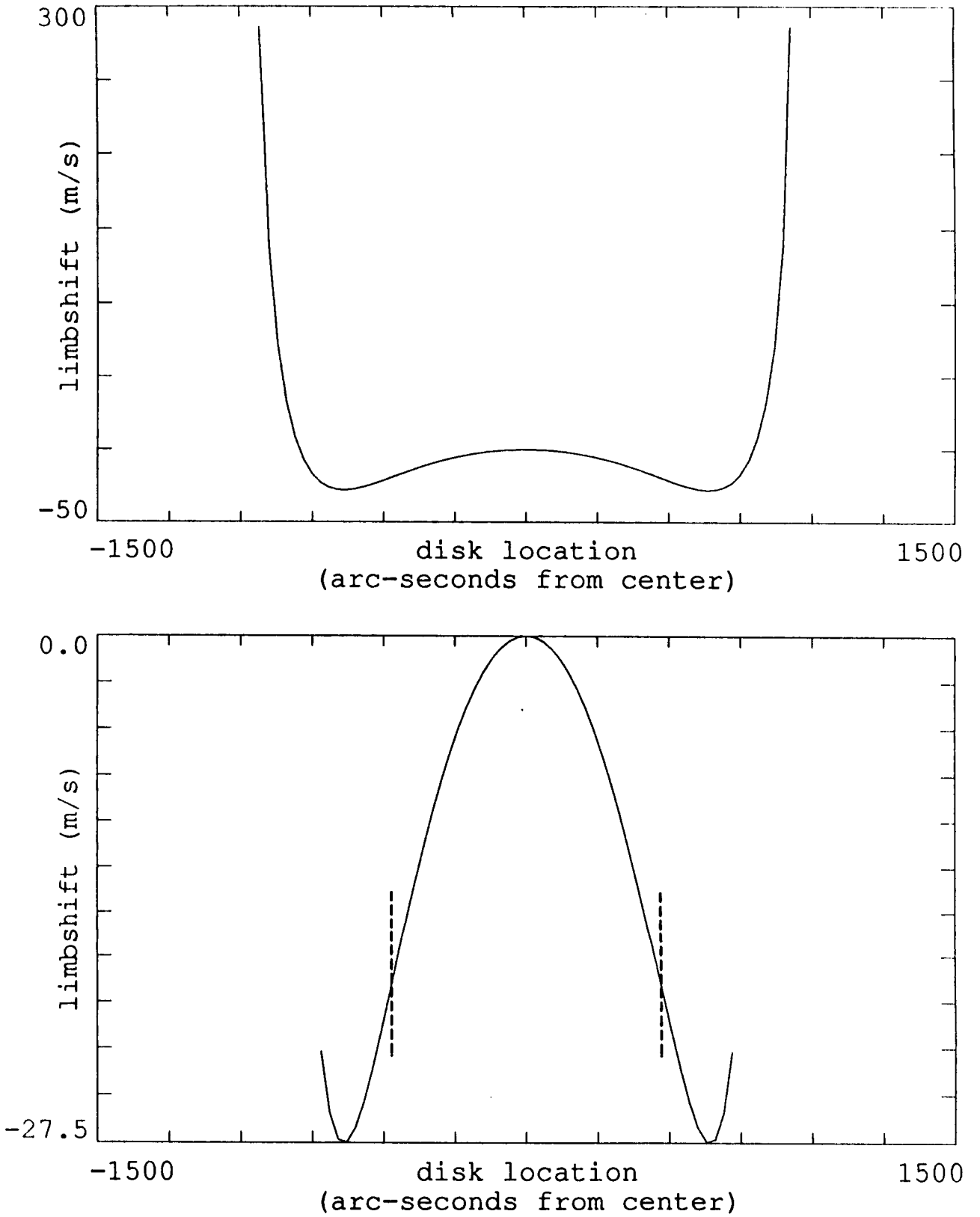

Figure 3.1b - Limbshift Curve. The top panel shows the whole curve, the bottom panel only the portion which lies inside the outer radius of the annulus. The dashed line segments mark the radius of the center of the circular polarization assembly.

The difference between the line positions of center and annulus is thus $-1 - (-10) = 9$ m/s. This signal would be directly measured as a velocity signal. As the transparency gradient varies over the day, rotating on the disk of the sun with respect to the solar rotation axis, lying in one direction on the solar image in the morning and the other in the evening, and changes in magnitude, this signal changes and produces a large drift in the data.

The calculation performed above is a back-of-the-envelope estimate which serves well to visualize the process. However, to accurately explore the effect of this signal on the data one needs a more complex model. The computer model which was used to explore the parameters of the transparency signal calculates the known solar and earth velocity signals which could influence the data to a reasonable degree and adds them up. This includes the earth's rotation and the earth's orbital motion, as well as the sun's rotation and the solar limbshift. Earth's rotational velocity at the latitude of the Wilcox Solar Observatory amounts to 370 m/s. The earth's orbital velocity is 3.0×10^4 m/s. The amount of these velocities that is projected onto the line-of-sight between the point of observation and the point on the solar disk changes in a well-known manner with time of day, time of year, and position on the disk, and is calculated by a standard ephemeris code. The solar rotation is derived from the equation

$$v_{rot} = (1996.0 + 275.0 \times \sin^2(B)\times(1+\sin^2(B))) \times \cos(B_0) \times \cos(B) \times \sin(l) \qquad (3.3)$$

where B is the heliographic latitude north from the solar equator, l is the heliographic longitude west of disk center, and B_0 is the solar latitude of the central point of the disk. Note again the definition of velocity away from the observer as positive. The solar limbshift is taken from LaBonte and Howard (1982):

$$v_{ls} = (-155.0)\times(1-\cos(\rho)) + (727.0)\times(1-\cos(\rho))^3 \qquad (3.4)$$

where ρ is the angle between the line of sight and the solar radius vector at the observed

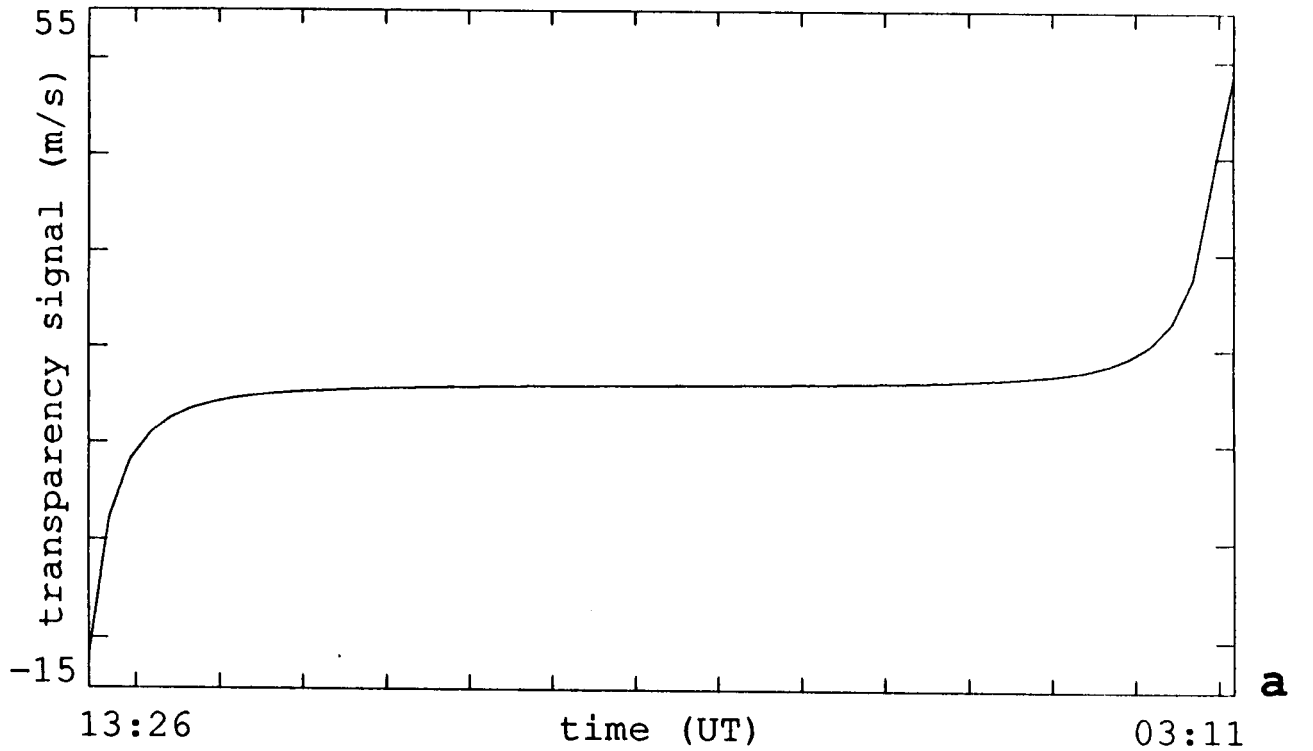

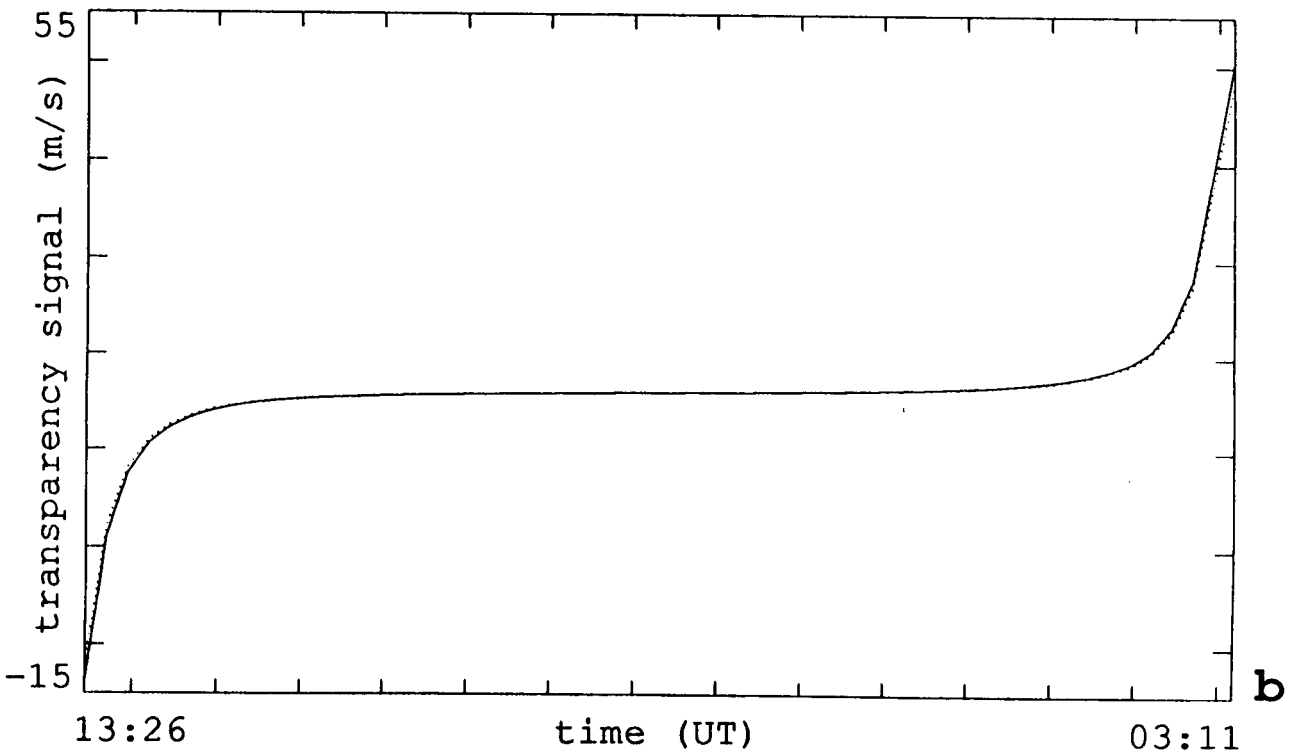

Figures 3.2a-b - Transparency Signal. a) is the full transparency signal. b) shows the signal with only solar rotation, the dotted line is the full signal.

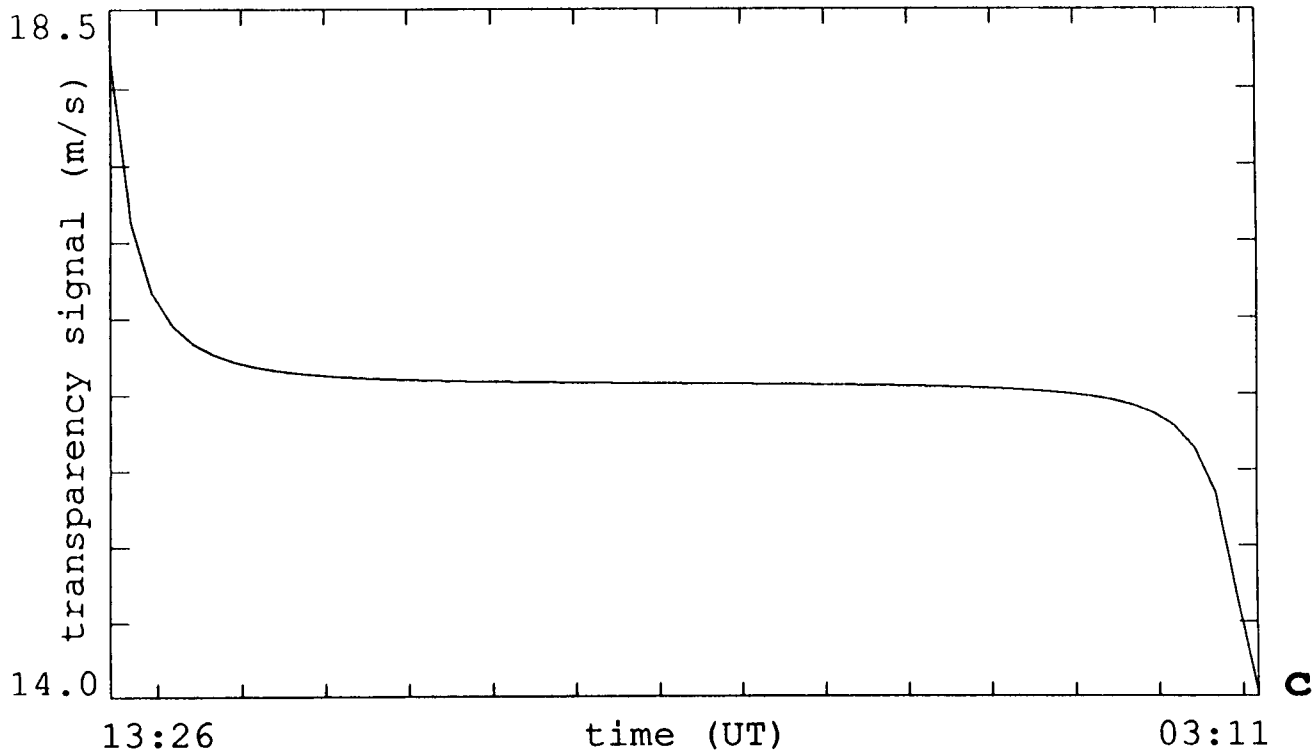

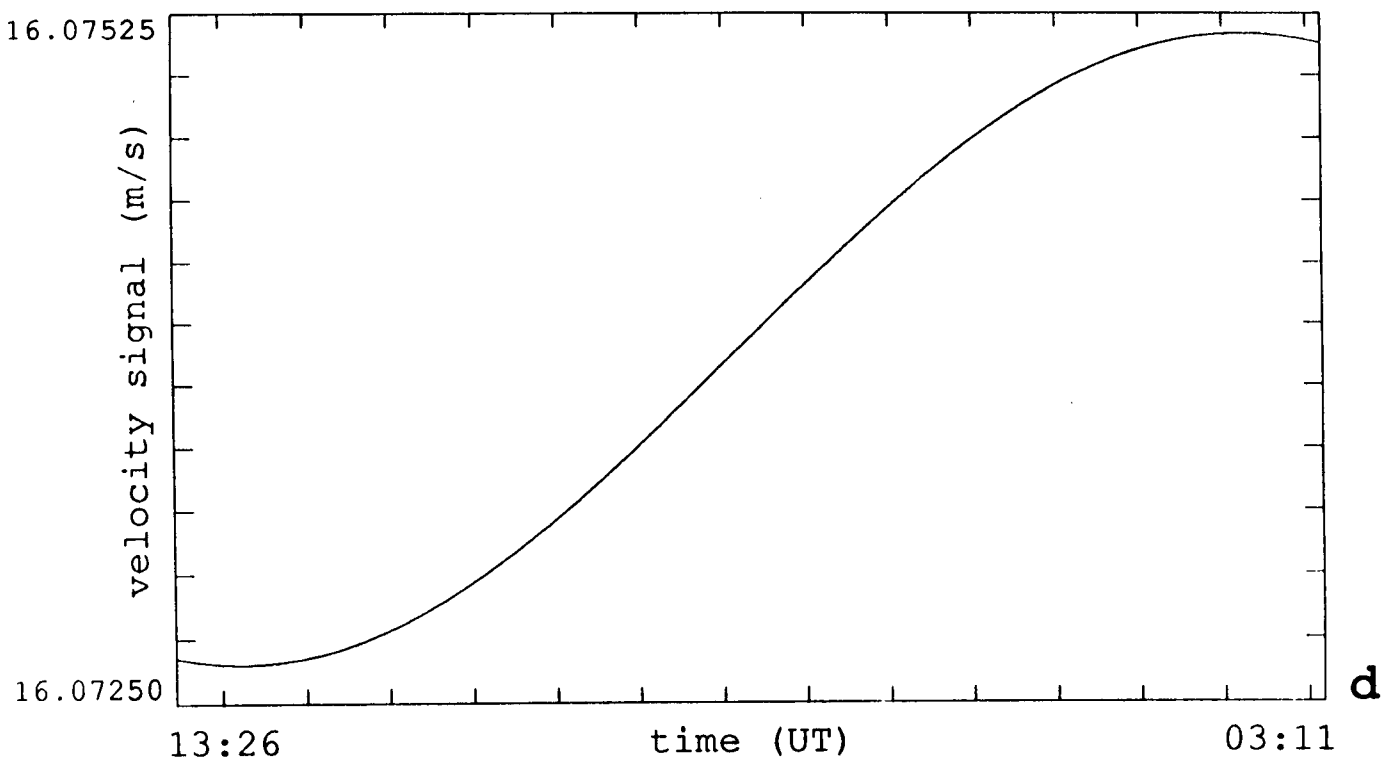

Figures 3.2c-d - Transparency Signal. c) is the transparency signal due to only earth's orbital motion and rotation. d) is the result if there were no transparency gradient.

point. This function is plotted in figure 3.1b. The upper panel shows the full function out to the solar limb, displaying the characteristic W shape. The lower panel shows only the portion of the limbshift which lies inside the outer radius of the annulus of the circular polarization assembly. The location of the radius of the center of the assembly is indicated by the dashed vertical line segments.

The program calculates the intensity, which is the weight for the velocity at a given point, from two multiplicative factors. The first is the atmospheric transmission as determined by the zenith angle of the observed point.

$$A = t\,(1.004 - 0.0026t - 0.0005t^2) \tag{3.5}$$

$$\frac{I}{I_{zenith}} = e^{-kA}$$

where t is the secant of the zenith angle, A is the airmass, and k is the constant 0.24. The second factor is the solar limb darkening function as determined for the location of the point on the solar disk through the use of the equation

$$f = log(1.0 - d^2) \tag{3.6}$$

$$\frac{I}{I_{center}} = 1.0 + f \times (0.30 + \frac{f}{80.0})$$

where d is the distance of the observed point from disk center in units of solar radius, i.e. from 0 to 1. Since only the relative intensity is of importance in the signal calculation, I_{zenith} and I_{center} are taken to be 1.

The program performs a numerical integration of the quantity *velocity* × *intensity*, as well as a simultaneous integration of *intensity*. The integrations are performed over two specified area of the solar disk, one the central section and the other the annulus around it.

The result is then obtained by the equation

$$signal = \frac{4I_cI_a}{(I_c+I_a)^2} \times \left[\frac{\int_c V \times I}{I_c} - \frac{\int_a V \times I}{I_a} \right] \tag{3.7}$$

where the intensity factor multiplying the velocity difference derives from equation 2.5.

Figures 3.2a-d illustrate the basic shape and magnitude of the transparency contribution to the data signal. The date used for these calculations, and many of the comparisons which follow, is July 7th. The reason for this is that it lies in the middle of the observing season and is the date when the position angle of the solar axis is 0, thus presenting the most simple picture to intuitive interpretation of the effects. The effect of changing time of year will of course be examined also in this section.

Figure 3.2a shows the complete transparency signal, including all velocity and intensity components. The shape, a sharply increasing signal in the early morning and late evening with a very gradually sloping curve during most of the day, is the distinctive signature of the transparency contribution to the data signal. In the data that is used for the analysis the early morning and late evening times are removed to avoid the large excursions at those times. The signal is symmetric about noon, since the extinction coefficient used is kept constant. In the actual data its changing value throughout the day would change the slope of the curve slightly. For the purposes of examining the other parameters which affect this signal it is adequate to keep it constant. The mean of the signal, which is the zero level which is not affected by the variation in the sky transparency throughout the day, is at a value of 16 m/s. This number derives primarily from the velocity limbshift. The limbshift is circularly symmetric and doesn't cancel in the integrations over the center or annulus. Thus, it introduces an almost constant velocity difference between the center and annulus. The shape of the curve seen in the bottom panel

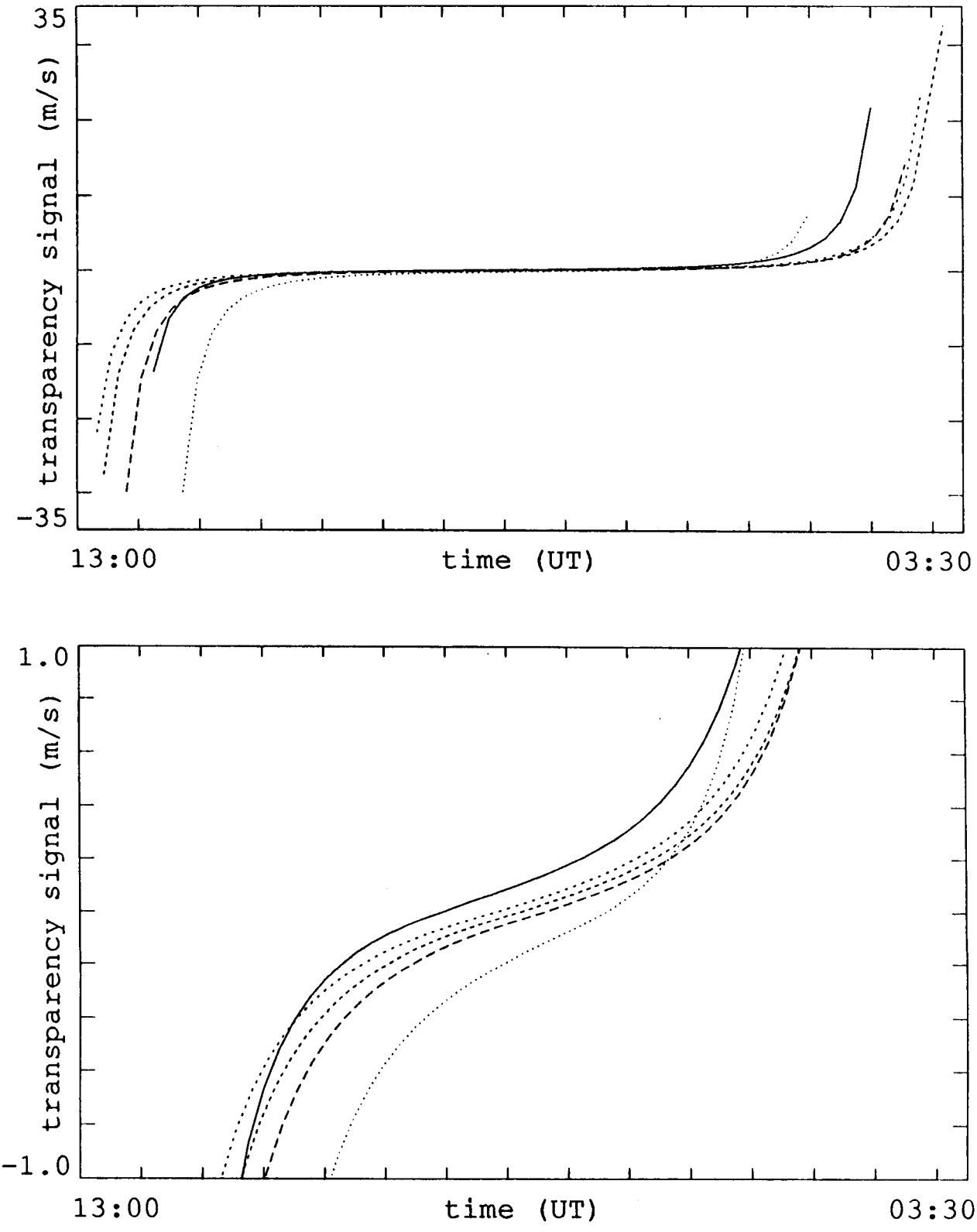

Figure 3.3 - Transparency Signal with Changing Date. The solid line is for April 8th, the short-dashed for June 7th, the dashed for July 7th, the long-dashed for August 6th, and the dotted for October 10th.

of figure 3.1b shows that the central region will have a small negative average, while the annulus will have a more negative average. Since the velocity average of the annulus is subtracted from that of the center the result is a positive velocity signal.

Figure 3.2b shows the transparency signal as it would appear if the motion of the observer relative to the sun were not considered. In other words, the earth's rotation and orbital motion are removed, leaving only the solar rotation to interact with the transparency gradient to produce a signal. The curve from figure 3.2a, the complete signal, is superimposed as the dotted line which is visible only in the morning and afternoon. Clearly the solar rotation is responsible for the majority of the varying transparency signal, and is actually larger than the combined signal.

In figure 3.2c the other part of the signal is plotted. In the calculation that results in this graph the solar rotation has been excluded. The signal has a much smaller magnitude, but a similar shape, although in the opposite sense. It decreases from morning to evening. The reason is straightforward. Solar rotation is an essentially linear gradient across the solar disk, with a magnitude of about 4 km/s, differing from this simple picture only through the tilt of the sun's rotation axis towards the earth and the differential rotation. The earth's orbital motion results in a gradient of about 260 m/s across the solar disk, with the earth generally moving toward the West limb of the sun, and away from the East limb. This magnitude changes negligibly as the earth moves along its elliptical path. The gradient is again essentially linear across the disk, but in the opposite direction as the solar rotation. The gradients are not generally parallel, but close enough to it to be able to state that the signal from solar rotation is about 15 times as large as that from the earth's orbital motion. The earth's rotation also produces a gradient across the disk. Its magnitude changes in a sinusoidal fashion through the day, and it only has a magnitude of 3.2 m/s at the most, really making it negligible compared to the other contributions.

Figure 3.2d shows the signal as it would look without any transparency gradient in the sky. Note the scale change on the vertical axis. The curvature of this line would not be visible at all in any of the other three graphs. The removal of a transparency gradient has removed all the signals except for the limbshift associated velocity difference and a sinusoidal variation which derives from the non-linearity of the gradient of the earth's rotation across the disk. It is visible because its magnitude is the only thing which changes on the time scale of a day. The graph demonstrates the importance of the sky gradient, without which the larger velocities cannot couple into the data signal on a daily time scale.

As mentioned above, most of the transparency investigation is undertaken by changing parameters for one particular date. However, it is important to understand what the effect of the long-term changes of the earth's position are. It is logical to address these changes next. To that purpose, figure 3.3 shows five calculated transparency curves for five different dates including April 8th, June 7th, July 7th, August 6th, and October 10th. The dates were picked to be 30 days apart extending over the period of interest, as well as on the dates of maximal absolute position angle of the solar rotation axis. The curves are calculated using a changing size of the circular polarization assembly to exclude the effect of the changing size of the solar disk. Also, the limbshift was excluded to prevent any erroneous contributions from the numerical calculation as the solar radius change is on the order of the same size as the integration step size. Thus, the only thing which is varying in the calculation is the position of the sun's axis of rotation and the position of the sun in the sky. The curves are plotted on the same scale vertically and horizontally. One clear change is the length of the day. The transparency curve is simply squeezed together on the time axis as the days get shorter. A smaller change is visible in the zero level of the curve, which varies by about 0.3 m/s. This tiny variation derives from a combination of the changing position angle of the solar axis of rotation, the height of the sun in the sky, and

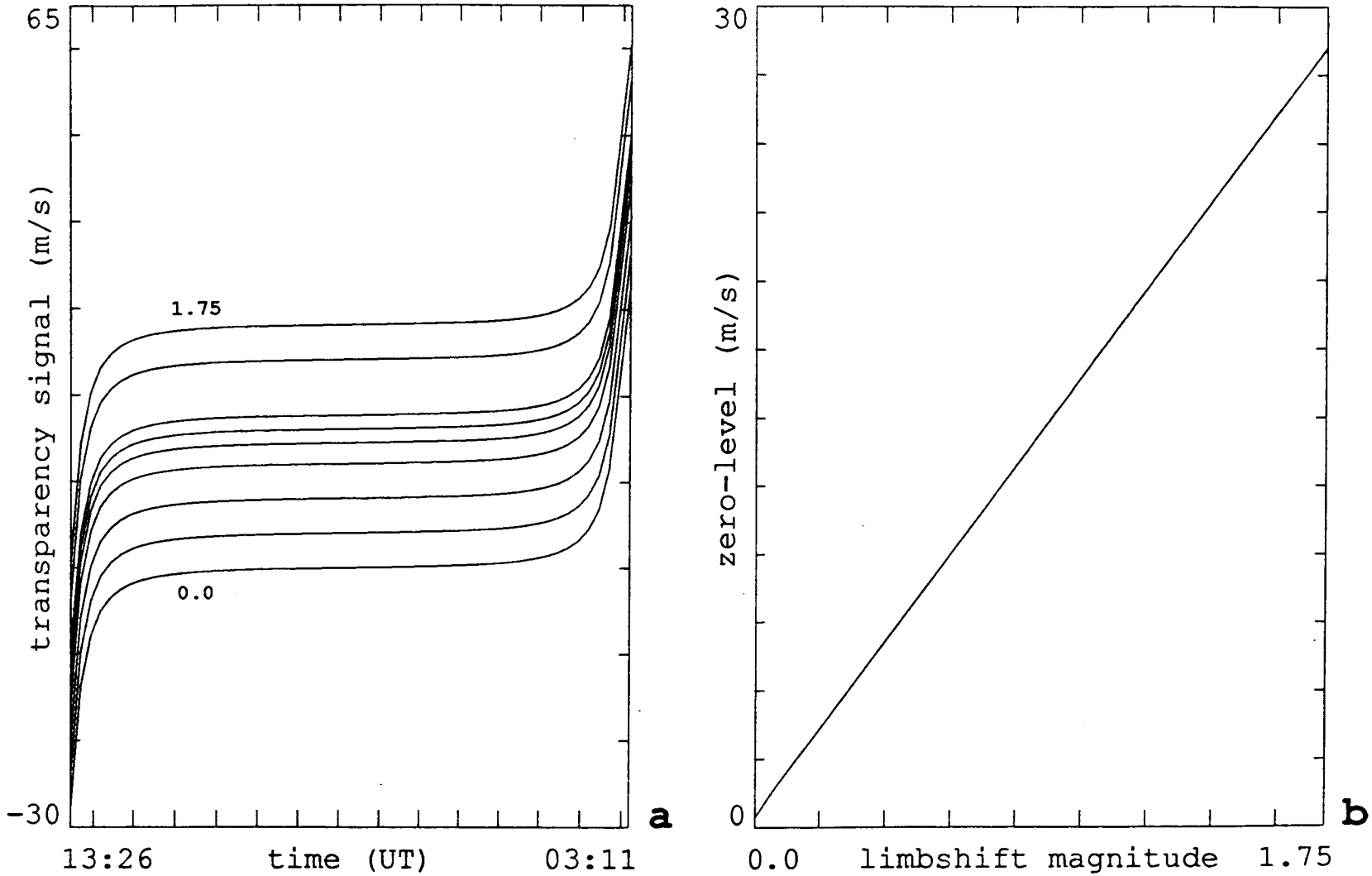

Figure 3.4 - Limbshift. a) the curves, in order, correspond to limbshift coefficients of 0.0, 0.25, 0.5, 0.75, 0.9, 1.0, 1.1, 1.25, 1.5, and 1.75. b) shows the exactly linear relationship of the zero-level offset to the limbshift coefficient.

the changing tilt of the solar axis toward the earth. The position angle comes in through the fact that when it is non-zero, the solar rotation gradient doesn't lie perpendicular to the transparency gradient around noon, producing a signal. The height of the sun in the sky determines the magnitude of the transparency gradient. The tilt of the solar axis changes the integrated solar rotational velocity. Since the zero level is removed from each day's observations for the analyses this very small and slow variation is not of any consequence to this investigation.

As mentioned above, the zero level of the transparency signal is primarily determined by the magnitude of the limbshift. To quantify this contribution several models were calculated with differing coefficients in the limbshift equation (3.4). The magnitude of the two coefficients was multiplied by the same factor, so that the shape of the limbshift curve is not affected. In other words, when this limbshift equation coefficient is 1.0, the two component coefficients are the standard -155.0 and 727.0. When the limbshift equation coefficient is 0.5, the component coefficients become -77.5 and 363.5 respectively. Figure 3.4a shows the calculated curves for various values of the coefficient. The zero level displacement is immediately obvious. Figure 3.4b is a graph of the offset versus the coefficient, and shows the linear relationship nicely. No other facet of the transparency signal is changed, the limbshift just causes a zero offset, as expected from its circular symmetry.

The limbshift comes in not just directly by varying in magnitude, it also can contribute indirectly to a changing signal through a change in the integration areas. One thing which certainly changes the effective area of light collection is the solar disk size change as the earth's orbit takes it closer or farther away from the sun. The change in solar image diameter over the observing season is small, from 1893 arc-seconds in the beginning of June, through a minimum of 1888 arc-seconds in early July, to about 1895 arc-seconds

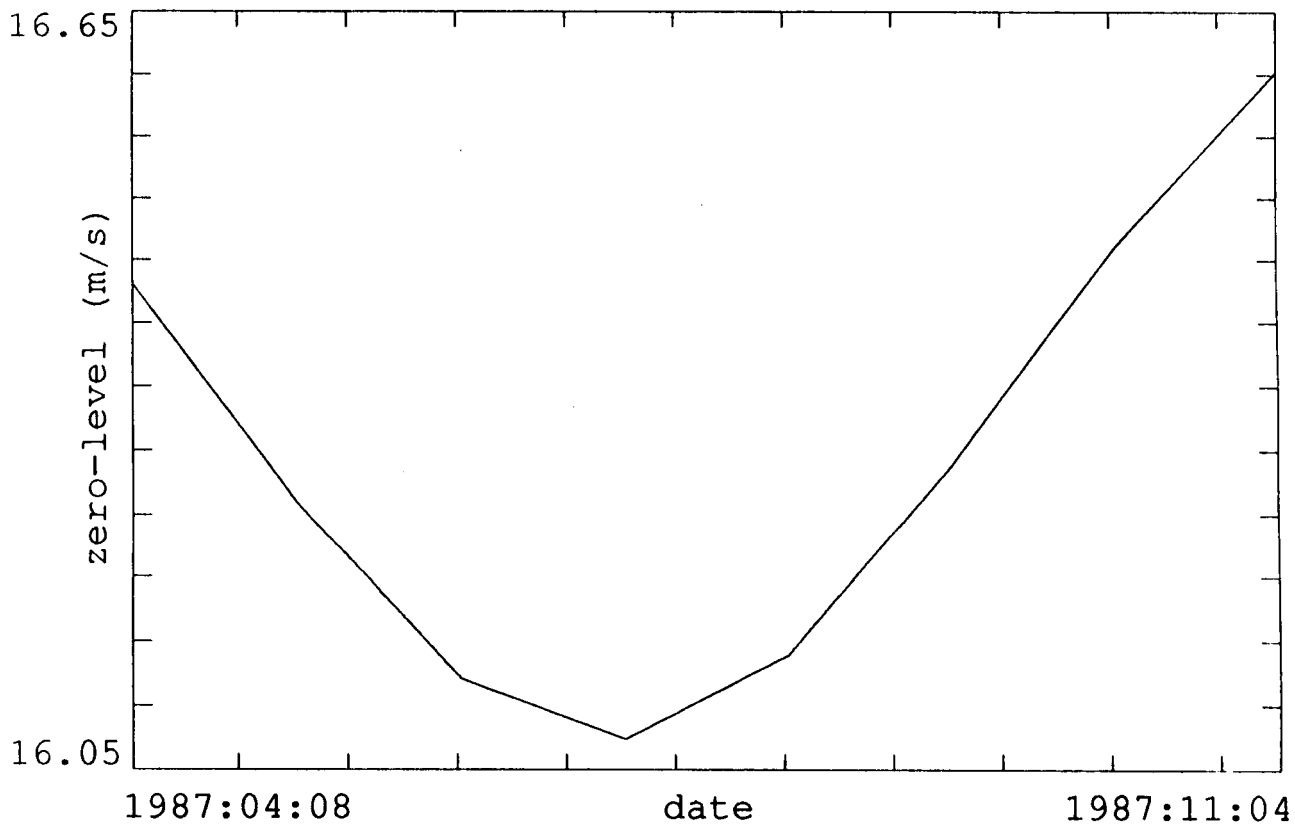

Figure 3.5 - Limbshift Zero-level Shift with Solar Radius Change. The sinusoidal shape is due to the earth's elliptical orbit.

by mid August. The maximum change is thus only on the order of 0.4%. Figure 3.5 shows a graph of the zero level offset due to limbshift through the changing radius calculated for different dates of the year. In the calculation the effects of the earth's motion and solar rotation were left out to prevent them from obscuring the pure zero level effect of the limbshift. Thus there is no daily variation at all in the curves, only a zero level change. Looking at the vertical scale of the figure, one can see that the change is small, following about a 0.8 m/s peak-to-peak sinusoidal variation through the year. During the observing season it is near the minimum of the curve, changing very slowly. This makes for a contribution of only around 10 cm/s, so that it has negligible impact on the data analysis.

If one leaves out solar rotation and limbshift, one can see the effect of the earth's motion over the year. The main effect derives from the changing height of the sun above the horizon. The variation of the gradient of the earth's orbital motion across the disk due to the elliptical path of the earth is negligible. Figure 3.6 shows the curves for different dates, with the vertical scale expanded to enable one to see the change. The effect is very small, amounting to only 2 cm/s of zero level shift. The slope of the curves in the middle of the day is also seen to change with a slightly larger variation, which confirms that most of the change is mainly due to the change of the sun's path through the sky.

The last parameter to investigate as the date of observation changes is the effect of the solar rotation. This will again be dominated by the changing path of the sun through the sky. It will also vary because the changing radius means a different value of rotational velocity will be integrated in the two areas. This should not cause a zero-level change as the previous two velocities, but rather a magnitude change of the S-shaped transparency curve. This change however is swamped by the similar effect of the changing position angle, and the height of the sun above the horizon. Figure 3.7 shows several curves for different dates which have been calculated without limbshift or earth's motion. The effect

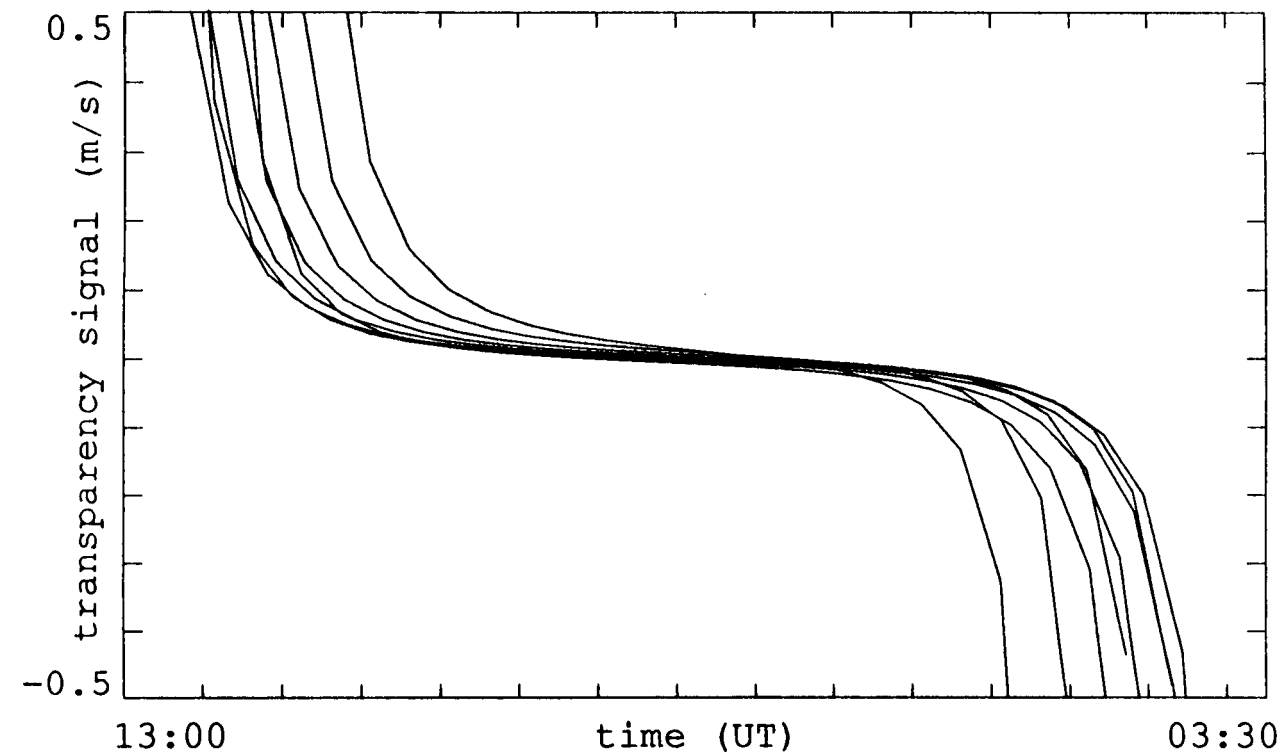

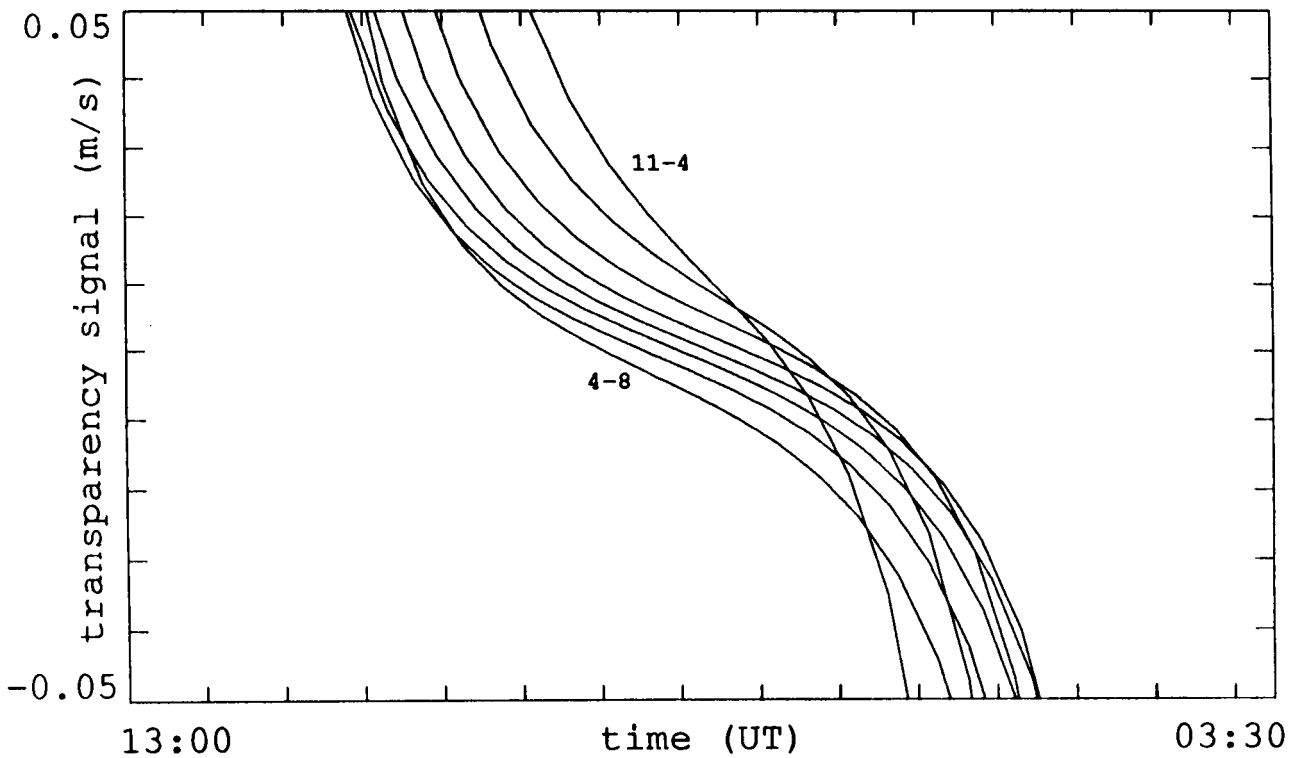

Figure 3.6 - Earth's Motion Effect with Date. The curves correspond, in order, to the dates of April 8th, May 8th, June 7th, July 7th, August 6th, September 5th, October 5th, and November 4th.

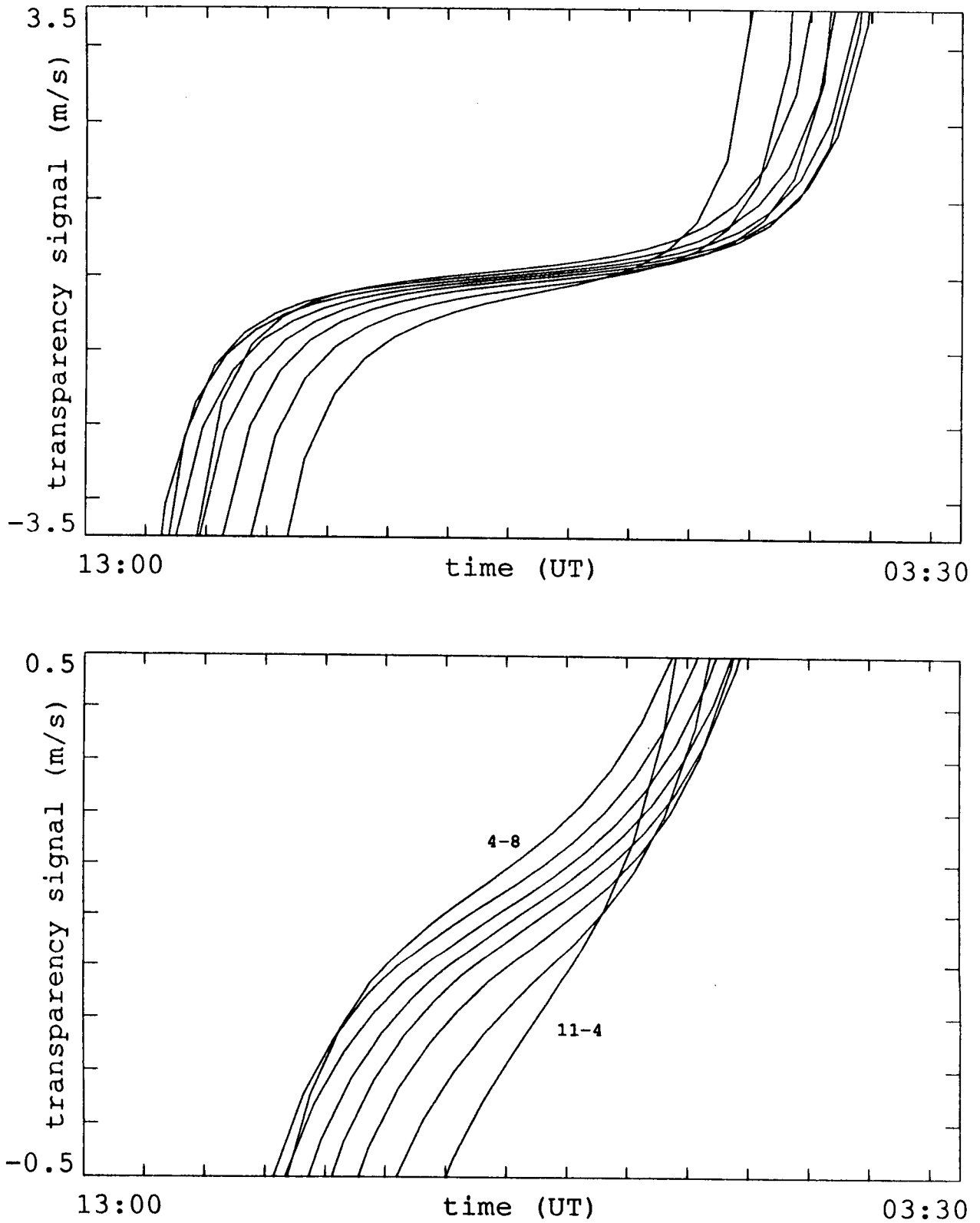

Figure 3.7 - Solar Rotation Effect with Date. The dates are the same as for figure 3.6.

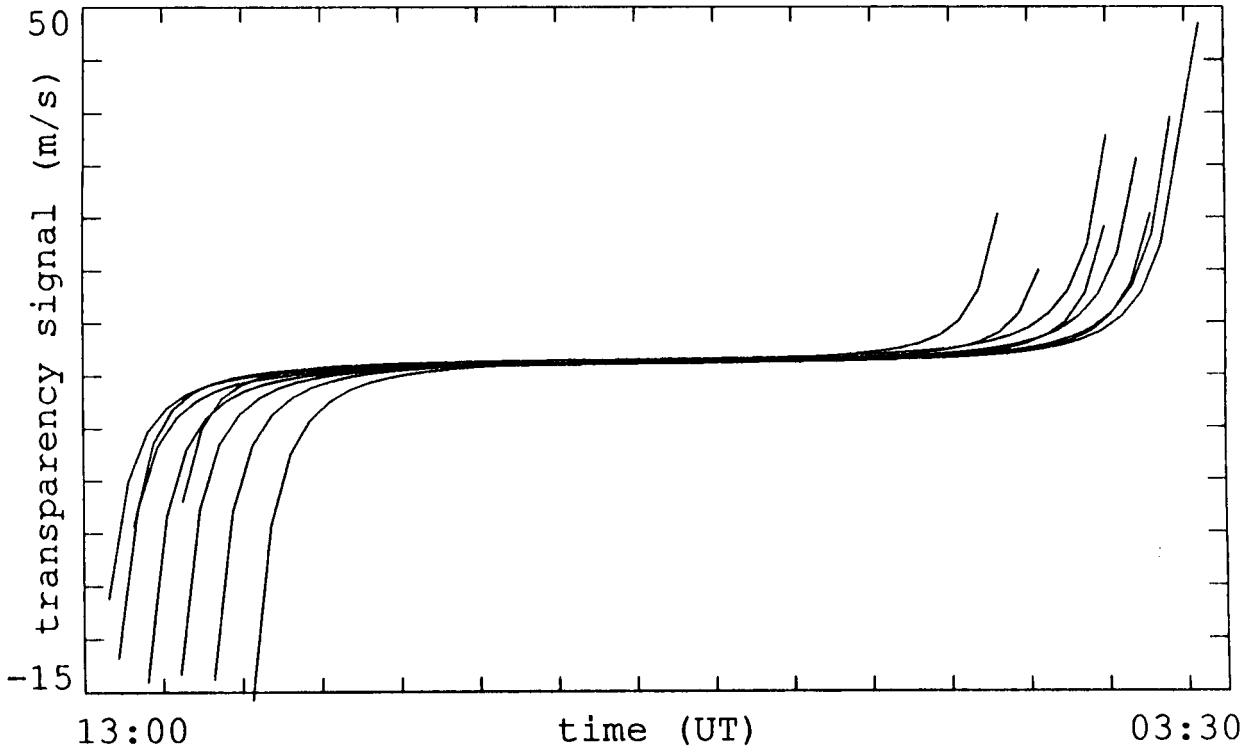

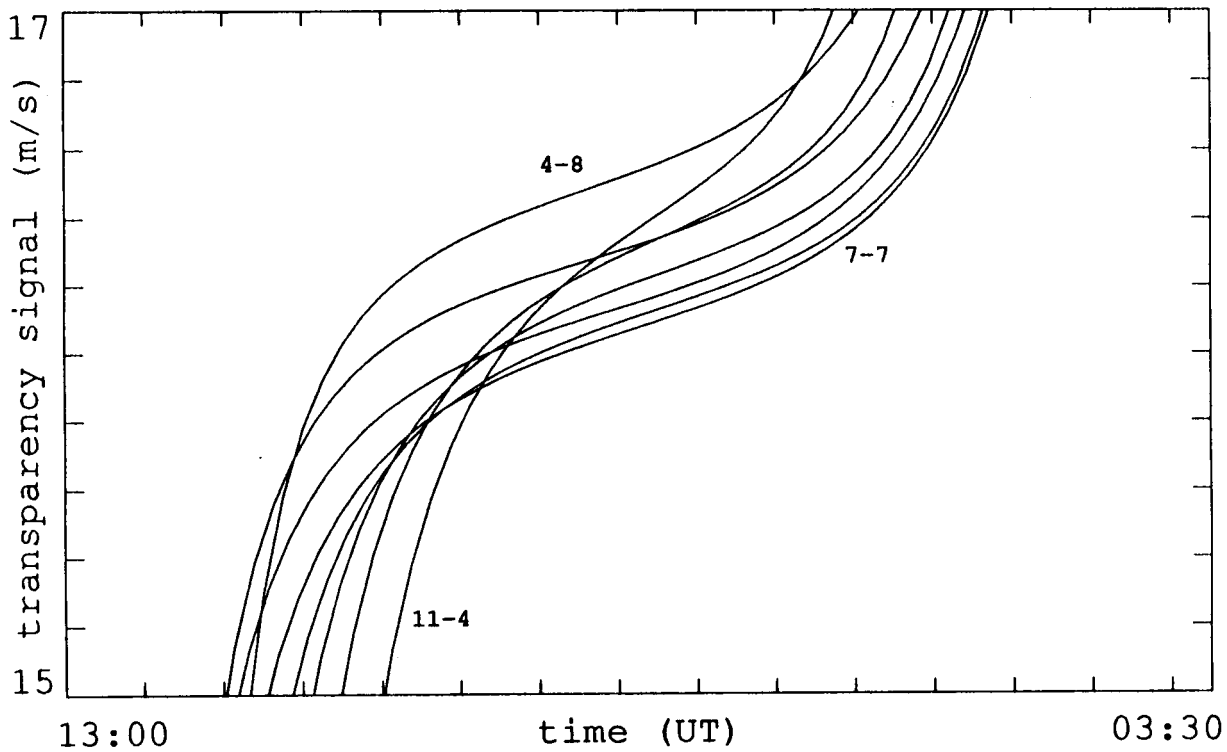

Figure 3.8 - Combined Effect with Date. The dates of the curves are as for figures 3.6 and 3.7, but the progression is not monotonic with date. The three curves which are labeled represent the extrema of the variation.

is small, but about 10 times as large as the change noticed when only the earth's motion was considered in figure 3.6.

All in all, the previous paragraphs demonstrate that the changes associated with the changing time of year are small. Figure 3.8 shows the transparency curves with all velocities included in the calculation. The major effect is due to the change of the length of each day's period of sunshine, which squeezes or elongates the time axis of the transparency curve. The largest zero level contribution comes from variation in the integration of the limbshift as the solar disk radius changes. Another contribution, of almost equal size, comes from the changing path of the sun through the sky. This effect can be considered a zero level shift, or equivalently a shift on the time axis as local noon changes. Overall, the yearly variations will only contribute effectively to the power spectrum through the changing length of the day. During the observing season, however, this change is also negligible. There are other considerations concerning the instrument which must be taken into account, however, which cause signals much larger than these.

The first consideration is the actual size of the circular polarization assembly. Any uncertainty in the size of a component will directly influence the integration area, changing the signal by bringing in a different zero level due to the integrated limbshift, as well as changing the curve's shape since the integration is performed over different areas of the disk. Figures 3.9a-b show the different curves calculated for varying configurations of the assembly. In figure 3.9a the radius dividing the center and annulus was varied from its ideal value of 0.5 times the solar radius R_S. When this value is decreased, the average limbshift velocity in both the center and annulus become less negative. Also, the ratio of central intensity to annular intensity decreases. The effects are opposite when the radius is increased. The changing intensity ratio will decrease the instrumental sensitivity whether it

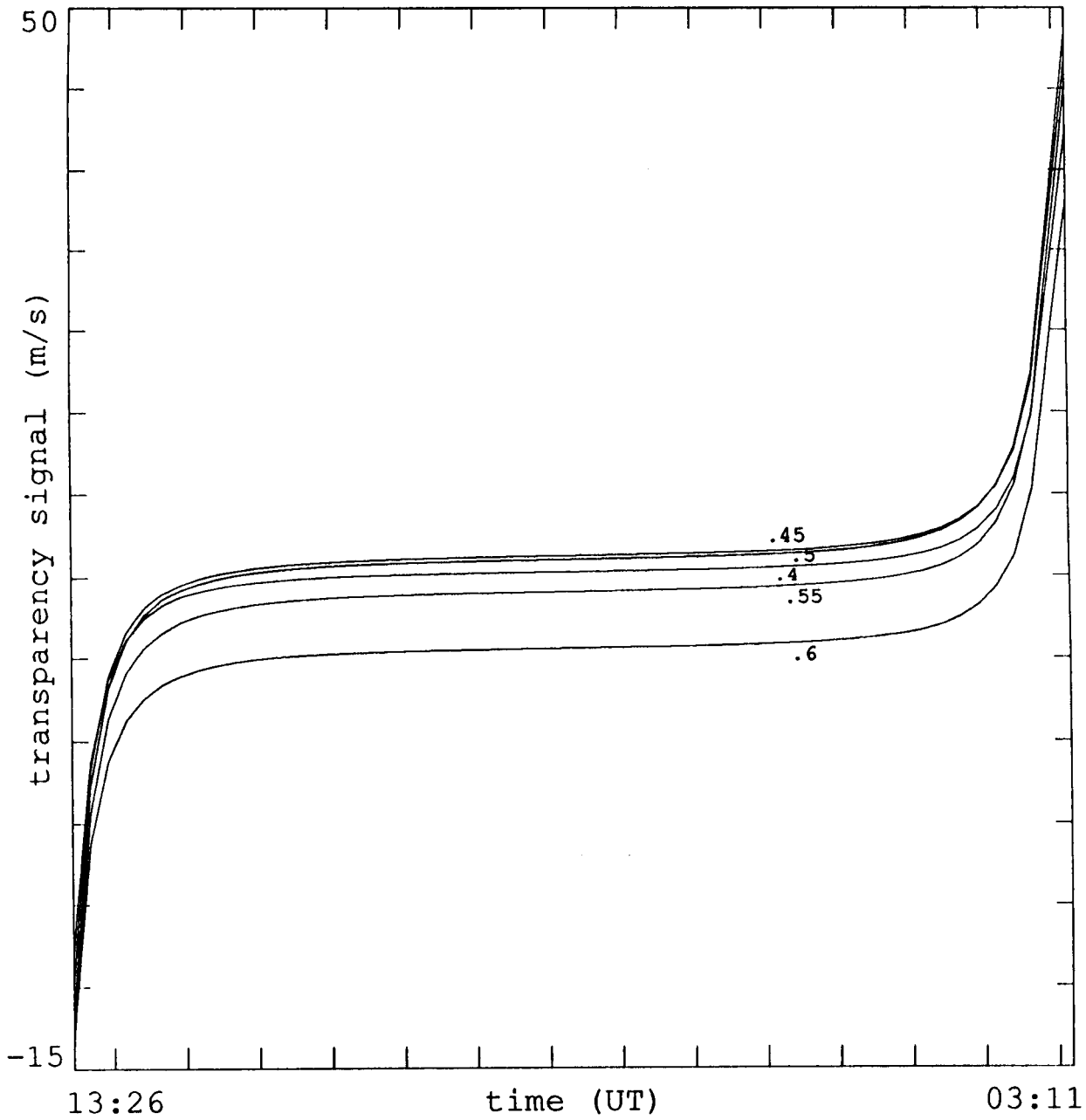

Figure 3.9a - Change with Center and Inner Annular Radius. The labels on the curves refer to the radius of the center of the circular polarization assembly.

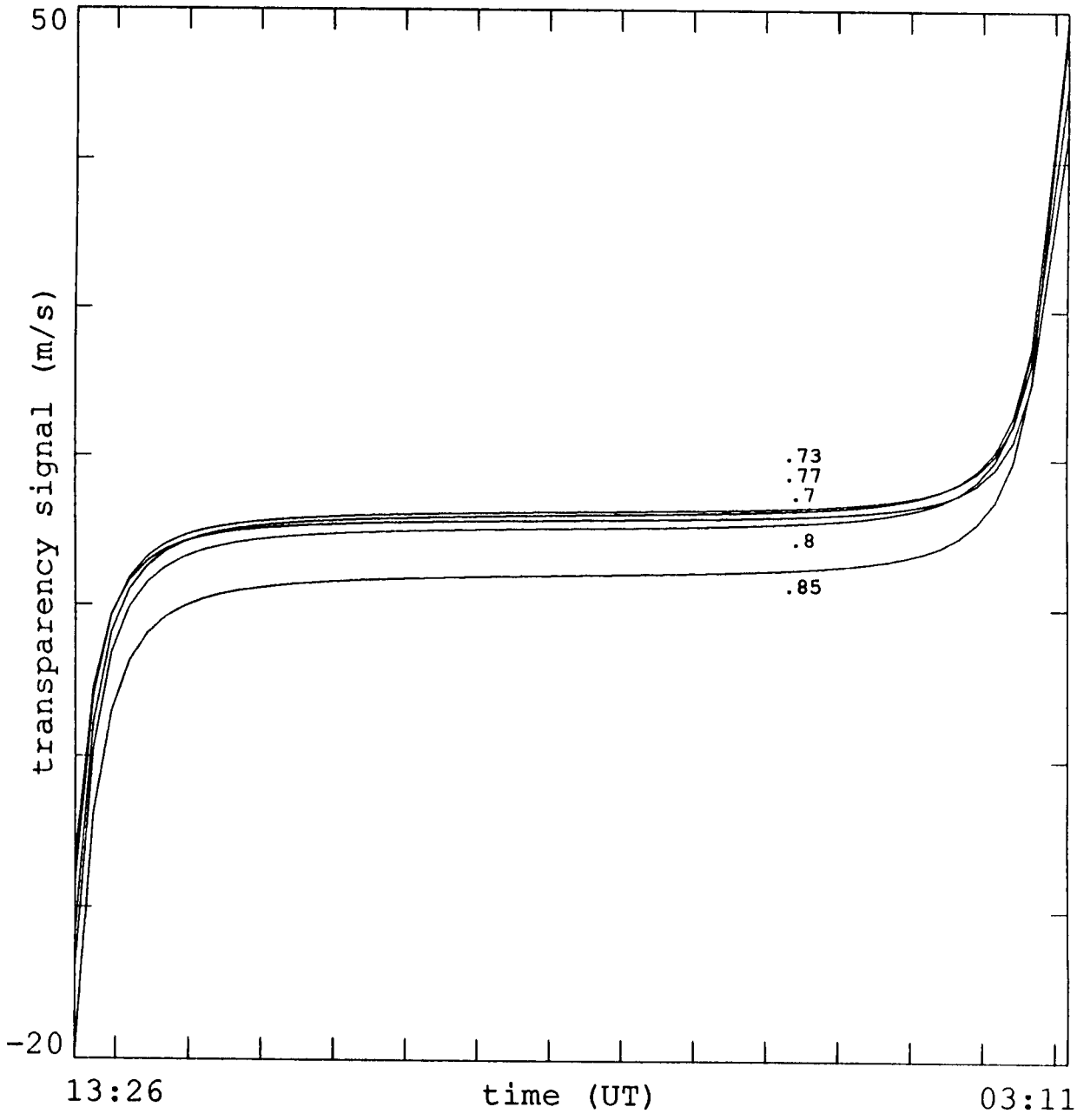

Figure 3.9b - Change with Outer Annular Radius. The labels on the curves refer to the outer radius of the annulus of the circular polarization assembly.

is larger or smaller than 1. This causes the S-shape's magnitude to decrease. This is apparent in figure 3.9a as the peak-to-peak magnitude of the transparency drift is nearly 60 m/s for the curve corresponding to a radius of 0.5 R_S, and only about 50 m/s for both the 0.4 R_S and 0.6 R_S cases. A velocity integration change, which should be a monotonic function of the central radius, is not noticeable, being overwhelmed by the sensitivity change due to the intensity ratio variation. The zero level shift due to the limbshift is noticeable, with a magnitude of nearly 7 m/s between the two curves of 0.45 R_S and 0.6 R_S. It is interesting to note that when the central radius is further decreased to .4 R_S, the zero level shift reverses direction and becomes lower rather than higher. This is due to the shape of the limbshift function.

In figure 3.9b the outside radius of the annulus was changed instead. This keeps the velocity and intensity being integrated in the center constant, but changes them both in the annular region. The intensity ratio change again decreases the sensitivity. The integrated limbshift introduces a zero level shift which is negative for a large increase in the radius because the average limbshift velocity in the annulus goes up and the annulus gets subtracted from the center. The magnitude amounts to 5 m/s difference between curves with outer annular radii of 0.73 R_S and 0.85 R_S. Again one notes that the limbshift change is not monotonic with radius, as the value for 0.7 R_S is less than that for 0.73 R_S. The changing area of velocity integration has a very noticeable effect, as compared to figure 3.9a. An increased velocity in the outer annulus results in an increased sensitivity to the transparency gradient as the difference in velocity between the center and annulus increases. This is visible as a nearly 70 m/s peak-to-peak magnitude of the 0.85 R_S curve, as opposed to only a 50 m/s magnitude in the 0.7 R_S case. On the other hand, as compared to the cases in figure 3.9a, the sensitivity decrease due to the changing intensity ratio is smaller for this configuration change, and is swamped by the changing velocity

integration.

Although it has been demonstrated that the size of the assembly components can cause a sizable change in the signal, especially its peak-to-peak magnitude, their size is known fairly accurately through the fact that the intensity is equal in both areas and the central area is a single half-wave plate of known dimension. The iris diaphragm is adjusted at the beginning of each season and theoretically stays fixed throughout the summer. However, as discussed in the previous chapter, a check made on the intensity values after the 1987 observing season revealed a 3% difference between the center and annulus. This is more than could be expected from a solar radius change coupled with limb darkening (about 0.6%), and thus leaves open the possibility of a change in the configuration of the circular polarization assembly. The possible causes range from a slight transparency change of either the filter or the linear polarizer due to heat from the sunlight, through an alignment change of the polarizer with respect to the quarter-wave plate, to a slight change in the iris diaphragm's opening, to dirt. Although inspection revealed no apparently mobile or impaired parts, another clue was provided in the fact that the light from the center was slightly less purely circularly polarized than could be expected. This points to a small alignment shift between the polarizer and the quarter-wave plate. The possible sensitivity change increases the uncertainty of the calibration of the data signal. However, overall the changes are so small as to be negligible. One can safely assume the theoretical sizes for the circular polarization assembly for purposes of modelling the transparency to get its power spectrum.

A contribution to the signal which is not at all negligible arises from the uncertainty in the horizontal position of the solar image with respect to the optics in the circular polarization assembly. The assembly is swung into the data beam before each observation, and swung out at the end of the observation. Thus it is not in a fixed location, being

locked into position by a magnet, and is liable to be slightly inexact. The whole package - assembly, motor, and switch - is removed as a unit at the beginning of each year to enable cleaning of the optics. When it is replaced there is no way to check accurately that the image is exactly centered. Furthermore, probably the largest contribution arises due to the lens which makes the image on the assembly. It is inserted by hand for every observation, virtually assuring small changes in its position on a daily basis. Combining these considerations, it is likely that there is an uncertainty of 1 to 2 mm in the position of the center of the assembly with respect to the solar image. This isn't much, but on an image of size 2.52 cm it is large.

The effect of such a shift of the solar image on the data signal is shown in figures 3.10a-b. Figure 3.10a shows the variation of the transparency signal with a shift of the polarization assembly in the East-West direction. Solid lines correspond to an eastward displacement, while dashed curves mark a westward offset. Figure 3.10b shows the variation with a North-South displacement, with dashed lines corresponding to a southward displacement. To clarify, the direction is defined in the observing room's coordinates of the imaged sky, not the cardinal directions in the observing room. Due to the reversal introduced by the imaging lens, an eastward direction in the sky actually points in the cardinal West direction in the room, and correspondingly for the other compass points. Since the calculations are performed for the date when the position angle is zero, the solar rotation axis coincides with the North-South direction. As can be seen in the graphs, there is a large zero level shift of the curve for a displacement in the East-West direction. This is to be expected, since that direction is perpendicular to the solar rotation axis. As the center of the assembly is moved, the solar rotation doesn't cancel any more in each area of integration. The effect is a large zero level shift proportional to the magnitude and direction of displacement. The symmetric limbshift signal then is added to the antisymmetric

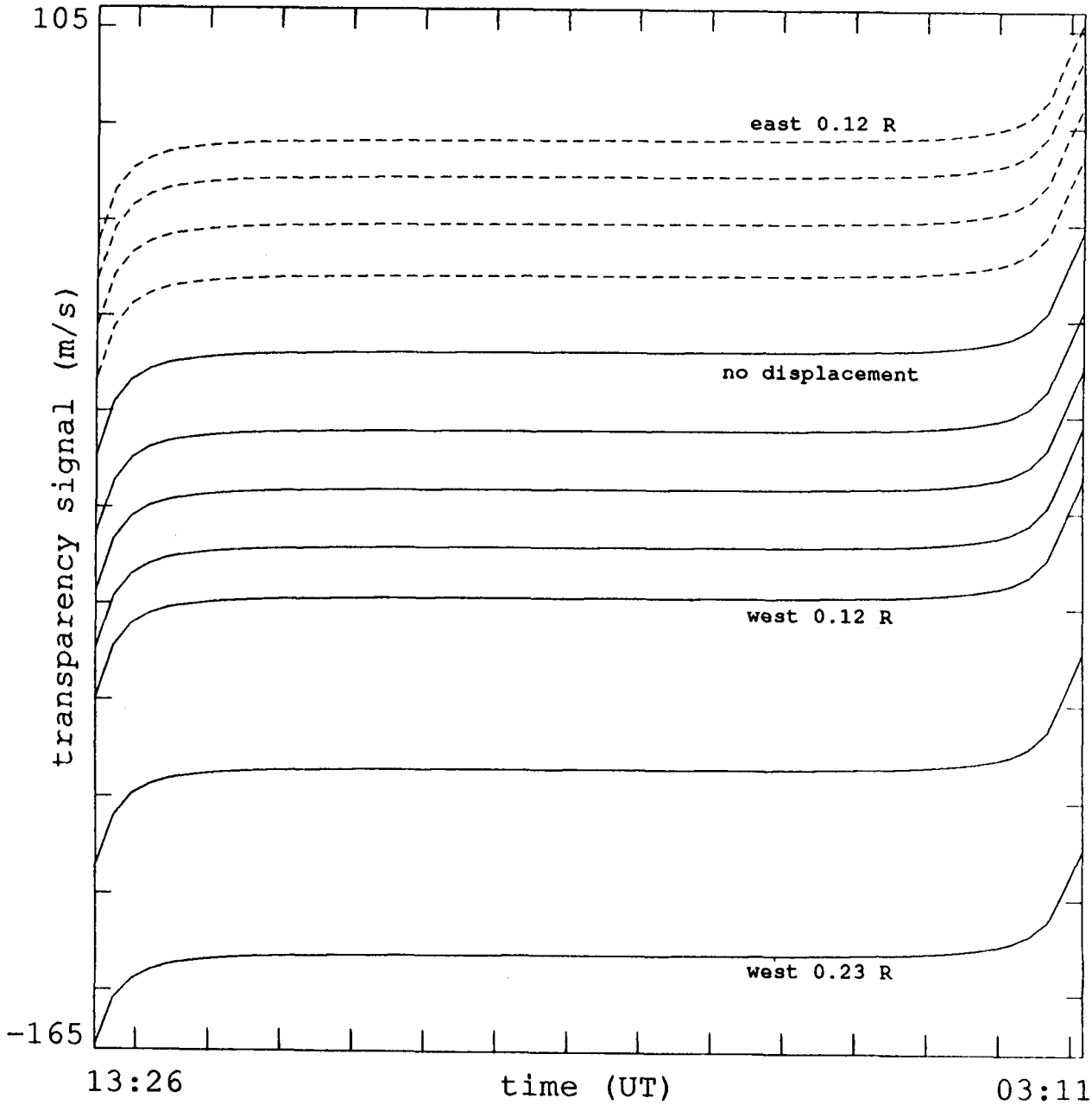

Figure 3.10a - Change with East-West Displacement. Dashed curves indicate an eastward displacement of the circular polarization assembly. From top to bottom, the curves correspond to a displacement of eastward 12%, 9%, 6%, and 3%, no displacement, and westward 3%, 6%, 9%, 12%, 18%, and 23% of a solar image radius.

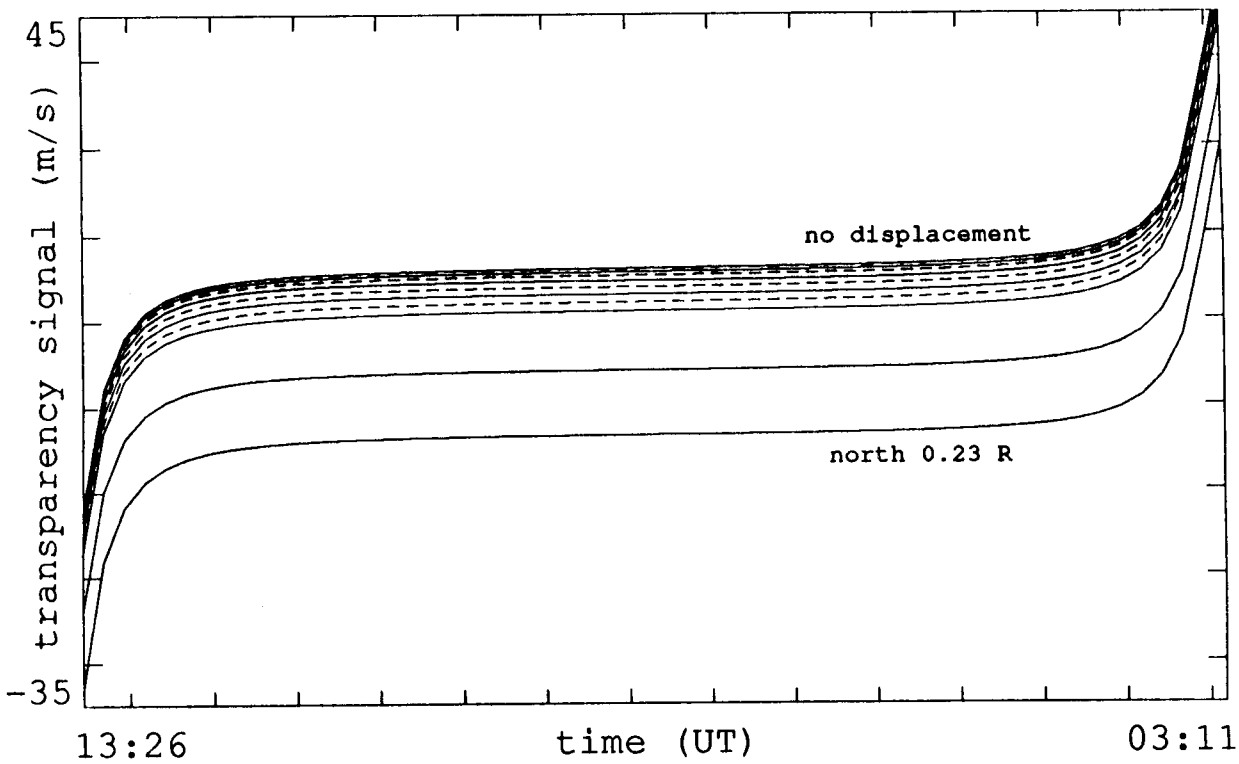

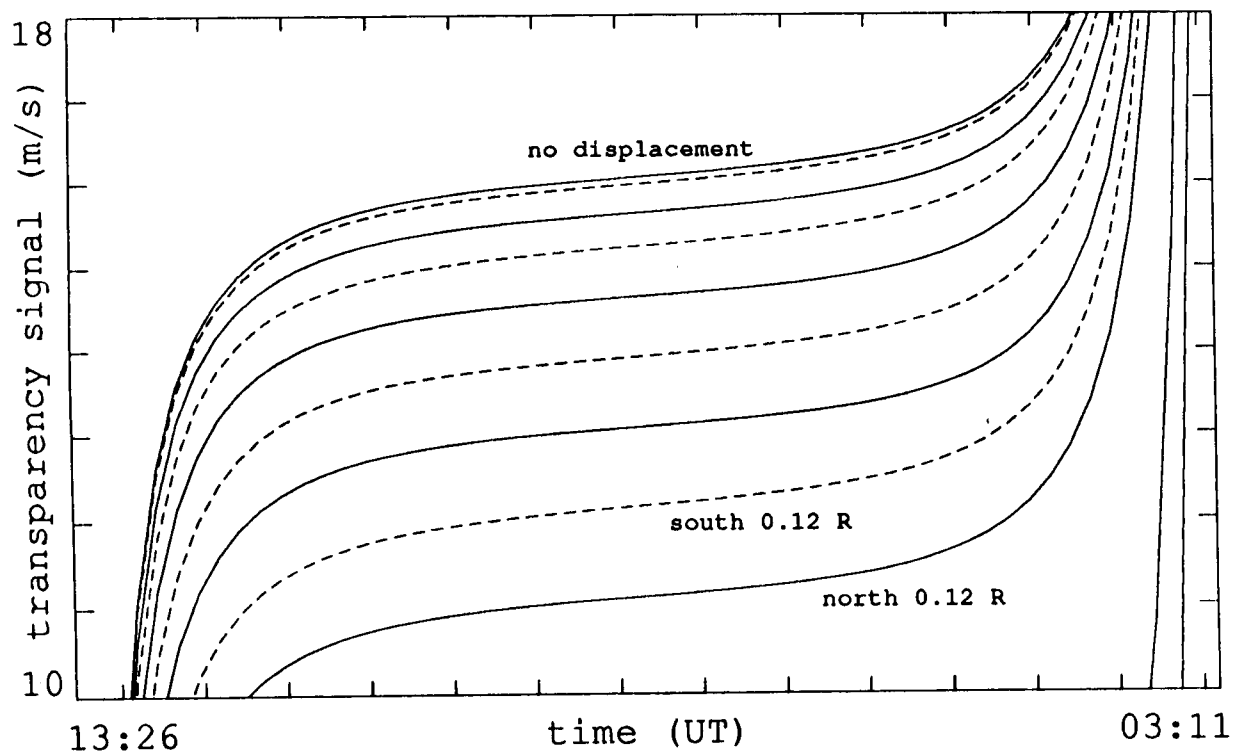

Figure 3.10b - Change with North-South Displacement. Dashed curves indicate a southward displacement of the circular polarization assembly. The amount of displacement is as for figure 3.10a, but the curves move down for a displacement in either direction.

rotational signal to result in the slightly antisymmetric behavior displayed in the graph. The North-South direction also shows a zero-level shift, but this is nearly symmetric for a North or South displacement and much smaller for most values of the displacement. This is also as expected since mainly the changing limbshift integration contributes in a North-South displacement, since the solar rotation is still cancelled in each area of integration. The small non-symmetry, which is best visible in the lower panel of figure 3.10b, is due to the fact that the position angle is not identically zero and so a small component of solar rotation can actually come in.

As the sun's position angle changes with the earth's motion, the solar image rotates on the circular polarization assembly. Any fixed physical displacement of the assembly will interact with the rotating image to produce a changing zero level throughout the season. The shift will be maximal when the rotation axis is lined up perpendicular to the displacement, and minimal when it is parallel. However, the change in the position angle over the two month season from June to August is only about 30 degrees, which makes a sinusoidal shape hard to detect. Figure 3.11 shows the zero level of the 1987 data. A systematic change is evident, with a magnitude of about 100 m/s. This is a large change and it is unlikely that it is solely due to the 30 degree rotation of the solar axis on a horizontally displaced detector. Moreover, the average zero level is a very large negative number, more than could be reasonably explained by a horizontal displacement. The displacement would have to be larger than is deemed possible. Other mechanisms suggest themselves for introducing such a large value of the zero level. One possibility is a systematic difference between the line shapes originating from the central area and the annulus. This could translate into a measured constant line separation. Another possibility is an error in the calibration, which could decrease the whole scale of the *D/I* signal. The changing value of the zero level could then be explained by the rotation of the solar axis

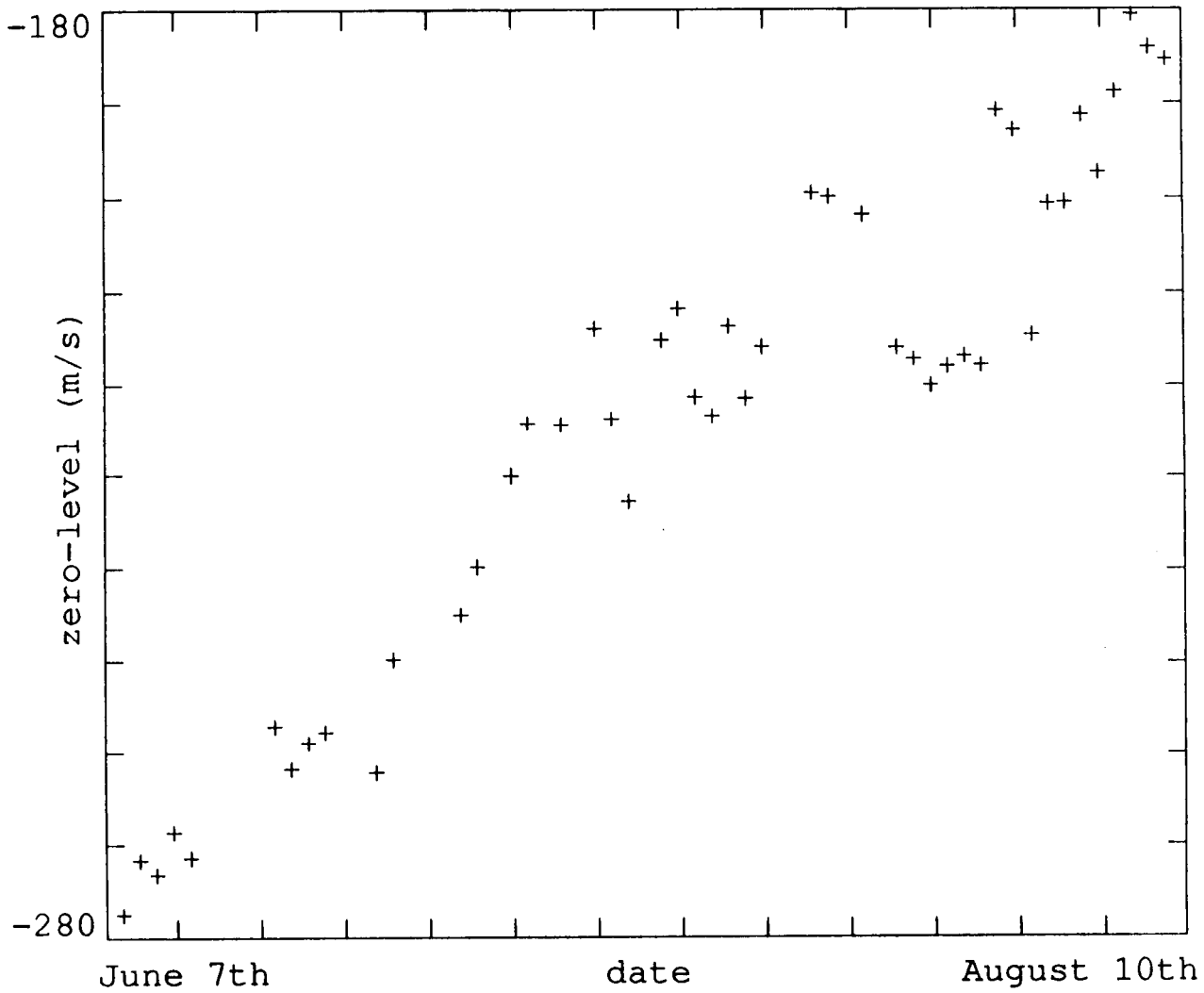

Figure 3.11 - Zero Level in 1987 Data. The points correspond to the average value of the data signal on each day of observation.

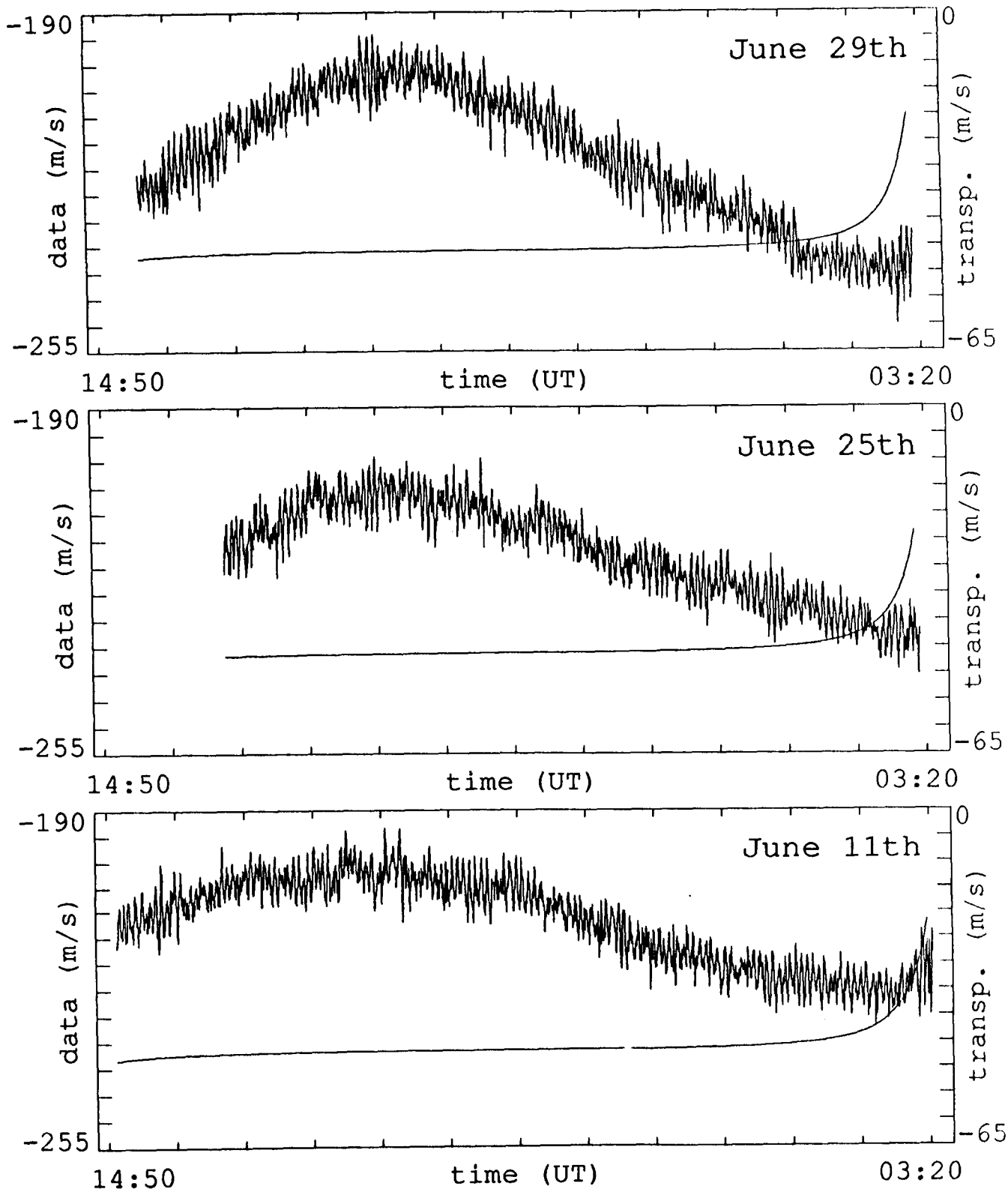

Figure 3.12a-c - Superposition of Data and Transparency Signals. Although the scale of the vertical axis is the same, the offset is not. The labels on the left refer to the actual data, while the right-hand labels are for the calculated transparency.

on a horizontally displaced assembly. A displacement of a few mm, corresponding to up to 0.2 R_S, is not unreasonable. Probably it is a combination of several such effects. The zero level itself is really of little consequence to the analysis, since it is removed from each day's observation. However, the implication that the calibration may be uncertain by more than the expected 10%, perhaps as much as 40% less, must be remembered.

The investigation into the effect of the transparency gradient has shown that most large drifts that can be expected and modelled affect mainly the zero-level of the data. Since this level is of no importance to the study of oscillations, its removal takes care of many of the errors. The exact modelling of the drift, and its subtraction from the data, is prohibited by the many unknowns that still exist. Firstly, even the effects which have been examined cannot be calibrated exactly for the actual data for several reasons. The exact calibration of the *D/I* signal to a value in m/s is uncertain. The exact limbshift magnitude and shape is unknown for the observation line FeI 5123.73Å. The position of the image on the assembly is uncertain and may change with time. The extinction coefficient for the transparency changes with time of day and sky conditions. These reasons combine to make it difficult to model the exact signal for each day. There is, moreover, another reason which makes it impossible. This is the large contribution made by the change of the phototube gain ratio. In figures 3.12a-c the calculated signal drift for several particular days is superimposed on a plot of the actual data. Clearly the shape of the drift in the data is not well matched by the calculated signal. There appears to be another contribution which is in synchronization with the time of the observation. From knowledge of the size of the gain drift, it was possible to calculate in appendix B the magnitude of a resulting signal change at 16 m/s. This value would account for a large portion of the remaining drift in the data signal. It is thus likely that the phototube gain ratio drift is also a main contributor to the signal drift.

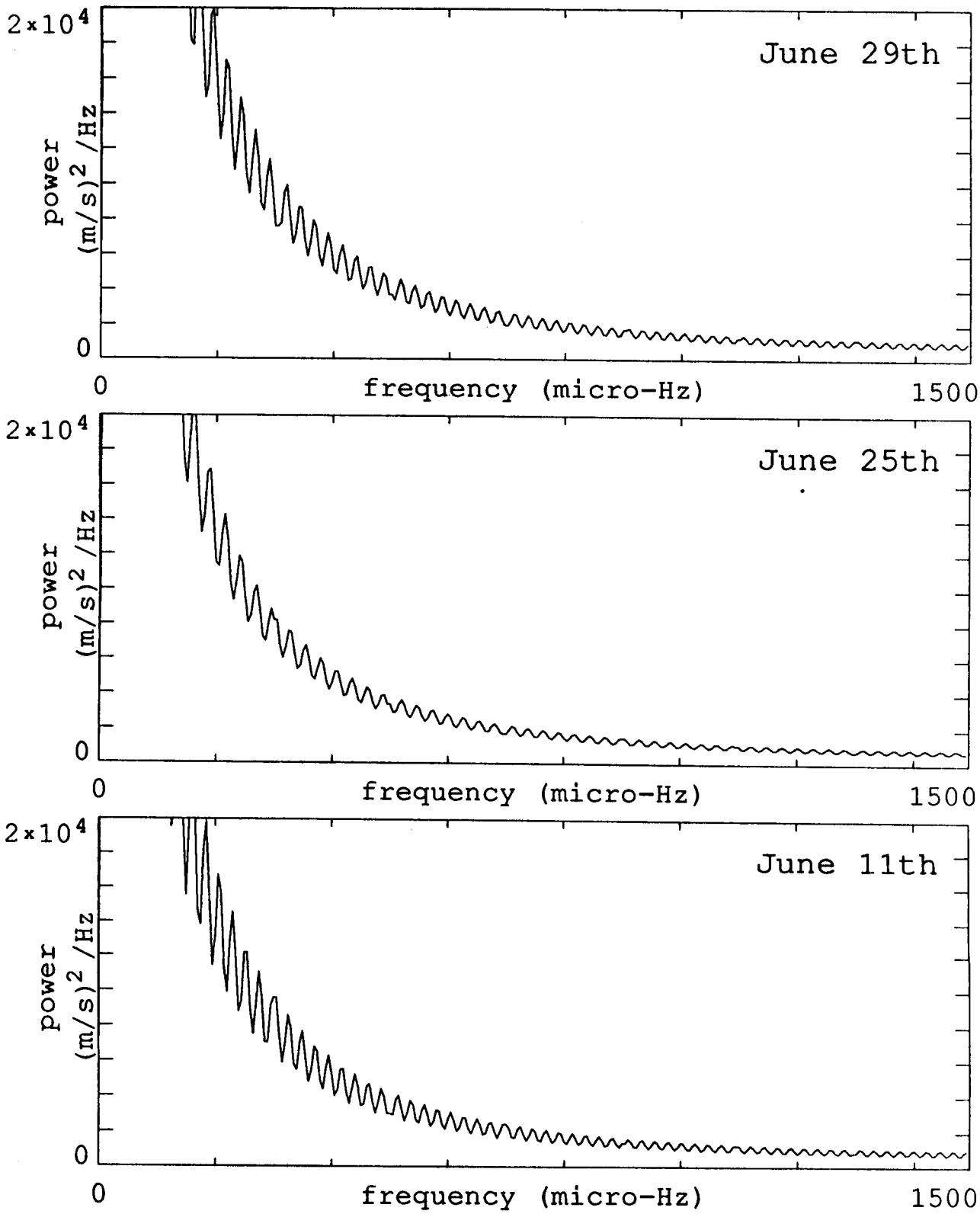

Figure 3.13a - Power Spectra of Calculated Signal. Each panel corresponds to one day.

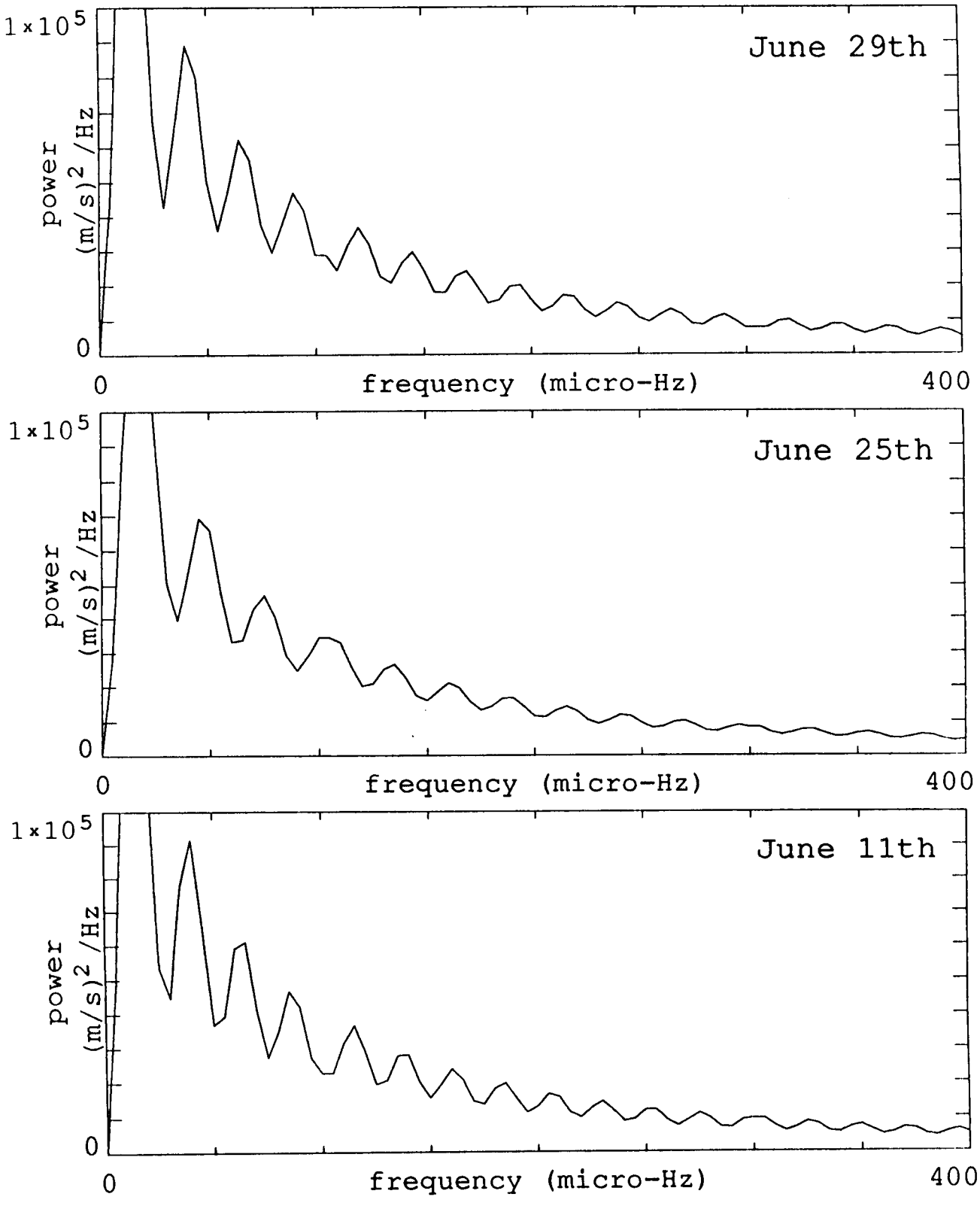

Figure 3.13b - Power Spectra of Calculated Signal, Low Frequency. Each panel corresponds to one day.

The goal of this chapter is to estimate the noise level originating from the transparency gradient. Figures 3.13a-b show the power spectra of the calculated signal for the days shown in figure 3.12. The oscillatory shape is an artifact of the FFT, corresponding to the length of the observation, and should be ignored. There is appreciable power at long periods, most of it well below the range of the p-modes, but large in the frequency range where g-modes exist. Comparing the power to figure 2.6, the actual power spectrum of a single day's observations, one can see that in the range where this analysis will look for p-modes the transparency power is a major contributor to noise. The noise power in the g-mode range likewise can to a large extent be explained by the transparency contribution.

In figure 3.14c is plotted the low frequency range of the power spectrum of the transparency signal calculated for the whole 1987 season of data and inserted into the data window. Figures 3.14a and 3.14b show the actual power spectrum of the 1987 season's data, with no attempt having been made at removing the daily drift. The two figures differ only in the vertical scale. Comparing these figures one sees that the largest peaks are at identical locations - at frequencies corresponding to 1/day times an integer. The daily drift's contribution to the power spectrum has been concentrated in these peaks by the concatenation of the time series. The first three such peaks in the real data are much larger than the calculated signal, reflecting the fact that the actual daily drift has other major contributions. However, beyond those peaks, which lie below 40 μHz, the two power spectra are of more comparable height. If we look only in this region above 40 μHz, the data spectrum displays some extra power between the 1/day peaks, above the level of the noise power from the transparency contribution. The 1/day peaks need to be removed from the data before an analysis searching for g-modes in that range can be effective. Chapter 5 describes the methods developed to that end.

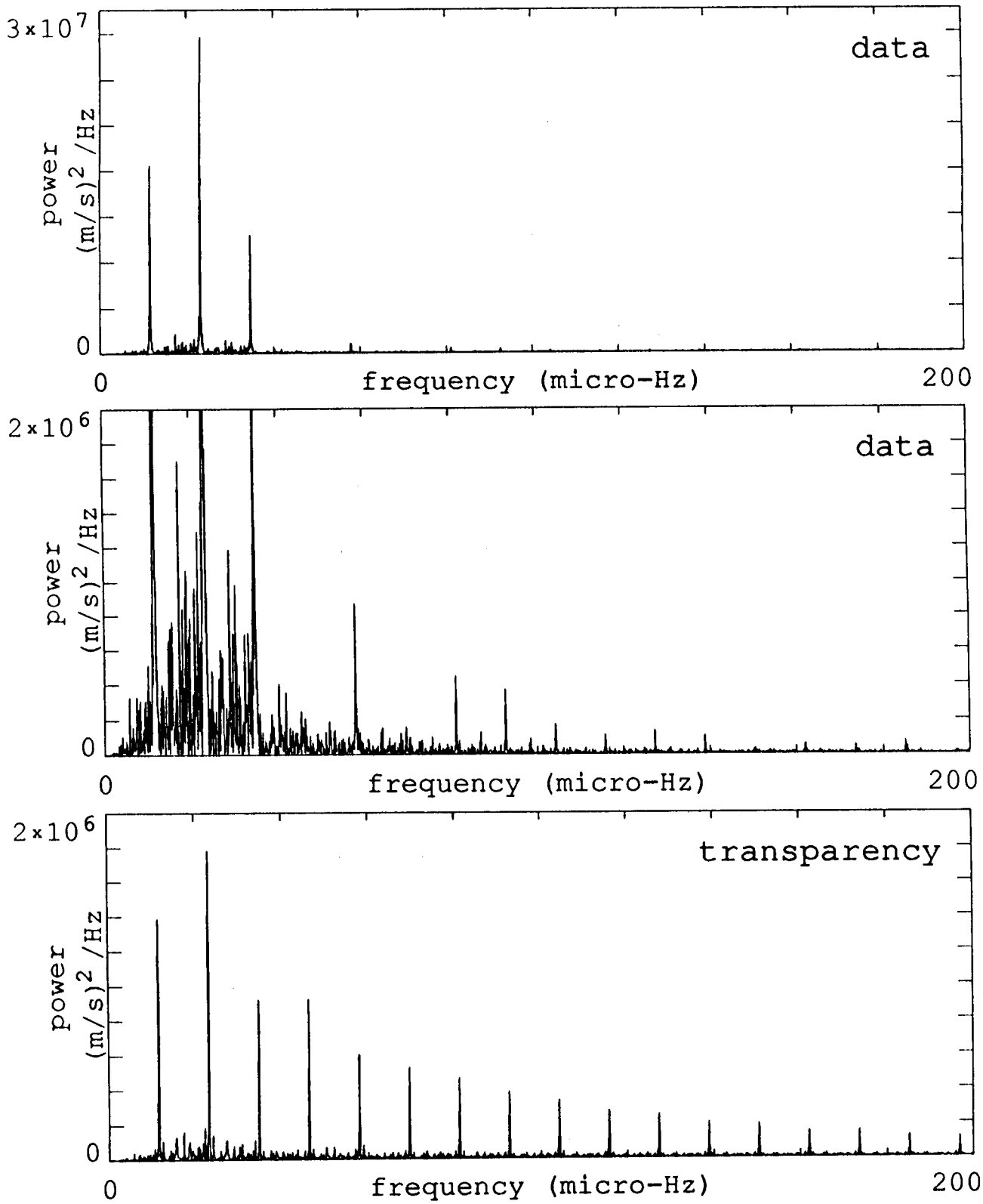

Figure 3.14a-c - Power Spectra of Data and Transparency in 1987. The top two panels show the power spectrum of the whole season of data, at two different vertical scales. The bottom panel is the spectrum of the calculated transparency signal.

3.2. Random Structure - Clouds and Haze

The previous section provided information about the level of power introduced by the transparency gradient at relatively low frequencies by modelling the extinction caused by the atmosphere. This section concerns itself with the smaller-scale structure in the sky. Although the oscillation observations used for this analysis are only performed in nearly cloudless conditions there are still periods when faint clouds cross the solar disk. Figures 3.15a-c show the record of the intensity signal *I* for the three days whose data signals are plotted in figures 3.12a-c. On two of the days there are clear periods where faint clouds cross the disc. It should be pointed out that these days were chosen as worst-case examples, and that the majority of the data looks like that for July 25th. However, to achieve the most complete period of coverage, days like these need to be used. Looking at figures 3.12a-c, the *D/I* signal doesn't seem to be greatly affected by the clouds, but close inspection of the figures does show some noise in the measurement. The effect of these clouds on the spectrum is of interest. In addition, however, all of the intensity curves display a marked amount of variation on a small scale. This variation is well above the photon noise level of the measurement. Its origin lies in transparency variations - haze and very faint clouds - which are in general not visible to the naked eye.

To calculate the power spectrum due to such transparency variations it is necessary to integrate the velocity on the disk of the sun with the spatial distribution of the intensity. With the available data several assumptions and simplifications have to be made. The first assumption must be that the spatial distribution is roughly isotropic in the sky, so that our sampling through the sky - in the form of the intensity signal *I* - is representative of the variation in all directions. On the size-scale which this section considers this is a reasonable assumption. The larger size-scales, which are non-isotropic, are dominated by the static transparency gradient which was examined in the previous section. The next step

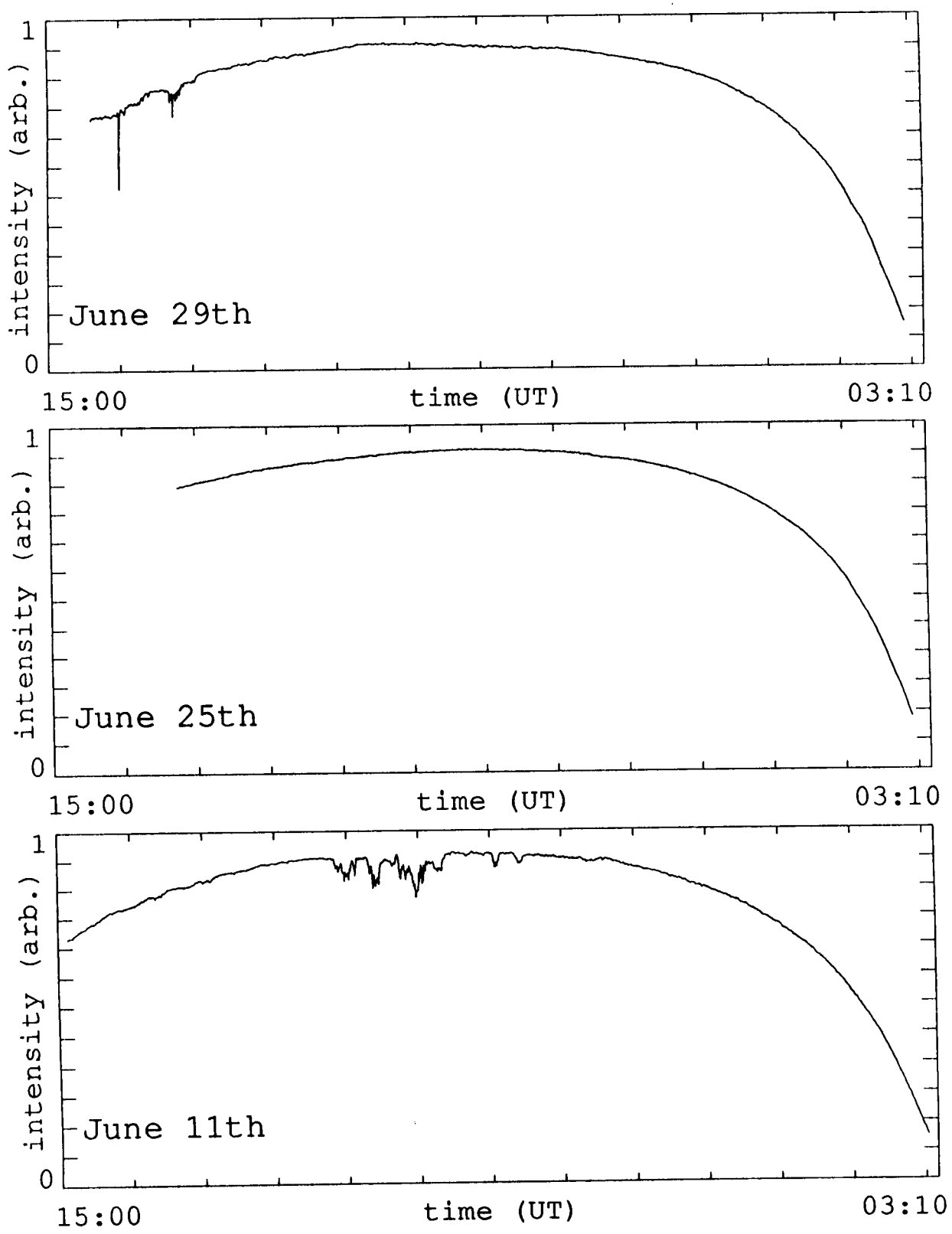

Figure 3.15a-c - Intensity Signals. The panels show the intensity data on three days of observation.

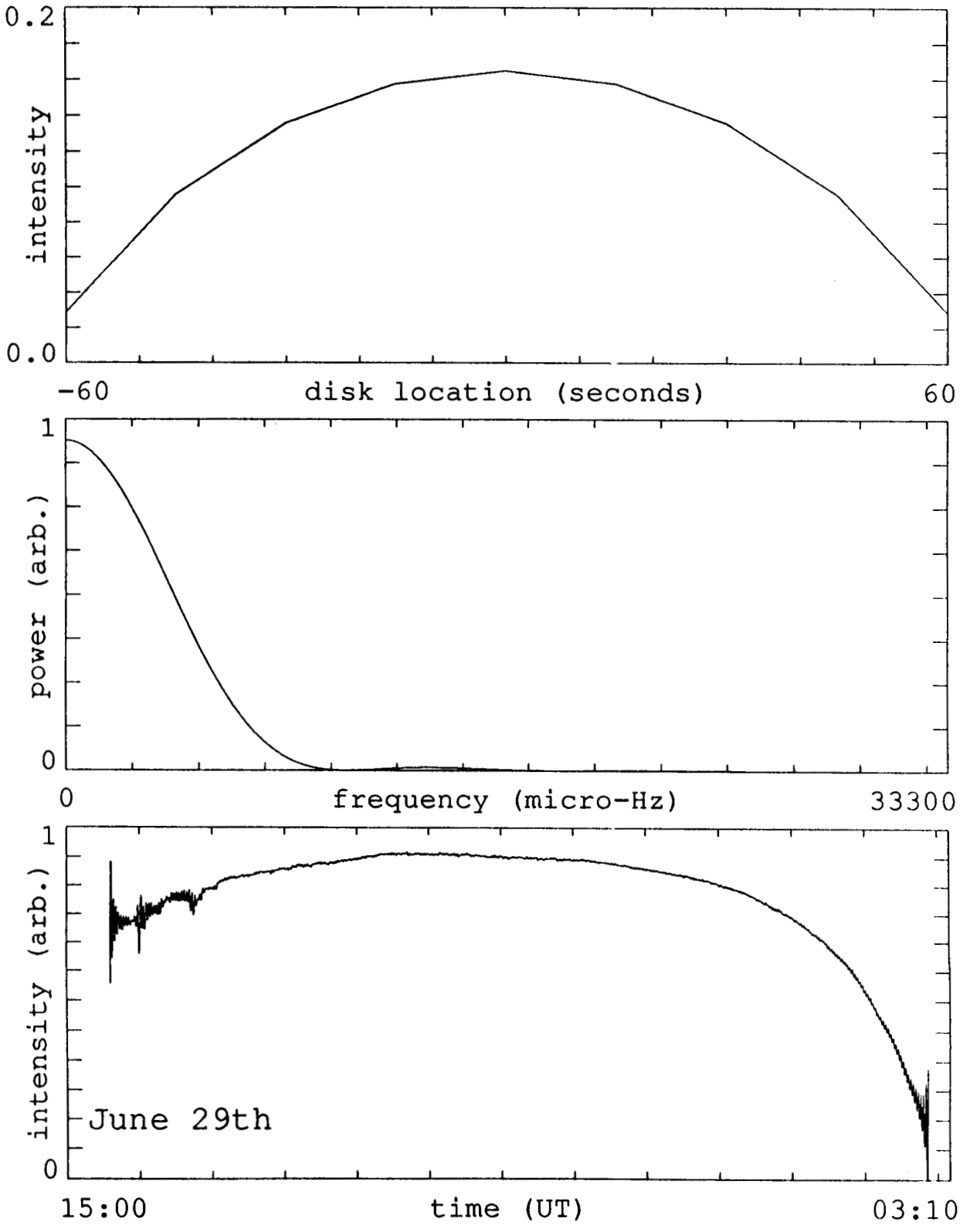

Figure 3.16a-c - Deconvolution Process of Intensity with Solar Disk. The top panel represents the average solar disk intensity in 15 second bands. The middle panel is the power spectrum of the top panel. The bottom panel shows an example of the result of a deconvolution of intensity with the solar disk function.

is to retrieve the transparency variation from the intensity information we have. The intensity signal *I* is a convolution of the solar disk with the spatial transparency variation. Ideally one can retrieve the transparency variation by deconvolving the intensity signal *I* with the solar disk. In figure 3.16a is shown the function which represents the solar disk. It is simply an integration of the intensity on the disk, including limb darkening, in bands which are 15 seconds wide. The reason for this choice of size is that the data measurement is a 15 second average. A deconvolution can be performed by dividing the Fourier transforms of the respective functions in the frequency domain, and retransforming to the time domain. Figure 3.16b shows the power spectrum of the deconvolving function from figure 3.16a. The deconvolution by division can only performed out to the point where the power spectrum reaches its first zero. If one further wants to avoid the large amount of power introduced when the power in the deconvolving function's spectrum is low, near zero, one must cut the frequency at a higher value. To be of value for this investigation, a cut at a frequency lower than about 8000 μHz is not feasible. When this is done, and the deconvolution performed, the result for July 29th is shown in figure 3.16c. There is a very pronounced regular oscillation, especially near the beginning, end, and clouds, which is certainly not a real structure in the sky, but rather an artifact of the deconvolution. The frequency of the oscillation, not surprisingly, is close to 8000 μHz. The reconstructed signal is dominated and contaminated by the large power introduced at this frequency since the power in the deconvolving function's power spectrum was quite low at this frequency.

This problem requires that one must make a further simplification, which is the admission that one cannot do much better with the recorded intensity data than sample the sky at the size scale of the sun. This corresponds to a time of a little more than 2 minutes as the sun moves through the sky, and thus a frequency of slightly less than 8000 μHz, just as good as the attempted deconvolution. One can thus use the intensity signal as a

monitor of the sky transparency without any further manipulations.

The next step is to integrate the velocity signal of the sun with the measured intensity signal. To do so one can convolve the function representing the weighted average of the solar velocity in bands 15 seconds wide with the 15 second intensity data. The weighted average will be calculated assuming that the sun's axis of rotation is perpendicular to the sampling motion. This is validated by the assumption that the spatial distribution of the variations is isotropic. The integration in bands parallel to the rotation axis, making the convolution one-dimensional, is adequate since any gradient parallel to the axis of rotation has no effect on the data signal. Figure 3.17a shows the velocity function which will be convolved with the intensity signal to calculate the transparency signal. Note that since a convolution inverts the abscissa of the convolving function, the East limb of the sun corresponds to the right hand side of the antisymmetric curve. The limbshift and earth's velocity are not included in the calculation, since the effect from these contributions is almost solely a zero level shift, and thus is of no consequence in this section. The velocity function is obtained by the integration of the solar rotational velocity multiplied by the limb darkening integrated over each band for center and annulus separately. The final result is the difference between the weighted velocity averages in each band. Figure 3.17b shows the function's power spectrum. It is interesting to note that the minimum in the power spectrum at about 12000 μHz implies that the data signal from this differential measurement is not sensitive to any transparency variations on the time scale of one and a half minutes, corresponding to a spatial size of about 1250 arc-seconds. However, since this calculation is not valid beyond about 8000 μHz, it remains a curiosity.

In figures 3.18a-c are plotted the convolutions, the transparency signals corresponding to the respective days. The first and last 2 minutes of each day's calculated signal have been removed, since the calculated signal is invalid there and displays large excursions.

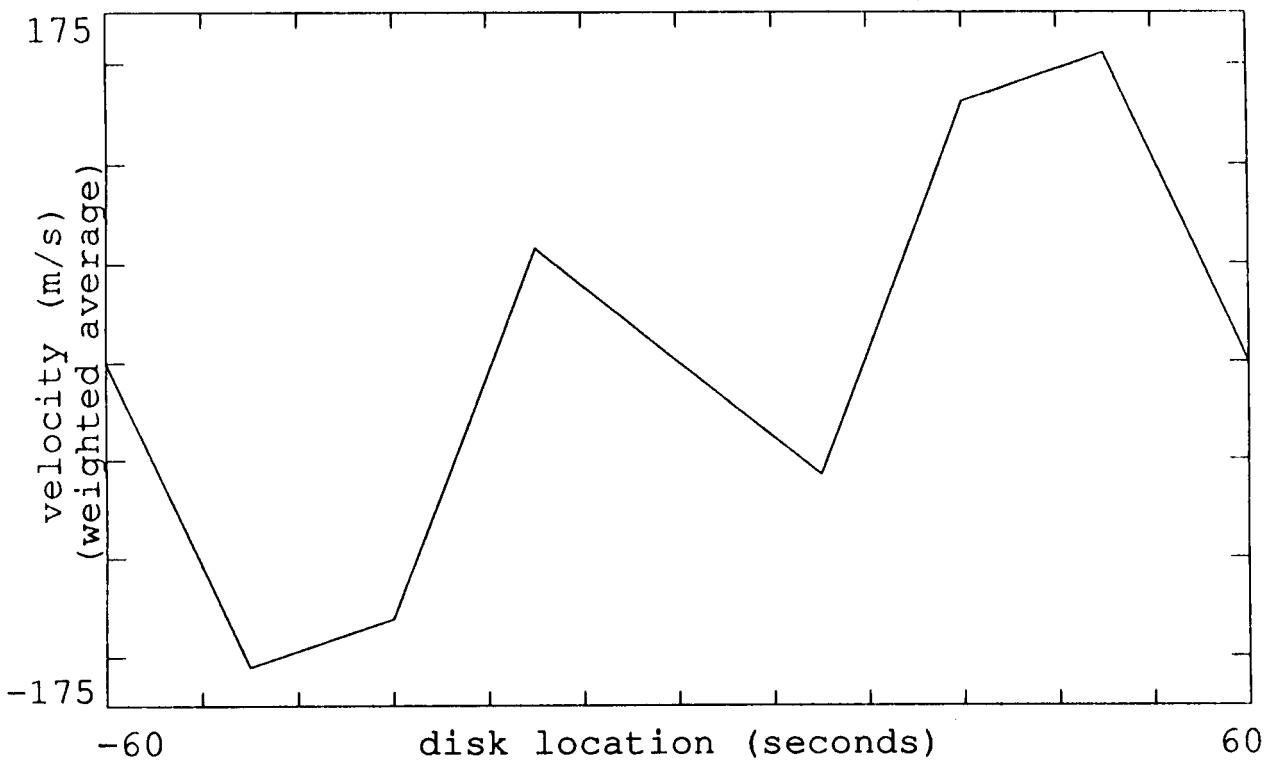

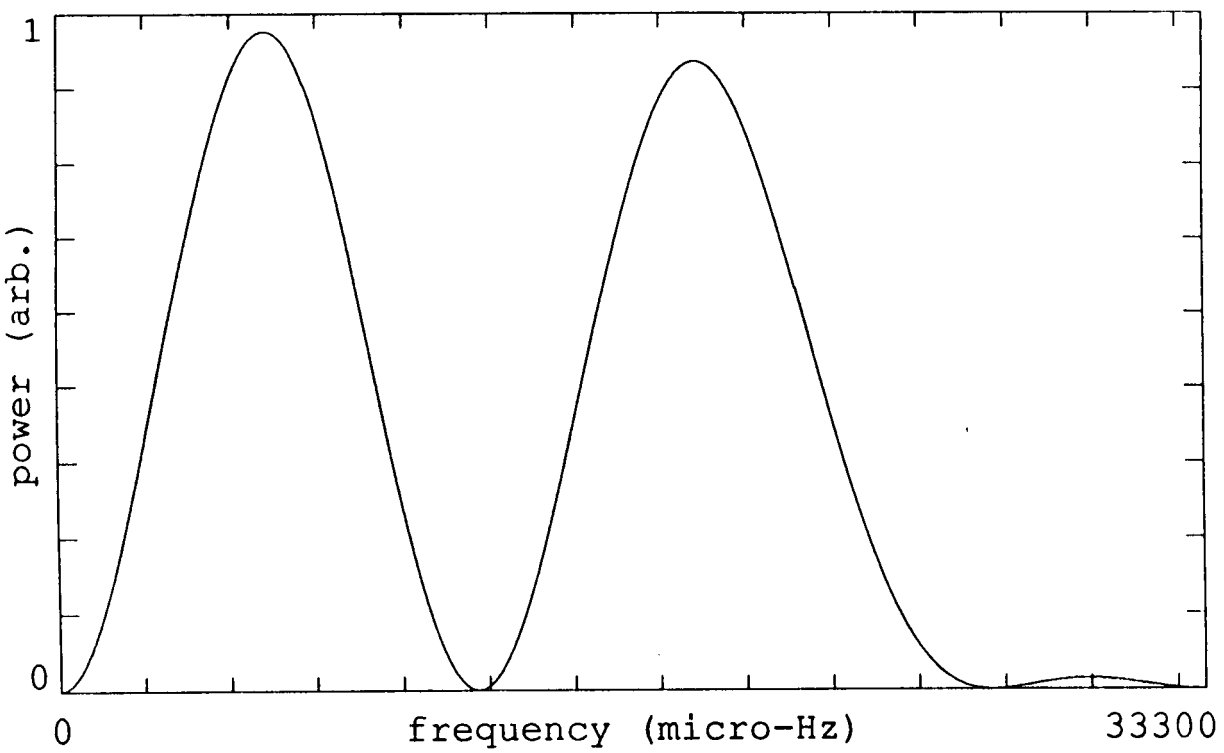

Figure 3.17a-b - Velocity Convolving Function. The top panel represents the average solar disk velocity difference in 15 second bands. The bottom panel is the power spectrum of the top panel.

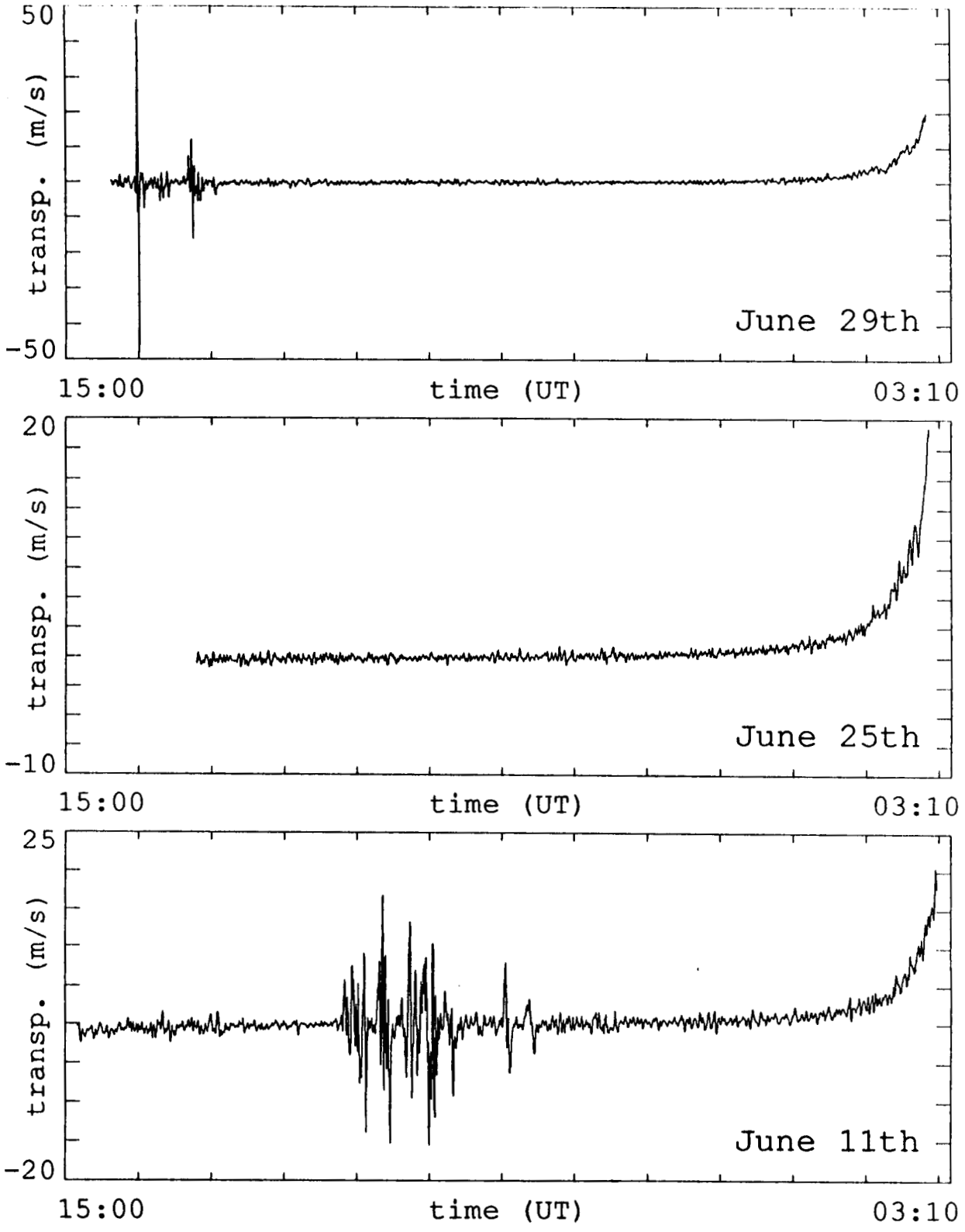

Figure 3.18a-c - Transparency Signals from Convolution. The three panels show the convolved signal of intensity with the velocity function in figure 3.17 for three days.

The remaining signal has fairly low peak-to-peak amplitude of about 2 m/s at most times, only showing large variations where there are clouds and when the sun is near the horizon. The effect of clouds is large, larger than is actually seen in the real data for these same days. This emphasizes the restriction of this method that it is a worst-case scenario, where the intensity variation measured in the data is assumed to be a true spatial variation on the size-scale of 15 seconds. In actuality a large part of the intensity variation with time probably is due to a much larger scale spatial variation which is blowing across the disk. If this is the case, then the 15 second intensity measurement will reflect the decrease in intensity, but the *D/I* data signal will not be affected as greatly since it is numerically integrated from 0.1 second averages. These 0.1 second averages of the data signal are not affected by an intensity decrease over the whole disk. Put slightly differently, while the intensity may vary with time, the spatial scale may be larger than implied by the time variation, decreasing the transparency variation across the disk at any given instant. The difference signal will thus be smaller at any given time, and so will its 15 second average which is eventually recorded. The general peak-to-peak amplitude, away from any clouds, is probably more accurate as a magnitude estimate of the actual noise, since this signal comes from a spatial distribution which is certainly more isotropic than the isolated clouds.

The overall shape of the random transparency signal matches the one calculated for the gradient signal in that it is fairly flat throughout the middle of the day and starts to curve where the atmospheric gradient gets large. The power spectra of the three days' signals are plotted in figures 3.19a-c. The spectra are fairly flat from about 1000 μHz to 8000 μHz, characteristic of a white noise distribution. The two days with clouds have a much higher level, but it must be remembered that this is a worst-case scenario. The spectrum for June 25th probably is a more realistic estimate of the actual noise power. Below 1000 μHz the static gradient starts to insert a lot of power, as has already been seen

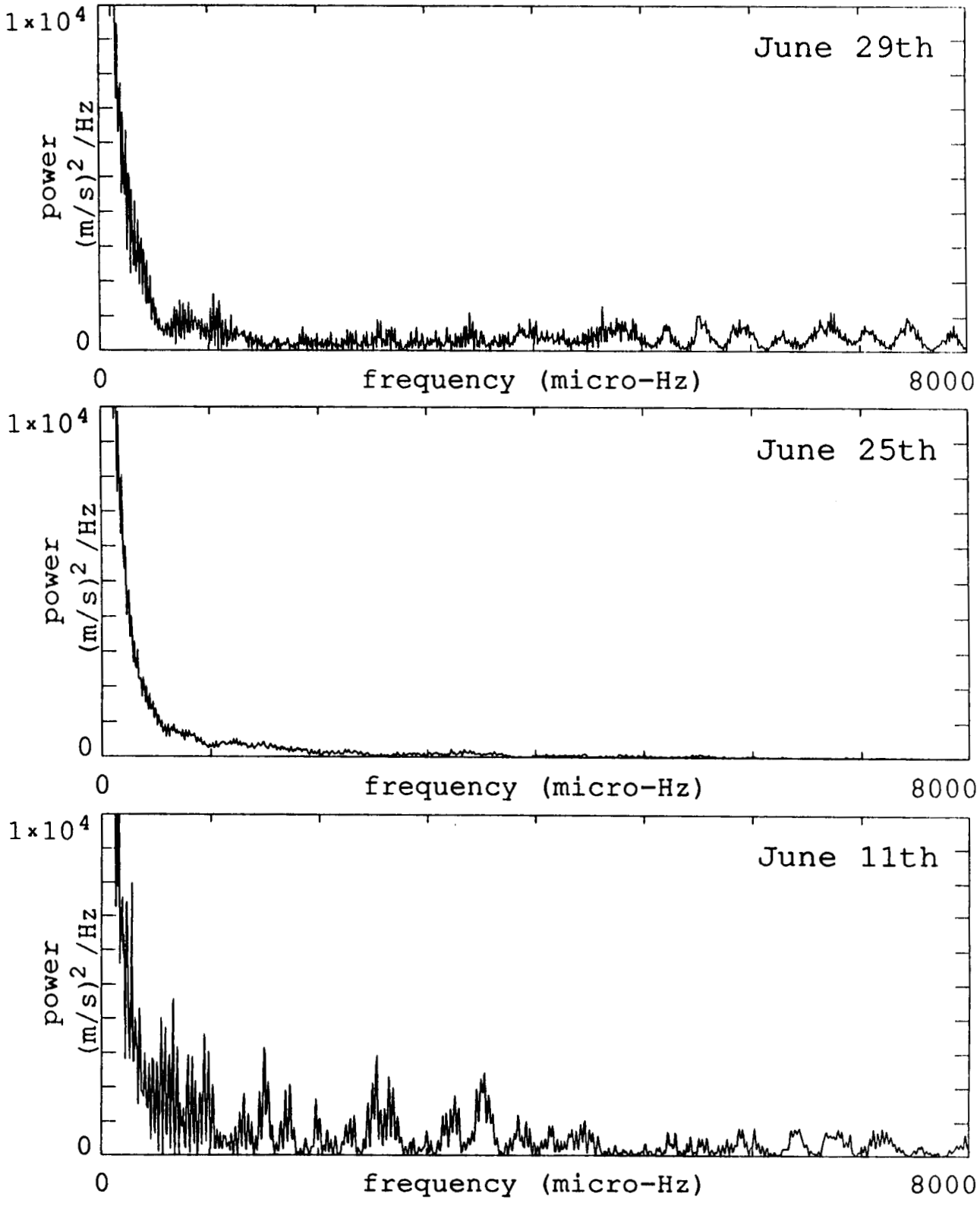

Figure 3.19a-c - Power Spectra of Transparency Signals. The three panels are the power spectra of the corresponding signal shown in figure 3.18.

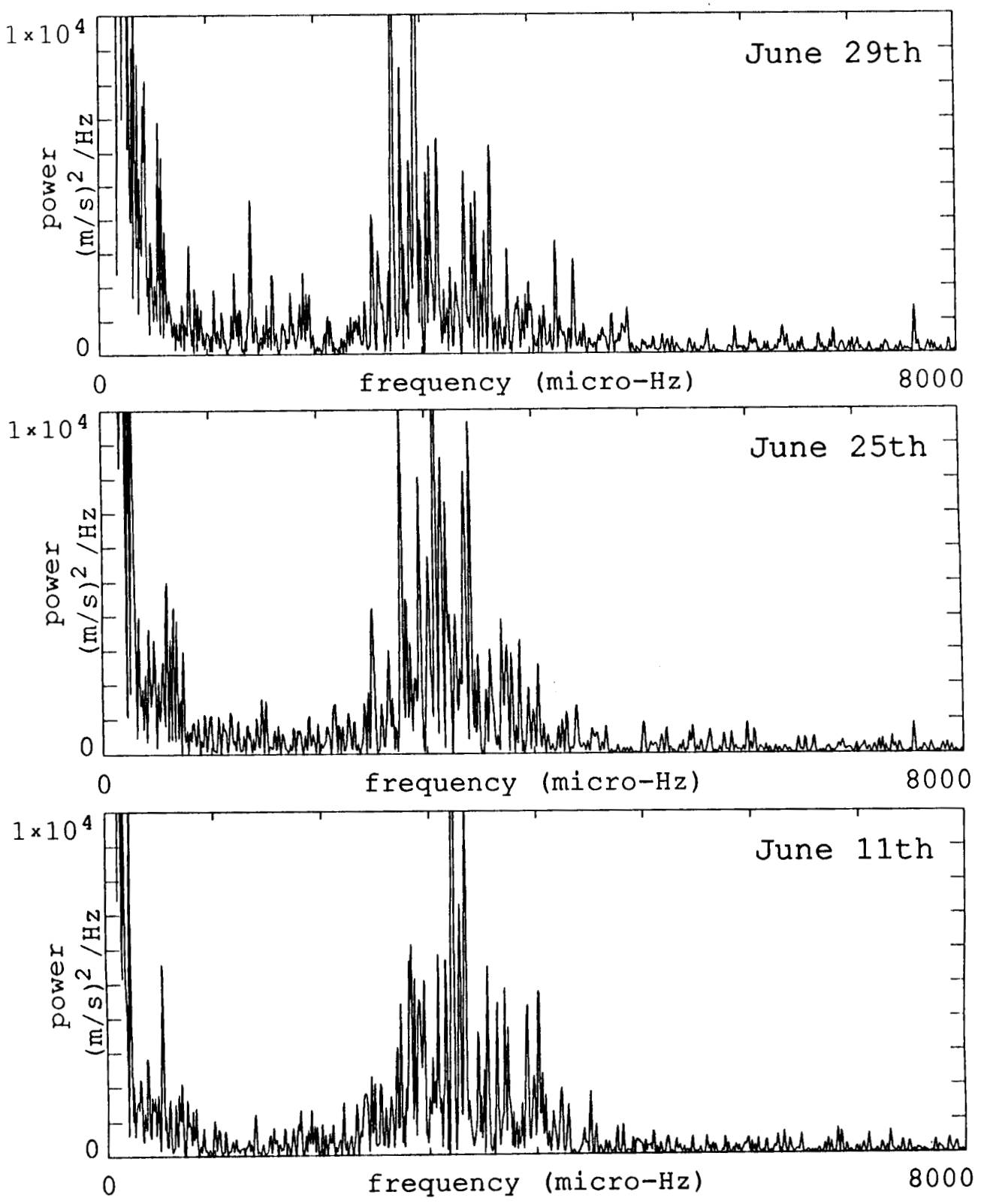

Figure 3.20a-c - Power Spectra of Data. The three panels correspond to the actual data signals of the same days as are shown in figure 3.19.

in the previous section. The power at these low frequencies is almost identical when calculated by these two methods, giving added confidence in the validity of both methods.

Figures 3.20a-c show the power spectra of the actual data from these days. The 5 minute power stands out clearly. At other frequencies, including those of interest in this investigation, the noise power calculated from the transparency signal is of comparable magnitude to the data. However, it is encouraging to note that even with a single day spectrum and worst-case transparency calculation, there is clearly power in the data above the level of the noise power, especially in the case of the nice day, July 25th. On the other hand, the comparison emphasizes that this analysis is dealing with data where the signal to noise ratio is very low. This fact will have a strong effect on the method of analysis, since most methods of peak detection require a much higher signal to noise ratio.

Figures 3.21a-c and 3.22a-c show the low frequency regime of the power spectra on an expanded scale to allow better comparison in the g-mode range. Comparing the two sets of plots, one sees that the transparency power lies well below the power in the data spectrum. This is again largely due to the larger actual drift in the data than is modeled by the transparency.

One other comparison which is of interest is with the solar noise power from such sources as granulation, supergranulation, active regions, and mesogranulation. The model power spectrum for integrated sun observations has been calculated by Duvall and Harvey (1986) and is reproduced in figure 3.23. It can be used as an estimate of the magnitude of solar noise for these observation, although there will be some difference for the differential observations. A comparison of the level of transparency noise power, as shown in figures 3.13, 3.19, and 3.21, to solar noise power shows that the noise from transparency variations is greater in the range above about 10 μHz, where the two contributions become

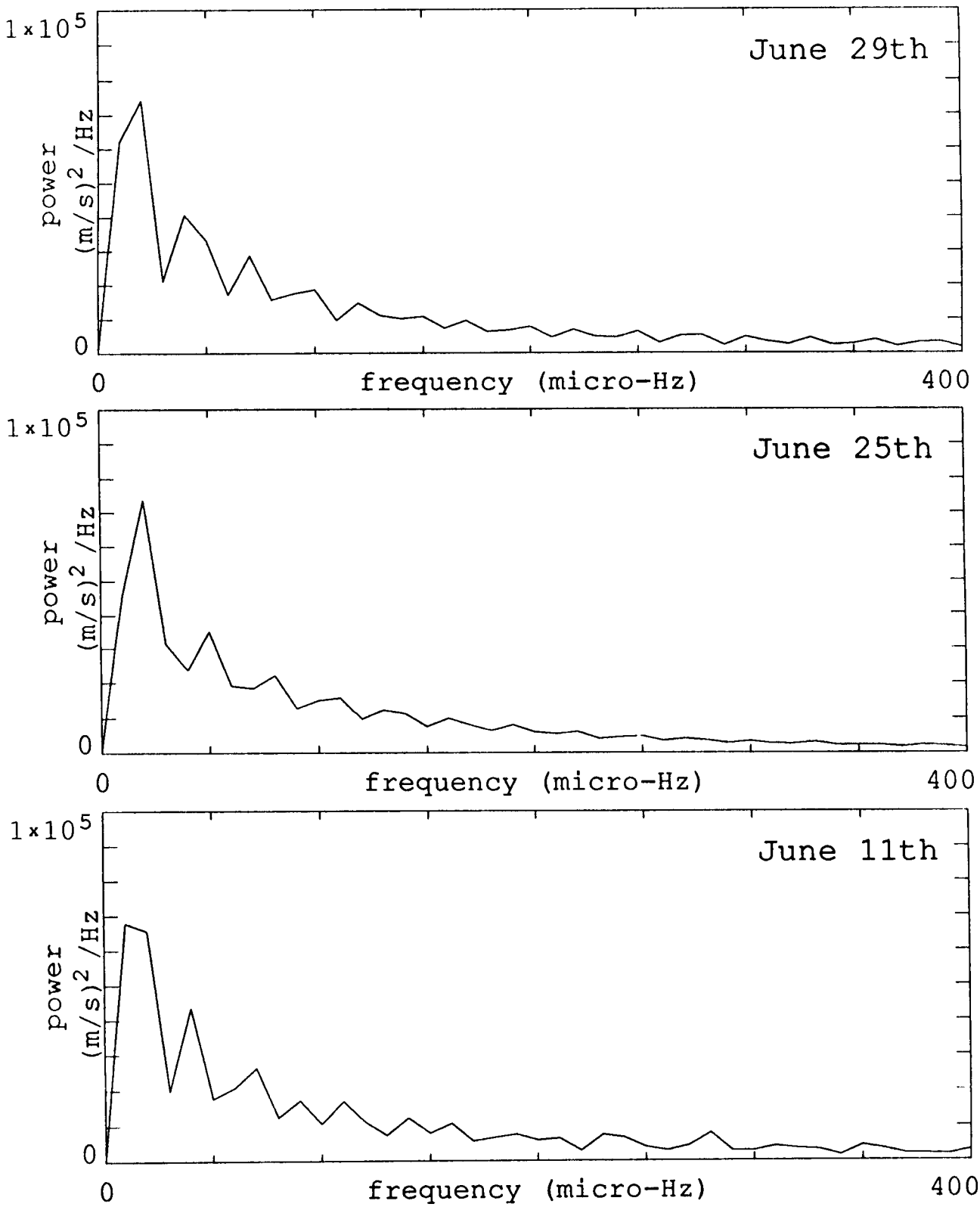

Figure 3.21a-c - Power Spectra of Transparency Signals, Low Frequency. These panels show the low frequency portion of the spectra of the calculated signal in figure 3.19.

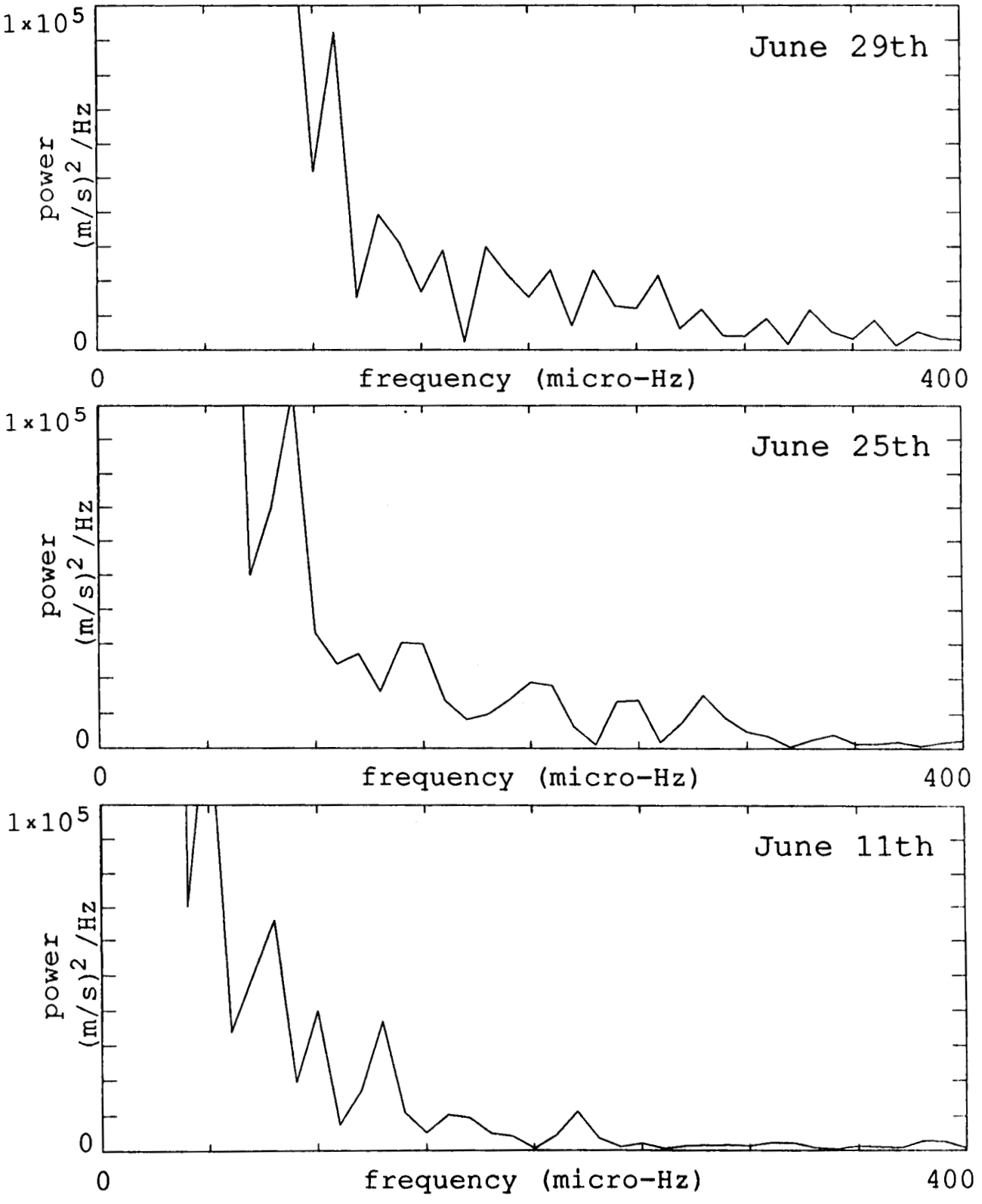

Figure 3.22a-c - Power Spectra of Data, Low Frequency. These panels show the low frequency portion of the spectra of the actual data signal in figure 3.20.

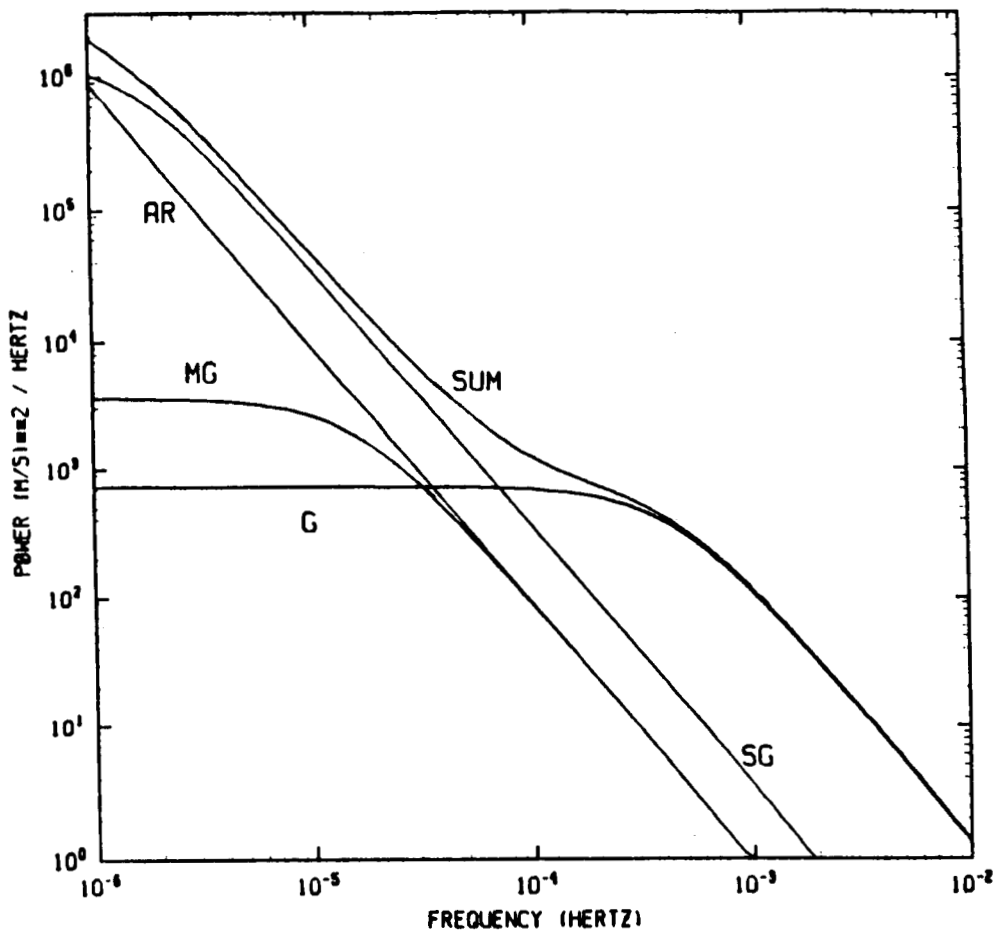

Figure 3.23 - Duvall and Harvey Solar Doppler Noise Power Spectrum. The curve labeled SUM is the total of the spectra for active regions (AR), granulation (G), supergranulation (SG), and mesogranulation (MG). Adapted from Duvall and Harvey (1986).

comparable. Below that frequency the solar noise power becomes greater, overwhelming the transparency noise contribution. However, in the frequency ranges of interest to solar oscillations, both for g-modes and p-modes, the signal from the transparency contribution is usually larger by about one magnitude.

This chapter has demonstrated that the power in the spectrum due to the transparency signal can be quite large. The regions where the modes being investigated lie have sizable contributions from the daily signal introduced by the transparency. Luckily the largest amount of noise power in the spectrum, which derives from both solar noise power and the transparency contribution, lies below 40 μHz. Moreover, the contribution from the unknown portion of the daily drift seems to contribute power mainly below 40 μHz, judging from the amplitude of the 1/day peaks above that level. The noise level would make an investigation of g-modes in this region more than likely impossible. The region of interest, between 50 μHz and 100 μHz, is still contaminated by large peaks at 1/day which must be removed to be able to search for g-modes, but the transparency and solar noise power there is otherwise at a lower level than the level of power in the data. For these reasons it is likely that the excess power in that region could correspond to g-modes.

The low order p-modes in the range between 1000 μHz and 1800 μHz lie in a region where the noise is mainly due to the transparency variations in the sky. The data level of power lies above the level of the transparency noise, but not by much. This low signal to noise makes the detection of modes in this region more difficult than in the region where the p-modes have a higher amplitude. The method developed for their detection is described in the next chapter.

Chapter 4

P-Mode Analysis

Having investigated the noise introduced into the data by the transparency signal and solar sources, one is left with the knowledge that p-modes are definitely present in the signal. The power in the spectrum around 5 minutes stands out clearly above the level of noise power. Low-degree modes in this range have been detected and identified by several authors (e.g. Scherrer et al. 1983, Grec et al. 1983, Harvey and Duvall 1984, Jiménez et al. 1987) The analysis described in this chapter will extend the range of identified modes to both lower and higher frequencies, using the previously identified modes as an anchor and as a test for the analysis method developed for this purpose.

The p-mode frequencies are individually identified for all four seasons used in this analysis - the summers of 1981, 1984, 1986, and 1987. This enables one not only to check the consistency of the frequency determinations, but also to use clearly defined modes in looking for a possible systematic frequency shift with time.

The p-modes of low frequency are of special interest, since they penetrate deeply into the sun. Their frequencies display some unexpected behavior when compared to currently available theoretical calculations. Their identification will enable new theoretical work to be performed to match solar models with the measurements. Such theoretical investigations are well beyond the scope of this experimental study, generally requiring extremely sophisticated solar computation codes. The low-frequency p-modes which are identified in this study have such low radial orders that the asymptotic approximations which were helpful in making previous identifications of modes are not applicable. That is to say, the

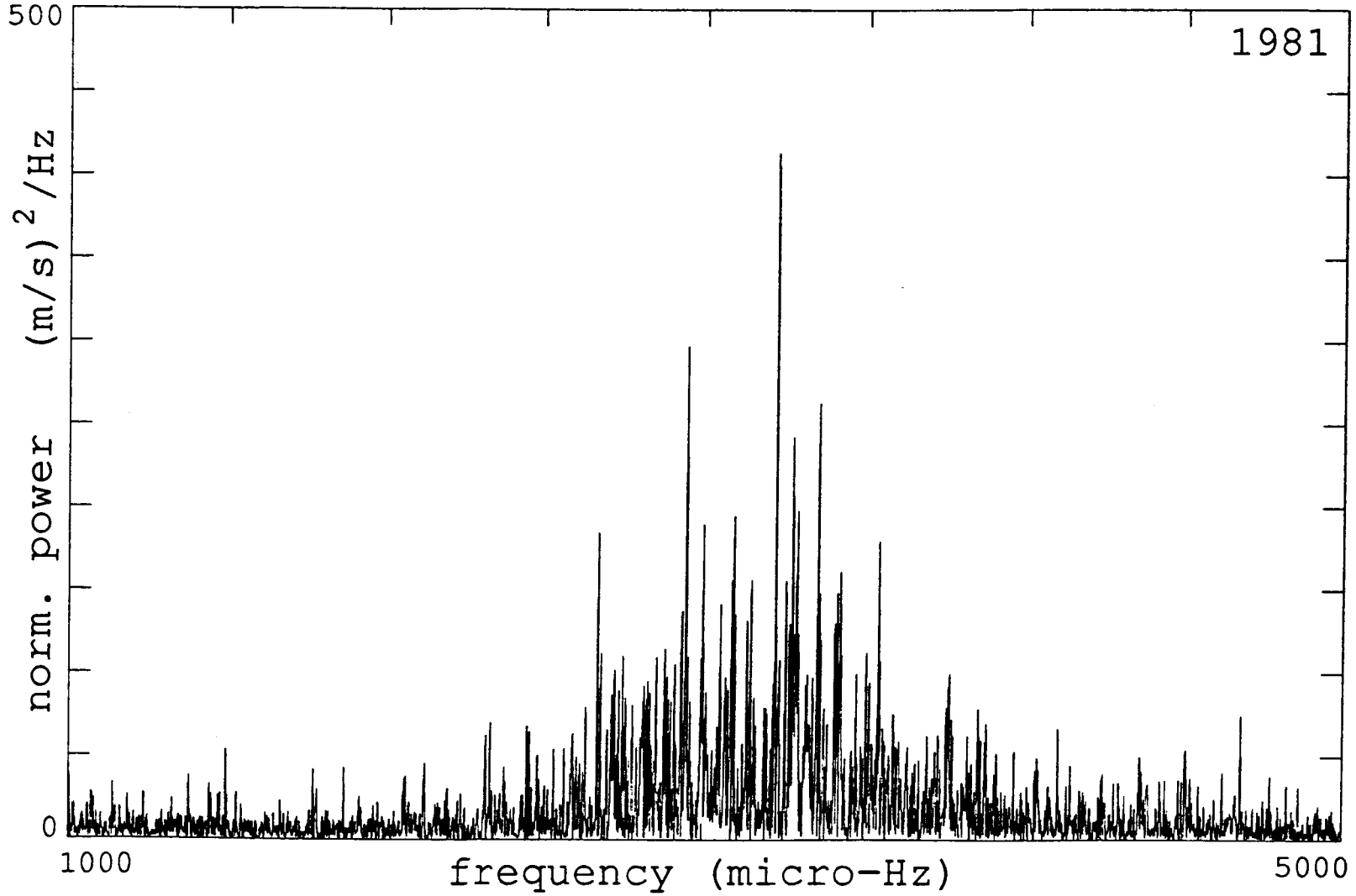

Figure 4.1a - Power Spectrum of the P-Mode Region, 1981. The region from 1000 μHz to 5000 μHz of the power spectrum of the whole season's time series is shown.

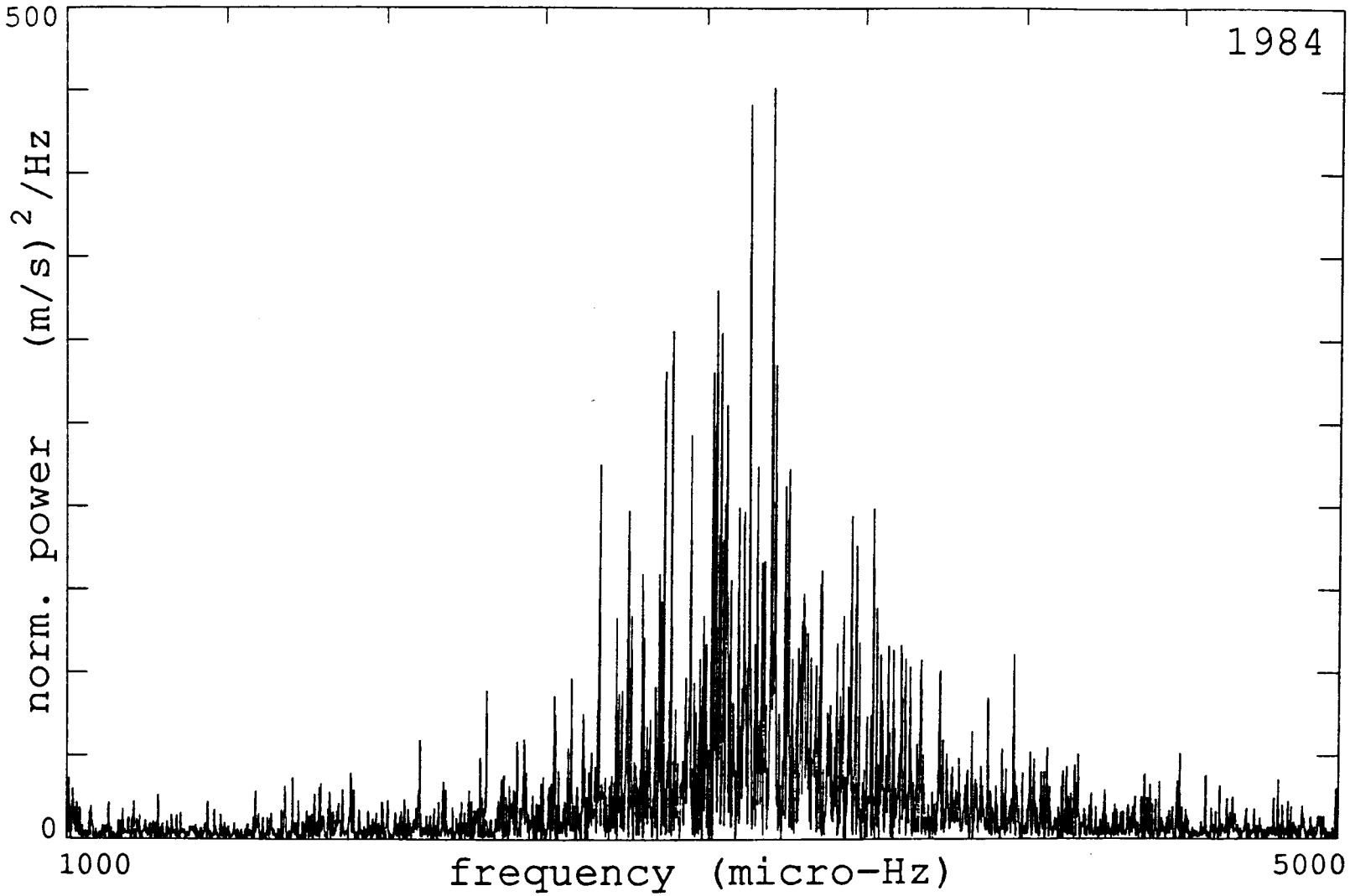

Figure 4.1b - Power Spectrum of the P-Mode Region, 1984. The region from 1000 μHz to 5000 μHz of the power spectrum of the whole season's time series is shown.

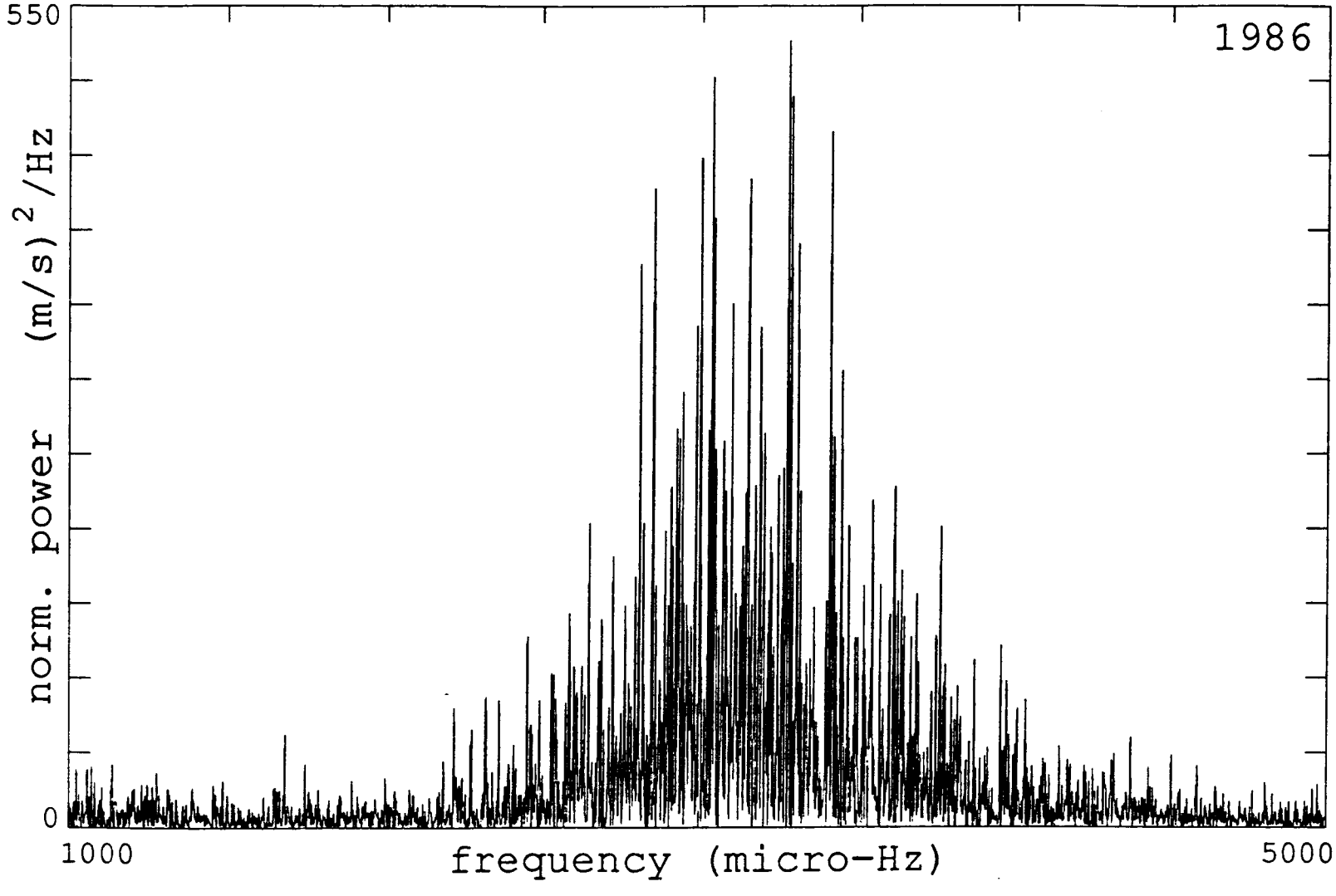

Figure 4.1c - Power Spectrum of the P-Mode Region, 1986. The region from 1000 μHz to 5000 μHz of the power spectrum of the whole season's time series is shown.

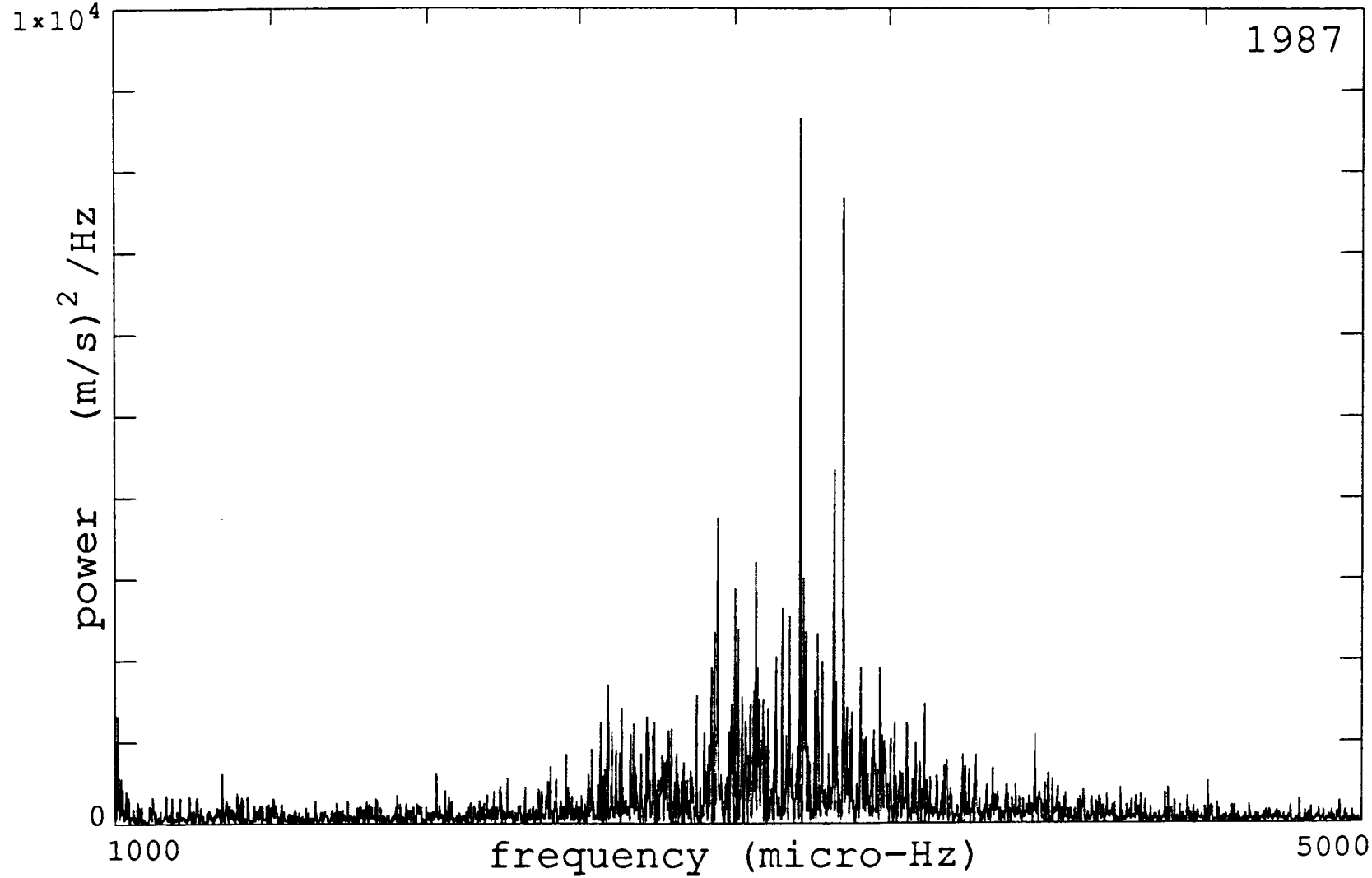

Figure 4.1d - Power Spectrum of the P-Mode Region, 1987. The region from 1000 μHz to 5000 μHz of the power spectrum of the whole season's time series is shown.

modes are not separated by fixed a frequency spacing. The theory of solar oscillations has not progressed to a point where these frequencies can be used to make definite statements concerning the solar variables which determine them. In this study only some simple speculations about the information contained in the new modes can be attempted.

4.1. Data Reduction and Treatment

The first treatment of the data has been described in chapter 2. This section describes the further treatment which is specific to the p-mode analysis. Since the search for these modes is restricted to frequencies above 1000 μHz the problems associated with the large amount of noise power at lower frequencies is avoided. Each day's data signal is processed by a 35 minute high pass filter, eliminating all power below about 500 μHz, where the noise power begins to increase rapidly. The days are then strung together, producing a time series similar to those in figure 2.4. These time series are transformed and the power spectra shown in figure 4.1a-d calculated.

There are clear peaks visible where the power is maximal, around 3000 μHz. While it is difficult to make out in figures 4.1a-d, the peaks are also seen to be accompanied by sidelobes at a distance of 11.574 μHz from the central peak. Figure 4.3 shows these sidelobes much better. The sidelobes are the contribution of the nightly data gaps, and can cause confusion in the peak identification especially when two sidelobes of different modes are superimposed and produce a peak comparable in amplitude to the primary peaks. If the power spectrum contained all the modes present on the sun it would be hopelessly confused without spatial resolution. However, the Stanford instrument acts as a spatial filter, letting only certain modes contribute to the measured data signal.

Identification of the modes for the Stanford instrument is possible because the sensitivity of the differential measurement to a particular mode depends on its degree.

Figure 4.2 is a graph of a calculation performed by Christensen-Dalsgaard (1980) of the spatial filter functions for the differential observations and whole-disk observations. For full-disk observations the sensitivity is largest for modes of degrees l=0 and l=1, dropping off rapidly at degrees higher than l=2. For the differential measurement, the sensitivity peaks at somewhat higher degrees, around l=3 to l=5, and appears to be sensitive even to modes of degree l=9 and higher. Examination and experience with the data has shown that the peak in sensitivity indeed lies at a degree of l=4. The amplitude of modes with degree l=3 in the power spectra is also quite large, whereas it drops off for modes of degree l=2 and l=5. Higher and lower degree modes are also visible sometimes, and certainly contribute to the power in the spectrum, but they are so small that they are dominated by the modes between degrees l of 2 and 5 and their sidelobes. The observations thus imply a very small leftward shift of the sensitivity peak plotted in figure 4.2. Such an uncertainty in the theoretical sensitivity is not unexpected, since the exact configuration of the circular polarization assembly affects the calculations, and it was demonstrated in chapter 2 and 3 that the assembly is likely to be off center. Moreover, the sensitivity calculations depend on the wave velocities and directions in the solar atmosphere near the reflection point of the mode. The exact distribution of the mode's velocity at the height of observation in the solar atmosphere is not easy to calculate and varies from mode to mode.

As the theoretical calculation shows, the sensitivity of the differential measurement to a mode can be greater than 1, even above a value of 2. This means that a mode with 10 cm/s amplitude on the sun could be observed as a 20 cm/s oscillation in the data signal. This is the result of the subtraction of the annulus from the center of the circular polarization assembly. In a simplified picture, if the mode's velocity distribution on the solar surface is right, the differencing scheme can measure the peak-to-peak amplitude between the mode's toward and away motions on the solar surface, doubling the magnitude

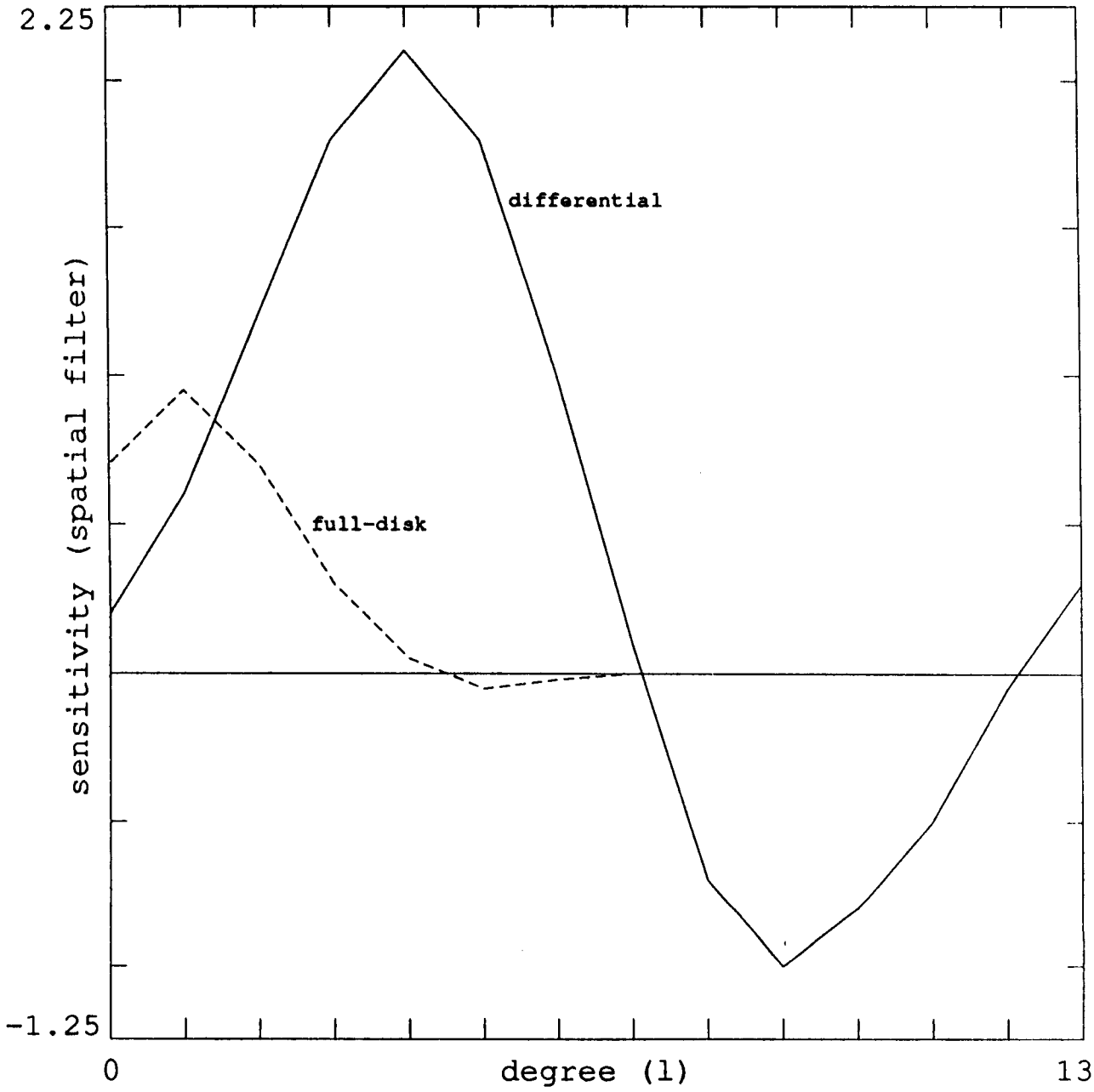

Figure 4.2 - Instrumental Sensitivity for Radial Velocities.

of mode in the data signal. This is potentially a substantial increase in sensitivity over the full-disk measurements for the l=2 and l=3 modes which are potentially visible in both methods of observation. If one assumes a differential measurement sensitivity of about 2 for the l=3 modes, the sensitivity ratio is 8 to 1. For the l=2 modes, a sensitivity of only 1.5 still gives the differential measurement a 2 to 1 edge in sensitivity.

Armed with this information on the instrument's sensitivity, one can now hunt for modes. The original detection of modes in the Stanford data was accomplished by the utilization of the echelle diagram (Scherrer et al., 1982; Scherrer et al., 1983). This tool is a composite graph which attains its usefulness from the asymptotic theory of p-modes. Theory predicted that modes of equal degree but different order would be equally spaced in frequency if the order was large enough. The echelle diagram is a vertical stack of frequency segments separated by a constant frequency spacing. Essentially the power spectrum is just cut into equal-sized pieces and stacked up. Figure 4.3 is an echelle diagram of the power spectrum of the 1987 data. Vertical structure corresponding to sets of p-modes of the same degree l are clearly visible. Also visible are the sidelobes separated by 11.574 μHz from each mode frequency. The data is plotted to the same height in each echelle panel, so that it becomes clear that the amplitude of the modes as well the power of the "noise" between the modes decreases to a very low level below 2500 μHz and above 3500 μHz. The true noise level, mostly from transparency variations in this frequency region, is too low to be seen in figure 4.3.

Figure 4.4 is an echelle plot of the modes with degree l of 2, 3, 4, and 5 which have been previously detected by several authors. The frequencies of these modes are well known (Duvall et al., 1987). Examination of the frequencies and referring to figure 4.1 reveals that the range of known modes encompasses the whole clearly visible 5 minute power bump. At frequencies which are lower or higher the modes lie in an area of the

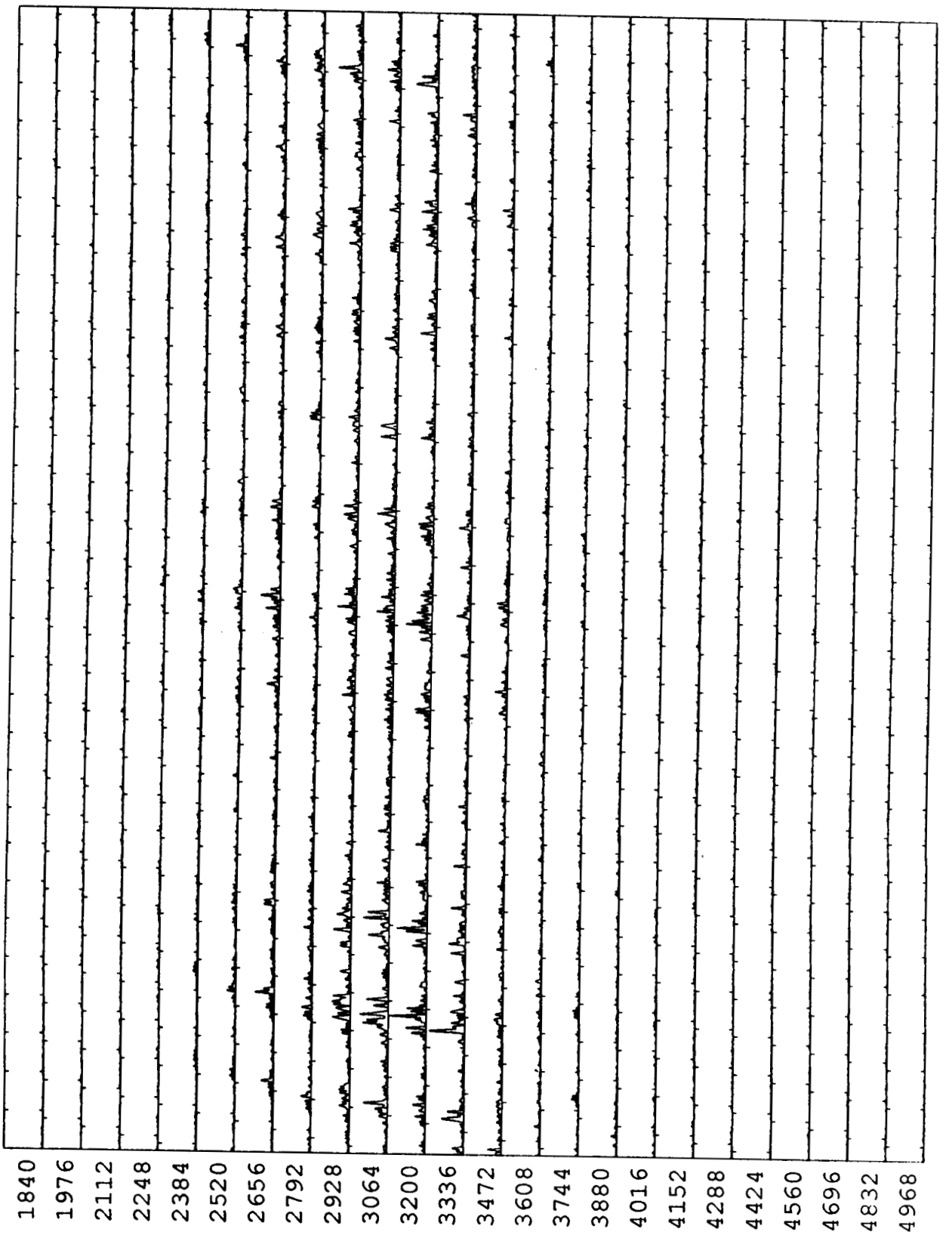

Figure 4.3 - Echelle Diagram of 1987 Power Spectrum. The individual panels are plotted to the same vertical scale, which is the maximum peak height in the power spectrum (see also figure 4.1d). The width of each panel is 150 μHz.

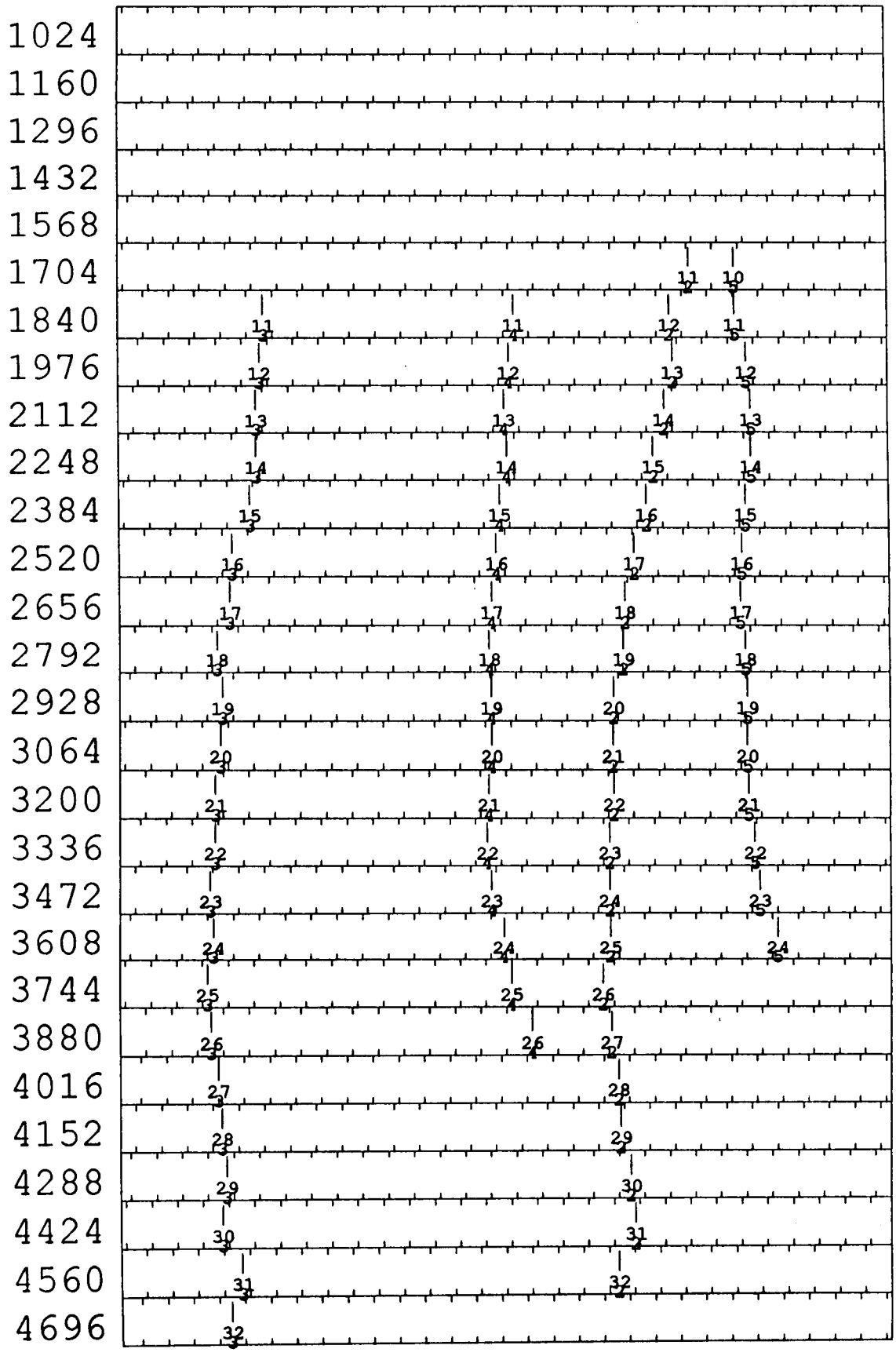

Figure 4.4 - Echelle Diagram of Known Modes. Each mode location is labeled with its value of n (the top number) and l.

power spectrum where the detection is much more difficult due to the low signal to noise ratio. However, the level of "noise" in this region is also much lower than the apparent "noise level" around the modes in the region of largest power. This is an indication of the combination of power leakage from the known modes due to the data window and the power present from modes of higher *l* values. As was examined in chapter 3, the true noise level from transparency and solar sources can be expected to be below the level of peaks which can be seen in the frequency range from 1000 μHz to 1800 μHz. This is an encouraging indication that modes can be detected there despite their low amplitude.

It became apparent in the beginning of the analysis that the data window introduces a confusion into the location of true peaks which is especially detrimental when the peak amplitude is not much higher than the noise level. The window causes the power in the mode to be distributed over a range of peaks which add to the noisy background. Under conditions where the peak is fairly weak to begin with the data gaps result in a spectrum that resists any attempt at automatic extraction of the solar mode by methods which try to "clean" the spectrum in a computational manner. Most sophisticated methods which can restore the original spectrum when there are data gaps require a signal to noise ratio of at least 100, and a filling factor of above 70% (Brown and Christensen-Dalsgaard, 1985). There has as yet been no success in developing a computational method which is applicable to the type of data produced by the differential measurements - data with gaps, and without spatial information which would allow isolation of specific values of degree *l* and azimuthal order *m*.

The method developed for the detection and identification of p-modes in this low signal to noise environment is computationally simple, but very labor intensive. This is because it utilizes a pattern recognition machine which is slow, but unparalleled in flexibility and discrimination - the human mind. Basically the method utilizes the

information contained in different resolution power spectra combined with an expectation of the signature of a solar mode to extract the peaks from the data.

Power spectra of the data are calculated at three different resolutions. For the first power spectrum the resolution corresponds to the full length of the data, utilizing the whole season's data in one FFT. This spectrum displays a multitude of narrow peaks, as can be seen in figure 4.1. A solar oscillation mode in this spectrum will be split into a group of peaks by the influence of rotational splitting, phase and amplitude changes, and the pattern of data gaps. Scherrer (1983) demonstrated effectively with a model calculation that a single frequency mode can appear as a very messy looking set of peaks depending solely on the length of the data time series and the lifetime of the mode. That calculation did not even include the effect of data gaps, but another part of the same paper shows the enormous influence that the exact pattern of gaps has on the amplitude and appearance of peaks in the power spectrum.

Nonetheless, modes can be identified just by referring to the high resolution spectrum if they have enough power. The mode appears as a multiplet of peaks of varying amplitude. In some cases one can even identify the peaks with separate values of m. Such identification is generally only possible for the largest amplitude modes which have periods around 5 minutes. It is not possible to look at this spectrum and identify modes in the low frequency range which is of interest for this study.

The possibility of identification is increased if one turns one of the drawbacks of the data to one's advantage by realizing that a true solar mode must display the sidelobes introduced by the data window. Looking at figure 2.8 one can see that the window structure is to a large extent comprised of two sidelobes to the central peak, separated from it by 1/day, or 11.574 μHz. A peak which is due to random noise in the data would not

display these sidelobes. This characteristic can be used to advantage by searching for a three-peak structure instead of trying to decide which single peak is significant enough to be of solar origin. At the frequencies of interest, however, this method is not effective in the high resolution spectrum, since there are such a large number of peaks.

The solution is to decrease the resolution of the spectrum, allowing the set of peaks which comprise a mode to combine into one broader peak. Essentially one is integrating the power in a certain frequency range, at the cost of giving up resolution of the fine structure of the mode. For the purpose of initial detection this is no detriment. For the calculation of a lower resolution spectrum, the data was divided up into sets of 8 days length. An FFT was performed on each 8-day time series, and the resulting power spectra added to give an average power spectrum. In each season there were three 8-day long stretches of good data which went into the average for each year. A third average spectrum of even lower resolution was also calculated for each year from a number of 4-day long time series of data. It is important to realize that these lower resolution spectra still utilize the information from the whole season of observations by averaging the power spectra of the shorter time series. This reduces the noise level relative to any solar peaks.

To further aid in the search for the modes, a computer code was written which searches through the power spectra and identifies frequencies where a peak may be present. The criterion for this program is simply the presence of 1/day sidelobes of magnitude between 0.3 and 0.8 times the magnitude at the frequency under consideration. In other words, the peak-structure search program identifies frequencies where the window signature is present, possibly indicating the presence of a solar mode. The program determines the magnitude of power by integrating over a short band of frequency centered on the value being examined and its sidelobes. The width of this band is a parameter which can be changed. This program is run three times for each power spectrum, the

bandwidth changing from 2 to 6 to 10 frequency bins. Since the power spectra are calculated oversampled by a factor of about 3-4, the varying bandwidths correspond to a width of less than, about twice, and about three times the natural resolution. The broader width of integration is an attempt to include any mode power which may be close to the central peak, as well as to check for chance detections of the three-peak pattern. The multiple searches make it easier to eliminate such random detections from consideration as a solar mode.

It is the combination of the information from all the resolutions and every peak-structure search which enables detection and identification of solar modes from a very noisy background. No single treatment of the spectrum is able to allow enough discrimination so that only solar modes stand out. During the search an agreement between the different spectra and searches must be found for there to be confidence in the detection of a mode. In practice it is in the two low resolution spectra where the peak-structure search finds and points out the region of frequency where there is modal power. The high resolution spectrum can then be helpful in confirming the presence of a set of modes, and zeroing in on the frequency.

Figures 4.5a-b show examples of the plots which were used in the detection of the modes in the 1987 spectrum. Each page displays 13 panels which extend over an identical frequency range of 150 μHz. Each of the top 12 panels displays a different treatment of the data. The first 4 panels show the lowest resolution spectrum (4 days) and the three peak-structure searches performed on it. The next 4 panels show the same thing for the 8 day resolution spectrum, and the last 4 panels correspondingly for the high resolution spectrum. The bottom panel shows the frequencies of any previously known modes.

Figure 4.5a shows a frequency range lying in the center of the 5 minute power peak,

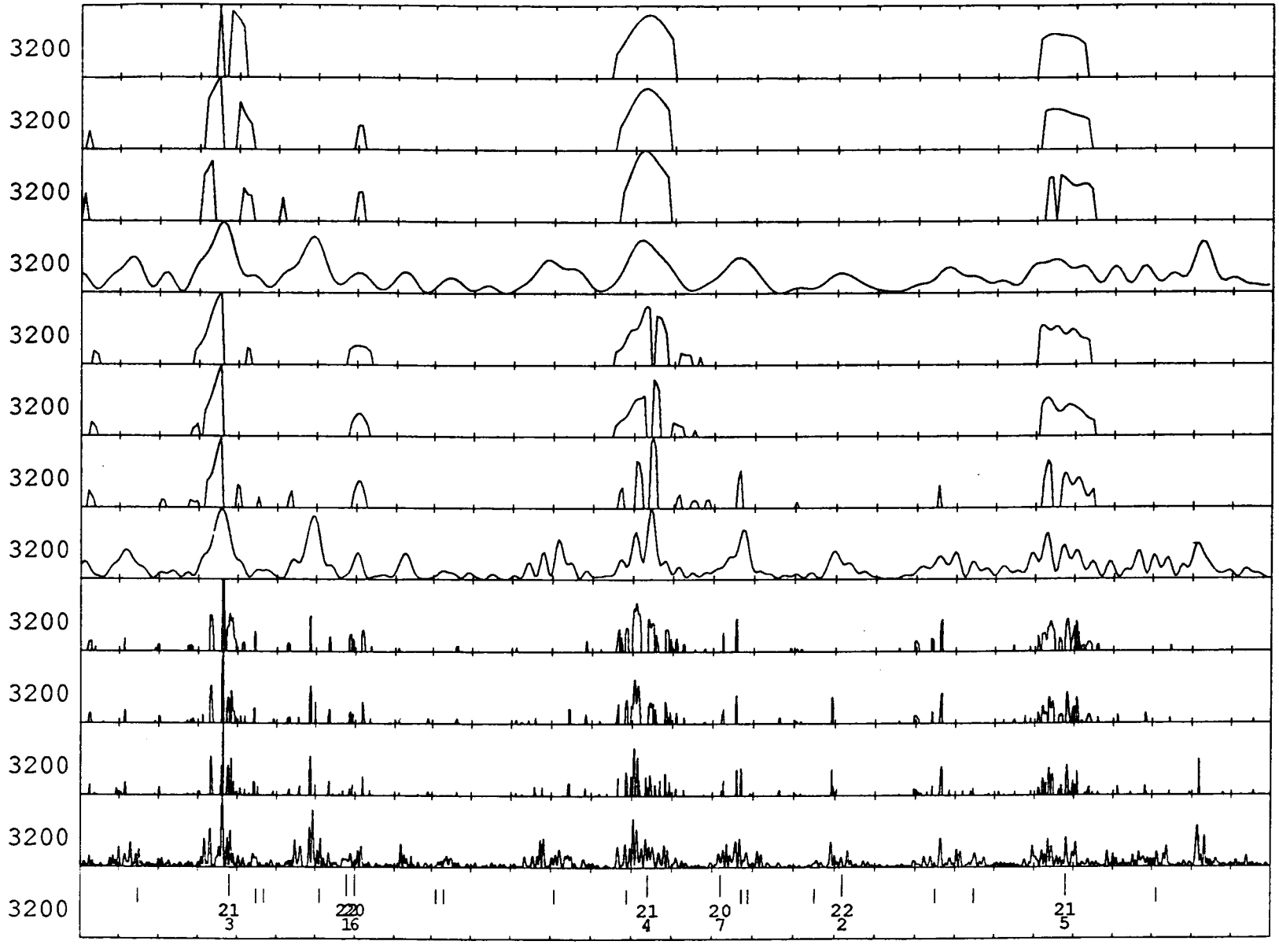

Figure 4.5a - Mid-Frequency Multigraph. Each 150 μHz wide panel shows an identical range of frequency starting at 3200 μHz.

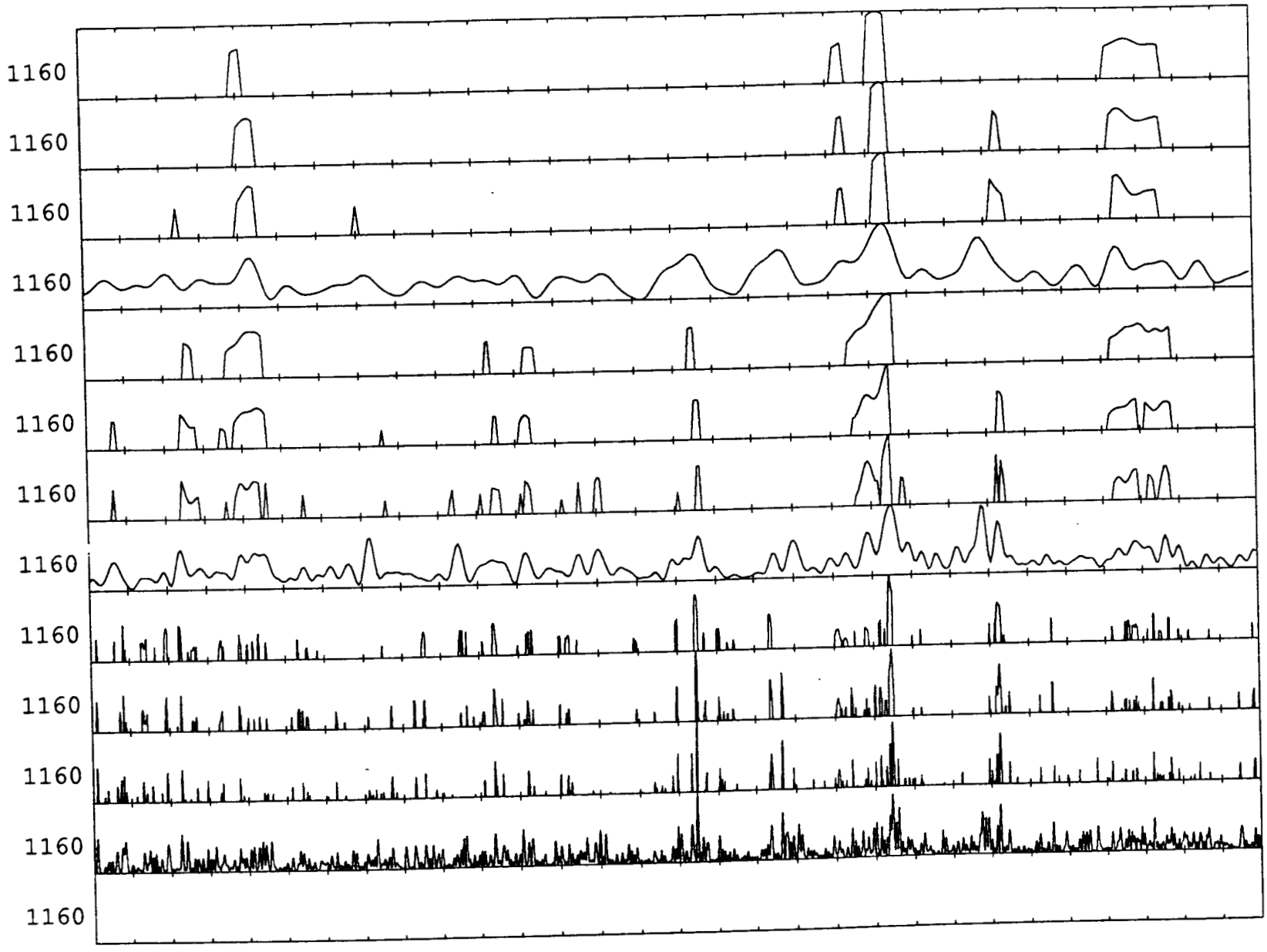

Figure 4.5b - Low-Frequency Multigraph. As for figure 4.5a, but the frequency range is from 1160 μHz to 1310 μHz.

where the modes have a large amplitude. The location of the modal power is clearly indicated by the low resolution peak searches, and the multiplet of peaks corresponding to each mode is visible in the high resolution spectrum. Even at these frequencies it is obvious that the automatic peak search on the high resolution spectrum is confusing and of little assistance in detecting the mode, while the low resolution spectra are quite useful for that purpose.

Figure 4.5b shows a frequency range at low frequencies, where the modal power is much less. The increased noise is noticeable in the low resolution peak structure searches, but there are clearly frequencies where peak structure is identified.

The manual procedure now followed in the detection of modes starts with the plotting of these multi-panel graphs for all frequencies. Each graph is separated by 136 μHz from the next one. This value is the asymptotic splitting of the p-modes, the same spacing as was used for the echelle diagram of figure 4.4. First the frequencies in the central frequency region are identified with the guidance of the values which are known. This effort serves to educate the searcher on the form of the peak structure which can be expected from the modes. In essence it is practice or training for the task of identifying modes in the unknown regions. Detection of modes in the known region also serves to validate the analysis procedure itself and provides information on which l values can be expected. The modes identified in this region can then be used as anchors for the identification of the new modes which are detected.

To avoid any possible subjective bias the modes at frequencies below 1840 μHz are searched for with no external guidance or expectation. Instead, each tentative mode detection is recorded, without any attempt at identification or comparison with other years. For the first year analyzed, 1984 (Henning and Scherrer, 1986), there is no possible

guidance which can bias the search, except for the expectation that the modes should lie separated by 136 μHz and thus at about the same location on the graph as for the previous frequency range. As it turns out this expectation is misleading as it is not met. One can speculate that one reason that the previously detected modes stop at frequencies above 1840 μHz is precisely that the modes' frequencies start deviating strongly from the asymptotic separation of 136 μHz. For the analysis of subsequent years this misleading assumption is not present, but care was taken not to provide any guidance from previous knowledge of the location of modes. The second year of data was actually analyzed over a year after the first work was done. This effectively prevents any knowledge of the frequency values from affecting that analysis. The peaks detected in this second year were simply recorded, without any attempt at identification or further plots of the detected values. Thus, when the other two years were analyzed shortly afterwards, the knowledge of the frequencies was essentially nil. It should be emphasized that each analysis takes some time, and so there is virtually no memory of a frequency value written down for the previously analyzed years.

The reason for this bias-blind approach is the preservation of the ability to compare the results for the different years. If the detected peaks lie at the same frequency each year it is virtually assured that they are of solar origin and not random noise. Of course there is the possibility of an instrumental origin which remains constant over the years, but in this case this is ruled out by the distribution of the peaks which clearly marks them as extensions of the previously identified modes.

4.2. Results of the P-Mode Analysis

Figure 4.6 shows the position of the modes detected in the analysis in the form of an echelle diagram. The crossbar on each frequency indicates the year in which that detection

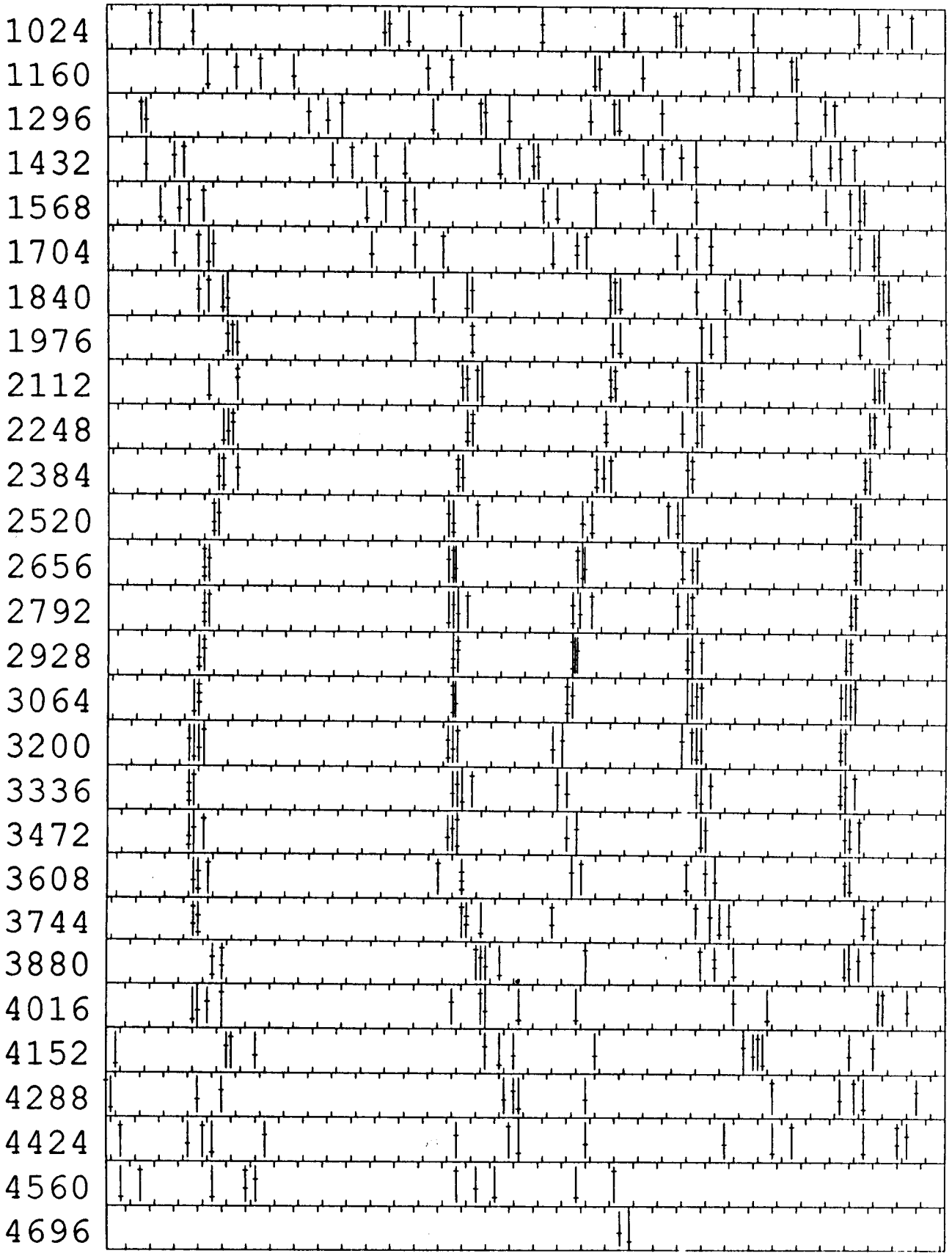

Figure 4.6 - Echelle Diagram of Peaks in all Years. The horizontal crossbars represent, from top to bottom, the years 1981, 1984, 1986, and 1987.

was made. The height of the crossbar progresses from top to bottom in four positions, corresponding to the four years 1981, 1984, 1986, and 1987 respectively. The peaks detected at both the low and high frequencies lie in an obvious pattern, extending the vertical ridges of modes of different l values. The modes become separated by progressively larger values of frequency as the order n decreases. This is expected as the modes depart from the asymptotic behavior followed by modes with large order n.

Knowledge of the order n and degree l of the known modes enables identification of the new modes. Figure 4.7 is an echelle diagram of the modes, with the frequencies averaged over all years. The horizontal crossbars are error bars indicating a measure of the uncertainty of the location of the mode. A minimum error bar of 1 μHz is plotted, as this is generally the accuracy which was adopted in the detection procedure. The meaning of the width of the error bar bears some discussion. While it is calculated simply as the standard deviation in the frequencies of the detected modes, the distribution of errors is unusual. This is due to the window structure, which makes it more likely that a mode's sidelobe is identified, at a distance of 1/day, than that a mode's position is misidentified by, for example, only 5 μHz. In other words, the standard deviation is a combination of small errors of a few μhz with a possible error of about 11.574 μHz. Thus the error bars are an indication of the uncertainty of the mode's frequency, and a warning that the frequency may be different by up to 11.574 μHz. It is advisable to keep in mind the distribution of the individual detections in each year. Tables II-V list the frequencies for all modes and years. In Table I are listed the average frequencies.

In figure 4.8 is plotted the frequency difference between the modes obtained from a current solar model, courtesy of J. Christensen-Dalsgaard, and the measured modes, as a function of frequency. The model is described in Christensen-Dalsgaard (1982). The linear trend followed by all modes until a frequency of about 2000 μHz has been known

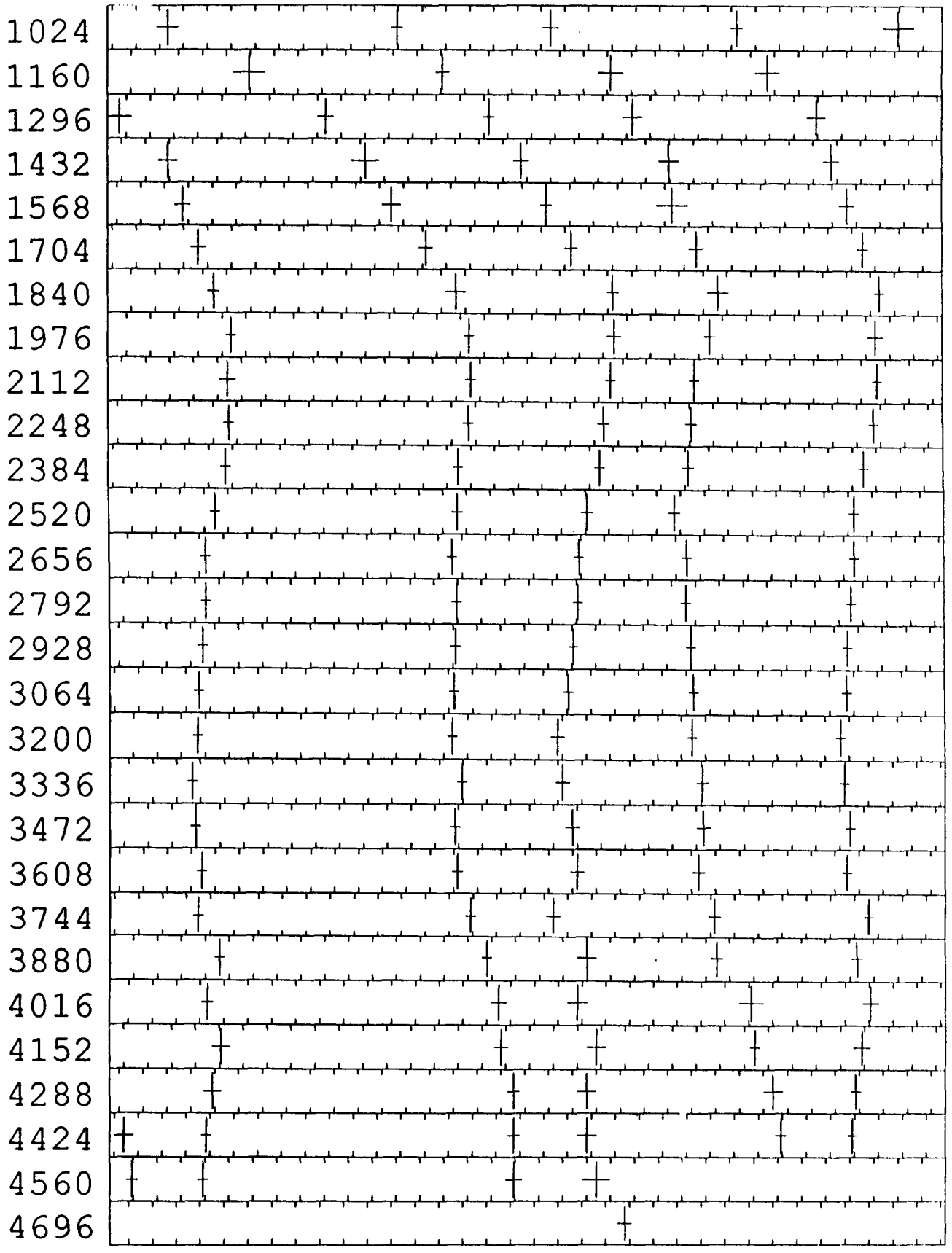

Figure 4.7 - Echelle Diagram of Average P-Mode Frequencies. The horizontal crossbars represent the standard deviation of the values in figure 4.6.

Table I - Average Frequencies				
n	l=2	l=3	l=4	l=5
5			1036.7 ± 2.2	1117.0 ± 1.6
6	1084.8 ± 1.1	1156.0 ± 1.2	1189.8 ± 3.3	1265.7 ± 2.6
7	1230.3 ± 1.4	1298.5 ± 2.6	1341.7 ± 1.7	1406.3 ± 2.0
8	1376.0 ± 1.2	1444.7 ± 2.0	1486.0 ± 2.8	1549.8 ± 2.1
9	1518.8 ± 1.6	1583.8 ± 1.6	1627.5 ± 1.9	1686.5 ± 3.2
10	1660.0 ± 1.2	1723.0 ± 1.5	1770.7 ± 1.4	1827.5 ± 1.4
11	1801.3 ± 1.3	1862.3 ± 1.2	1913.0 ± 2.1	1968.0 ± 2.2
12	1946.0 ± 1.2	2001.8 ± 1.0	2051.8 ± 1.0	2102.3 ± 1.2
13	2082.3 ± 1.4	2137.0 ± 1.6	2188.0 ± 1.0	2235.0 ± 1.0
14	2217.5 ± 1.0	2273.3 ± 1.0	2323.5 ± 1.0	2370.3 ± 1.2
15	2352.0 ± 1.2	2408.5 ± 1.0	2457.3 ± 1.0	2505.7 ± 1.2
16	2487.1 ± 1.0	2542.3 ± 1.0	2593.0 ± 1.2	2638.7 ± 1.2
17	2620.3 ± 1.2	2676.3 ± 1.0	2727.9 ± 1.0	2777.3 ± 1.0
18	2754.6 ± 1.0	2812.3 ± 1.0	2864.8 ± 1.0	2913.0 ± 1.0
19	2890.4 ± 1.0	2947.5 ± 1.0	3000.5 ± 1.0	3050.0 ± 1.0
20	3025.4 ± 1.0	3082.8 ± 1.0	3136.1 ± 1.0	3186.5 ± 1.0
21	3160.3 ± 1.0	3218.5 ± 1.0	3271.8 ± 1.0	3322.3 ± 1.0
22	3294.0 ± 1.4	3353.3 ± 1.0	3409.8 ± 1.0	3460.3 ± 1.2
23	3431.0 ± 1.4	3490.0 ± 1.0	3544.3 ± 1.0	3596.5 ± 1.4
24	3569.0 ± 1.4	3627.3 ± 1.0	3680.8 ± 1.1	3731.5 ± 1.3
25	3706.0 ± 1.4	3762.5 ± 1.0	3819.5 ± 1.0	3870.8 ± 1.3
26	3837.0 ± 1.4	3903.0 ± 1.0	3959.0 ± 1.0	4007.3 ± 1.2
27	3980.0 ± 2.0	4036.5 ± 1.1	4097.5 ± 1.6	4150.5 ± 2.5
28	4114.0 ± 2.0	4175.3 ± 1.8	4234.0 ± 1.4	4287.3 ± 1.0
29	4254.0 ± 2.0	4309.5 ± 1.8	4372.7 ± 1.2	4427.0 ± 2.0
30	4388.0 ± 2.0	4444.3 ± 1.0	4508.7 ± 1.2	4564.7 ± 1.2
31	4524.0 ± 2.0	4579.5 ± 1.0	4644.7 ± 1.7	
32	4662.0 ± 2.8			
33	4804.0 ± 1.4			

Table I. The table lists the frequencies, in μHz, of all modes detected, averaged from the individual values measured each season. The error is the standard deviation of the individual values, with a minimum of 1.0 μHz.

Table II - Frequencies in 1981 Season

n	l=2	l=3	l=4	l=5
5			1033	
6	1087	1154	1192	
7	1232	1303	1345	1402
8	1374	1448	1483	1548
9	1518	1588	1626	
10	1659	1723	1774	1827
11	1804	1861		
12	1946	2002	2052	2100
13		2139	2189	2233
14	2218	2274	2324	
15		2408	2457	2506
16	2489	2542	2597	2637
17		2676	2728	2776
18	2754	2813	2867	2914
19	2893	2948	3001	3052
20	3025	3083	3136	3188
21	3160	3220	3273	3322
22		3354	3412	
23		3492	3545	
24		3629	3677	3729
25	3707	3762	3818	3867
26	3837	3904	3957	4004
27	3980	4040	4094	
28		4178		4288
29				4427
30		4444	4508	4567
31		4578	4645	
32	4666			
33				

Table III - Frequencies in 1984 Season

n	l=2	l=3	l=4	l=5
5			1035	1115
6	1083	1155	1187	1263
7	1227	1292	1338	1412
8	1375	1446	1488	1552
9	1522	1585	1630	1691
10	1659	1726	1768	1830
11	1802	1859	1916	1963
12		2001	2052	2105
13		2139	2187	2236
14	2217	2274	2324	2372
15	2352	2411	2457	2505
16	2486	2543	2591	2640
17	2621	2677	2727	2779
18	2754	2812	2864	2911
19	2889	2948	3001	3050
20	3026	3083	3136	3187
21	3161	3217	3271	3320
22	3295	3353	3409	3462
23	3430	3490	3544	3597
24	3570	3627	3682	3733
25	3705	3763	3819	3870
26		3902	3958	4007
27		4037	4099	4147
28		4177	4231	4285
29		4312	4373	
30		4446	4508	
31		4580		
32				
33				

Table IV - Frequencies in 1986 Season

n	l=2	l=3	l=4	l=5
5			1042	1121
6	1082	1159	1199	1272
7	1232	1304	1342	1408
8	1380	1440	1479	1555
9	1521	1583	1632	1682
10		1718	1770	1823
11	1802	1865	1908	1972
12	1945	2003	2051	
13	2082		2186	2236
14	2218	2273	2323	2368
15	2352	2407	2458	2506
16	2488	2542	2592	
17	2619	2676	2729	2778
18	2756	2812	2865	2914
19	2891	2947	3000	3049
20	3026	3083	3137	3186
21	3160	3219	3272	3324
22	3293	3353	3408	3459
23	3432	3489	3543	
24	3568	3626	3682	3735
25		3762	3819	3874
26	3837	3904	3959	4007
27		4035	4095	
28		4171	4237	4287
29	4254	4307	4371	
30	4388	4441		4564
31	4524	4578	4648	
32				
33	4803			

Table V - Frequencies in 1987 Season

n	l=2	l=3	l=4	l=5
5				1115
6	1087		1181	1262
7		1295		1403
8	1375		1494	1544
9	1514	1579	1622	
10	1662	1725		1830
11	1797	1864	1915	1969
12	1947	2001	2052	2102
13	2083	2133	2190	2235
14	2217	2272	2323	2371
15	2352	2408	2457	
16	2486	2542	2592	2639
17	2621	2676	2728	2776
18	2755	2812	2863	2913
19	2889	2947	3000	3049
20	3025	3082	3136	3185
21	3160	3218	3271	3323
22		3353	3410	3460
23		3489	3545	3596
24		3627	3682	3729
25		3763	3822	3872
26		3902	3962	4011
27		4034	4102	4154
28	4114		4234	4289
29			4374	
30		4446	4510	4563
31		4582	4641	
32	4658			
33	4805			

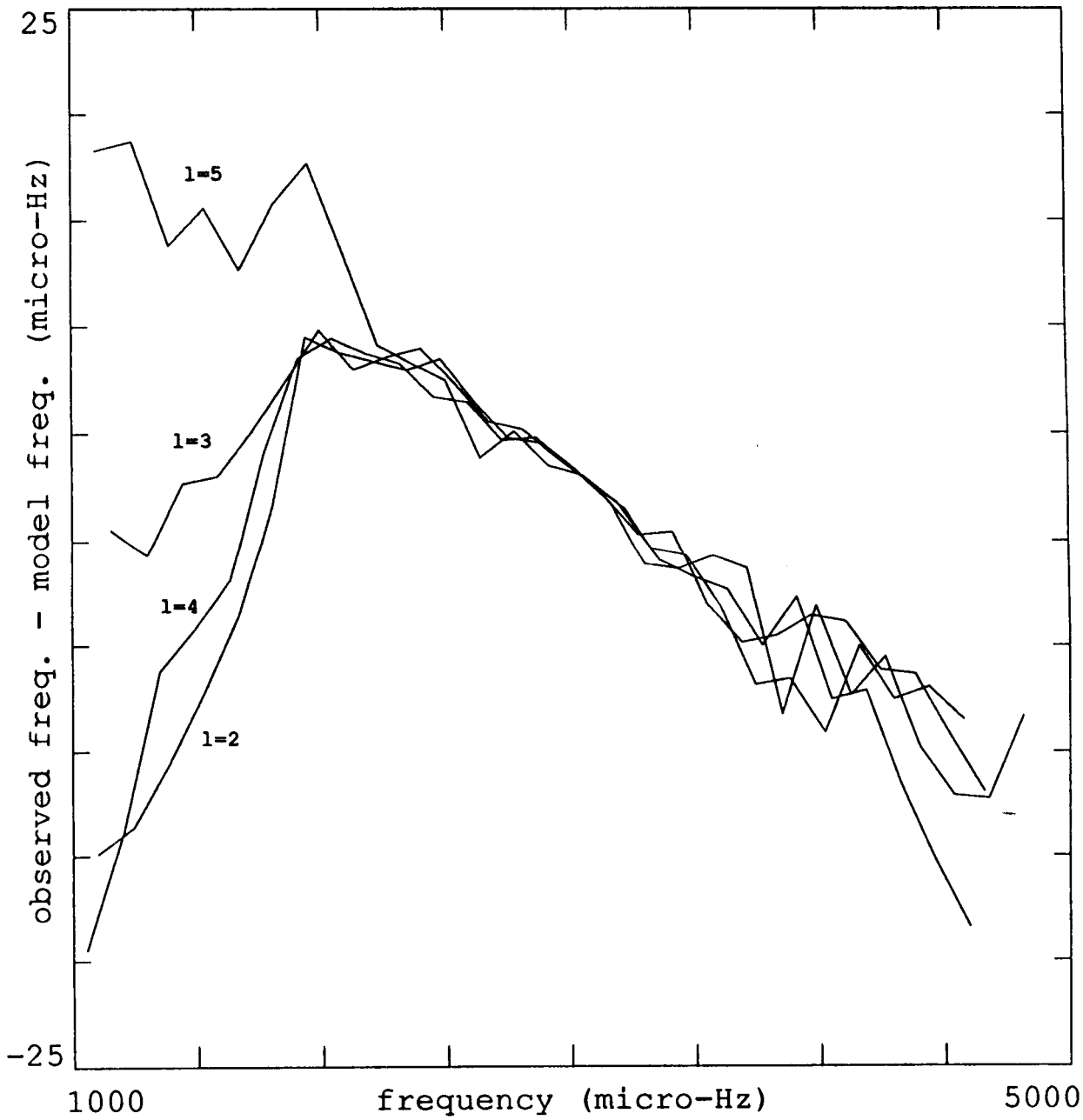

Figure 4.8 - Difference between Measurement and Model. The vertical axis corresponds to the difference between the observed mode frequencies and the model frequencies. Points corresponding to modes with the same degree l are connected.

previously. The new information contributed by the low frequency modes shows some different activity. The modes with l=5 continue to generally follow the linear trend, while the other modes bend off. Roughly speaking, only the modes with l=5 below the frequency where the others turn off do not penetrate the core of the sun, their turning point lying above the core radius, while the other modes penetrate to some degree. This indicates that the model has some trouble in the core. The frequencies are lower than the model frequencies, which corresponds to a longer period or travel time of the wave than expected by the model. The travel time of the wave is the inverse of the integrated sound speed along the path of travel. A longer period thus implies a lesser sound speed. As sound speed is proportional to the squareroot of temperature the measurements could indicate a lower temperature in the solar core. A higher mean molecular weight could affect the sound speed similarly. One must however be cautioned that this simple reasoning may not hold up under the complex conditions which affect the modal frequencies.

It is of interest to know the amplitude of the modes, for comparison both with other data and with theoretical predictions. As discussed previously, the amplitude information was only preserved in the 1987 data. Secondly, the amplitude of any individual mode is affected by the particular data window, so that it is generally only the envelope of power which can be considered. Also, one must keep in mind that the calibration of the data signal is probably only accurate to within 10%. Figure 4.9 shows the amplitude of the modes in 1987. Also plotted is the shape of a theoretical prediction assuming energy equipartition (Christensen-Dalsgaard, 1986; Libbrecht et al., 1986). The modal power appears to decrease less rapidly than the equipartition curve would imply, especially at lower frequencies. This behavior can also be seen in the modes measured by Libbrecht et al. (1986). Thus the measured amplitudes at lower frequencies imply a larger energy in those modes than the higher frequency modes. At high frequencies the amplitude decreases

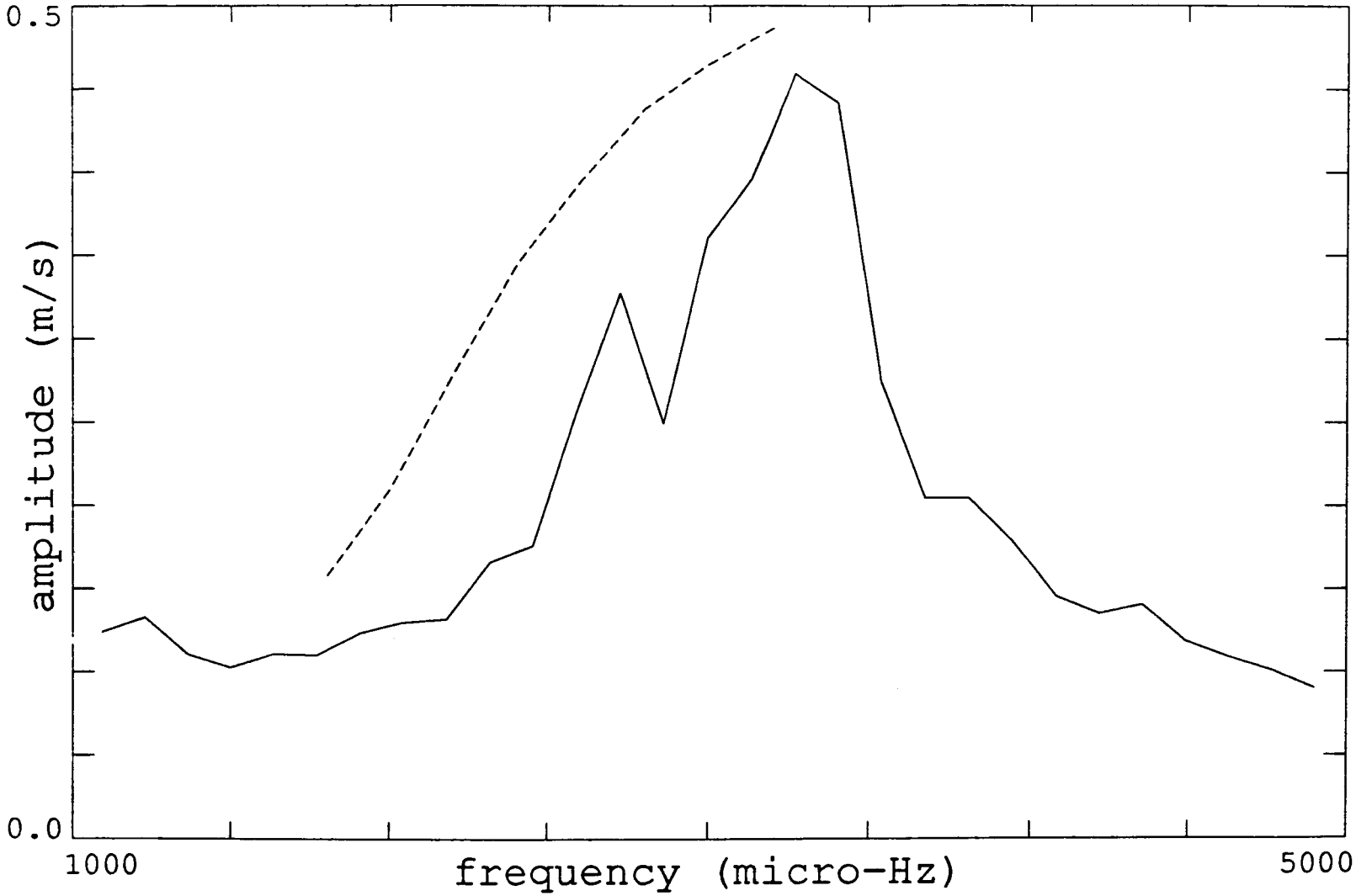

Figure 4.9 - Amplitude Envelope of Detected P-Modes and Theory. The solid curve is the envelope of power of the 1987 power spectrum of the data. The dashed curve, adapted from Libbrecht (1986) shows the expected shape assuming energy equipartition.

because of the shortening lifetime of the modes (Libbrecht et al., 1986). The absolute amplitude of the modes measured in this study is quite high, reaching almost 70 cm/s at the peak of the envelope. This is higher by a factor of about 3 or 4 than the amplitudes measured by other groups (Grec et al., 1983; Libbrecht et al., 1986). However, if one remembers the sensitivity factor of the instrument, which implied a factor of up to 8 between the differential measurement and the whole disk measurement, the amplitudes are comparable to those measured previously. Assuming an average factor of 6, the low order p-modes which are measured at about 30 cm/s in this study would lie at about 5 cm/s for the measurements of Fossat (Grec et al., 1983). It is interesting to note that their published spectrum actually shows peaks of that amplitude in the range below 1800 μHz. Also, the low frequency amplitude envelope of their spectrum looks similar to the envelope of the Stanford data, with a slight increase at 1000 μHz.

Another item of interest is the possible frequency change of the modes with time. There have been several reports on such frequency shifts, some contradictory in nature (Fossat et al., 1987; Henning and Scherrer, 1987; Woodard and Noyes, 1985). The method which is used in this analysis is an attempt to avoid the problems caused by the window function and the uncertainty of the frequency identification.

The statistical method used is a cross-correlation between the power spectra of the real data and artificial data. To build artificial time series, the list of p-mode frequencies listed in table III were used as representative of the whole data. Since the frequencies for each year are almost identical in the range where the amplitude is large, any of the tables I-V could have been used with no change to the analysis, but for consistency with the previous report (Henning and Scherrer, 1987) the 1984 results were used as a base. Each tabulated mode provides the frequency for a sinusoidal function which was put into the window of the real data. The amplitude of each sinusoid was set to the average power in a

136 μHz section of the spectrum of the real data centered at that frequency. This results in a time series of coherent noise-less data from a non-rotating sun. The power spectrum of this constructed data will be complicated solely by the window function. A correlation between the observed power spectrum and this idealized power spectrum is not sensitive to systematic pulling that might be introduced by the window function. This important advantage helps to make the correlation a powerful tool for comparing a large number of spectral peaks to find a systematic shift.

However, the real data is quite noisy, and the real peaks are not single-frequency sinusoids, but rather are split into a broad band of spikes by rotation, phase changes and amplitude changes. These effects broaden the correlation maximum to a few μHz, and can also cause a systematic shift of the maximum.

The cross-correlation function was filtered with a 4 μHz low-pass filter to eliminate high-frequency variations resulting from the sources mentioned in the paragraph above, as well as from the window. The centroid of this curve gives the systematic shift.

To get some idea of the error of a systematic shift determined in this way several different time intervals were used for each year. The first time series used all usable data in the summer months of each year. Two different phases of the peaks in the artificial data in this time series provided two shift estimates. It was found that the scatter due to a different (but still constant) phase was minimal. However, when each summer was divided into several sub-intervals the variations in average frequency shifts were found to be quite large.

The resulting samples, numbering from 4 to 7 depending on the quality and quantity of the data in a given year, were averaged and the standard deviation calculated. Figure 4.10 shows the results, with time running along the abscissa, and frequency shift along the

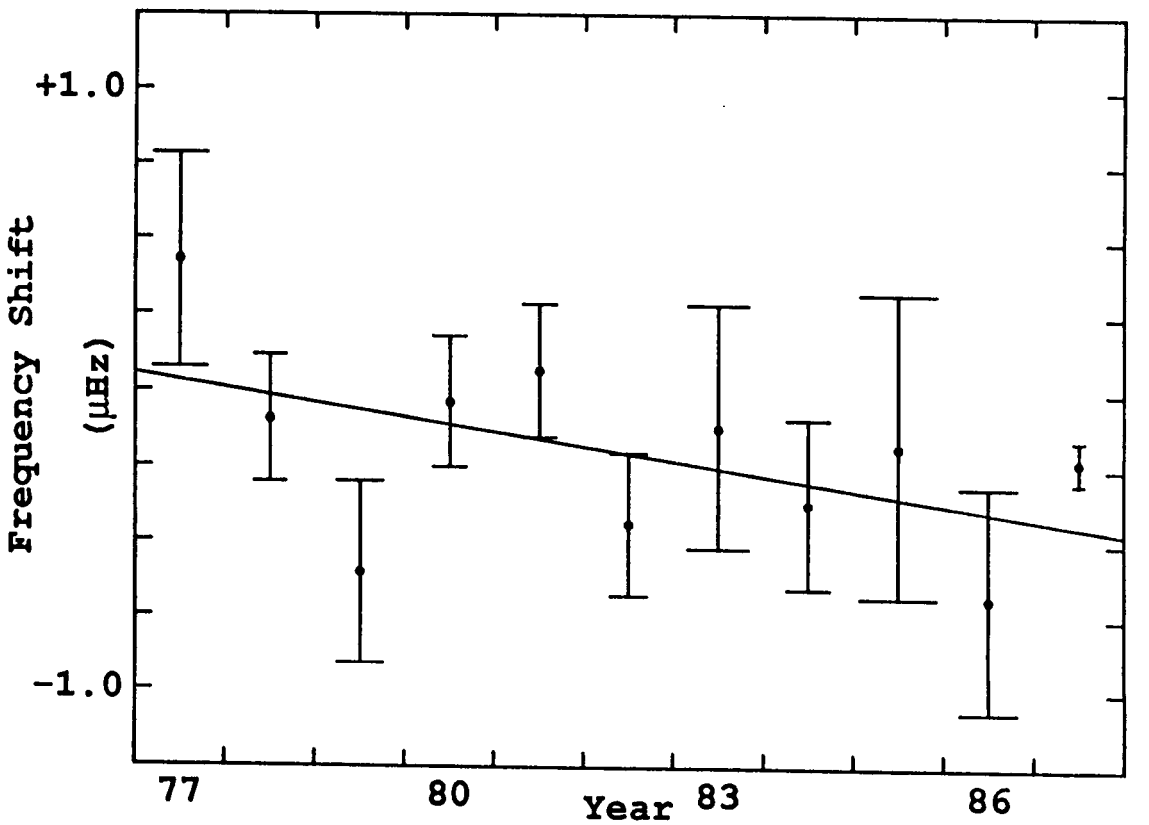

Figure 4.10 - Frequency Shift of P-Modes with Time. The line is the least-squares fit to the points.

ordinate. The value for 1987 stands out due to the small error bar. This is a good demonstration of the better quality of the 1987 data, which has not had any normalization performed on it.

For the analysis performed earlier (Henning and Scherrer, 1987), which included only the years through 1986, a linear least squares fit to the data gave a decrease in frequency in time with a slope of -0.06 μHz per year. If only the data from 1981 onwards were used, leaving out the time before solar maximum which includes some of the years with the worst data window, the slope becomes -0.09 μHz.

This decreasing trend does not seem to be continued in the 1987 data. Whether there is a real solar cycle dependent shift, or whether the 1987 point indicates that the data points are consistent with no systematic frequency change cannot be determined from this data. After the addition of the 1987 point, the slope of a line fit to all the years is not much different from a slope fit to only the data from 1980 onwards. Its value is still a rather large -0.05 μHz. However, in this fit the 1987 was weighted equally to all other points, which does not consider the improved quality of the 1987 data. More observations will have to be made over the next years to gain insight into the question of a systematic frequency shift with time.

Another investigation which was performed on the data was the possible determination of the magnitude of the rotational splitting of the modes. Only the year 1984 was able to provide any useful data for this purpose, as the time series used for the p-mode analysis in all other years was too short to allow good resolution of the split peaks. 1984 has the longest time series, running from June 20th through August 8th. In 1987 the data is cleaner, but only the data from July 7th through August 14th were used for the p-mode analysis.

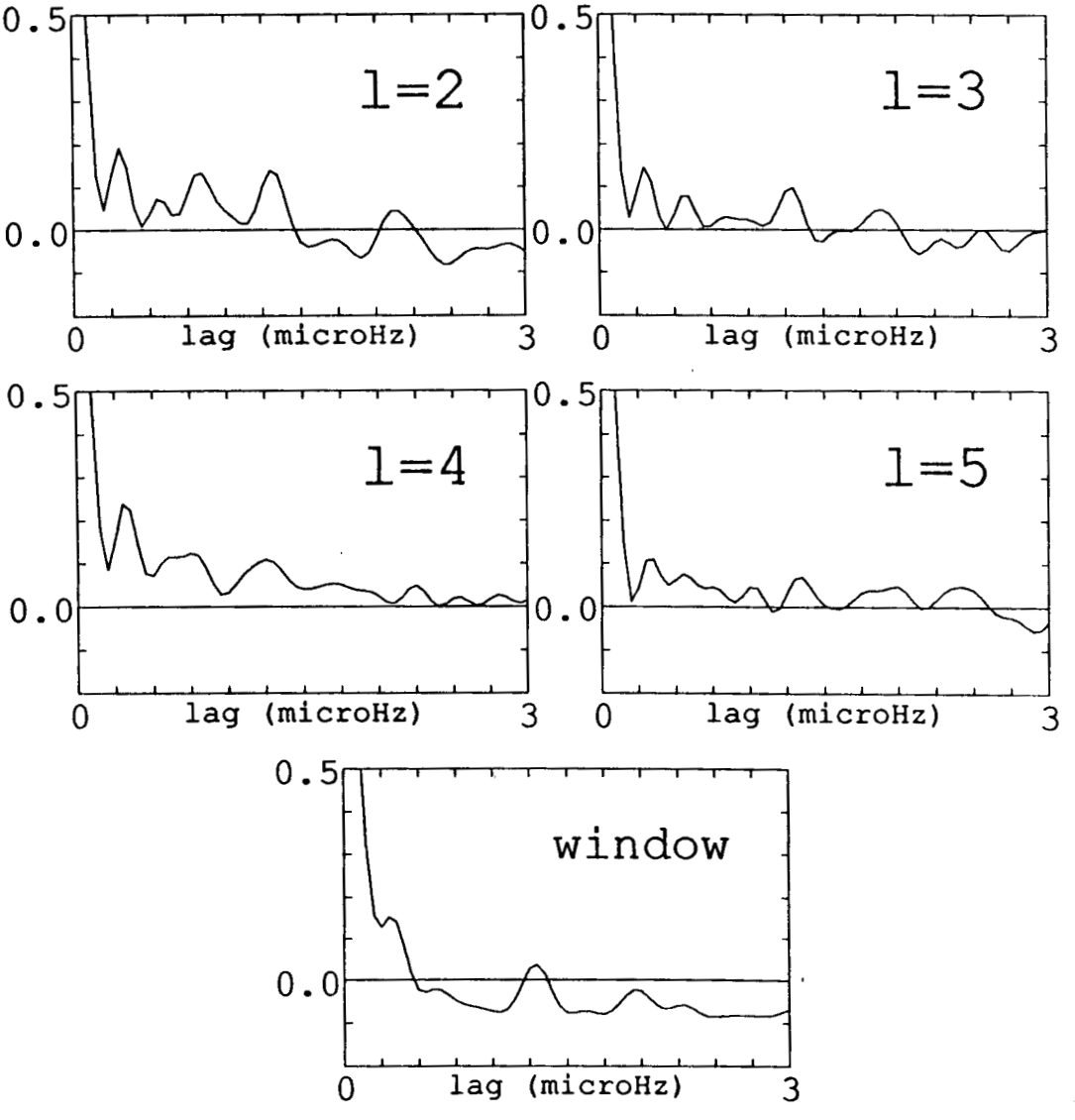

Figure 4.11a-e - Autocorrelations of the Power Spectrum. The top four panels are the average of the autocorrelations of the 1984 spectrum around the well-known modes with degree l as labeled. The bottom panel shows the autocorrelation of the 1984 window function.

As mentioned before, the power of each mode is split into a multitude of peaks resulting from a combination of mode lifetimes, window function, and noise, as well as rotational splitting. This confusion effectively prevents one from assigning m-values to given peaks and directly measuring the splitting. Rather, the spectrum has been analyzed using autocorrelations. Using the determined frequencies an autocorrelation is calculated of a small section of the full spectrum around each mode. All autocorrelations with a given degree l, but different order n, were then averaged together. The assumption is that any rotational splitting will not change much with order n. The results are plotted in the first four panels of figure 4.11. An autocorrelation of the window function is shown in the last panel of the figure.

It can be seen that the window is responsible for much of the systematic splitting, as evidenced by the peaks in its autocorrelation which are repeated and actually dominate the autocorrelations of the modes. However, all degrees show a peak around 0.8 μHz, which is close to twice the rotational splitting as measured by Duvall and Harvey (1984). Since the Stanford instrument is sensitive only to modes with $l+m$ even, this peak can be identified as the result of rotational splitting.

Chapter 5

G-Mode Analysis

The history of the search for buoyancy oscillations, commonly referred to as g-modes, has been markedly less triumphant than the research performed on p-modes. While the 5 minute pressure oscillations have yielded a wealth of knowledge regarding the structure and physics of the sun, the g-modes have stubbornly resisted even the first step of concrete and unequivocal detection, much less providing any information about the sun. G-modes have great potential for revealing the structure of the solar interior, since they probe deep into the energy generating core of the sun. For this reason they have been looked for despite imposing difficulties with the available data. Several reports of detection and identification of g-modes have been published (Delache and Scherrer, 1983; Fröhlich, 1986; Isaak et al., 1983; Scherrer, 1984), but the results disagree with each other.

The difficulty of the g-mode detection arises from a combination of problems. Firstly, the g-modes lie at very low frequencies, below 300 μHz, with the vast majority actually below 100 μHz. At such frequencies the amount of power deriving from the transparency gradient signal and other non-solar drifts starts to get large, as discussed in chapter 3. Below 50 μHz the solar noise contribution also becomes large, making detection in that region even less likely. Moreover, the amplitude of the g-modes is theoretically expected to be less than for p-modes, perhaps so small as to be undetectable with current data. The reason for this low amplitude is that buoyancy waves do not propagate in the convection zone. The g-modes decay exponentially throughout the convection zone, leaving only a small magnitude visible at the sun's photosphere. Thus the first problem is to be able to

reduce the level of noise in the data to allow g-modes to be seen in the first place.

The second problem arises from the requirement to be able to look at a peak in the spectrum and declare that it is actually a solar g-mode. Theoretical guidance is necessary for this discrimination. Solar models can certainly produce lists of g-modes, but the true solar parameters which go into the determination of the actual frequencies are uncertain, so that the frequencies cannot be used for a search in the observational data. For practical use with actual data, theory only provides the fact that for large values of order n modes of the same degree l are asymptotically equally spaced in period. The asymptotic equation, however, is really only completely valid for modes with very large n. These modes generally lie at very low frequencies swamped by noise and are so closely spaced in frequency that they cannot be resolved in the data. Figure 5.1 shows a set of theoretically calculated g-modes. There are a large number of potential peaks, even without considering that each mode's power is further subdivided by data window sidelobes. Rotational splitting produces peaks separated from the central mode frequency by up to a few μHz. Window sidelobes appear mainly at a distance of 1/day, or 11.574 μHz. Both effects result in peaks which intermix with all the other modes, producing a forest of possible peaks which may be impossible to penetrate, especially at frequencies below 50 μHz.

These considerations leave the range between about 50 μHz and 100 μHz where the asymptotic assumption is approximately valid, the noise level appears manageable, and the resolution of the spectrum and the spacing of the modes allows identification of peaks and avoids mode beating in the spectrum. It is this range which will be considered in the analysis.

Theoretical considerations provide two more pieces of information which are helpful in the development of a search method. Firstly, the amplitude of a g-mode at the surface of

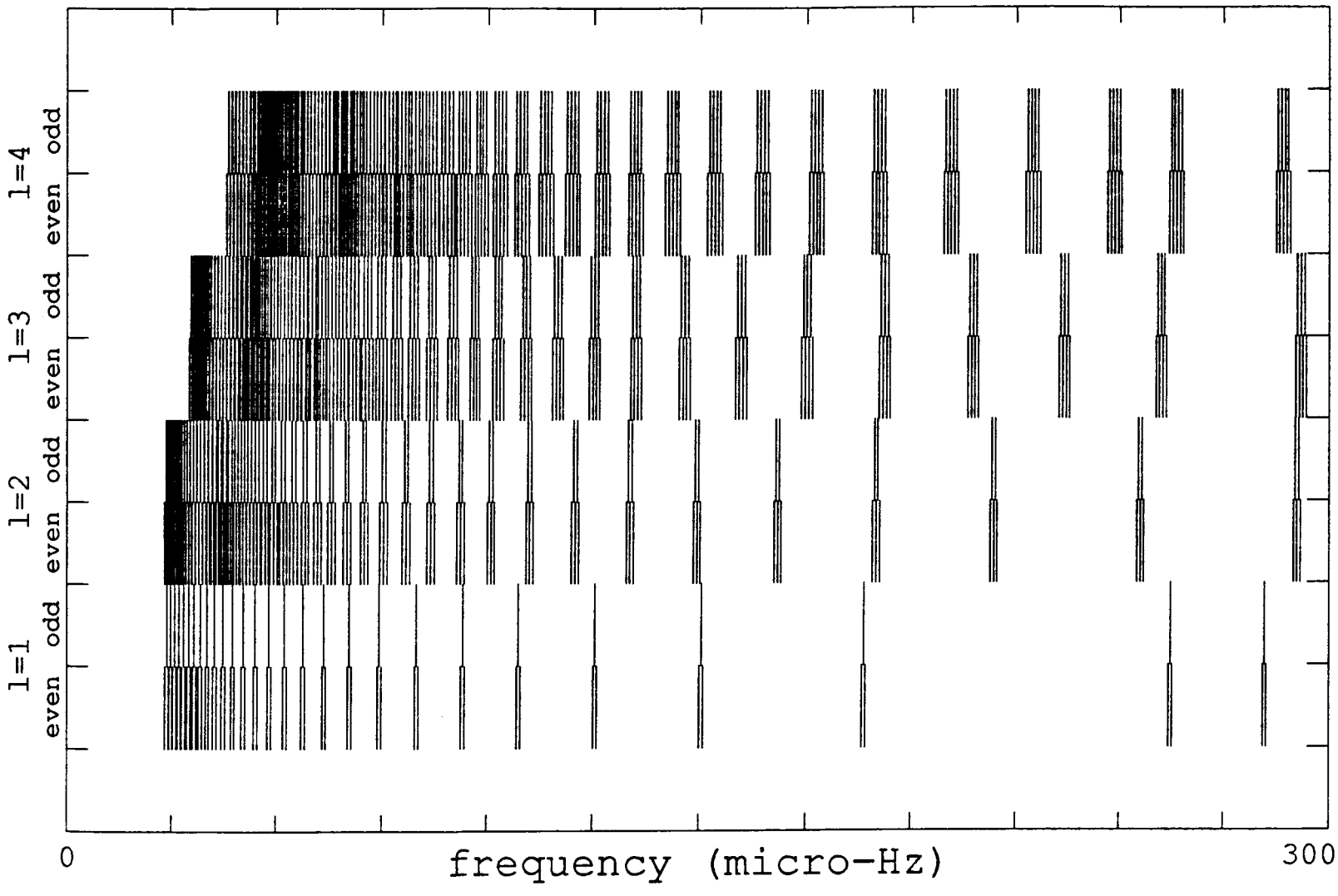

Figure 5.1 - Model Set of G-Mode Frequencies. Each calculated mode's $2l+1$ rotationally split peaks are shown, vertically separated by l, and whether $l+m$ is even or odd. In a real power spectrum all these modes would be superimposed.

the sun decreases rapidly with increasing degree l. Secondly, the pattern of velocities in the photosphere which is the signature of a g-mode is such that the Stanford differential measurement is most sensitive to g-modes of degree l=1 and l=2. This is to be contrasted with the sensitivity to p-modes, where the maximum sensitivity was attained for modes with l=4, while there was almost no sensitivity to modes with l=1. Roughly speaking, a g-mode oscillation lifts the material under the photosphere causing the flow in the photosphere to be largely horizontal as the material flows away or toward the extremum of the mode. The horizontal motions expected for g-modes change the sensitivity profile of the differential detector from what it was for the primarily vertical motions of the p-modes. Combining that information with the expected g-mode amplitudes one can reason that the Stanford data should display mostly modes of degree l=1, with perhaps also some peaks of l=2 modes. This reduces the number of possible peaks, eliminating the rows corresponding to l=3 and l=4 in figure 5.1.

In this study a statistical method is developed which succeeds in detecting g-modes in the Stanford data. The process involves removal of most of the noise power introduced by the combination of the data window and the daily drift of the data signal. After the appropriate treatment a program is run which searches recursively for the largest peak and removes it and all its window-associated sidelobes from the data. After a large set of peaks has been determined, a statistical search is then performed on them to detect structure which corresponds to g-modes. This study also includes a thorough examination of the effect of the data window on the data and on the detectability of any modes in the data.

5.1. Data Reduction and Treatment

Each day's data is processed though a bandpass filter with cutoffs at frequencies of 50 μHz and 500 μHz. The low frequency cutoff is necessary to remove the noise power

which continues to increase steeply at lower frequencies. The filter requires a shortening of the data which is proportional to the period of the filter. The value of 50 μHz is thus a compromise between a desire to keep the periods with data as long as possible and a need not to interfere with the g-modes which lie at these frequencies. By applying the low frequency cut at 50 μHz the detection search is being explicitly restricted to g-modes of higher frequency. After this treatment the filling factor of the data is reduced to 20.1% for 1981, 22.6% for 1984, 22.0% for 1986, and 23.6% for 1987. The high frequency cutoff removes the short period power which is of no interest in this analysis. Removal of the higher frequencies also allows the rebinning of the data into 5 minute bins, decreasing the amount of computing space necessary.

When the data is combined into a time series and an FFT applied to it, the resulting power spectrum looks as shown in figure 5.2. The spectrum plotted is for 1987, the year when the data is best by virtue of not needing to be multiplied by a different normalization factor for every day. Despite this, while there appears to be power in the region of interest, between 50 μHz and 100 μHz, the spectrum is dominated by peaks which lie exactly on frequencies of 1/day times an integer. These are the result of the daily drift, which is synchronized by a 24 hour period, and thus produces power mainly at harmonics of that frequency. The power introduced at other frequencies by this error signal is less, but nonetheless present. The removal of this power is of paramount importance for the investigation.

The daily drift was discussed in great detail in chapters 2 and 3. One of the largest components derives from the transparency gradient of the earth's atmosphere. This component can be modelled, although its exact magnitude and shape are uncertain enough to prevent it from being used as a direct correction to the data. A sample calculation, reduced as the data, is shown in figure 5.3. The transparency signal was calculated for that

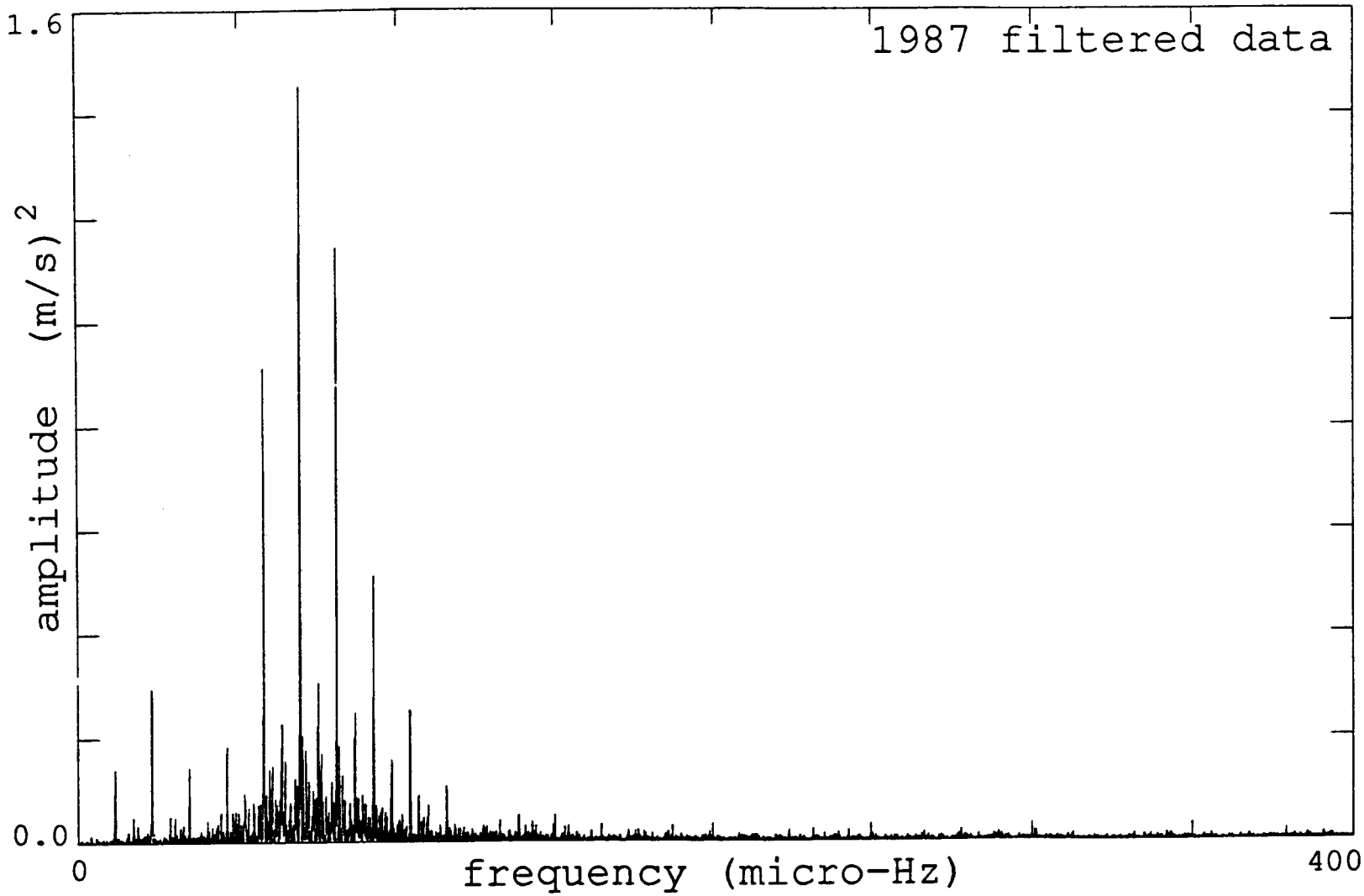

Figure 5.2 - Power Spectrum of Filtered 1987 Data. The spectrum is the result of a concatenated time series of days which have been passed through a 50 μHz to 500 μHz bandpass filter. The large peaks are at positions of 1/day times an integer.

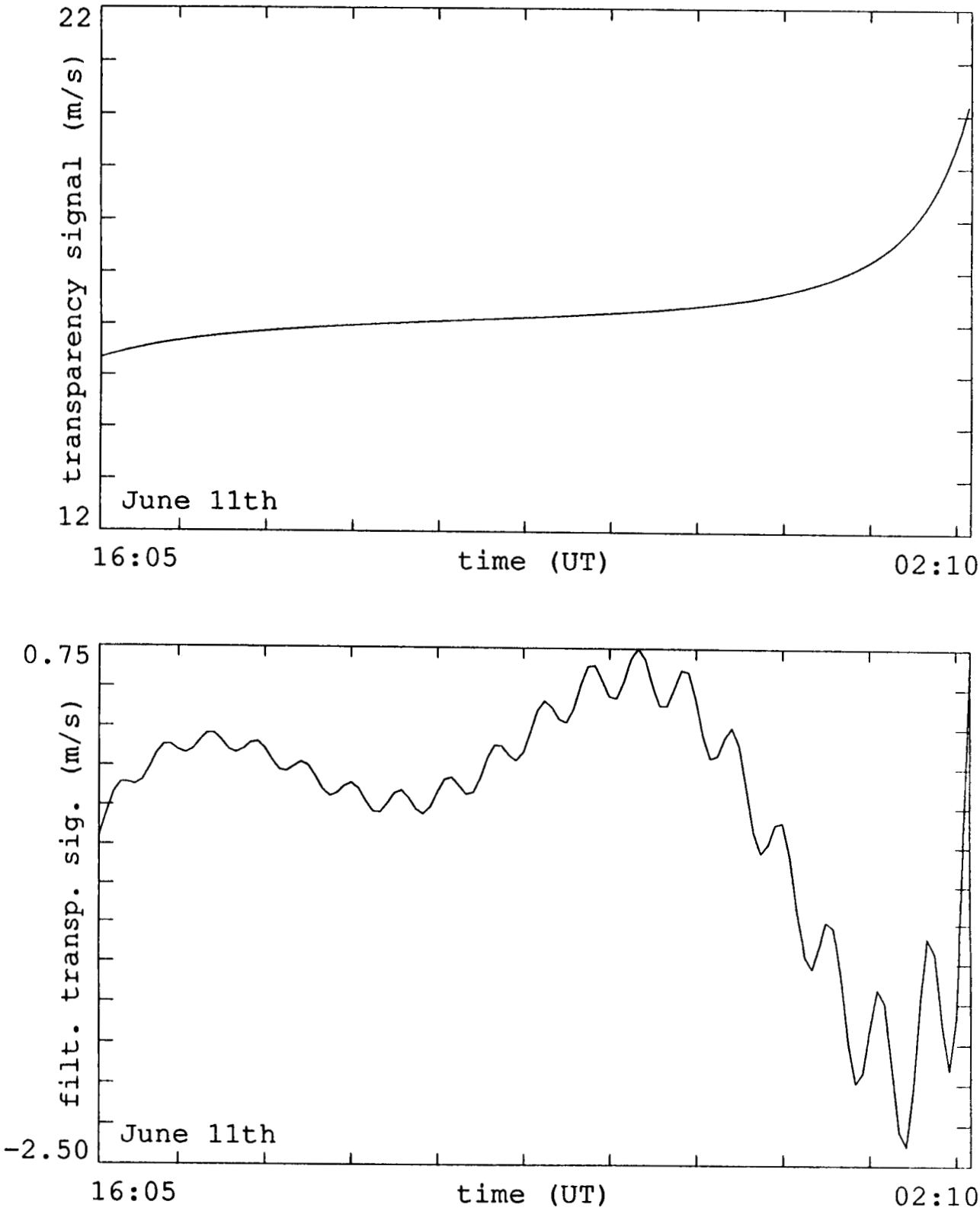

Figure 5.3 - Calculated and Filtered Daily Transparency Signal. The top panel shows the signal due to the transparency gradient. The bottom panel is the result of a 50 μHz to 500 μHz filter of the top.

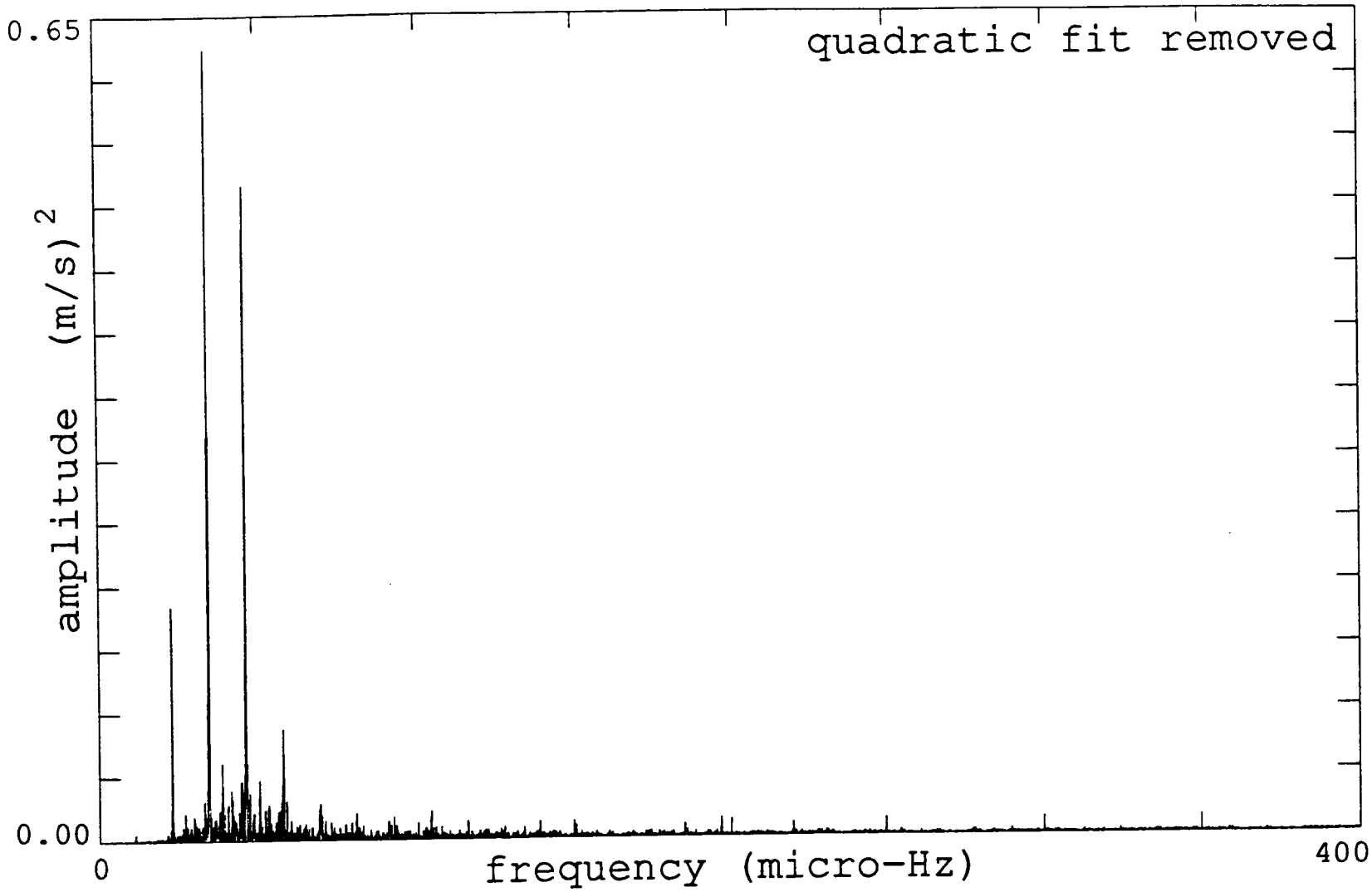

Figure 5.4 - Parabolic Fit Power Spectrum. To obtain this spectrum, instead of a bandpass filter, a quadratic fit was removed from each day before concatenation of the days.

particular day, then filtered as the data is filtered. The peak-to-peak magnitude of the unfiltered signal is about 5 m/s. The bottom panel of the figure shows the filtered signal, with a peak-to-peak amplitude of about 3 m/s. A short period oscillation, with about a half hour period, is visible. This is due to the 500 μHz cutoff of the filter, and only introduces power at a frequency well outside the region being analyzed. The error signal has other components which cannot be modelled. The drift associated with the change of the phototube gain ratio has been estimated to be as much as 16 m/s (Appendix B). These two components, transparency and gain change, probably comprise most of the daily drift, since the calculations show their combined magnitude could account for the peak to peak amplitude of the observed daily signal variation. Other daily variations, such as temperature and barometric pressure, are other candidates for sources of a signal drift, but it is not clear how they could enter into the differential measurement. The power around 1000 μHz demonstrates that it is apparently possible though.

Several different methods for removing the daily drift were examined. The 1979 data analyzed by Delache and Scherrer (1983); Scherrer (1984) were treated by the fitting and subtraction of a parabolic curve. The data being considered in this analysis consist of periods of observation which are generally several hours longer than in the 1979 season. Examining the data, e.g. in figure 3.12, one sees that the shape of the drift cannot be well fit by a parabola. For comparison to the earlier analysis, though, a parabolic fit was calculated for the unfiltered data of each day and subtracted. The power spectrum of the resulting 1987 time series is shown in figure 5.4. The 1/day peaks are still dominant in the signal, and the majority of power lies below 50 μHz where the noise is known to be prohibitively high.

Expanding on the idea of a calculated fit which is subtracted from the data, one can attempt to remove the remaining drift from the filtered data by fitting a higher order

polynomial to the signal. Chebyshev polynomials have nice behavior at the edges of the interval which is being fit. Thus a fourth order Chebyshev polynomial fit was calculated and subtracted from each day. The power spectrum of the resulting 1987 time series is plotted in figure 5.5. The method, while slightly better than the parabolic fit at removing noise power, still leaves the spectrum dominated by the large 1/day peaks. Moreover, comparing the amplitudes of this spectrum and others, it becomes apparent that the treatment has actually removed a lot of power from the whole signal without removing the 1/day peaks. This treatment of the data, used in Henning and Scherrer (1987), is unsatisfying since one is removing and introducing power in a broad range in a somewhat uncontrolled manner.

When examining the data it was noticed that the filtered data signal and the filtered exit slit encoder signal were at times highly correlated. This correlation is believed to be to a large part the result of the phototube gain ratio drift, which affects both of those signals to varying magnitude (see Appendix B). Thus the possibility suggests itself that the drift could be partially removed in the data signal by subtracting an appropriate fraction of the exit slit encoder signal. For each day the cross correlation of the two signals was computed. On those days where a strong correlation was manifested the ratio between the two signals was recorded. The average of these values provides a calibration constant which is then used to multiply the exit slit encoder signal on every day and subtract the result from that day's data signal. The power spectrum of the resulting 1987 time series is plotted in figure 5.6. The noise power, as indicated by the 1/day peaks, has not been reduced adequately. However, the treatment is more successful than the polynomial fits since it did not remove the power between the 1/day peaks which is possibly of g-mode origin. Rather it only decreased the size of the 1/day peaks. However, the decrease was only by a factor of 3 from the original data (compare to figure 5.2), which still leaves the

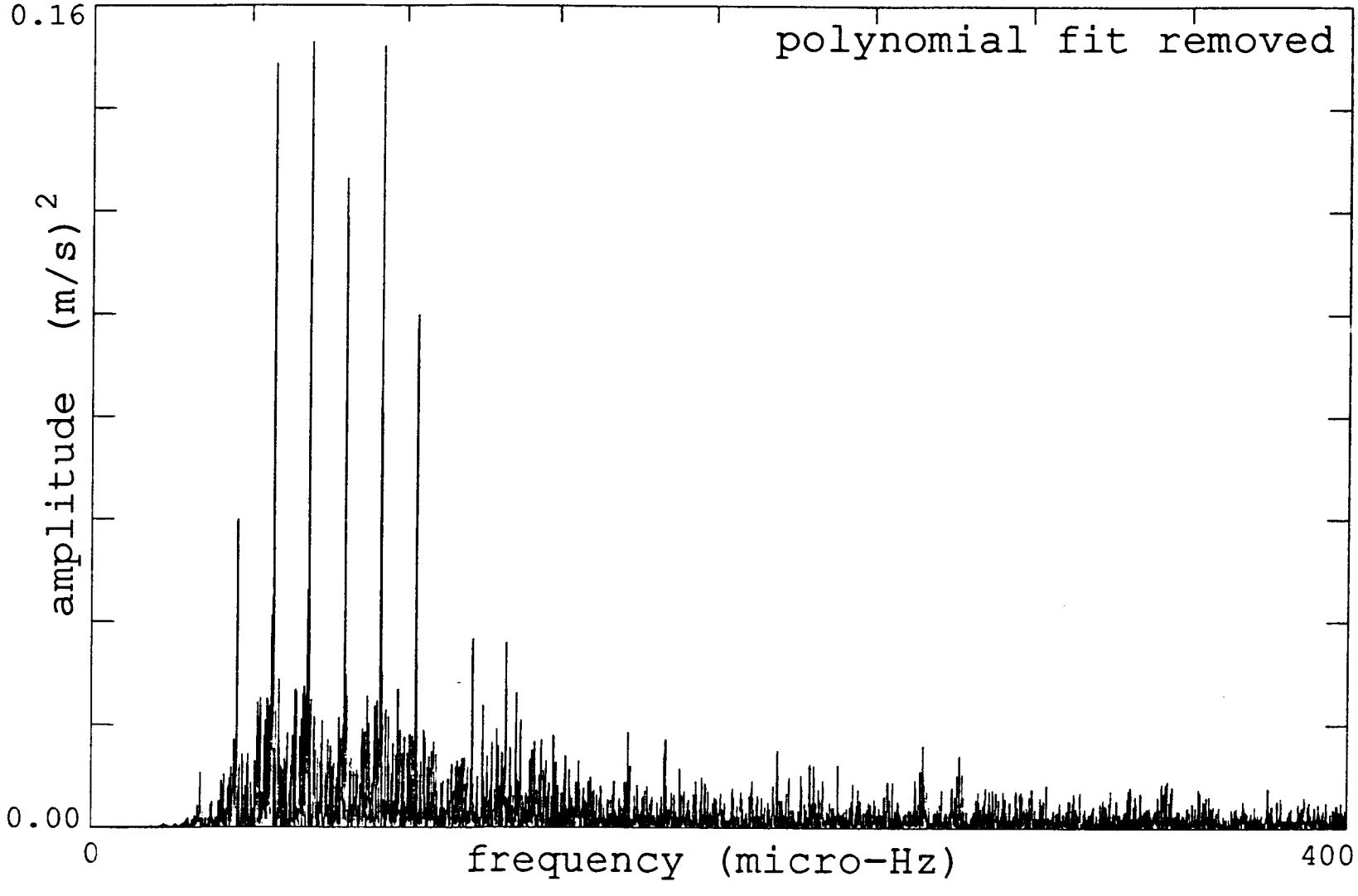

Figure 5.5 - Polynomial Fit Power Spectrum. This figure shows the resulting spectrum when a fourth order Chebyshev polynomial fit is removed from each day before concatenation of the days.

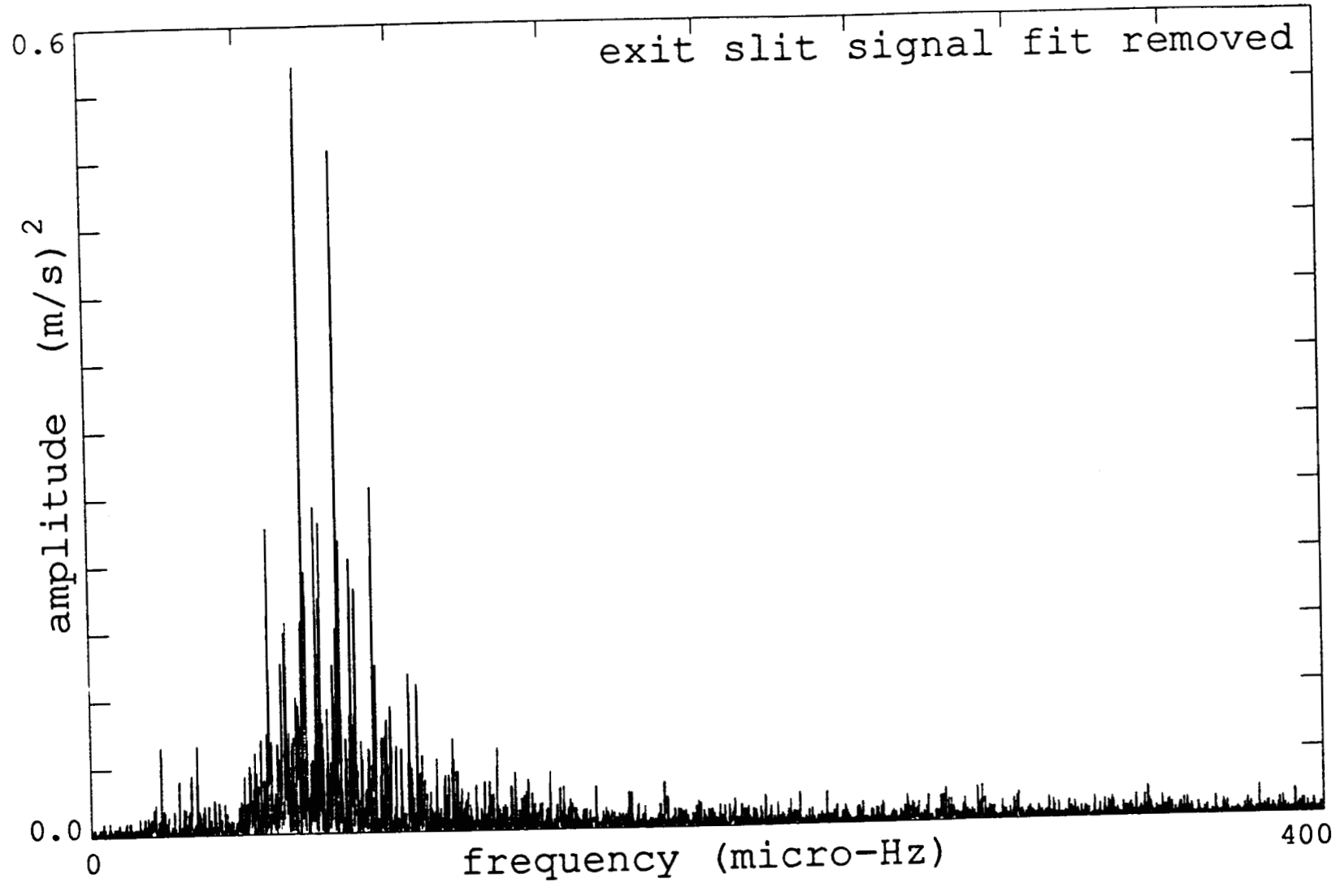

Figure 5.6 - Correlated Fit Power Spectrum. A fraction corresponding to the correlated portion of the day's exit slit encoder signal with the data signal is subtracted from the day's data signal before concatenation of the days.

1/day peaks dominant.

The method which finally proves successful derives from the realization that the signal which is introducing most of the power appears to be well synchronized to the time of day. This is to be expected for the part of the error signal which is due to the transparency gradient. However, in addition the gain ratio drift is probably fairly well synchronized to the time of day, since it depends on the history of light on the phototubes. Since the observations are started at close to the same time every day, the intensity of light falling on the phototubes has approximately the same variation every day. Therefore, the phototube gain is likely to change in the same way and on the same time scale every day. The data substantiate this consideration as one can see in figure 3.12. To calculate the part of the signal which actually is the same every day, the data from each season was subjected to a superposed epoch analysis around the time of local noon on each day of data. The answer produced by the superposed epoch analysis is the average daily signal for all observations in that season. This epoch signal is then subtracted from every day separately. The power spectrum of the resulting 1987 time series is shown in figure 5.7. The improvement to the spectrum is remarkable - the 1/day peaks have disappeared completely from the visible spectrum leaving only the power between them.

Following up on this success, an attempt was made to further improve the method by combining it with the subtraction of the correlated exit slit encoder signal. Examination of data which has been filtered and the epoch subtracted still shows frequent times when the data signal and the exit slit encoder signal are fairly highly correlated, although less so than before the subtraction of the superposed epoch signal. This seems to indicate that there is still some presumably non-solar signal which could be taken out of the data by subtracting an appropriate fraction of the exit slit encoder signal. When the procedure earlier described for this process is followed, the power spectrum of the result for 1987 appears as shown in

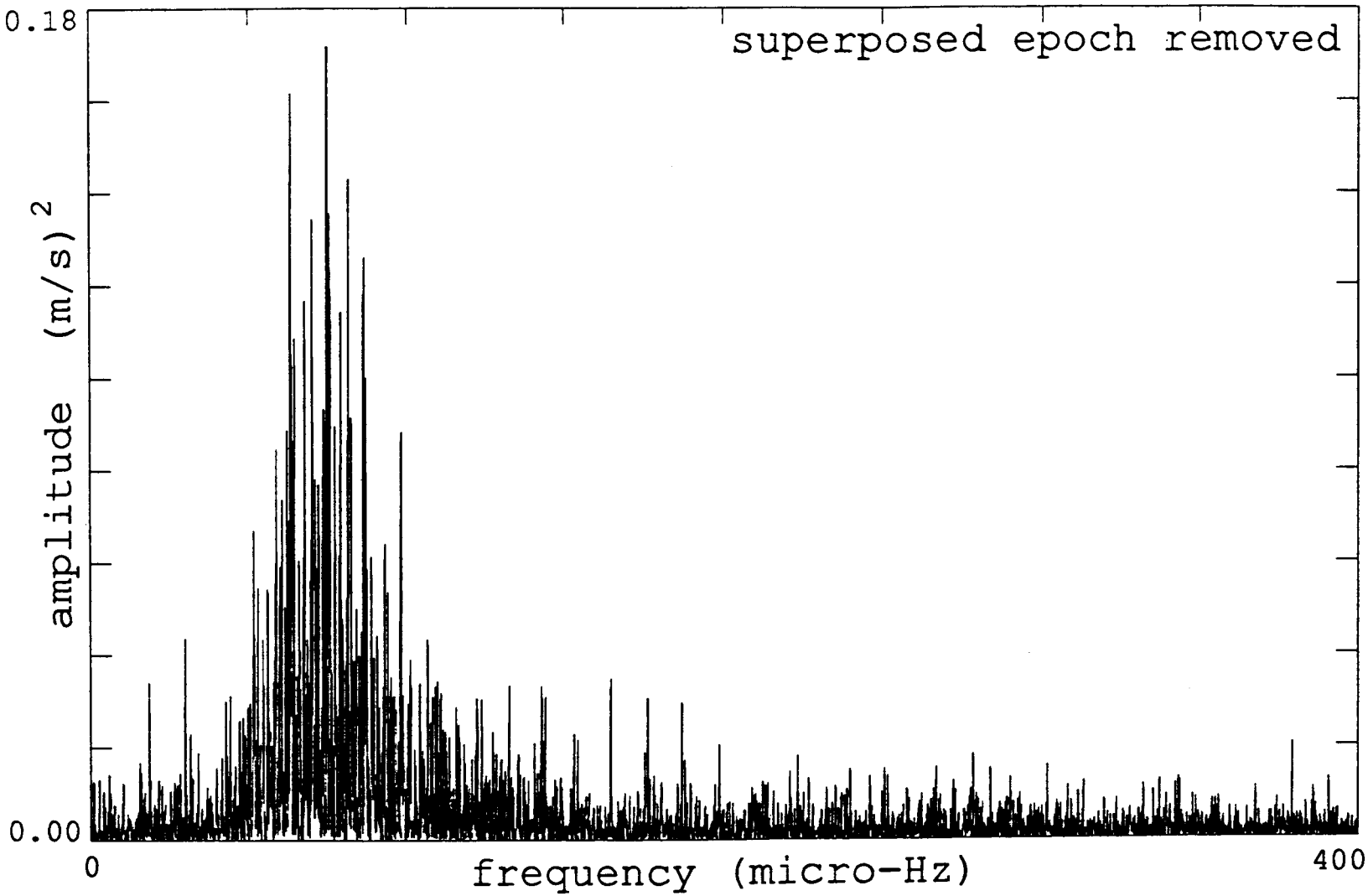

Figure 5.7 - Superposed Epoch Subtraction Power Spectrum. The average of all days in the season, synchronized to the time of day, is subtracted from each day before concatenation of the days. The 1/day peaks have disappeared from the region of interest between 50 μHz and 100 μHz.

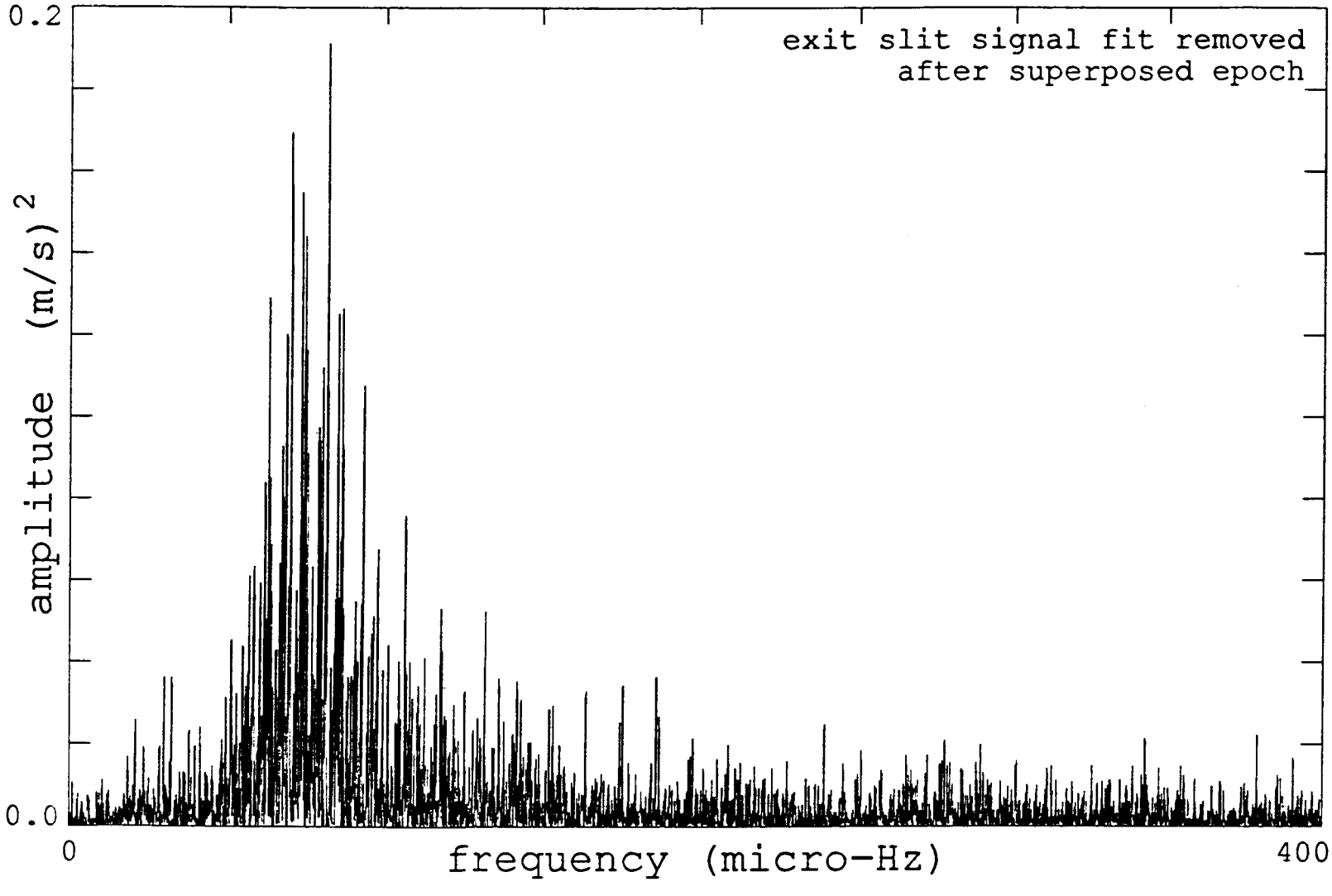

Figure 5.8 - Correlated Fit Subtraction of SPE Power Spectrum. This spectrum is the result of a combination of the processes resulting in figures 5.7 and 5.6, applied in that order.

figure 5.8. One sees that the 1/day peaks have been reintroduced, although at a low level. The highest two peaks again correspond to 1/6 day and 1/7 day. Thus this treatment worsened the power spectrum for the purposes of g-mode detection. Therefore this method was not employed in the g-mode search, instead stopping the data processing after the superposed epoch subtraction.

Before this data is used to look for g-modes, it is desirable to understand what the data processing actually does to the data. This is easy to see when considering the filter, which simply removes most of the power below 50 μHz and above 500 μHz. The filter is applied to each day separately, and so when the individual days are put together in the time series some power can reappear outside of the filter cutoffs, but its level is quite low.

Not as obvious is the effect of the superposed epoch subtraction. Figure 5.9a shows the superposed epoch signal for the 1987 season. The magnitude of the signal is sizable, about 5 m/s, accounting for most of an average day's peak-to-peak variation of the filtered data signal. In figure 5.9b is shown the power spectrum of this signal put into the actual window of the 1987 data, i.e. repeated on every day, but only at those times when there is actual data. The spectrum is dominated by the large peaks at frequencies of multiples of 1/day, with the same amplitude as the original data, not surprisingly since figure 5.7 demonstrated that those peaks were removed from the data signal by the subtraction of the superposed epoch. The superposed epoch subtraction then acts almost like a very nice notch filter, mostly removing the power at frequencies of 1/day times an integer. However, it is better than a notch filter since it removes just the correct amplitude and also removes other noise power not at the exact 1/day frequencies without introducing aliased power such as a numerical filter could.

To investigate the effectiveness of this technique on removing the transparency signal

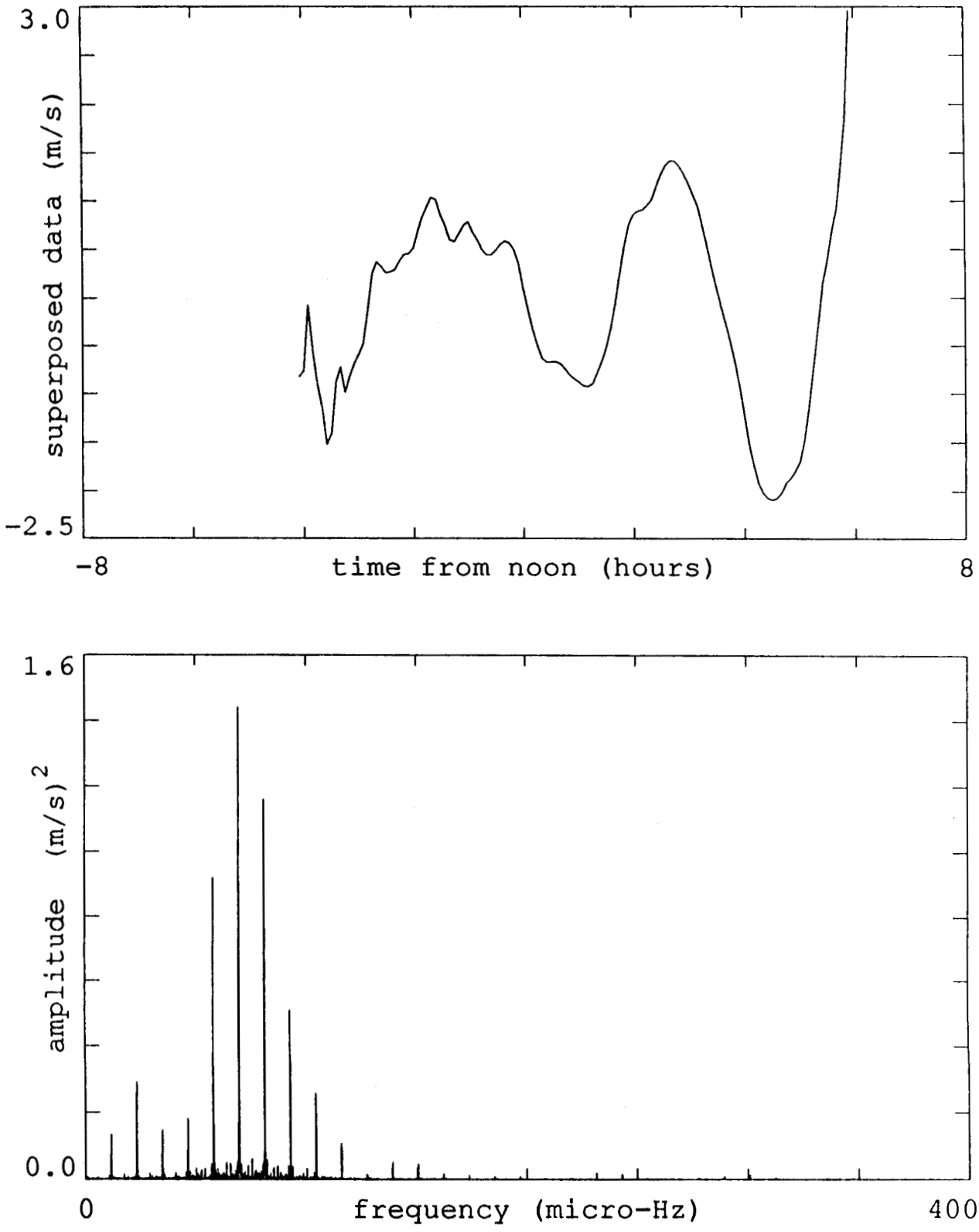

Figure 5.9a-b - Superposed Epoch for 1987. The top panel shows the average data signal of all days, synchronized to the time of day. The bottom panel shows its power spectrum after it has been inserted into a window corresponding to the data.

one can use the model calculation described in chapter 3. The computer model calculates the expected transparency signal for each day where observations are present in the 1987 season. Then each day is filtered just like the real data, with a bandpass filter running from 50 μHz to 500 μHz. One can refer back to figure 5.3 as an example of the results for one particular day. These artificial data signals are then strung together to form a time series of data which consists solely of error signal, but which exactly corresponds to the real data in the shape of the window. The power spectrum of this time series is plotted in figure 5.10a. The dominance of the 1/day peaks clearly demonstrates that the transparency signal is regulated with a 24 hour period, and further confirms that the origin of those peaks in the real data is in the daily drift. The magnitude of the power is lower than in the real data in some of the 1/day peaks by a factor of about six, which again implies that the transparency signal comprises a little less than half of the daily drift. The superposed epoch signal is calculated from the artificial time series in the same way as for the actual data. The signal is plotted in figure 5.11. Its shape is remarkably similar to the signal calculated from the actual data plotted in figure 5.9a. Comparing the magnitude of the two signals, one can see that the calculated signal is about 40% of the size of the data's superposed epoch. This agrees with the information we already have. This is encouraging as it indicates that the superposed epoch signal really does derive most of its power and shape from the error signals introduced by the transparency and another approximately equal part which is also synchronized to a 24 hour period. The part of the data's epoch signal that is not present in the transparency model's epoch signal is a combination of the phototube gain ratio drift with the uncertainty in the calibration of both the data and the calculated transparency signal.

Continuing the check of the effectiveness of the method, the artificial epoch signal calculated from the modelled transparency data is subtracted from each day in the artificial

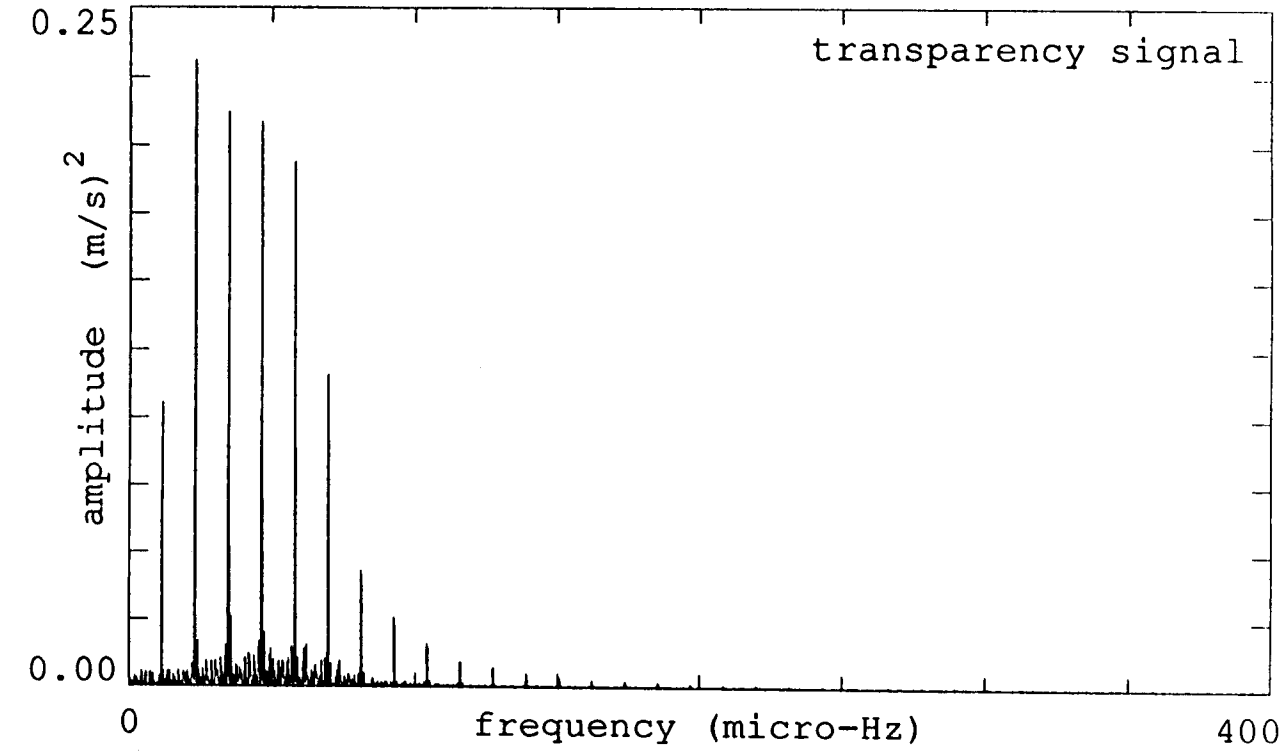

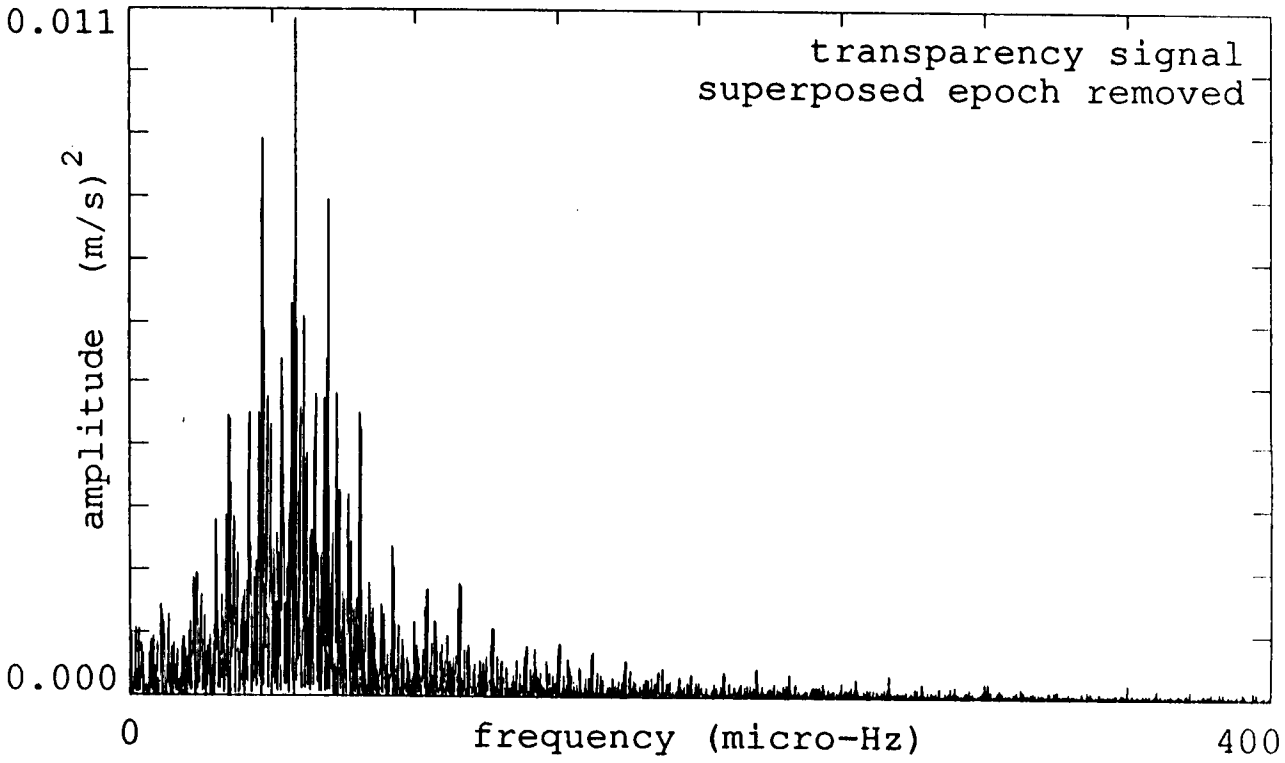

Figure 5.10a-b - Spectrum of Transparency Signal before and after SPE. The top panel shows the power spectrum of the calculated and filtered transparency signal for the 1987 data window. The bottom panel shows the remainder after the average signal has been removed from each day (see figure 5.11).

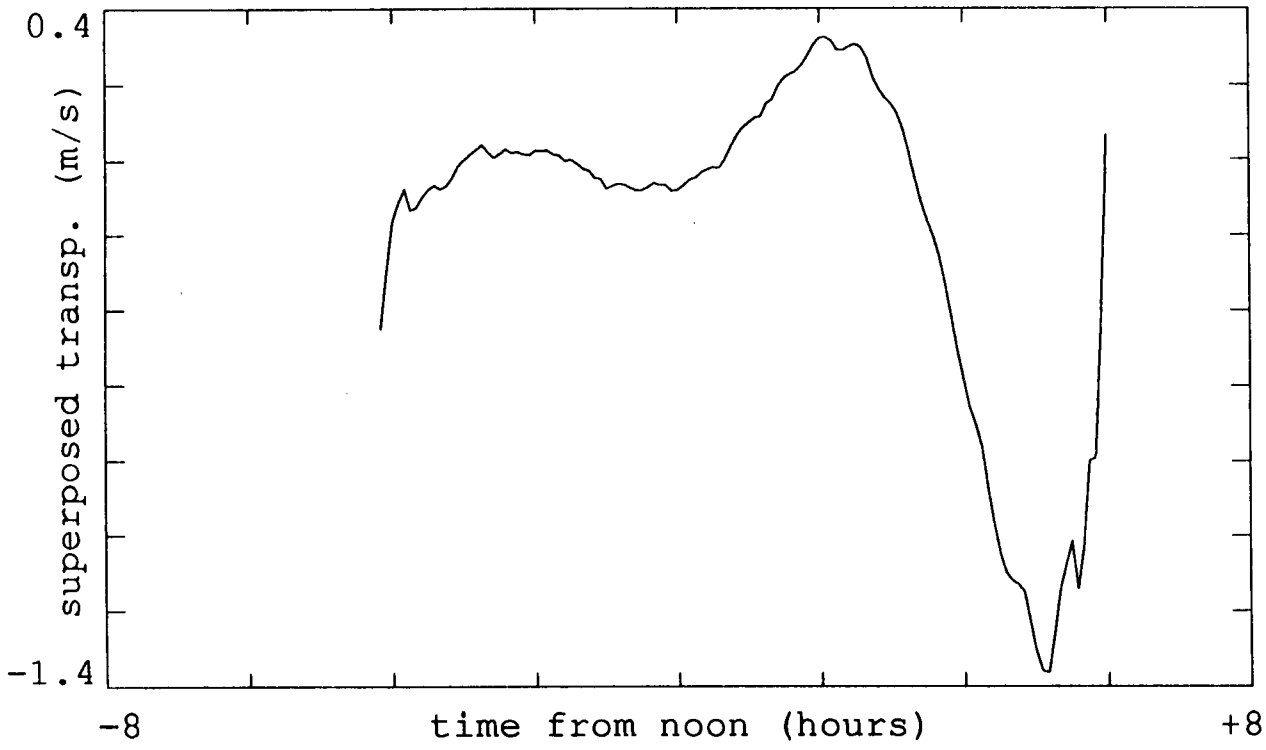

Figure 5.11 - Superposed Epoch of Transparency Signal. The average of the filtered calculated transparency signal of all days in the 1987 data window, synchronized to the time of day.

time series. The power spectrum of the resulting time series is plotted in figure 5.10b. The reduction in power is remarkable and very encouraging. The peaks at fractions of a day have been lowered by a factor of over 25. Moreover, the power between the 1/day peaks has also been reduced by a factor about 10. If one multiplies the magnitude of the resulting spectrum by 6 (the factor between the calculated 1/day peaks due to just transparency and the 1/day peaks in the actual data) to attain an estimate of the power left in the real data, the highest peak lies at less than .06 $(m/s)^2$, well below the level of peaks in figure 5.7. The level of the power between the 1/day peaks is even lower at only .02 $(m/s)^2$.

This analysis has shown that the technique of subtracting the superposed epoch works very well for removing the power which was introduced by the transparency gradient. It also implies that any power which is roughly synchronized on a daily period will be reduced by this method. This is particularly useful for those error signals which cannot be modeled, but are presumably roughly similar each day, such as the gain drift and possible temperature variations. The data signal is seen to have a drift which is very similar from day to day. This method removes that drift very effectively. It should also be noted that one effect of using this method is to preclude any investigation of the well-known 160.01 minute oscillation, since any power at a period at or close to 160 minutes is removed by the superposed epoch subtraction.

Even if one takes into consideration the uncertainty in the relative magnitudes of the signals, and the fact that the 1/day peaks in the real data include power from non-transparency sources, one can say that the power left in the real data is significantly higher than the level of power left in the artificial spectrum. This implies that the data does contain peaks which are not derived from the transparency gradient or other source of error. The next section will examine this data for the presence of g-modes.

5.2. Detection Schemes

Although the power spectrum has now been cleaned of the dominating noise peaks which were introduced by the daily drift in the data signal, the remaining peaks do not display any easily visible periodic structure. Figure 5.12 shows the 50 μHz to 100 μHz range of the reduced power spectrum of the 1987 data. The level of noise, the window function, and the solar rotational splitting of the peaks would make it difficult to perceive such a structure in the resulting multitude of peaks even under the best of conditions. Furthermore, in addition to the large number of peaks, the solar amplitude of the various modes is not likely to be the same, and in any case its measurement is also affected by the data window.

The confusion of peaks with overlapping window sidelobes makes it difficult to approach the problem in the same way as the p-mode detection - where individual peaks were identified as solar modes. The method of reducing the resolution to better identify the frequencies where there is solar power, which worked so well in the p-mode detection, cannot be used at all in the g-mode regime, since the modes lie so closely together that the possible distribution of peaks from different modes (due to rotational splitting and the window function) overlap. The full 40 day resolution is necessary for the investigation of g-modes. Thus a new scheme for detection must be developed along statistical lines.

In the following description of schemes of detection the effectiveness of the particular method is estimated by using a set of model modes provided by J. Christensen-Dalsgaard. The frequencies of the modes were calculated from a full solar model, described in Christensen-Dalsgaard (1982), they are not asymptotic approximations. In the analysis of the observational data, however, one must search for an asymptotic structure since it is practically just not possible to calculate a full solar model for each possible set of frequency-determining parameters. Thus the use of Christensen-Dalsgaard's model modes

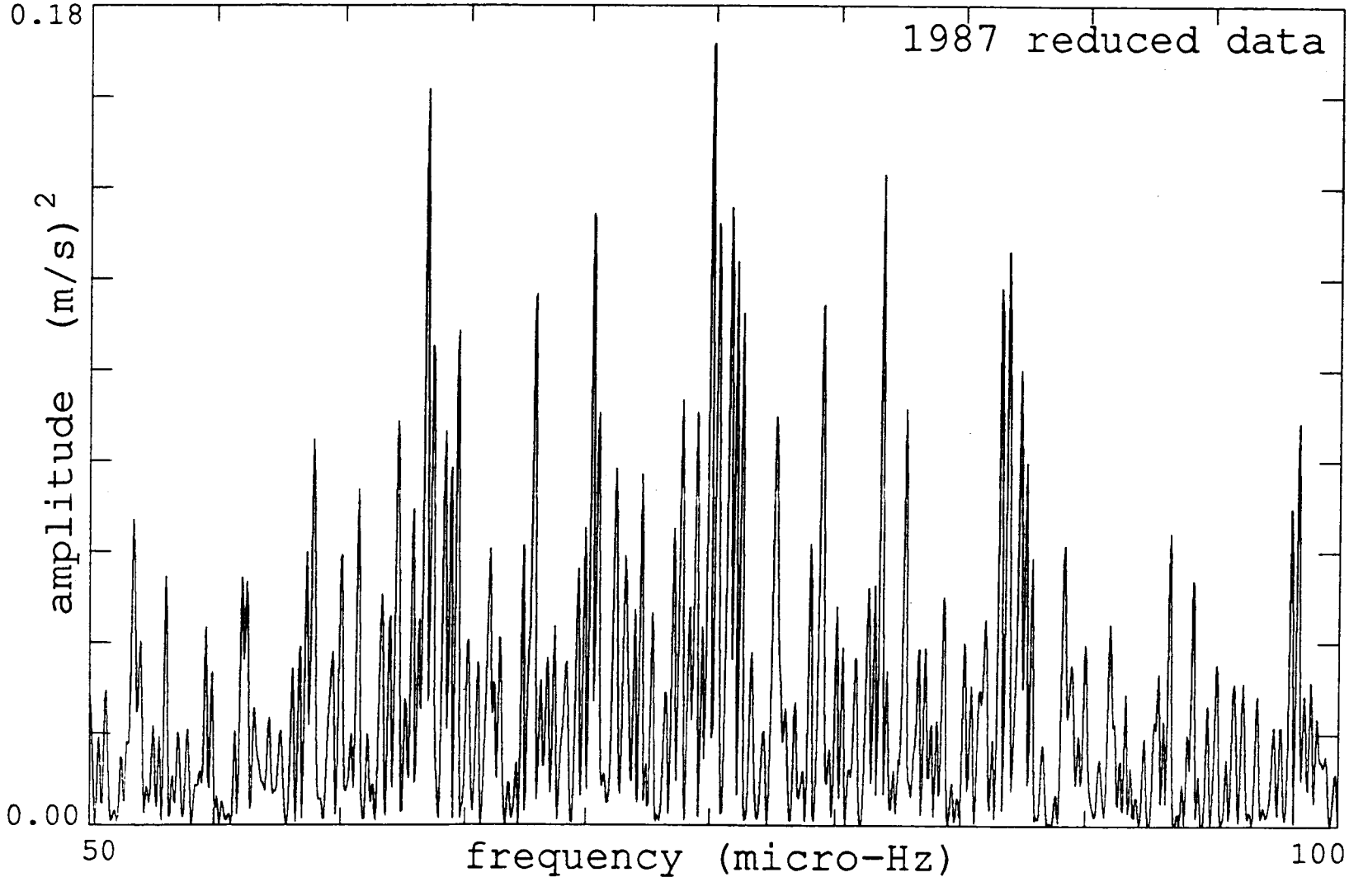

Figure 5.12 - Reduced Low Frequency Power Spectrum. The spectrum, cleaned of the peaks at 1/day times an integer by the superposed epoch subtraction, in the region of interest. This figure is an expansion of part of figure 5.7.

provides a good test for the effectiveness of the detection method. If the detection method can retrieve the model modes from an artificial power spectrum, then it may be able to retrieve g-mode structure from the real data. Of course the real data is contaminated by noise and window structure, so the artificial spectrum must be constructed to include these effects. The difference in amplitudes between real solar modes, which can be expected in the real data, is also a consideration to be remembered.

The artificial spectra are constructed from the set of model peaks as follows. The discrimination between the magnitudes of peak amplitudes which can be expected in the real data takes two forms. Firstly, as discussed previously, the Stanford differential measurement is only sensitive to g-modes of degree l=1, and probably to a lesser extent l=2. Thus the only model peaks which are included in the artificial data are of modes with those degrees l. Furthermore, the modes with degree l=2 are given a power half that of modes of degree l=1. In other words, the amplitude of l=1 modes is set to be $\sqrt{2}$ times the amplitude of the l=2 modes. Secondly, because of its circular symmetry the Stanford instrument is also only sensitive to oscillations which are not antisymmetric about the solar equator. These are modes which have $l+m$ even, where m is the azimuthal order. Therefore, all model peaks with odd $l+m$ are also left out of the artificial data. The resulting set of modes is still comprised of 66 peaks between 50 μHz and 150 μHz. To appreciate the degree to which the modes become more closely spaced as the frequency decreases, one can note that between 100 μHz and 150 μHz lie only 16 of those peaks. Since the data is filtered at 50 μHz, the set of model peaks is also cut off at 50 μHz, although as one can imagine there are many more modes below that frequency. Although the real data is filtered at 500 μHz, the set of model frequencies can safely be terminated at 150 μHz since the region which will be examined for g-modes lies between 50 μHz and 100 μHz.

Given this model set of frequencies, they are then put into an artificial time series by inserting a sine wave for each mode into a data window. The sine wave has the appropriate frequency and amplitude, but a random phase. The data window is constructed by taking the length of the actual data time series - about 40 days in 1987 - and filling it with gaps separated by 24 hours to simulate the night/day cycle of observations. The sine wave is then put into the time series only in those places where there are no gaps. The length of the gaps can be changed, varying from about 1 hour to a whole day. In this way the effect of different filling factors can be examined. The power spectrum of the artificial time series is calculated with an FFT in the same way as the data. Figures 5.13a-e show five power spectra for increasing gap length., i.e. decreasing filling factor. Figure 5.13a shows the spectrum of the model as it would appear if there were no gaps at all, corresponding to 100% filling factor. The only degradation of the peaks has occurred because of the finite length of the time series. The spectrum becomes markedly more confused by 1/day sidelobes of the original peaks as the gap size increases. Figure 5.13b corresponds to a filling factor of about 75%, figure 5.13c to a filling factor of slightly less than 50%. The real data has a filling factor of about 22%, corresponding to the power spectrum in figure 5.13d. The changes in amplitude caused solely by the window structure is clearly apparent, as are the strong sidelobes at 11.574 μHz distance from other peaks. The mode structure is still visible, but with difficulty. The final panel shows the power spectrum for a filling factor of only 10%. Most of the original mode structure has disappeared as a few peaks duplicated at 11.574 μHz intervals dominate the spectrum.

Another thing which must be considered is that the real data window is actually worse than the artificial one constructed above, since each day's observation is not the same length and there are whole days missing where clouds prevented any observations. To examine the effect of this more messy window, the construction of the artificial window

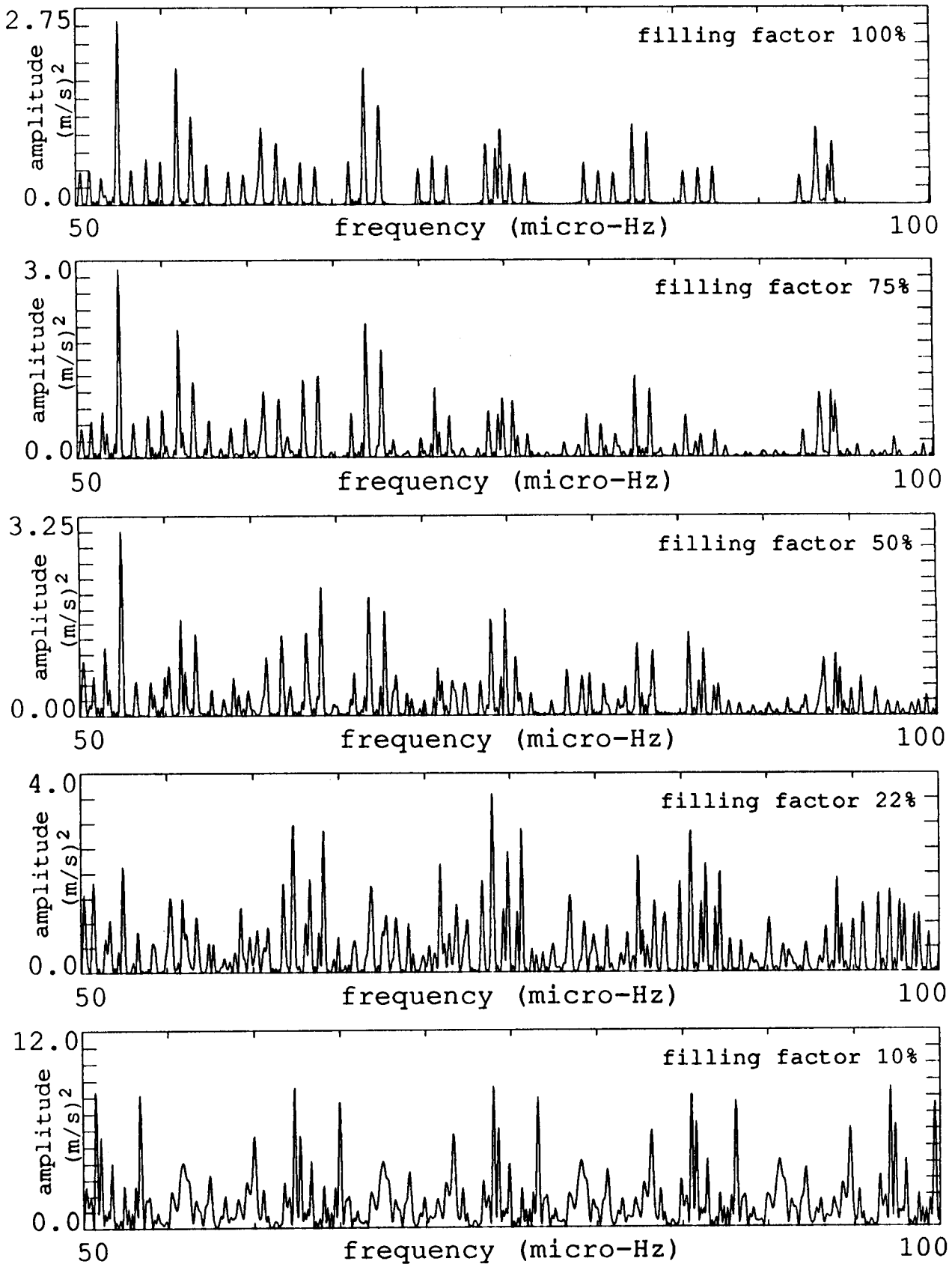

Figure 5.13a-e - Power Spectra of Artificial Data with Gaps. The top panel is a), progressing down to e). The input peaks had an amplitude squared of 1.0 (l=1) and 0.5 (l=2).

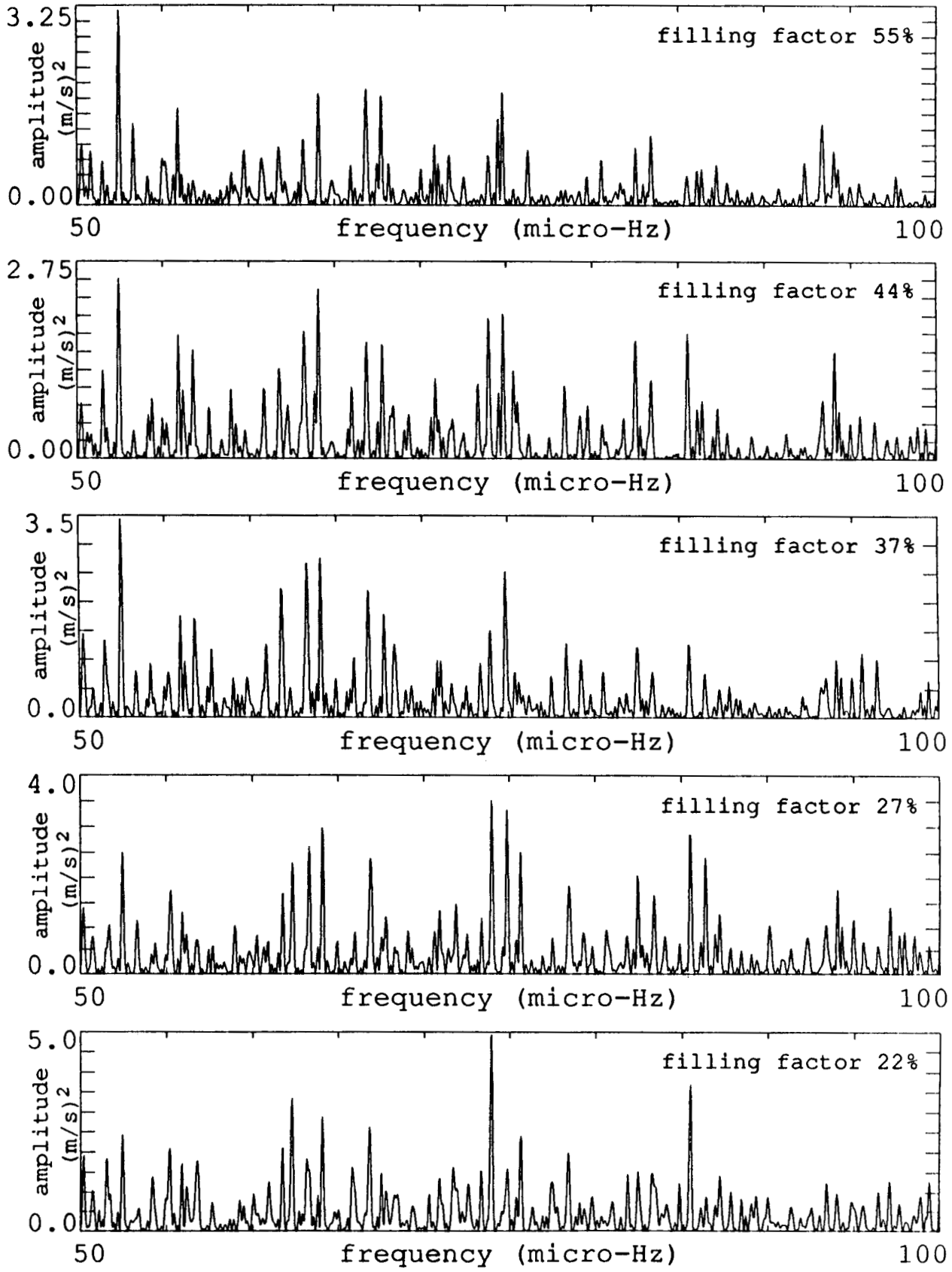

Figure 5.14a-e - Power Spectra of Artificial Data with Messy Gaps. As for figure 5.13, but the gaps include whole days.

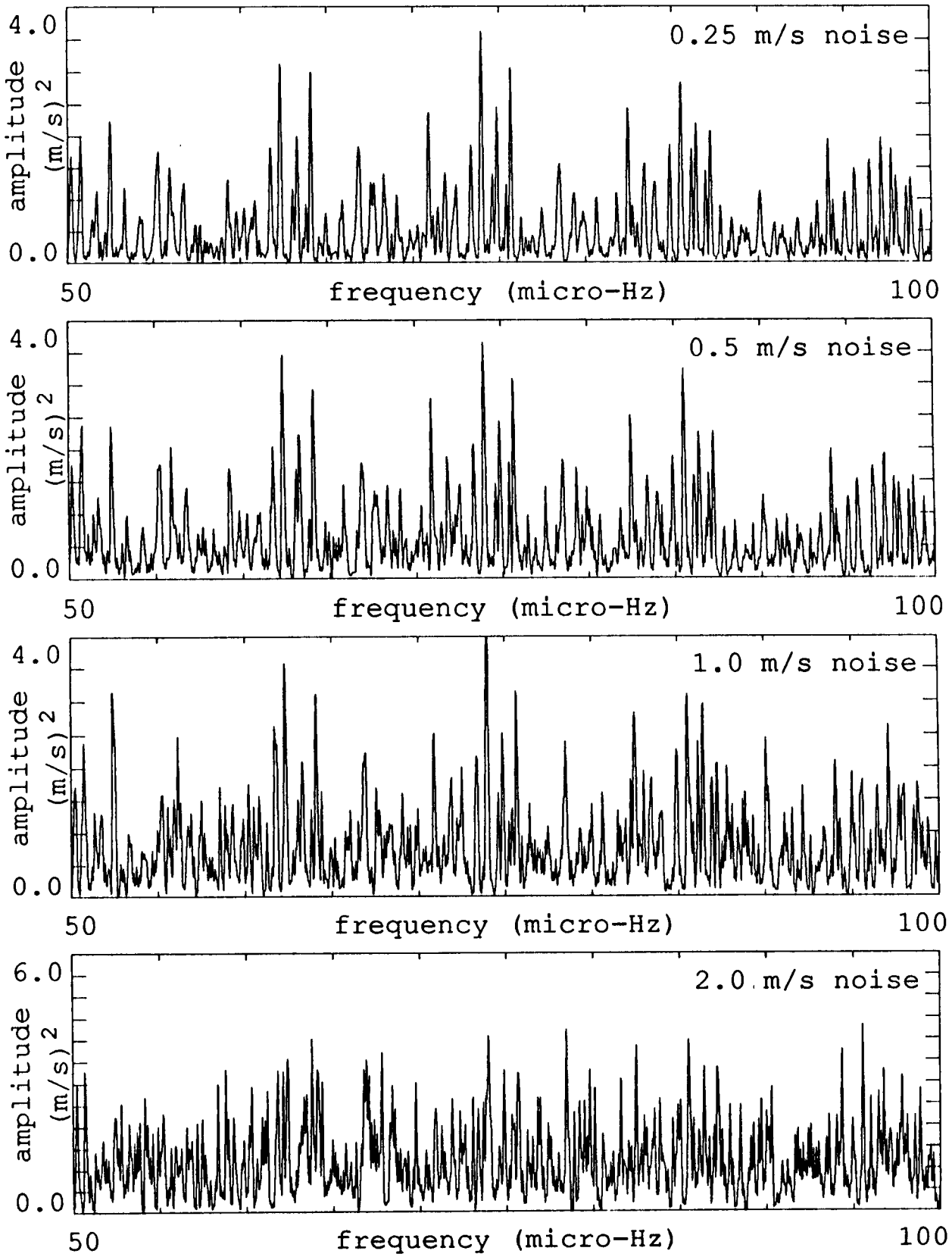

Figure 5.15a-d - Power Spectra of Artificial Data with Added Noise. The filling factor of the data corresponds about to the fourth panel (d) of figures 5.13 and 5.14.

was changed slightly. A random factor was included which caused whole days to be designated as gaps, in addition to the regular nighttime gaps. This has the effect of decreasing the filling factor for a given gap size. Some examples of resulting spectra are plotted in figures 5.14a-e. One can see that the spectra look even more noisy, although the filling factor still seems to be a reasonable indicator of the quality. The panels, from a to e, correspond to filling factors of 55%, 44%, 37%, 27%, and 22%. The power spectrum of the actual data thus could be expected to look like figure 5.14d or e if there were no additional noise and a clean spectrum of g-modes with identical amplitudes was present on the sun.

To make things even worse, however, the real data has noise in it which does not derive from the window. This was simulated by adding a random spectrum of white noise to the spectrum determined by the window function. Figures 5.15a-d show the impact of adding noise to a power spectrum with filling factor of 24%, approximately the same as in the real data. The level of noise is measured by the level of an absolute variance σ_n which is defined as the level which 68% of the noise values lie under. This noise distribution is obtained by simply taking the absolute value of a Gaussian distribution with mean zero and variance σ_n. The panels correspond to values of σ_n of 0.25, 0.5, 1.0, and 2.0 respectively for panels a through d. Recall that the amplitude of the l=1 peaks which were used to construct the time series is 1.0. At a noise level of $\sigma_n = 1$, the l=2 peaks are pretty much buried. If one compares the artificial power spectra with figure 5.12, and assumes that the larger peaks in the real data correspond to g-modes, one can estimate the level of noise in the real data at $\sigma_n = 1$, corresponding to about 20 cm/s.

Asymptotic G-Mode Model Search Method

So it is a spectrum like that of figure 5.15c from which the g-modes must be extracted. The first statistical peak detection method which will be examined is a two-parameter search. This technique was used by Fröhlich (1986) in an investigation of ACRIM data. The method is based on the asymptotic formula derived by Tassoul (1980)

$$\nu_{n,l,m} = \frac{\sqrt{l(l+1)}}{T_0\left[n + \frac{l}{2} - \frac{1}{4}\right]} + \nu_R m\left[1 - \frac{1}{l(l+1)}\right]$$

where T_0 is the basic asymptotic g-mode period separation and ν_R is an average rotational splitting frequency. This equation is used to calculate the frequencies of a set of peaks, given a particular T_0 and ν_R. The resulting asymptotic model is overlaid as a mask on the power spectrum, and the power in a small range around each frequency is added up. The total summed power is then divided by the number of peaks which went into the sum to determine an average power. If the two parameters correspond to a good fit to g-modes in the data, the average power should be large. On the other hand, if the parameters determine a model which does not fit the structure of the g-modes in the data, the average power should be less. The statistical search consists of varying the two parameters and building up a two-dimensional array from the outputs of the various models. The range of the parameters runs from 25 minutes to 45 minutes for T_0, stepping every 0.05 minutes, and from 0.3 μHz to 2.5 μHz for ν_R, stepping by 0.05 μHz. This more than covers all reasonably possible combinations which apply to the real sun, as it is theoretically understood at this time. Finally, the standard deviation of the values in the output is calculated, and used to divide each of the numbers to get a two-dimensional array which is now in units of standard deviation σ. This array can be plotted as a contour plot, and a distinctive peak identified as the result of g-modes.

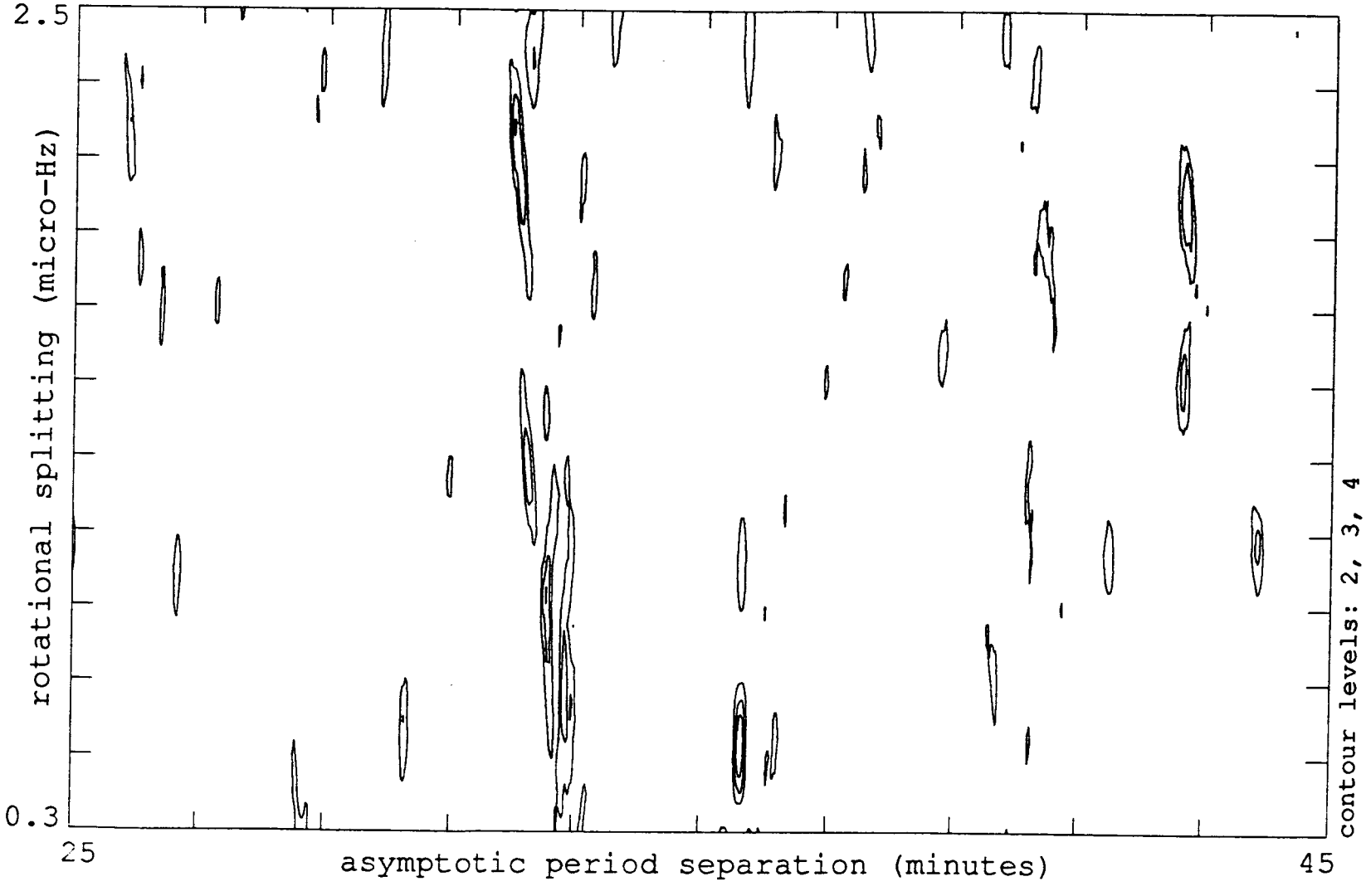

Figure 5.16 - G-Mode Search Map - No Gaps or Noise. The contour levels are measured in standard deviations σ of the whole map. The peak at 35.6 minutes, 0.5 μHz corresponds to the model g-modes.

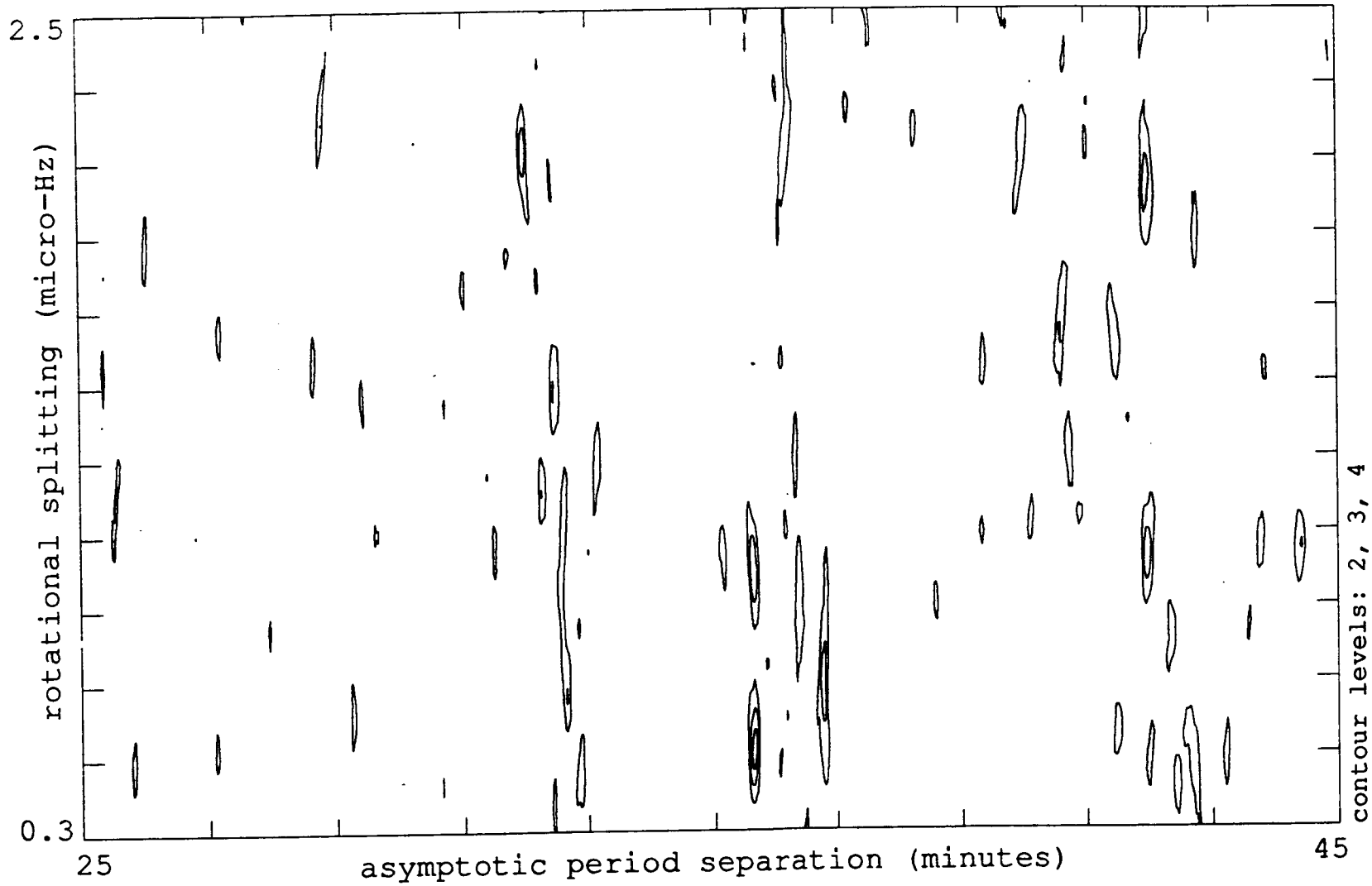

Figure 5.17 - G-Mode Search Map - Filling Factor as Data. As for figure 5.16, but the artificial data was constructed with gaps similar to the real data.

Fröhlich (1986) used this technique on ACRIM data and found a maximum in the map for $T_0 = 29.85$ minutes and $\nu_R = 1.05$ μHz. With these values for the parameters he then identified the peaks published by Delache and Scherrer (1983); Scherrer (1984). The frequencies of his identifications differ from the observed peaks by an average of 0.10 μHz. This may look impressive at first glance, but if one generates a set of completely random peaks in the range in which the published peaks lie and calculates the average distance between these peaks and the closest mode frequency using the asymptotic model and the parameters given above, then the statistical average is only 0.08 μHz. This underscores the fact that there are a very large number of possible g-modes which may exist in this frequency range. The ability to choose values for n, l, and m which result in a frequency which lies close to a measured value is easy in a region where the g-modes are so dense. One must be careful with such identifications.

Continuing with the discussion of peak detection methods, the next step is to examine the effectiveness of the two-parameter model method described above. To do so in a controlled manner the artificial data produced from the model peaks provided by Christensen-Dalsgaard will be used. The technique is applied to each artificial power spectrum for varying filling factor, producing a set of maps. Figure 5.16 shows the map resulting from a power spectrum which has no gaps or noise in it. A clear peak appears in the map at the values of $T_0 = 35.6$ minutes and $\nu_R = 0.5$ μHz. The peak is unique, being the highest on the map, and can be identified as resulting from the model modes. However, even in this extremely clean spectrum the method generates a number of other fairly large peaks. Figure 5.17 is an example of the appearance of the map resulting from the power spectrum in figure 5.13d, which corresponds to the filling factor present in the real data. The previously identified peak is still the largest, but there are many other peaks of similar height. In other words, the model would have trouble being identified in the real data with

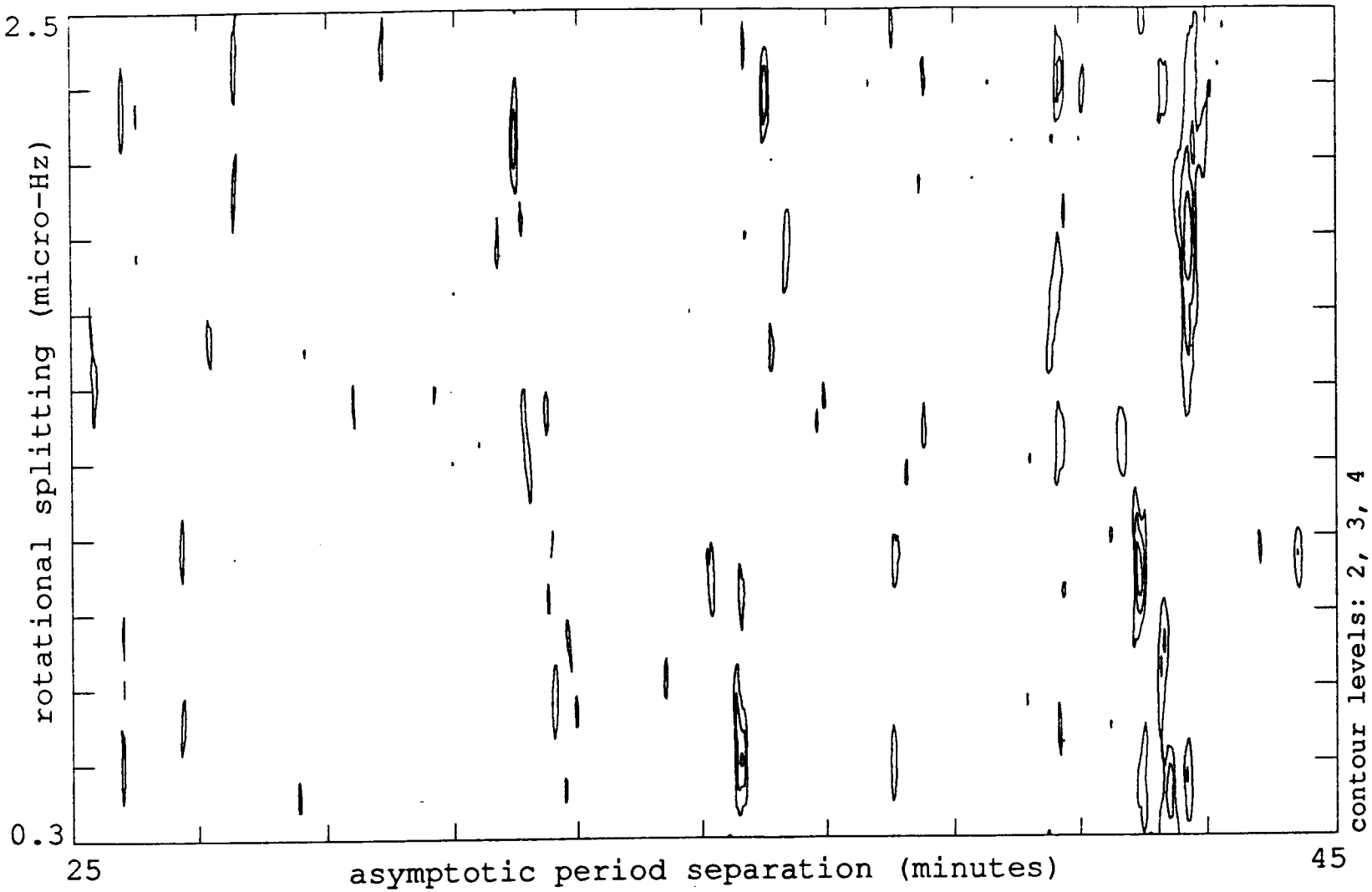

Figure 5.18 - G-Mode Search Map - Filling Factor as Data, Plus Noise. As for figure 5.17, but additionally noise was added to the spectrum at a level corresponding to the real data's noise level.

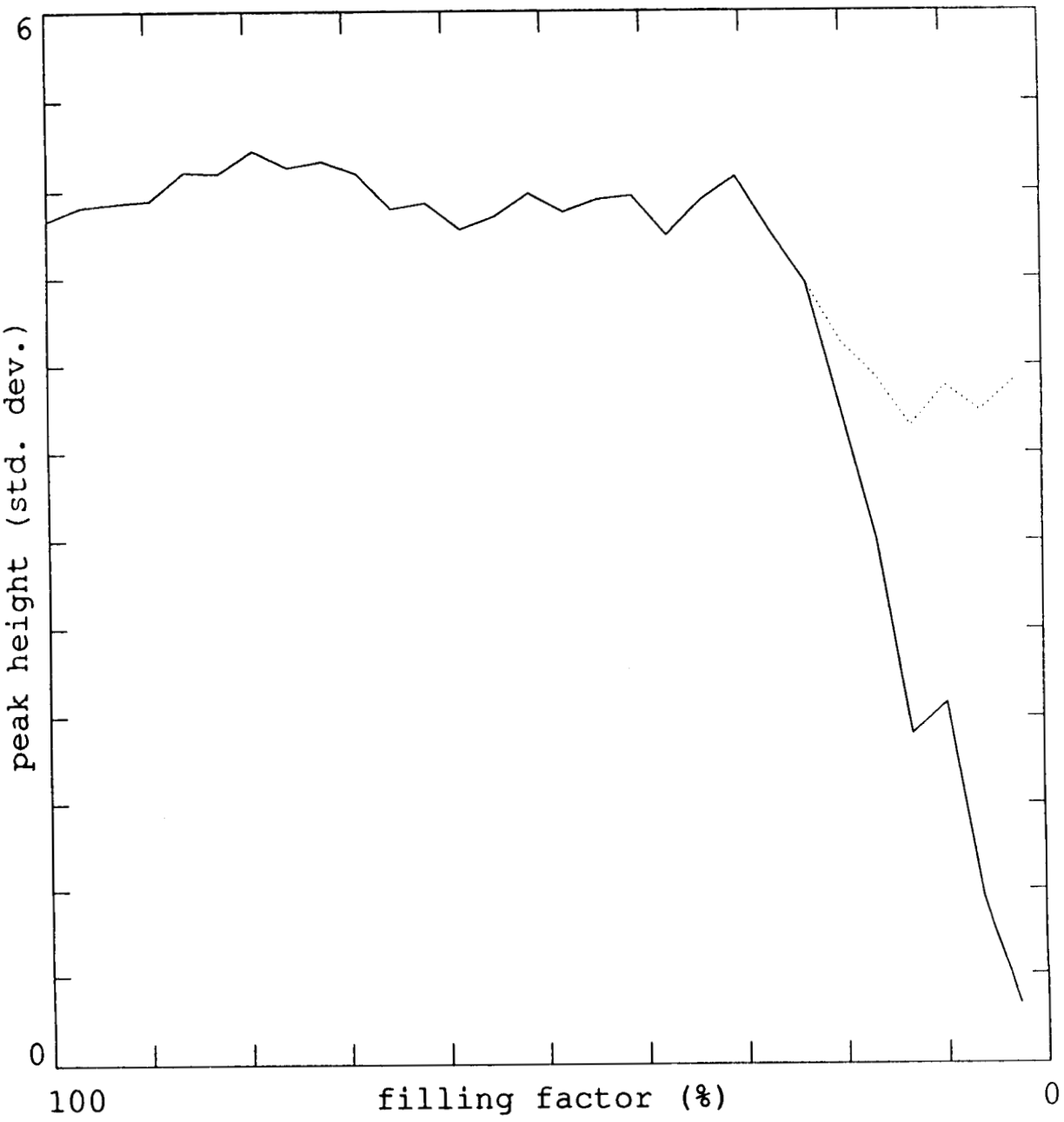

Figure 5.19 - G-Mode Search - Peak Height vs. Filling Factor. The solid curve shows the height of the peak corresponding to the model g-modes. The dotted curve shows the height of the highest peak on the whole contour map.

this method even if all its modes were present in the data without noise, solely because of the degradation produced by the window function. If one adds noise, the picture gets even worse, as figure 5.18 shows. Here noise with $\sigma_n = 1$ has been added to simulate the real data. The correct peak, which would identify the g-modes of the model, is only noticeable if one knows where to look for it. There are a number of other peaks which are actually larger than the desired peak. Thus this search method could not be used to detect g-modes in the spectrum even if they are present at a constant amplitude for each mode.

Figure 5.19 is a summary of results from the tests on the model. In it is plotted the height of the peak which corresponds to the Christensen-Dalsgaard model as a function of the filling factor in the data. Surprisingly, the curve is almost flat for a large range of the filling factor starting at 100%. This shows that the data window does not adversely affect this method until the filling factor drops below about 30%. After this point the peak height starts dropping rapidly. Also plotted in the figure is the level of the highest peak in the whole map. At a filling factor above 24% this peak is the g-mode peak. Below that filling factor the level is relatively constant at slightly below 4σ and represents the magnitude of the highest peak that one can statistically expect in the distribution of the 36000 map values. In other words, if a real peak drops below this level there is no hope of identifying it in the noise of the other values. The real data's filling factor lies at 23.6% for the best year and has added noise, which means that this method probably cannot be expected to isolate any g-modes. To reinforce this conclusion one can examine the effect of adding noise to the artificial power spectra. Figure 5.20 is a graph similar to figure 5.19, displaying the height of the correct model peak as a function of filling factor. There are several curves, corresponding to two different levels of noise and the two peak values - correct and maximum in the data. The solid curve shows the magnitude of the correct peak at a noise level of $\sigma_n = 1$. The long-dashed curve shows the magnitude of the correct peak

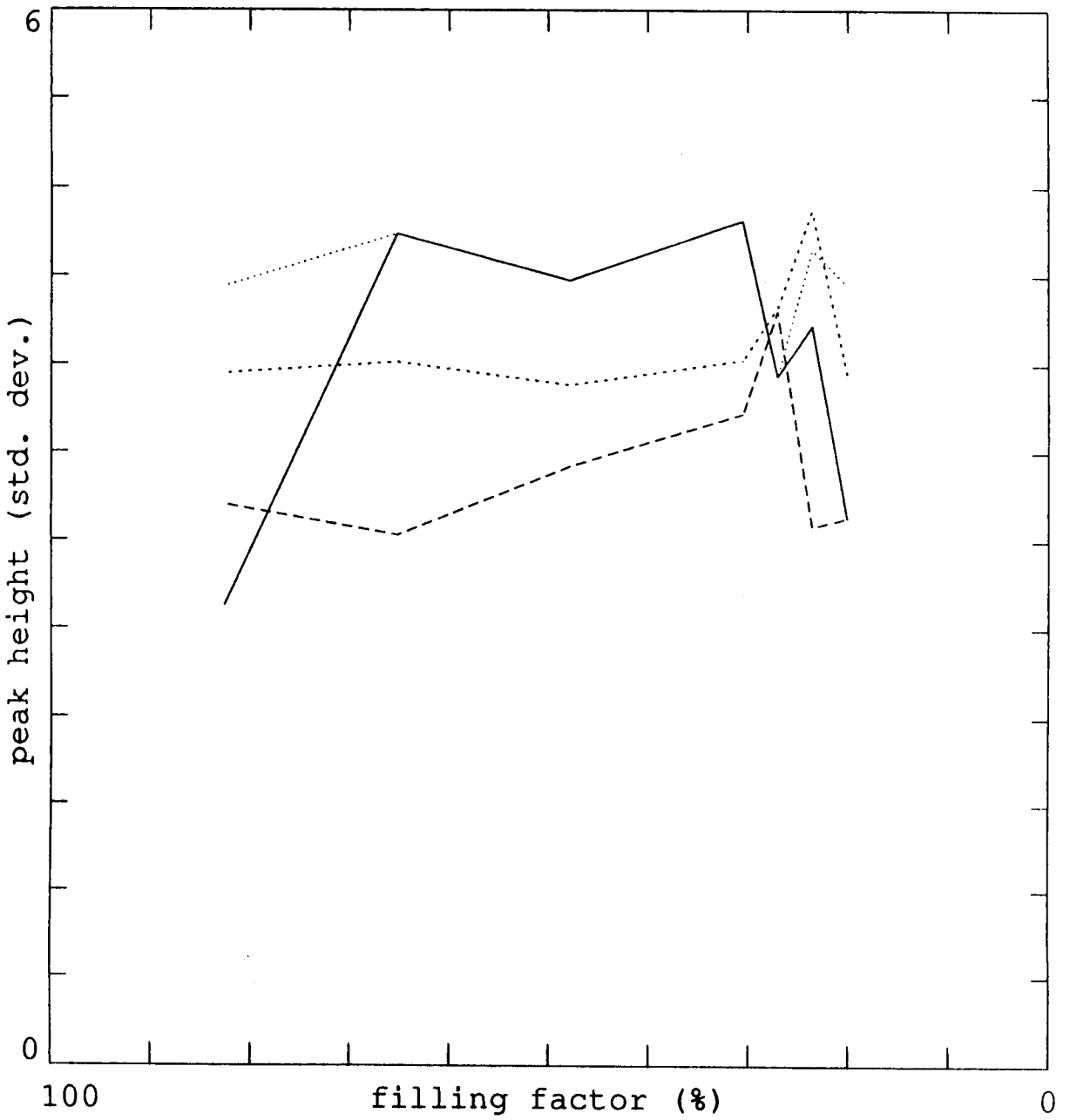

Figure 5.20 - G-Mode Search - Peak Height vs. Filling Factor, Plus Noise. At a noise level of 1 m/s the solid curve corresponds to the model g-mode peak, the dotted curve to the highest peak on the map. At a noise level of 2 m/s the long-dashed curve corresponds to the model g-mode peak, the short-dashed curve to the highest peak on the map.

at a noise level of $\sigma_n = 2$. The dotted curve shows the maximum peak in the whole map for the power spectrum with $\sigma_n = 1$. The short-dashed curve shows the maximum peak in the whole map for the power spectrum with $\sigma_n = 2$. The addition of noise proves very troublesome for this method. One can see that the noise level lowers the height of the g-mode peak, until at a data noise level of $\sigma_n = 2$ it has dropped well below the level where it can be distinguished from the noise of the map. Even in the case of $\sigma_n = 1$ the added noise can cause confusion if one is unlucky, as is demonstrated by the abnormally low correct peak value at a filling factor of over 82%. Clearly noise only worsens an already bad situation.

To design a better search method one must examine the reasons why the g-mode map search fails. This reveals an interesting conclusion. It appears that the method is too constraining, too rigid, in its attempt to fit the g-modes into an asymptotic model. If one uses the frequencies of the solar model directly to calculate what values of T_0 and ν_R best should fit that model, one finds out that both the value of T_0 and of ν_R are different for the set of modes with degree l=1 and for the set of modes with l=2. The parameters indicated by the peak in the g-mode map search method as shown in figure 5.16 correspond to a weighted average of the actual, different values in the model. Moreover, the value of the "constant" of $\frac{1}{4}$ in the Tassoul equation is also different for both sets of l if one attempts to fit the model peaks to the equation. In other words, the asymptotic model could not possibly determine the correct values of T_0 and ν_R, since there are none which fit the model. It could only approximate an average. The reason for these problems is that the asymptotic equation is simply not a good enough determination of the frequencies in this region. This leaves the observer with even less guidance from theory.

Linear Search Method

To explain the second search method, which applies a less constraining test to the power spectrum, it is helpful to look at figure 5.21a. This figure is a diagram similar to the echelle diagram described for the p-modes. However, this echelle diagram is plotted in period, with a separation of 15 minutes between panels, since the g-modes are asymptotically equally spaced in period rather than frequency. The width of each panel is 25 minutes, and thus each panel partially duplicates the preceeding and succeeding panels. The vertical line segments which are plotted in the diagram correspond to the J. Christensen-Dalsgaard model modes. The roughly straight vertical arrangement of three groups of modes is due to the set of l=2 modes. There are three vertical lines because there are three rotationally split peaks for every mode - $m = -2,0,2$. In figure 5.21b is a similar plot, but the echelle spacing is 25 minutes instead of 15 minutes. This allows the structure of the l=1 modes to be seen as vertical lines, although it is harder since the l=2 modes, of which there are more than the l=1 modes, obscure the pattern. The idea of the second technique of searching for g-modes is to search the spectrum for such linear sequences of modes. This is a relaxation from the previous method which required all modes to fit into one given pattern. Examining the echelle diagrams, one can see that the linearity of the spacing between modes does not become clear enough to search for until the period is larger than about 200 minutes. Below that period the mode ridges curve too strongly to be fit by a linear band of reasonable width. The linear search will thus start at this period, corresponding to a frequency of 83.3 μHz, and go to higher period, or lower frequency.

The procedure followed by the method is similar to that of the first technique. A mask is calculated which corresponds to a set of linearly separated peaks in the range of periods from 200 minutes to about 333 minutes, or 83 μHz to 50 μHz. The mask is overlaid onto the power spectrum, and the power in a small range around the

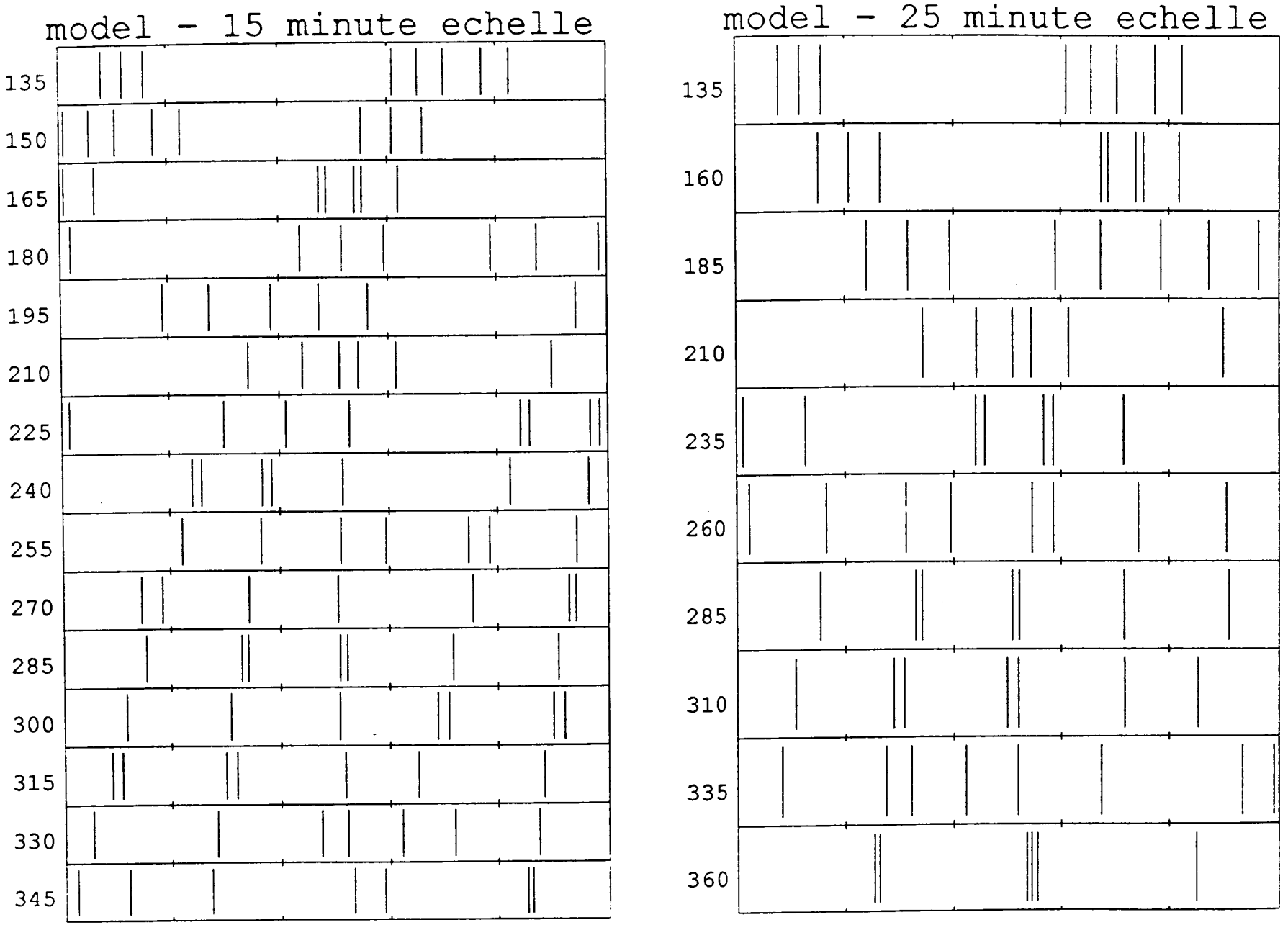

Figures 5.21a-b - Period Echelle Diagram of Model Peaks, 15 and 25 min. The width of each panel is 25 minutes. The vertical structure in the 15 minute echelle diagram corresponds to the l=2 modes, while in the 25 minute echelle diagram the l=1 modes form a near-vertical pair of ridges.

corresponding frequencies is averaged. This is done for a range of two parameters: the separation of the peaks and the location of the first peak, running from 10 minutes to 32 minutes and 200 minutes to 232 minutes respectively. One can imagine running a comb with varying spacing along all possible positions in the period spectrum. The map is not calculated for parameters which would duplicate the information from other sets of parameters. For example, if the peak separation parameter is 12 minutes, the first peak location only runs from 200 minutes to 211.9 minutes, since it would repeat itself beyond that.

Figure 5.22 shows the resulting map for a power spectrum with no gaps or noise. The triangular slice left blank in the figure is due to the non-duplication mentioned above. The improvement over the first technique, as compared by examining figure 5.16, is quite good. Almost all the peaks in the linear search map correspond to a g-mode signature, and they are significantly larger than for the first method. The largest peaks, at the over six σ level, correspond to the two sets of l=1 modes, with $m = -1$ and $m = 1$. To prevent confusion, one should point out that because of the choice of starting parameters the l=1 peaks are actually cut off at the triangular non-duplication region and continued at the bottom of the map.

The l=2 modes can show up in a total of nine possible peaks. This is because the linear search picks them up at their correct separation of about 15 minutes, but also at double that separation. There are three sets of l=2 modes, corresponding to $m = -2,0,2$, and three possible positions on the map where they can appear (base separation, double separation starting at first peak, double separation starting at second peak) - hence, 9 peaks. The linear search picks out eight of these peaks, with hints of the ninth being visible. The highest l=2 peaks are found at a position where there was some contribution of power from the l=1 modes to the search. One also notices that the l=2 mode peaks are much smaller

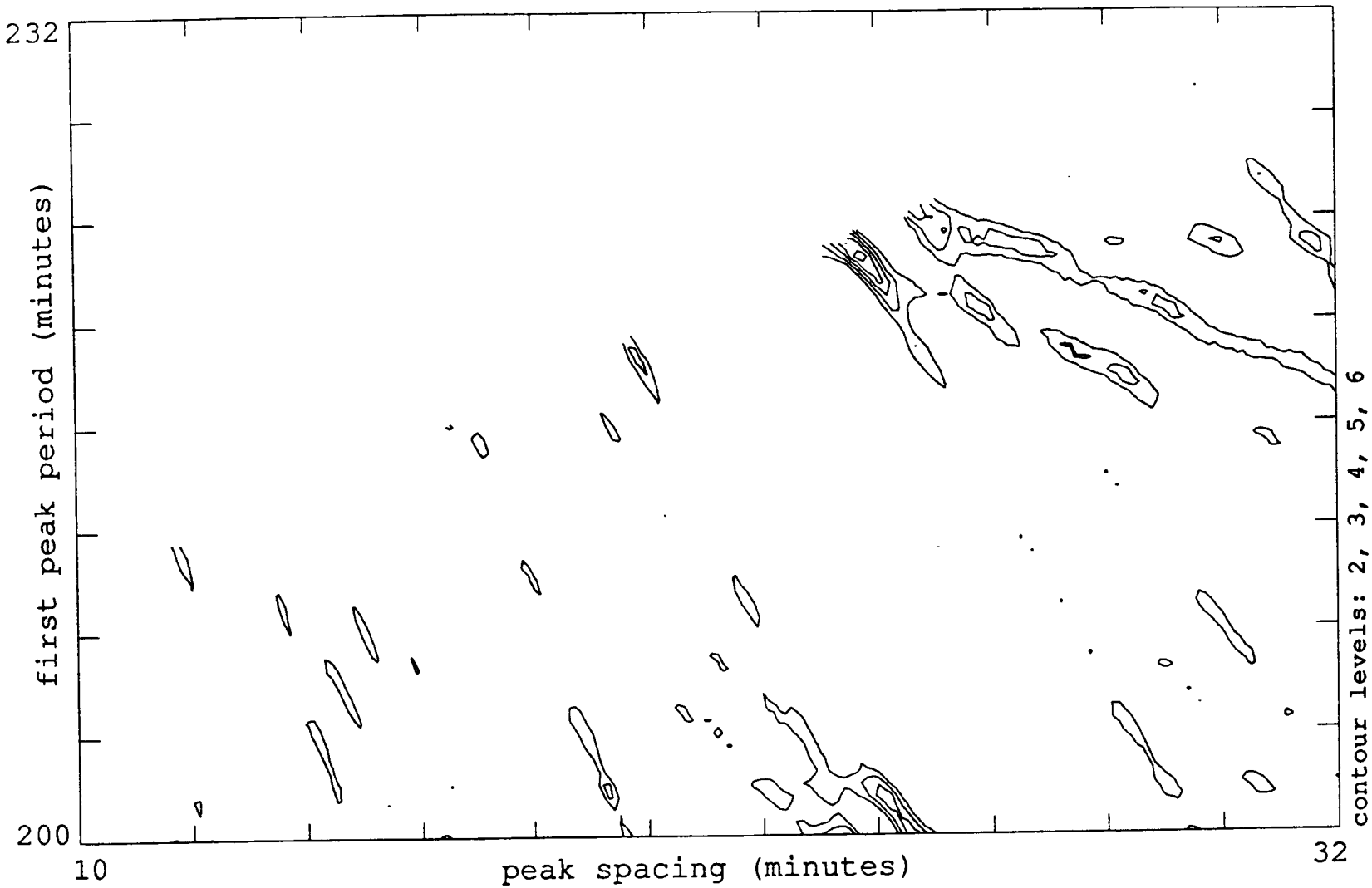

Figure 5.22 - Linear Search Map - No Gaps or Noise. The contour levels are measured in units of the standard deviation σ of the whole contour map.

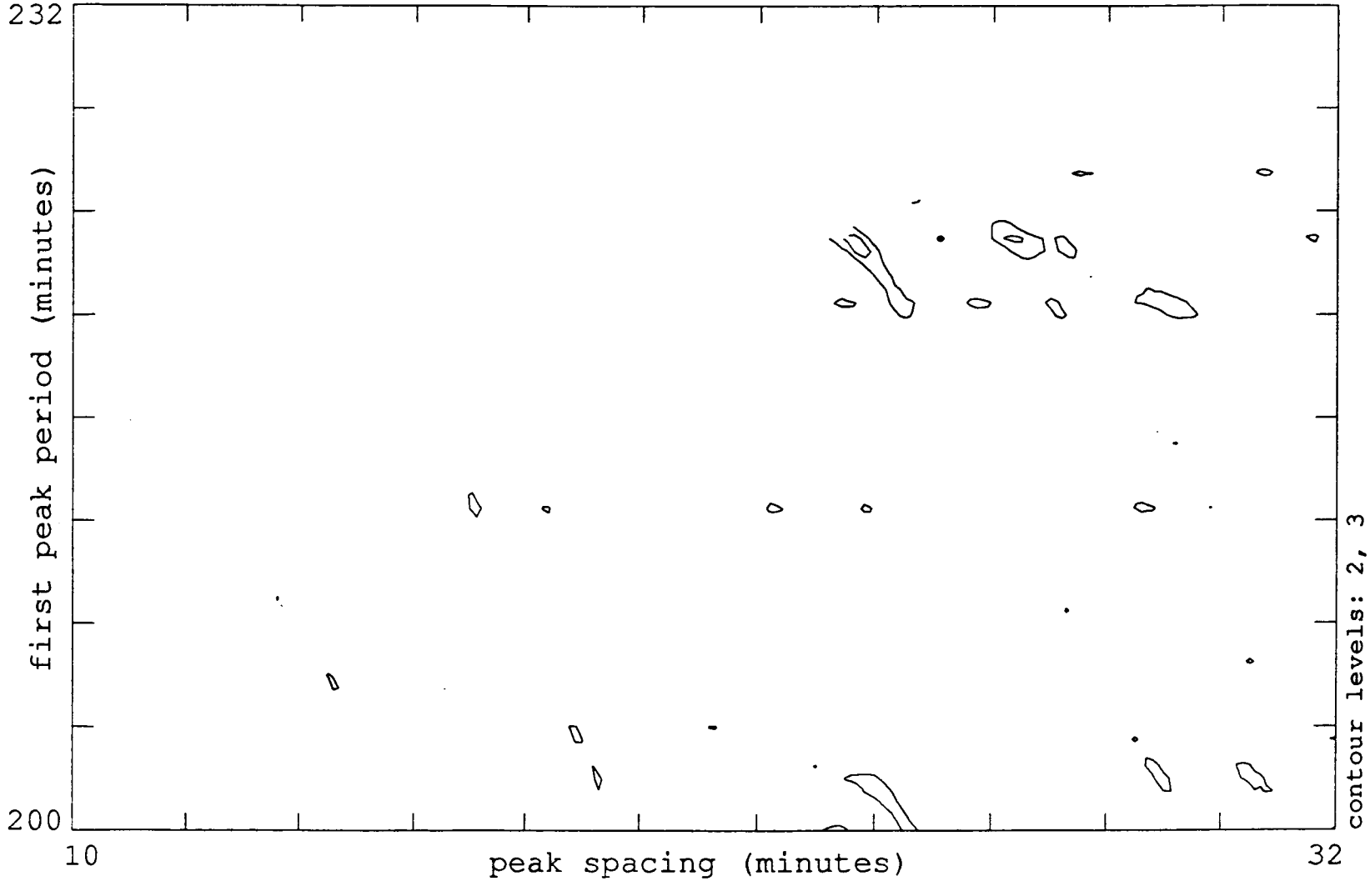

Figure 5.23 - Linear Search Map - Filling Factor as Data. As for figure 5.22, but the artificial data was constructed with gaps similar to the real data.

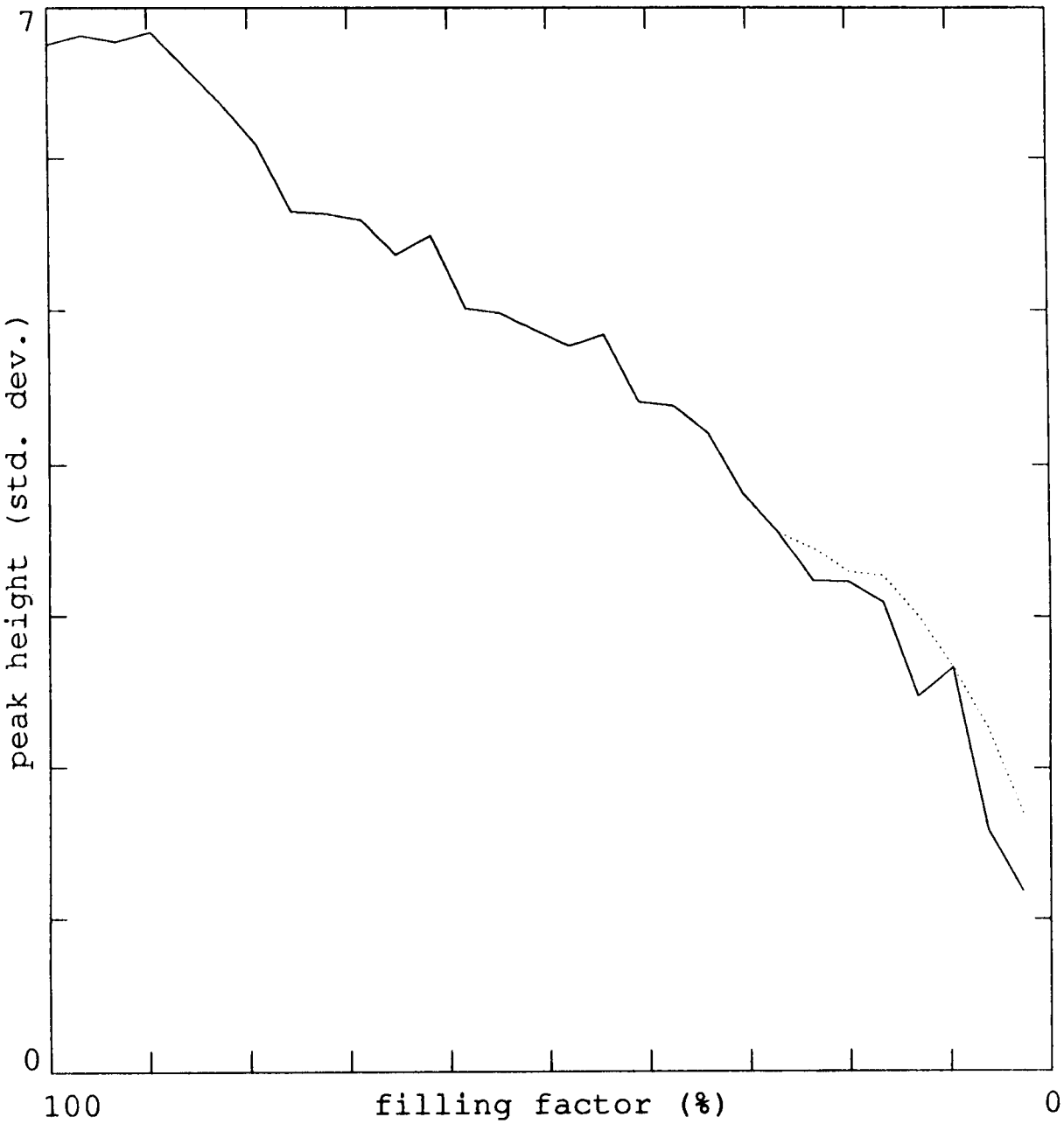

Figure 5.24 - Linear Search Peak Height vs. Filling Factor. The solid curve shows the height of the peak corresponding to the l=1, m=1 set of modes. The dotted curve corresponds to the highest peak on the whole contour map.

than the l=1 peaks. Nevertheless, the linear search was able to pick out the correct values for all sets of modes, with virtually no interference.

The method must now be subjected to the same tests as the first technique. First the method is applied to the power spectra which have been produced by windows with different filling factors. Figure 5.23 shows the result when applied to a power spectrum with a filling factor corresponding to the real data. Again, comparison with figure 5.17 shows the improvement attained by this method. One of the l=1 peaks is clearly the largest peak and there are few other peaks to confuse the map. The other l=1 peak is also present, but the l=2 peaks are essentially lost. Figure 5.24 is a graph of the height of the peak of the l=1,m=1 mode versus the filling factor, as well as the height of the highest peak. Compared to figure 5.19, the behavior of this method is quite different. The magnitude of the l=1 peak drops almost linearly with decreasing filling factor, and so does the value of the highest peak where it falls above the "correct" peak. This indicates that the highest peak is related to the l=1 peak, but at the wrong position - sort of an aliasing effect. This can be seen in the maps, where the highest peak which is not the "correct" peak is always at the position where the l=1 and l=2 modes can both contribute to the linear fit. The peak is visible as the second highest peak in figure 5.23. The implication of the continuing decline is that the method is still valid even after the highest peak fails to be the correct one, in that no truly random peak has emerged at the height of the mode related peaks. The point where the method fails to produce the highest peak at the l=1 position is at a filling factor of 27%, similar to the first method, but with the caveat that the presence of mode power is still detected by the second method. If the real data has no such interference from the l=2 set of modes, the method could be usable on it. The effect of added noise is the last thing which must be examined. Figure 5.25 shows the result of the technique on a power spectrum which has a filling factor comparable to the data's, as well

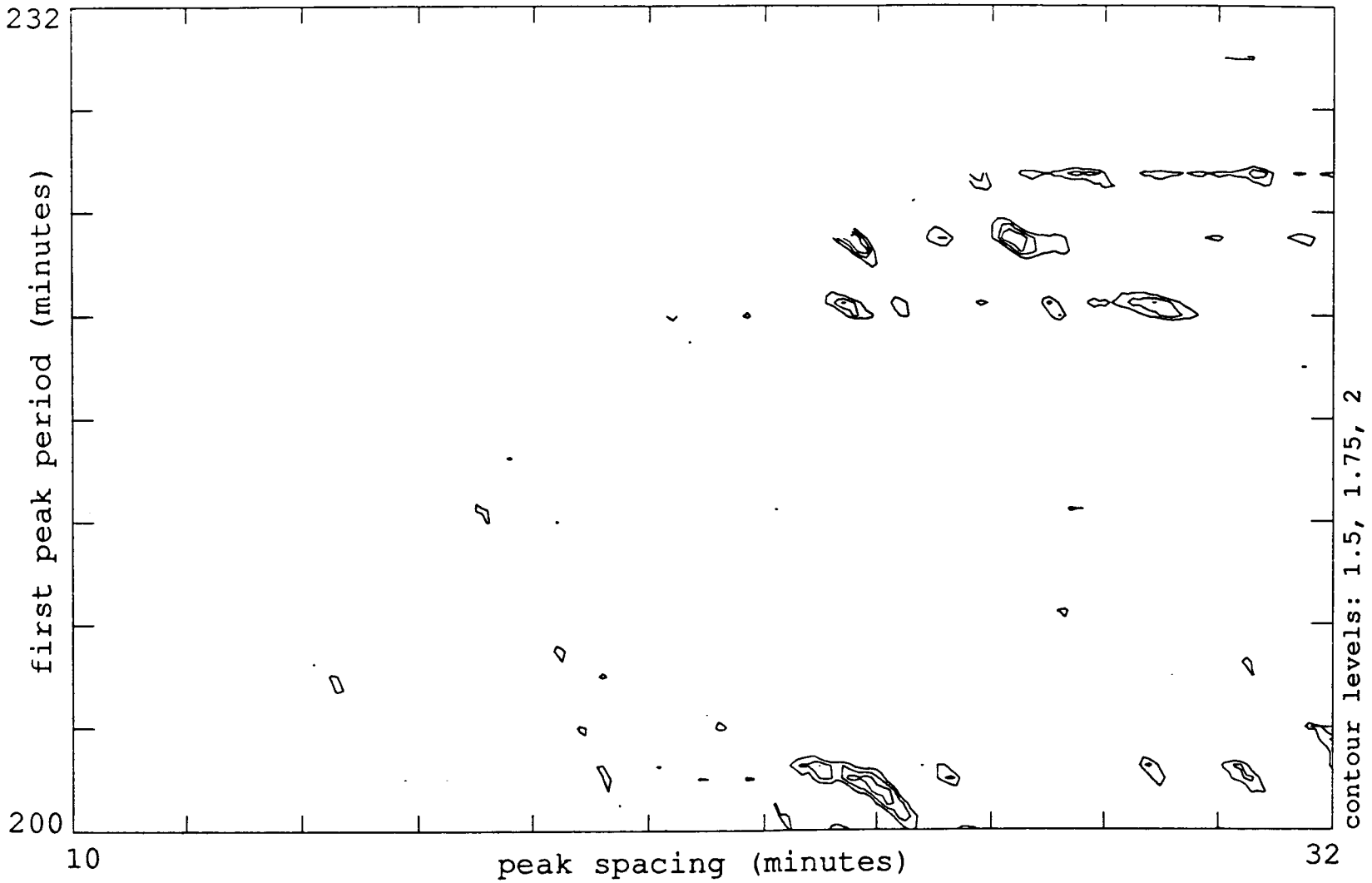

Figure 5.25 - Linear Search Map - Filling Factor as Data, Plus Noise. As for figure 5.22, but additional noise at a level appropriate for the actual data was added.

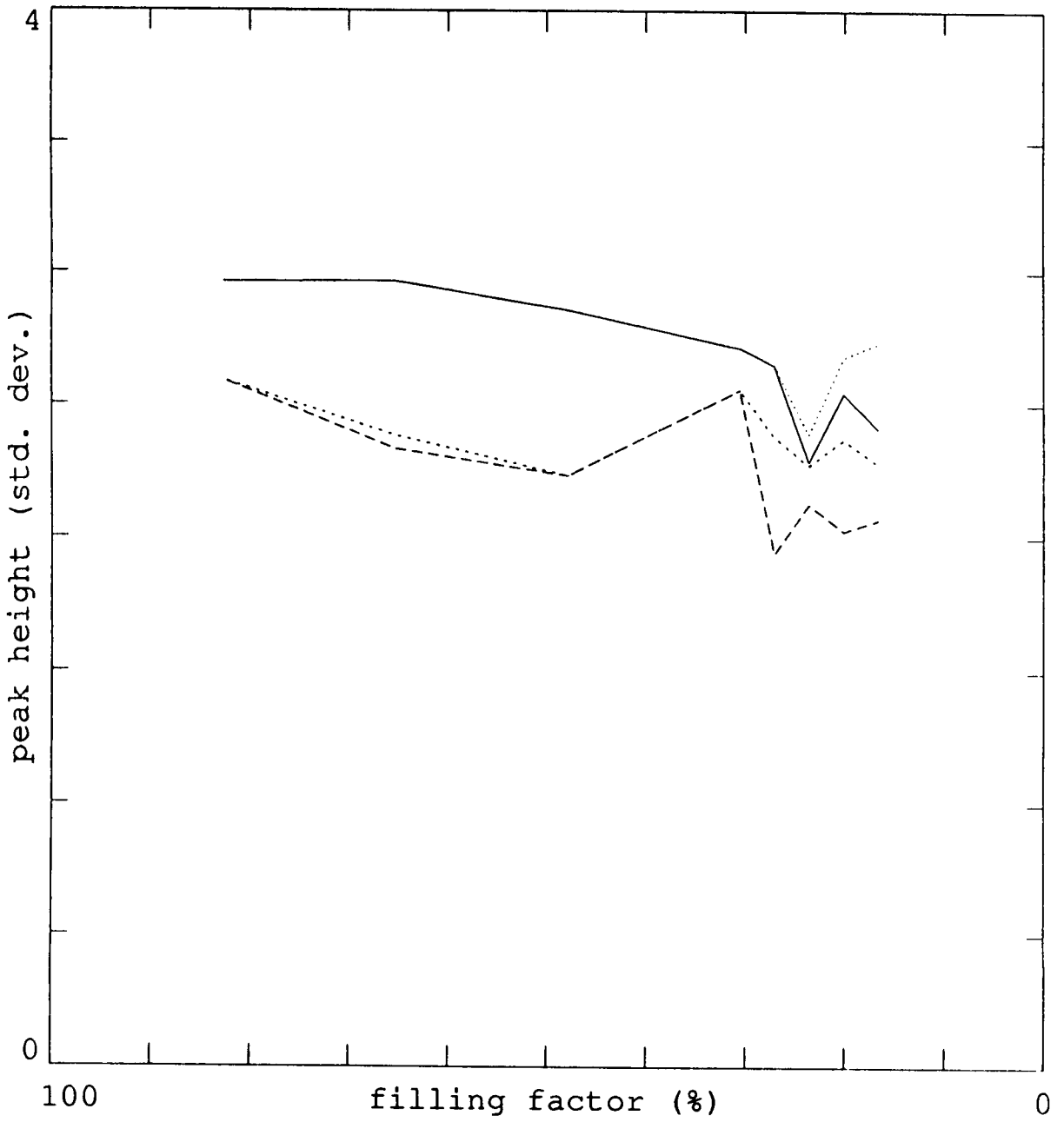

Figure 5.26 - Linear Search Peak Height vs. Filling Factor with Noise. Similar to figure 5.24, but with added noise. The solid and dotted lines correspond to a noise level of 1 m/s. The long-dashed and short-dashed lines correspond to a noise level of 2 m/s. The dotted and short-dashed lines show the highest peaks on the map, while the others show the "correct" peak.

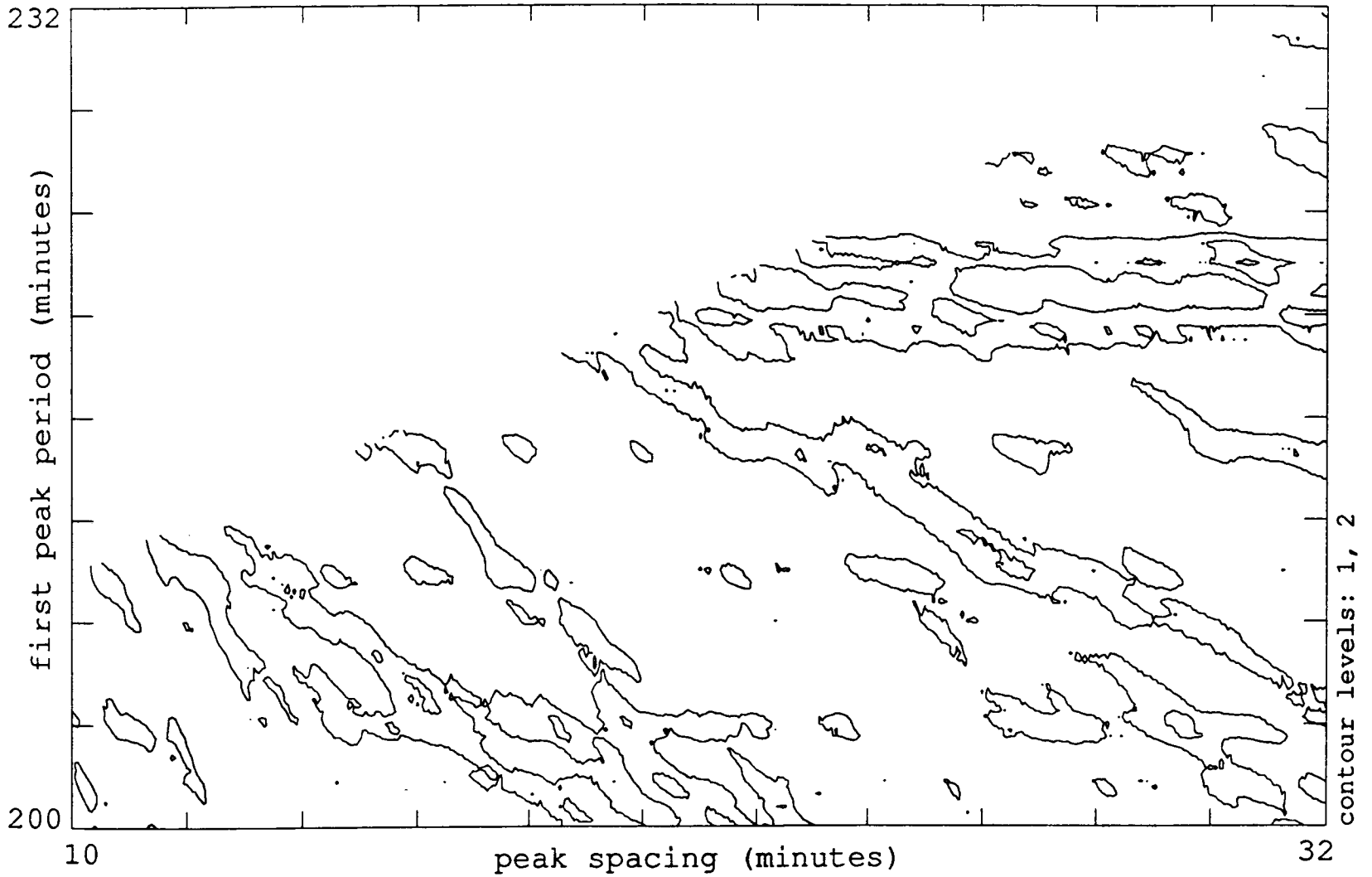

Figure 5.27 - Linear Search Map - 1987 Data. The contour levels are measured in units of the standard deviation σ of the whole contour map.

as added noise at a level of $\sigma_n = 1$. The l=1 peaks are still present at a dominant level, with the only other peak in contention being the one due to combination between the l=1 and l=2 modes. The effect of noise is markedly less severe on this method than on the first technique, which failed completely when noise was added. This is also visible in Figure 5.26, which shows the effect of noise on the height of the l=1,m=1 peak, similar to figure 5.20. While noise does decrease the height of the peak significantly, its effect is not as severe as on the previous model search. This is especially visible when one compares the $\sigma_n = 2$ case, where the correct peak is still generally the maximum peak in this method. The method, however, does seem to be at the limit of its capabilities when considering the low filling factor of the real data.

After these somewhat encouraging tests the final step is to apply the method to the real data. The result of the technique on the 1987 power spectrum is shown in figure 5.27, and immediately points out one problem that the method does have. The map is dominated by horizontal and diagonal streaks. Their origin is easy to figure out. The method calculates the average power in its search mask. If there is a high amplitude peak it will produce a high average power in any mask which happens to include it. This produces streaks of power in the map as the different search patterns sweep across the strong peaks. Thus the strength of the method, which lies in the detection of a pattern among a set of points, is clearly thrown off if the points carry different weight.

The solution to this problem represents the final refinement of the g-mode detection method developed in this investigation. The requirement which is necessary for the linear search to work is that its input is a set of peaks of approximately the same amplitude. The linear search then can determine whether there is any g-mode structure, and what the parameters are that describe it. To acquire a set of peaks the method that was used by

Delache and Scherrer (1983); Scherrer (1984) will be utilized. Briefly described, the method involves finding the largest peak in the spectrum, recording it, and removing it from the data by subtracting a sinusoid of the correct amplitude and phase at all times when there is data. The strength of this procedure is that it not only removes the peak, but also automatically any sidelobes introduced by the data window. Iterative application of the algorithm thus allows extraction of successively smaller peaks, down to the noise level. The output of this peak finding algorithm run on the 1987 data is shown in figure 5.28 in the form of an echelle diagram with a separation of 25 minutes between panels. The structure seen is certainly suggestive of a g-mode pattern, but looks very sparse when compared to the structure of the model peaks shown 5.21b. However, to get a better estimate of what to expect from the peak extraction program one can run it on artificial data. The model peaks were thus inserted into the 1987 data window, similar to the procedure which produced the artificial power spectra described earlier, the only difference being that the window corresponds to the actual 1987 data. The peak finding program then extracted the peaks which are plotted in figure 5.29.

One can immediately see that the window and noise have in effect wiped out a number of the peaks, by dropping their amplitude to a very low level compared to others, so that the peak extraction program did not find them. Moreover, there are instances where peaks are extracted which did not exist in the original spectrum. However, in almost all cases these extra peaks lie close, within 0.5 minutes, to the position of an actual peak, indicating that they arise due to the window's effect on the original peak. In the range of interest, between 200 minutes and 333 minutes, the peak extraction program was able to find 8 out of the 10 l=1 model peaks. The l=2 modes, being of lower amplitude, fare far worse, with less than 50% of the original peaks being recovered. The peak extraction thus produces an echelle diagram which looks just as ragged as that for the real data. This

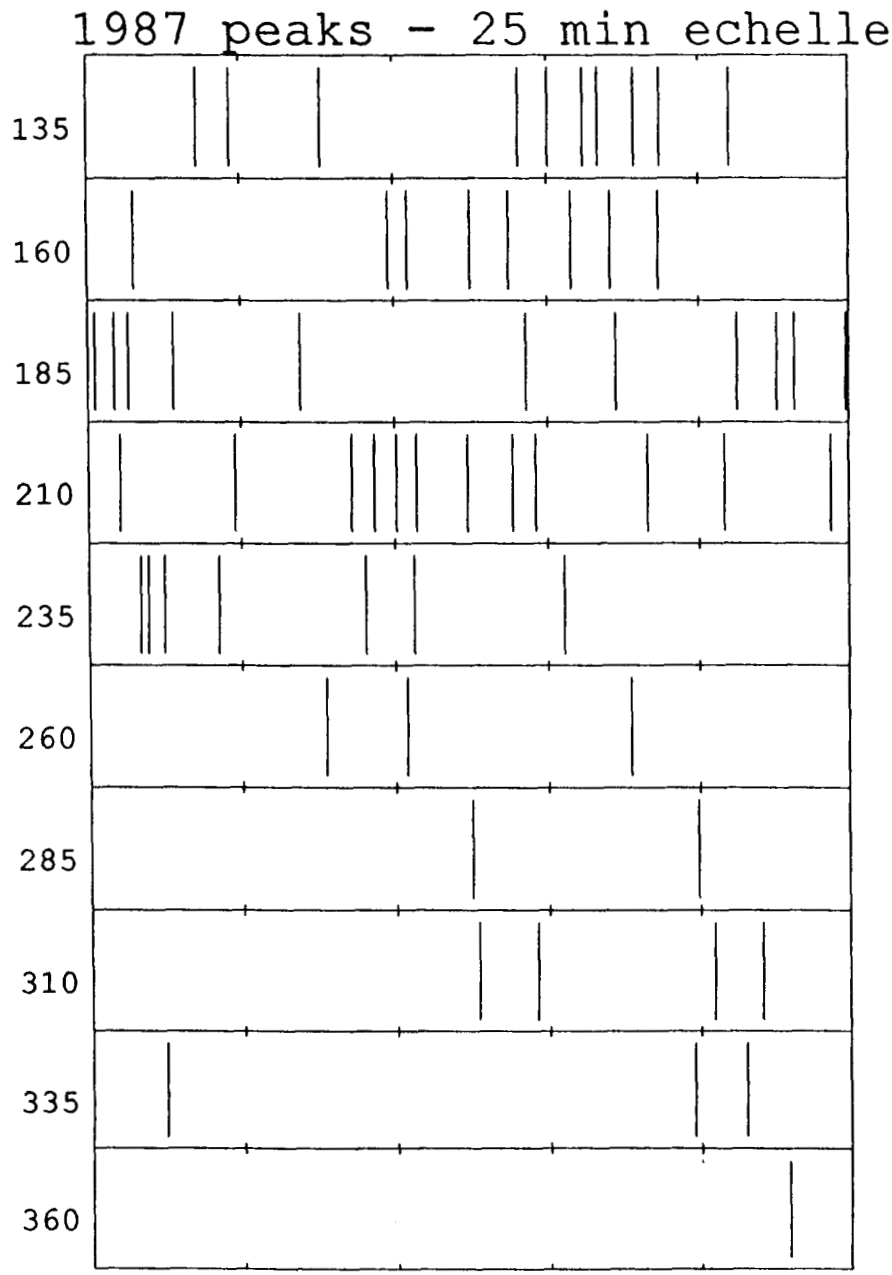

Figure 5.28 - Echelle Diagram of Extracted 1987 Peaks. The width of each panel is 25 minutes. The separation of the panels is also 25 minutes.

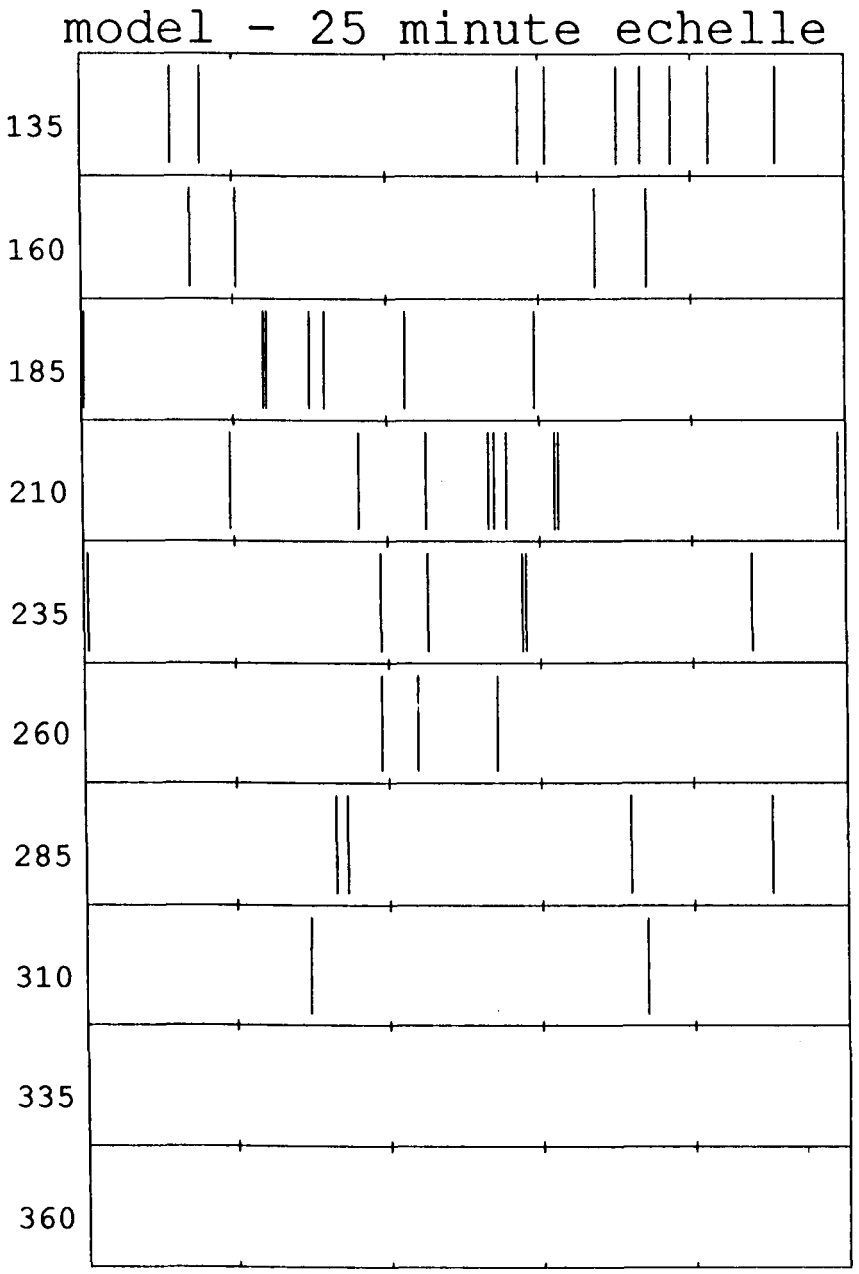

Figure 5.29 - Echelle Diagram of Extracted Model Peaks. The width of each panel is 25 minutes. The separation of the panels is also 25 minutes.

provides encouragement that the indications seen in figure 5.28 actually do correspond to g-modes.

To test the effectiveness of the linear search method on such an extracted set of peaks the search was run on a power spectrum constructed from the model peaks which had been extracted. The result is shown in figure 5.30 and shows a remarkable improvement over figure 5.23, which corresponds to a similar filling factor but did not have the peak extraction performed on it. Thus the peak extraction successfully picked out a sufficient number of the correct peaks from data with gaps to enable the linear search to clearly find the g-mode structure. The l=1 double peak is the dominant structure in the map, although one ridge is quite a bit higher than the other, which is to be expected since the peak extraction found 5 of the peaks of the $m = 1$ set and only 3 of the $m = -1$ set. The l=2 modes are only apparent near the l=1 peak. Their lower amplitude has lowered their already low map peaks to a barely detectable level.

Returning to the real data with this improved method, the peak finding program was run on the power spectrum of each of the 4 seasons, and the output recorded as a list. To process these peaks through the linear search they were simply entered as square boxes of a width equal to the natural resolution of the data in an otherwise empty power spectrum. The amplitude of each peak in this reconstructed power spectrum was set to be identical. The linear search was then performed on each reconstructed power spectrum with the results shown in figures 5.31 through 5.34. Looking first at figure 5.31, the output of the 1987 data, one can immediately see a dominant double peak, looking extremely similar to the peaks which are the signature for the model's l=1 modes. The location and separation of the two map peaks is exactly right to correspond to two sets of peaks in the spectrum with pairs separated by a fixed splitting in frequency. The resemblance is highly suggestive of the conclusion that g-modes have been detected in the 1987 data.

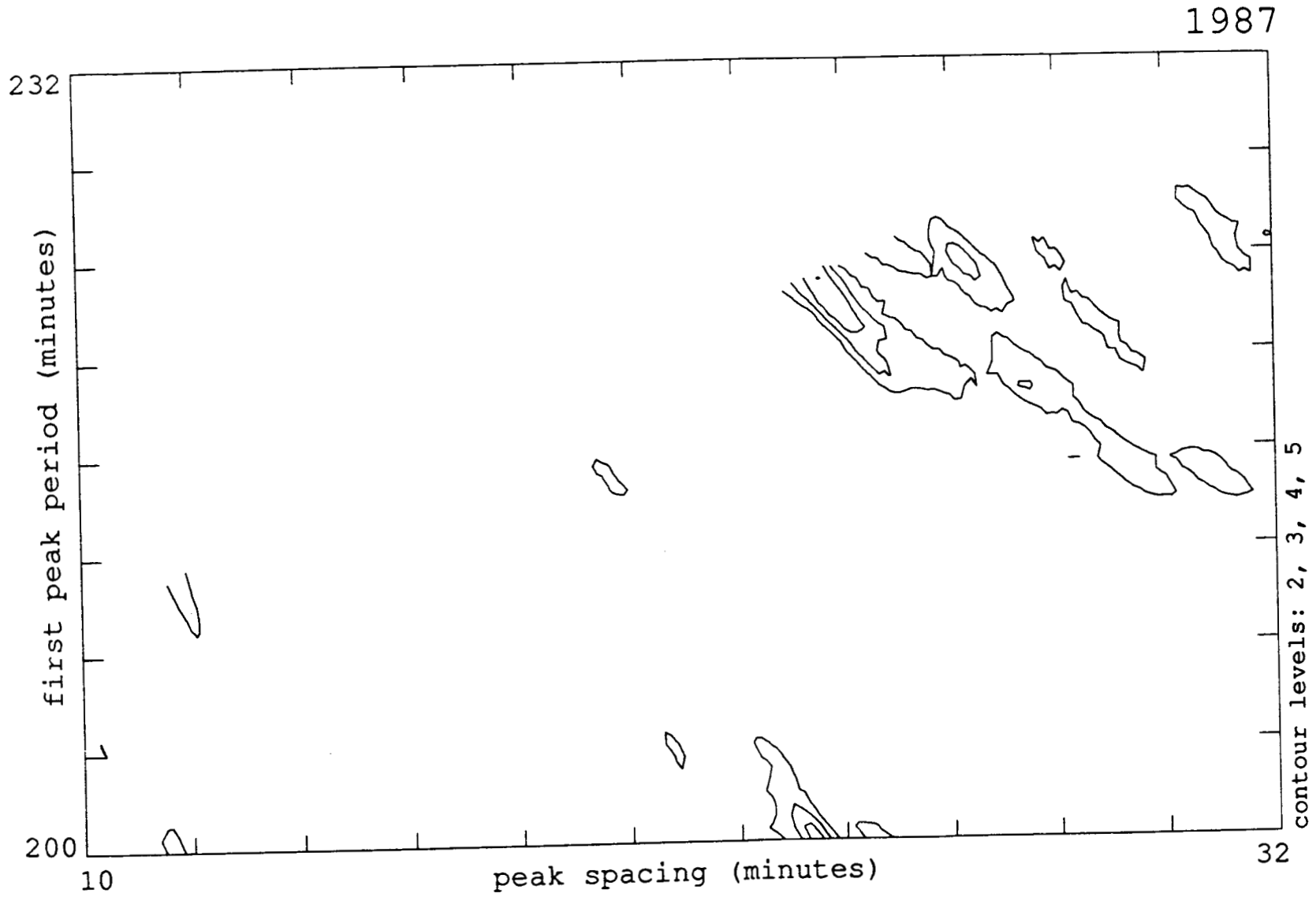

Figure 5.30 - Linear Search of Extracted Model Peak List. The large double peak corresponds to the l=1 model g-modes. The contour levels are measured in units of the standard deviation σ of the whole contour map.

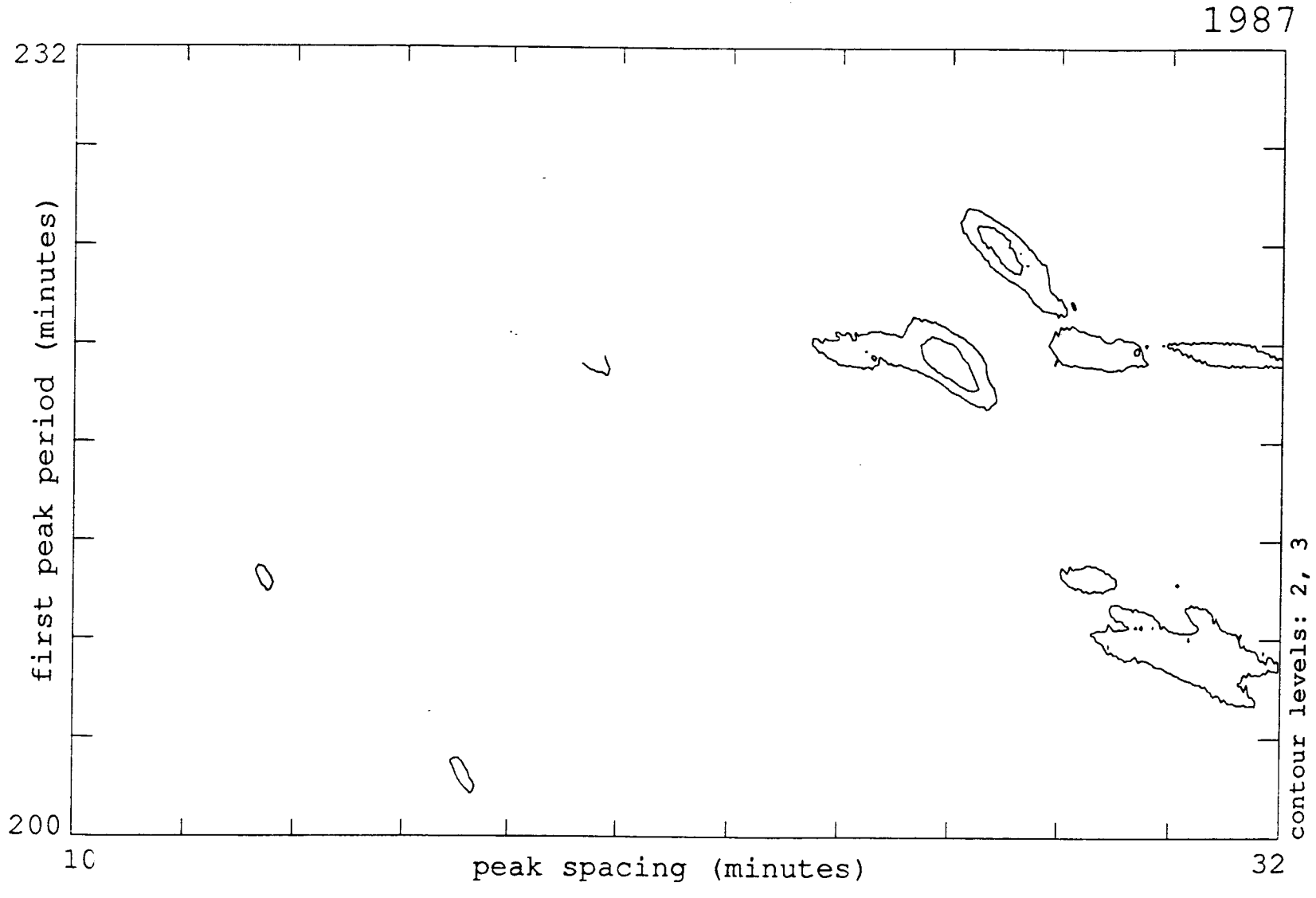

Figure 5.31 - Linear Search of Extracted 1987 Peak List. The double peak corresponds to the l=1 g-modes detected in the data. The contour levels are measured in units of the standard deviation σ of the whole contour map.

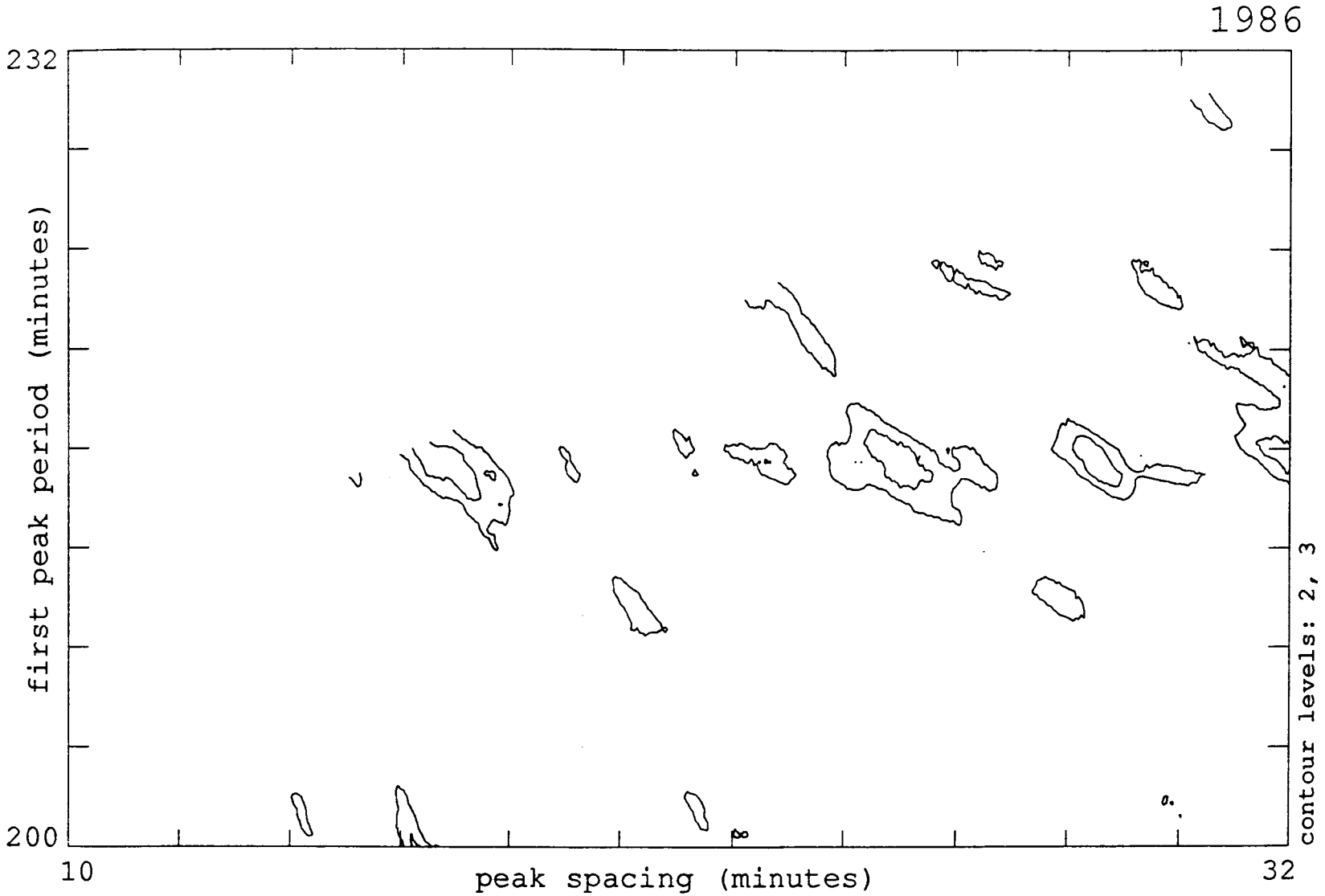

Figure 5.32 - Linear Search of Extracted 1986 Peak List. The contour levels are measured in units of the standard deviation σ of the whole contour map.

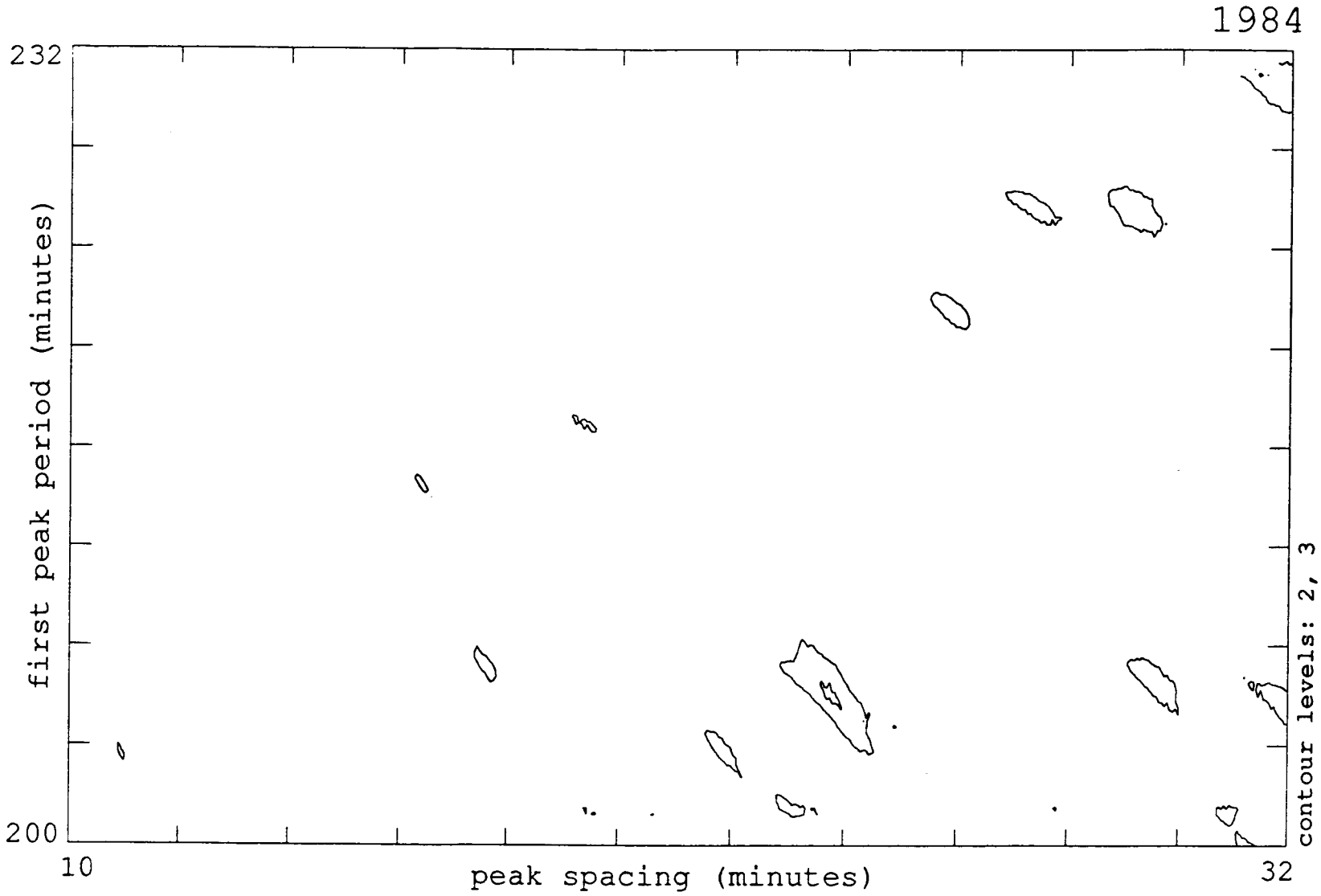

Figure 5.33 - Linear Search of Extracted 1984 Peak List. The contour levels are measured in units of the standard deviation σ of the whole contour map.

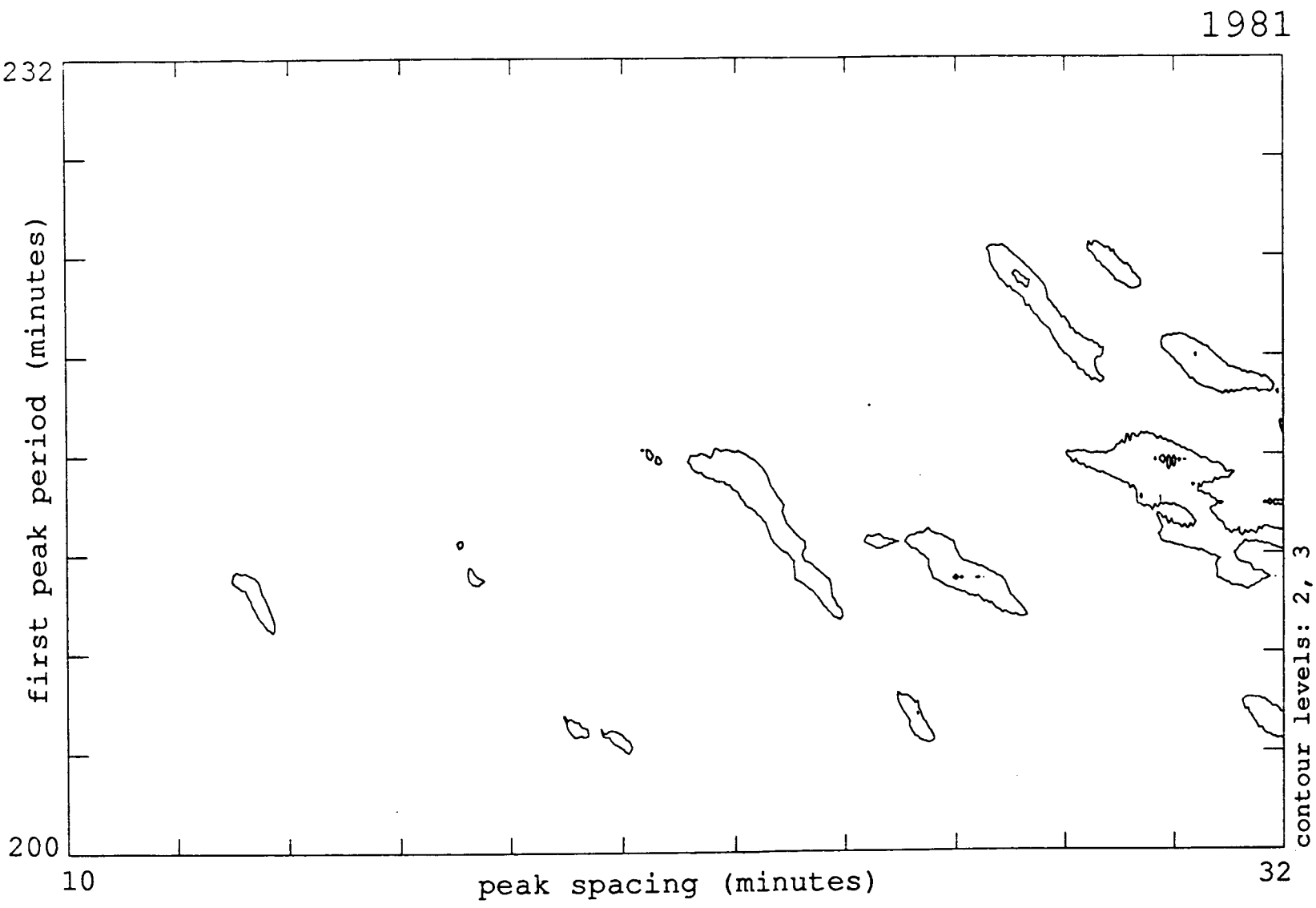

Figure 5.34 - Linear Search of Extracted 1981 Peak List. The contour levels are measured in units of the standard deviation σ of the whole contour map.

To attach a statistical significance to this detection requires some knowledge of how the method acts on a random set of peaks. To this end a Monte Carlo simulation was devised which generates a set of peaks distributed randomly in the spectrum. The number of random peaks in the detection region between 50 μHz and 83.3 μHz is on the average kept the same as the actual number of peaks extracted from the data in that region - 27. The linear search is then performed on the random spectrum. If the two highest map peaks in the linear search are located with respect to each other so that they correspond to two sets of spectrum peaks separated by a constant splitting in frequency then they could be misinterpreted as a g-mode detection. In 100 iterations of this procedure there were only 5 occurrences of that condition. One can conservatively conclude that the double peak in the 1987 data corresponds to g-modes with a confidence level of over 95%. However, 3 of the 5 cases would have an unreasonable frequency splitting of over 4 μHz. The other 2 cases had barely feasible frequency splittings of 2.5 μHz and 3.3 μHz. Thus assuming a reasonable limit on the range of the rotational splitting further increases the confidence level to over 98%.

The claim would be strongly bolstered if such strong peaks exist for all of the years. G-modes have a theoretical lifetime of years, which means that the same modes should be visible in other years. Examining figures 5.32 through 5.34, which show the results of the linear search on peaks extracted from the 1986, 1984, and 1981 data, is at first somewhat disappointing, since they are clearly noisier than the 1987 results and no large peaks of the sought-after double structure stand out. For that matter, the double peaks of 1987 are the largest peaks in all the maps. This is actually a positive factor since it means that the other seasons had poorer quality data. If the other years had peaks of the same size, but distributed elsewhere, then the chance that the 1987 detection is a chance coincidence would be increased. As it is, the 1987 peaks stand out, demonstrating the better quality of

the 1987 data. If one examines the other years' maps at the points where the 1987 peaks are located, one finds that in every one of the years there is some power in that area. 1986 is the worst, displaying only a small ridge located between the 1987 peaks. One should notice, though, that the whole 1986 map is dominated by a horizontal streak of power, indicating a range of frequency where a number of overlapping peaks exist. This would throw off the linear search just like a strong peak did before. 1984, however, actually has a small double peak at almost the exact expected position. The 1981 season also makes a positive contribution, in that its strongest peak lies right on top of one of the 1987 peaks. The other ridge though, although present, is only visible at a lower level than plotted in the figure.

It has been stated before that the 1987 data is by far the best data, since it has not had to be renormalized on each day. This amplitude change in the other years has a very adverse affect on any signal which in the real data has a constant amplitude, since the peak gets split up into a group of smaller peaks by the introduction of phase changes - which is essentially the effect of an amplitude variation from day to day. Moreover, 1987 had the best filling factor (23.6%), followed by 1984 (22.6%). Although the difference is small, the steep drop-off with filling factor visible in figures 5.19 and 5.24 indicates that it could be an important difference.

With these considerations one can say that the three other seasons are consistent with the detection of g-modes in the data. The double peak structure identifies them as l=1 modes of azimuthal orders $m = 1$ and $m = -1$. This also agrees with the knowledge that the Stanford instrument is most sensitive to these g-modes. The value of the separation between successive l=1 modes of $m = 0$, obtained by taking the separation at the middle between the two peaks, is measured to be 26.25 minutes. Multiplying by $\sqrt{2}$ one obtains a value of 37.1 minutes for T_0. Taking the position of the two peaks, which corresponds to

Period (min)	Frequency (μHz)	degree (l)	azimuthal order (m)	radial order (n)
219.4	76.0	1	1	8
224.1	74.4	1	-1	8
245.1	68.0	1	1	9
250.9	66.4	1	-1	9
270.8	61.5	1	1	10
277.7	60.0	1	-1	10
296.5	56.2	1	1	11
304.5	54.7	1	-1	11
322.2	51.7	1	1	12
331.3	50.3	1	-1	12
207.5	80.3	2	0	13
222.7	74.8	2	0	14
237.9	70.6	2	0	15
253.1	65.8	2	0	16
268.3	62.1	2	0	17

Table VI. This table lists the frequencies of the g-modes detected in the 1987 data, as calculated from the values corresponding to the location of the l=1, m = −1,1 double peak in the linear search map. The list is only extended up to the limits of the linear search region, between 50 μHz and 83.3 μHz. The l=2 modes are stopped at n=17 since there is no evidence for higher order modes in the extracted peak list (see figure 5.34).

the position of the first peak of each set in the power spectrum, one measures 219.4 minutes and 224.1 minutes. These correspond to 74.4 μHz and 76.0 μHz, which gives a value of 1.6 μHz for the rotational splitting ν_R using the Tassoul formula. This implies a rotation about 3 times the surface rate in the core of the sun. This agrees with the strong increase found by measurements of rotational splitting of p-modes (Duvall et al., 1984).

If one assumes that the T_0 also applies for l=2 modes, which is asymptotically true, but probably not exact in this range, one can calculate the expected period splitting for those modes. The resulting number is 15.3 minutes. It is interesting to note that at double that separation (30.6 minutes) the 1987 linear search map displays its only other large group of power, at a position of 207.5 minutes. This is again similar to the pattern seen in the artificial data, where the l=2 modes were more visible at a separation of twice their expected separation. This identifies virtually all the peaks in the 1987 map with g-modes. The measured values of the peak positions allows one to calculate the periods of the peaks. The results are summarized in Table VI.

In figure 5.35 the actual peaks which were extracted from the 1987 data are plotted together with the location of the modes as calculated from the measured values of the separation, and the position of the first peak. The arrows corresponding to modes which lie outside the range of the linear search (above 83.3 μHz), and are thus only an extrapolation using the linear calculation, are drawn dashed. The lower row of arrows corresponds to both m values of the l=1 modes, and is extended throughout the whole frequency range. One can see that below 80 μHz the locations match up quite well and completely with extracted peaks. The upper row of arrows corresponds to the position of the l=2,m=0 mode. The locations again match up well with groups of extracted peaks, especially below 85 μHz. One can say that all extracted peaks below about 82 μHz are

accounted for as g-modes. Figure 5.36 shows the same spectrum, but with the actual data from which the peaks were extracted. It is clear that the visual detection of all the corresponding peaks in this spectrum is almost impossible due to the window function. However, one can identify some of the peaks. The highest of the peaks has an amplitude of about 40 cm/s. The g-modes detected by Isaak et al. (1983) lie at levels from a few centimeters to about 10 cm, indicating that the ratio in sensitivities between the differential and full-disk observation methods may be as large or even larger for the g-modes than for the p-modes.

The peaks previously identified in the 1979 Stanford data (Delache and Scherrer, 1983; Scherrer, 1984) must be compared to this new identification. Figure 5.37 shows the location of the g-modes identified in this study, marked by arrows as described for figures 5.35 and 5.36. Underneath the arrows are two sets of peaks. The bottom set corresponds to the published list of peaks. In the range below 83.3 μHz three of the published peaks lie right at the frequency of a g-mode identified in this study, another three lie very close or could be l=2 peaks with $m = -2,2$, while the final three lie relatively far from an identified g-mode. At the natural width of these peaks, one can statistically expect in this case one chance superposition. That there are three, with three more close ones, is suggestive, especially in light of the fact that the 1979 data from which the peaks are derived is of significantly lower quality than the data analyzed in this study. The filling factor is only 8%, which has been shown to have severe effects on the spectrum. This is demonstrated by the second set of peaks, located above the published peaks in figure 5.37, which were extracted from a 1979 time series which differs only by one day of observations from the original one. It is shorter, but has a slightly higher filling factor of 11.9%. Only two of the original peaks are repeated, with another one close. The low filling factor of the 1979 data may cause some of the extracted peaks to be spurious. Moreover, the parabolic fit used in

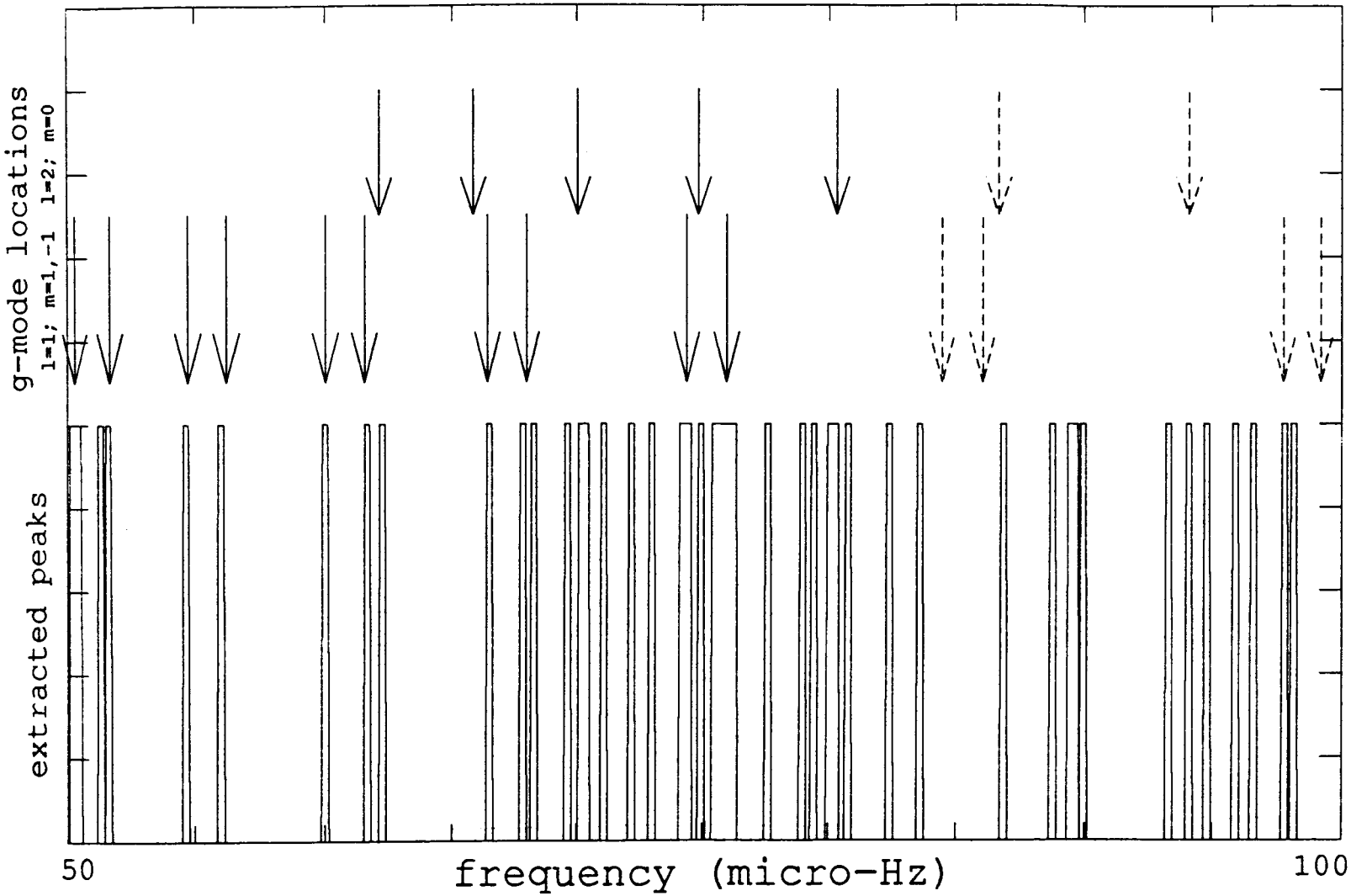

Figure 5.35 - Extracted Peaks and G-Mode Locations. The row of narrow rectangles represents the peaks which were extracted from the data. The arrows show the locations of the g-modes which were identified by the linear search. Dashed arrows are extrapolations beyond the region of the search where the modes become strongly non-asymptotic. For l=2 modes only the central location of each mode is shown ($m = 0$), for l=1 both peaks ($m = -1,1$) are indicated.

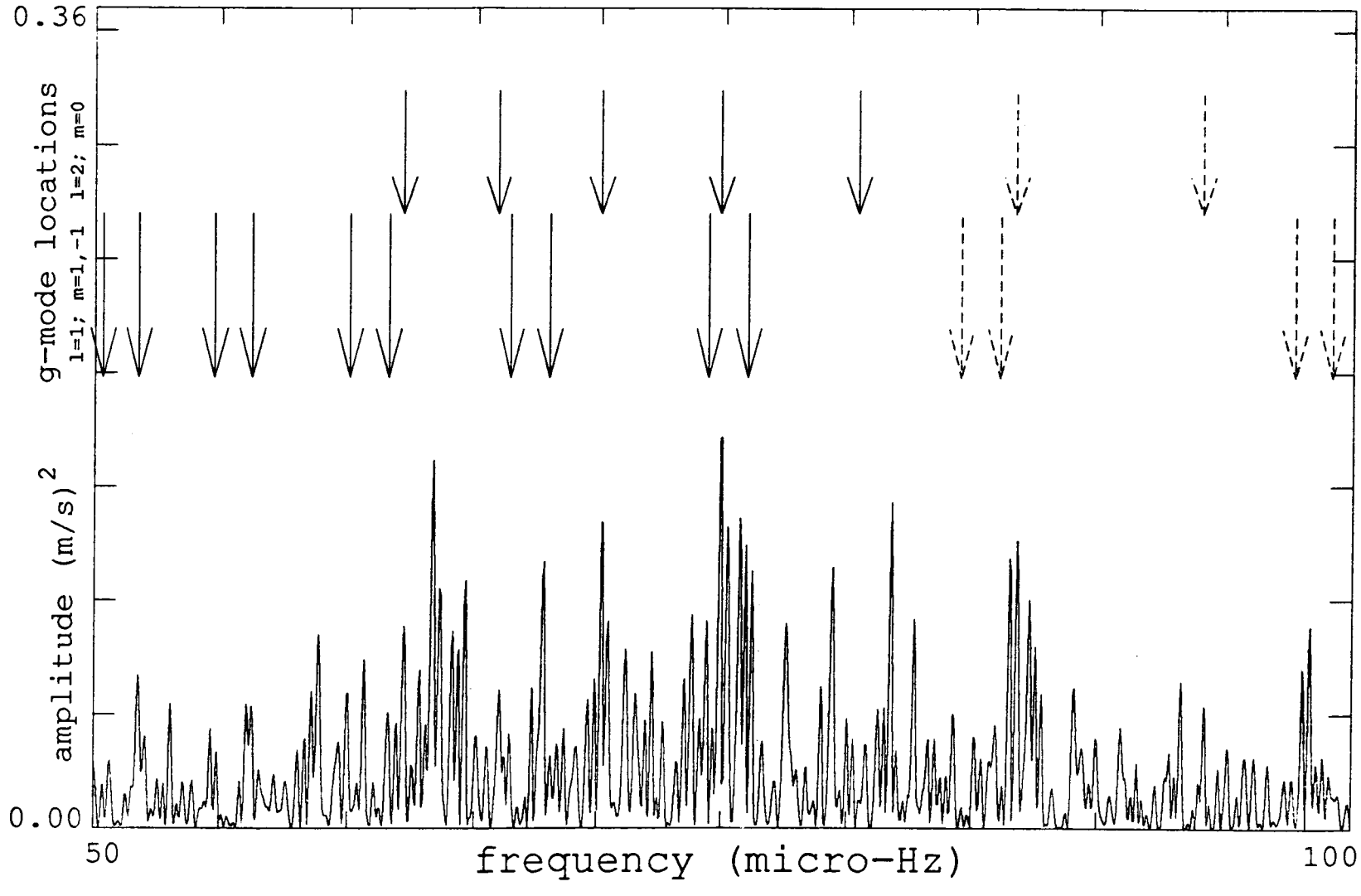

Figure 5.36 - Data Spectrum and G-Mode Locations. As for figure 5.35, but showing the actual data from which the peaks were extracted.

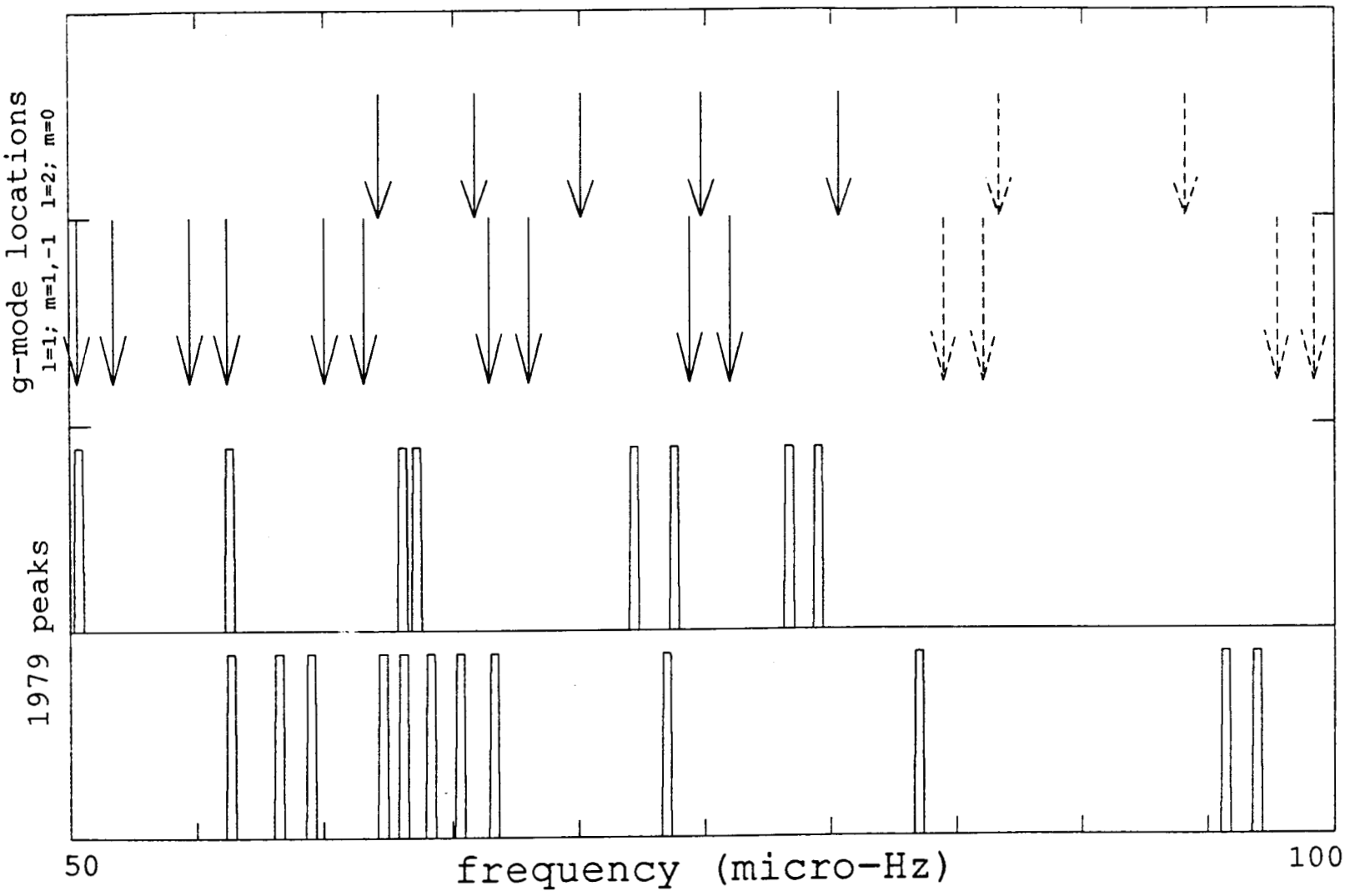

Figure 5.37 - 1979 Peaks and G-Mode Locations. As in the previous two figures, the arrows indicate the g-mode locations identified in this study. The bottom row of peaks shows the published peaks of the 1979 data (Delache and Scherrer, 1983). The second row shows peaks extracted from shorter time series of the 1979 data, but with a slightly higher filling factor.

that analysis (Scherrer, 1984) introduces power in a broad region of the spectrum, which has further potential for resulting in erroneous peaks. The data used in this analysis, as well as the reduction method, are a significant improvement over these first studies.

The value of T_0 as measured is accurate to within ±0.2 minutes. However, it is possible that this value has a systematic error in it which gives a value lower than its actual one. One need only look at the echelle diagrams in figure 5.21 to see that the lines curve in such a way as to have a larger separation at higher periods. A linear fit to such a slightly curved line would give a lesser slope than the curve is asymptotically approaching. Therefore the measured T_0 may actually be too small. The amount of systematic error is hard to estimate. In the model peaks the l=1 and l=2 modes have a separation which results in two values for T_0 which differ by 1.3 minutes, with the l=2 modes having the higher value. If this is taken as an indication of the possible systematic error, the measured value for T_0 is then 37.1 -0.2/+1.3 minutes. Another number which comes out of these calculations is the value of the constant ϵ in the Tassoul equation, which is generally taken to be $\frac{1}{4}$. The calculations give a value of $\epsilon = .05$ for the l=1 modes, and $\epsilon = .3$ for the l=2 modes. However, these values are extremely sensitive to the exact value T_0, meaning that those values for ϵ are as consistent with each other as they are with $\frac{1}{4}$ or 0.

The measured value of T_0 is higher than the value calculated with the best current solar models, which lies around 34.5 minutes. To raise the value in the models would require a reduction in the buoyancy frequency. This could be achieved either by mixing the interior, or by reducing the initial Helium abundance Y_0 (Deubner and Gough, 1984). Either of these changes would have the tendency to decrease the temperature in the interior, which agrees with the results from the p-mode analysis in chapter 4. However,

these changes would also increase the discrepancy between the models and the well-established frequencies of p-modes in the 5 minute region (Deubner and Gough, 1984).

Chapter 6

Summary of Conclusions

In this study the data obtained in the last 8 years of solar differential doppler observations at Stanford have been considered. The four best time series of data have been examined in detail. The sources of errors in the data have been investigated and removed where possible. In particular, the contribution resulting from transparency variations in the sky has been examined in detail. Detection methods applicable to data with low signal to noise ratio and low filling factor have been developed and utilized for the investigation of global solar modes of oscillations in the data.

The frequencies of p-modes, oscillations whose restoring force is dominantly pressure, have been measured and identified in the data. While the bulk of the p-mode power lies in the well established modes between 1800 μHz and 4500 μHz, the identification of these modes in the data was mainly used as a starting point from which to determine the degree l and order n of previously unidentified modes. New p-modes have been detected and identified which lie both above and below the previously identified frequency range of low degree modes. The most significant new identifications are those of 22 p-modes of low order n. These modes probe far into the sun and have high sensitivities to conditions in the deep interior. They display a systematic difference from frequencies calculated from a solar model, such that model frequencies are too high for modes which penetrate the energy-generating core. This can be interpreted to suggest that current models have a sound speed which is too high in the solar core. This could indicate a lower core temperature, or a higher mean molecular weight.

The presence of g-modes, buoyancy oscillations confined to the radiative region of the sun, has also been determined in the Stanford data. The frequencies which have been identified lie between 50 μHz and 83 μHz, and correspond to g-modes with degree l=1 with a 98% confidence level. Modes with degree l=2 have also been detected, although at a much lower level of confidence. The asymptotic period separation of g-modes is determined to be 37.1 minutes, higher than the value derived from current solar models calculations. This indicates a lower buoyancy frequency than expected in the models, which can be accomplished by mixing in the core, or a decrease in Y_0. Both of these would suggest a lower temperature in the solar core. The rotational splitting measured between the $m = 1$ and $m = -1$ modes of degree l=1 is 1.5 μHz, which implies a core rotation of about triple the surface rate.

The results from the low order p-modes and the l=1 g-modes which have been identified in this analysis agree in the conclusion that the solar core temperature may be lower than current models determine. Detailed model calculations utilizing the full capacity of current numerical stellar evolution codes will be necessary before the degree of this change can be established.

Independent observational confirmation of the frequencies established in this study is perhaps the most immediate desirable goal after this work. The p-mode frequencies have been clearly confirmed in all the years of Stanford data which were examined. It falls to other observers to examine their data at the frequencies identified for the low order modes. Concerning the g-modes, the 1988 season at Stanford, if it produces a good time series of data, should prove as much of an improvement over the previous years as the 1987 data. Thus one could expect that the g-mode frequencies should be detectable using the method developed in this analysis in that year also.

The detection of modes of oscillation on the sun with amplitudes at a level of tens of centimeters or less is a sensitive undertaking which requires that great care is continually exercised to avoid systematic errors. The field of helioseismology is advancing rapidly, and will reach full maturity with the advent of data from such endeavors as GONG or SOI. These data will hopefully avoid from some of the problems which have beset this analysis and others. The data will be largely gap-free, reducing the window problem which affects the peak amplitudes and the structure in the spectrum so adversely. More importantly perhaps, the data will hopefully be free of the large systematic errors which have been examined in this analysis in connection with the g-mode search. While both GONG and SOI excel in their high spatial resolution ability, their improvements in the method used to measure the Doppler shift of sections of the solar surface should also bring the noise level in the data down far enough to effect remarkable increases in the knowledge of the low degree modes examined in this study.

Appendix A

Calibration of the Data Signal

In its oscillation observation mode the Stanford instrument measures the difference in position between an absorption line in right circularly polarized light coming from the central portion of the solar disk and the same line in left circularly polarized light coming from an annulus around the central section. This measurement is proportional to the average velocity difference between those two sections of the sun. The solar oscillations are measured by virtue of the fact that the average of the line-of-sight displacement of the solar surface corresponding to a mode is different for the central portion and the annulus. As one of the first steps in the data reduction the signal which is recorded must be calibrated by the conversion factor which turns it into m/s.

Because of the mechanics of this measurement, as described in chapter 2, the calibration presents a non-trivial problem which must be carefully considered. Its dependence on the exact line shape probably prevent the calibration factor from being known to better than about 10%, although the individual calibration attempts which measure it best are consistent to a better degree than that.

The basic equations which describe the measurement process are given by

$$I = \left[\frac{G_B I_+^B + G_R I_+^R}{2} + \frac{G_B I_-^B + G_R I_-^R}{2}\right] \times ½ \tag{A.1}$$

$$\frac{1}{G_D} D = [(G_B I_+^B - G_R I_+^R) - (G_B I_-^B - G_R I_-^R)] \times ½ \tag{A.2}$$

$$0 = (G_B I_+^B - G_R I_+^R) + (G_B I_-^B - G_R I_-^R) \tag{A.3}$$

In these equations I is the intensity in the wing of a line, where B indicates the blue side and R the red side, and + indicates right circularly polarized light and – corresponds to left circularly polarized light. G is the gain factor of the appropriate phototube, B again corresponding to the blue exit slit and R to the red exit slit.

Equation A.1 describes the intensity measurement, which is just an average of the two exit slits, averaged over a complete KDP cycle (actually integrated over 11 cycles) of right and left circular polarization as represented by the factor of ½.

Equation A.2 is the difference signal which determines the separation between the lines. G_D is a gain factor between the D and I channels. Measurement of the ratio D/I when the instrument is configured such that the red exit slit signal is grounded ($R \rightarrow 0$), and the light falling onto the KDP assembly is only right circularly polarized ($- \rightarrow 0$) gives a value of $D/I \approx 200$. Using the equations above

$$I = G_B I_+^B / 4$$

$$D = G_D G_B I_+^B / 2$$

which then implies that

$$G_D \approx 100 \tag{A.4}$$

The direction of the subtractions in equation A.2 must also be checked to avoid a possible error in the phase of the data signal. To check that the red exit slit signal is subtracted from the blue exit slit signal (B–R) the exit slit assembly is manually driven across the absorption line. The unmodulated difference signal (equation A.3) uses the identical electronic channel as the modulated difference signal D for the differencing of

blue and red signals. As the slits encounter the line, the unmodulated difference signal can be watched easily as is goes from a high negative value to a high positive value, or vice versa depending on the direction of the differencing. Performing the check validates the phase shown in the equations.

To check that the signal from the annulus (left circularly polarized, or –) is subtracted from the center (right circularly polarized, or +) the instrument is configured so that only right circularly polarized light enters the KDP assembly. Then the outputs of the modulated and unmodulated difference channels are watched as the assembly is scanned across the line. They are seen to change in phase, confirming the phase of this subtraction.

1. Mathematical Derivation

The calibration constant of the data signal *D/I* could be exactly calculated mathematically if one knows the exact line shape. One can make a very good analytical approximation by assuming symmetric linear slopes in the wings of the lines and point-width exit slits. This is a valid approximation for the magnitudes of velocity differences which are generally measured, corresponding as they do to a much smaller shift in wavelength than the line width. Thus, using symmetric triangular line profiles and point slits, the measured intensities become

$$I_-^R = I_-(f_- - m_-(S-d))$$

$$I_-^B = I_-(f_- + m_-(S+d)) \qquad \text{(A.5)}$$

$$I_+^R = I_+(f_+ - m_+(S-d-\Delta))$$

$$I_+^B = I_+(f_+ + m_+(S+d-\Delta))$$

In these equations, $I_\pm$ is the brightness of the spectrum. The intercepts $f_\pm$ are the depth of

the triangular line measured as a fraction between 0 and 1, where 0 corresponds to 100% absorption, and 1 to 0% (in other words, no line). The slopes $m_\pm$ are defined as

$$m_\pm = \frac{1 - f_\pm}{\delta_\pm} \geq 0$$

where $\delta_\pm$ is the halfwidth of the triangular line profile. The value S is the position of the center of the exit slit assembly measured with respect to the position of the left circularly polarized line such that a displacement towards the blue is greater than 0. The variable Δ is the separation between the left and right circularly polarized lines such that it is larger than 0 when the right circularly polarized line is to the blue side of the left circularly polarized line. Finally, the value d is half the separation between the two exit slit positions, a constant which is equal to (18 + 75)/2 mÅ, or 46.5 mÅ.

Equation A.3 can be rewritten as

$$g \equiv \frac{G_R}{G_B} = \frac{I_+^B + I_-^B}{I_+^R + I_-^R} = \frac{I_+(f_+ + m_+(S+d-\Delta)) + I_-(f_- + m_-(S+d))}{I_+(f_+ - m_+(S-d-\Delta)) + I_-(f_- - m_-(S-d))}$$

where g has been defined as the ratio between the two phototube gains. Extensive algebraic manipulation allows extraction of the value of the exit slit position S

$$S = \frac{I_+ m_+ \Delta - \left[\frac{1-g}{1+g}\right](I_+ f_+ + I_- f_- + d(I_+ m_+ + I_- m_-))}{I_+ m_+ + I_- m_-} \tag{A.6}$$

Using equation A.3 to simplify the expressions for D and I, the data signal D/I can be written as

$$\frac{D}{I} = 2G_D\left[\frac{G_B I_+^B - G_R I_+^R}{G_B I_+^B + G_B I_-^B}\right] = \frac{I_+(f_+ + m_+(S+d-\Delta)) - I_+(f_+ - m_+(S-d-\Delta))g}{I_+(f_+ + m_+(S+d-\Delta)) + I_-(f_- + m_-(S+d))}$$

where g has been defined as before. Substituting for S using equation A.6 and manipulating

the result yields

$$\frac{D}{I} = \frac{G_D I_+ I_- \left[-m_+ m_- \Delta + \left[\frac{1-g}{1+g} \right] (m_- f_+ - m_+ f_-) \right]}{(I_+ m_+ + I_- m_-)(I_+ f_+ + I_- f_- + d(I_+ m_+ + I_- m_-)) \frac{g}{(1+g)^2}} \qquad \text{(A.7)}$$

At the beginning of each observing season the circular polarization assembly is adjusted so that the intensity from the center is the same as the intensity from the annulus. In other words, $I_+ = I_-$. This equality holds roughly true for all observations. Chapter 3 explores some of the changes one may expect and the effect they have. For purposes of the calibration it suffices to set them equal. Furthermore, at the beginning of each observation the phototube gains are balanced, so that g=1. Its change also affects the measurement, and is further explored in Appendix B, but for obtaining the calibration factor it is sufficient to assume that the phototube gains are equal. Equation A.7 then simplifies to

$$\frac{D}{I} = \frac{-4 G_D m_+ m_- \Delta}{(m_+ + m_-)(f_+ + f_- + d(m_+ + m_-))} \qquad \text{(A.8)}$$

This equation clearly displays the linear relationship between the data signal D/I and the line separation Δ.

The quantities which determine the calibration factor are all constants which can be measured. To do so, the instrument was configured so that only the light from either the central portion or the annulus of the circular polarization assembly would reach the spectrograph. This is easily accomplished by applying a constant voltage across the KDP crystal which causes it to pass either only right or only left circularly polarized light. Furthermore, the light level from only one of the exit slits (either would do) was passed into the computer by grounding the signal from the other exit slit. The exit slit assembly was then scanned manually across each line, and the intensity recorded as a function of

position. In this manner the two line profiles are obtained, convolved with the instrumental windows as is the case for the data measurement. The linear section of the wings of the lines are then used to measure the halfwidths $\delta_{\pm}$ and depths $f_{\pm}$ of the lines, giving the slopes $m_{\pm}$. The results are

$$m_+ = .00011 \qquad m_- = .00010$$

$$f_+ = .27 \qquad f_- = .31$$

where the slopes $m_{\pm}$ are in units of $(m/s)^{-1}$. The error in the measured values is about ±4%.

At the spectral resolution at which the observations are made the conversion factor from a doppler shift in wavelength to a velocity is 5.855×10^4 (m/s)/A. This makes the value of $d = 2.7\times10^3$ m/s. Using these values in equation A.8 gives a calibration factor of 55 (m/s)/(unit *D/I*).

2. Line Scan Calibration

Another method of calibration utilizes the fact that the lines from the annulus and the center of the circular polarization assembly are almost identical in shape. The method records the data signal *D/I* of a single line as a direct function of the displacement of the exit slit assembly. One can then get the factor relating the output *D/I* to the displacement in m/s. This differs from the way the measurement is taken in the actual observations, but the resulting calibration factors are closely related. Because this method measures only the signal from one line rather than the separation between two, and because of the way the displacement is measured (as positive when it is on the red side of the line), the difference between the actual data calibration factor and the number measured with this method is a multiplicative factor of -2.

For this method of calibration the circular polarization assembly's iris diaphragm is adjusted so that it completely blocks the annulus. Thus only light from the center of the disk, right circularly polarized, continues toward the KDP. The exit slit assembly is then scanned across the line manually. The output curve displays a large almost linear region when the slits are near the center of the line. The slope of this line gives the calibration constant. A slope of -26.5 (m/s)/(unit *D/I*) is measured, with an error of about 3%, which after the appropriate multiplication results in a calibration factor of 53 (m/s)/(unit *D/I*).

3. Half-Disk Integration

Both of the previous two methods of calibration are somewhat indirect, in that the first one relies on a theoretical formula, while the second one relies on the conversion of the wavelength scale to a velocity in m/s. It would be more satisfying to be able to measure an actual known velocity difference between the two lines and get the calibration constant that way. The problem is that such a known velocity difference must originate on the sun so that the line profiles are the same.

One possibility is to physically block off half of the image of the sun, with the edge of the mask lying along the solar rotation axis. In this way the light which reaches the exit slits is integrated over only half the disk. Since solar rotation then doesn't cancel any more in either the center or the annulus the two lines should be separated by a value which can be calculated from knowledge of the functional form of solar rotation. The model described in chapter 3 was used for this purpose. Blocking off first the East half, then the West half, two values of *D/I* are measured. The difference between them avoids any zero level offset and together with the known velocity difference provides a calibration. The resulting number is 99 (m/s)/(unit *D/I*).

Clearly something is amiss. The main problem lies in the fact that the line profiles

being measured have been changed drastically by the blocking of light from half the disk. Instead of approximately triangular, they are now more closely a saw-tooth shape. This changes the whole measurement as the exit slit assembly is positioned differently by the servo motor as it attempts to obey equation A.3. This can actually be seen in the exit slit position signal, which changes by a factor of 4 less than it should as determined by a calculation of the average velocity of the West and East halves. Another problem is the uncertainty of the position of the image on the polarization assembly, preventing one from exactly knowing what part of the image is not being blocked by the mask. Thus this method of calibration cannot be compared well to the actual data calibration.

4. Drift Scan

Another attempt to obtain a more direct calibration by introducing a known velocity difference involves letting the image of the sun drift across the circular polarization assembly with the earth's rotation. This is accomplished simply by turning off the clock drive and guiding system.

As the image drifts across the polarization assembly different sections of the sun will fall on the center and assembly. This changing signal is modelled with the code described earlier to get the input velocity difference. Comparing to the D/I signal, a calibration constant of 100 (m/s)/(unit D/I) is calculated, with an error of about 10%.

Clearly, this method of calibration has the same problems as the half-disk integration. It is aggravated by the fact that the image is continuously moving, complicating the modelling.

The conclusion that one can draw from these experiments is that there is no known signal that can be put into the instrument which doesn't change the line profiles enough to be nigh useless as a calibration. The indirect methods of calibration, however, agree well

with each other and with the calibration measurements made previously (Dittmer 1977). Thus the calibration constant adopted for this study is 54 (m/s)/(unit *D/I*).

Appendix B

Sensitivity of the Data Signal to Phototube Gain Changes

The two phototubes which measure the light from the two exit slits are balanced at the beginning of each observation so that their output is the same for identical input. However, it is known that the phototube gain changes with time, as a function of the history of light falling on it. The two phototubes change differently, so that the gain ratio g in equations A.6 and A.7 is generally close to, but not equal to 1. Experimental adjustment of the balancing knob and measuring the output from each phototube separately reveals that the gain ratio varies by 1.0% for a 1.7% change of the balancing voltage (around the value of 6.7 on the balancing scale which corresponded to a gain ratio of 1.0 at the time of the experiment). From experience it is known that the balancing adjustment varies by about 5% to 10% throughout the day. This thus reflects a gain change on the order of 5% through the day.

The effect of such a change on the observations can be calculated using equations A.6 and A.7. The partial derivative with respect to g of the exit slit assembly position, equation A.6, is

$$\frac{\partial S}{\partial g} = \frac{-2(I_+ f_+ + I_- f_- + d(I_+ m_+ + I_- m_-))}{(I_+ m_+ + I_- m_-)(1+g)^2} \tag{B.1}$$

while the result for the data signal D/I, equation A.7, is

$$\frac{\partial D/I}{\partial g} = \frac{G_D I_+ I_- \left[(-m_+ m_- \Delta)\frac{g^2-1}{g^2} - (m_- f_+ - m_+ f_-)\frac{g^2+1}{g^2}\right]}{(I_+ m_+ + I_- m_-)(I_+ f_+ + I_- f_- + d(I_+ m_+ + I_- m_-))} \tag{B.2}$$

For the purpose of estimating the effect of the phototube gain change it is again sufficient to assume that $I_+ = I_-$. Using the measured values for $m_\pm$, $f_\pm$, and d, the equations then become

$$\frac{\partial S}{\partial g} = \frac{-1.1\times10^4}{(1+g)^2} \text{ m/s} \tag{B.3}$$

and

$$\frac{\partial D/I}{\partial g} = (-4.15\times10^5)\left[(1.1\times10^{-8}\Delta)\frac{g^2-1}{g^2} + (7.1\times10^{-6})\frac{g^2+1}{g^2}\right] \tag{B.4}$$

For the exit slit encoder signal S a 5% gain change from the initial g=1 results in

$$\delta S \approx \frac{(-1.1\times10^4)}{4}(0.05) \text{ m/s} \approx 140 \text{ m/s}$$

This drift is close to half the magnitude of the earth's rotation in the signal, a large contribution.

For the data signal D/I, the effect is smaller by a factor of about 10, but very significant in a signal which is measuring oscillations of an amplitude of a few tens of centimeters. One needs first to know the value of the splitting Δ. Its value averages around 200 m/s due to the zero level offset of the data signal. Combined with the small factor g^2-1 one can see that the term involving Δ can be ignored compared to the second term in the equation. Then a 5% gain change produces the following change in D/I

$$\delta(D/I) \approx (-4.15\times10^5)(7.1\times10^{-6})(2)(0.05) \approx 0.29 \approx 16 \text{ m/s}$$

where the value in m/s is obtained by using the 54 m/s/(unit D/I) calibration factor. The result is high enough to account for a large fraction of the observed daily drift.

Bibliography

T. Appourchaux, Correction of Atmospheric Transparency Gradient effect on solar radial velocities, Presented at Conference on 'Space Research Prospects in Stellar Activity and Variability', Meudon Observatory, France, 1984.

G. Berthomieu, G. Gonczi, P. Graff, J. Provost, and A. Rocca, *Astron. Astrophys. 70*(1978), 597-606.

G. Berthomieu, J. Provost, and E. Schatzman, *Nature 308*(1984), 254-257.

T.M. Brown and J. Christensen-Dalsgaard, A Technique for Filling Gaps in Time Series with Complicated Power Spectra, Preprint, High Altitude Observatory, NCAR, 1985.

T.M. Brown, *Nature 317*(October 1985), 591-594.

T.M. Brown and C.A. Morrow, *Ap. J. 314*(March 1, 1987), L21-L26.

J. Christensen-Dalsgaard, Solar Oscillations (Theory), Invited Paper at the Fifth European Regional Meeting: Variability in Stars and Galaxies, Liege, July 28-August 1, 1980.

J. Christensen-Dalsgaard and D.O. Gough, *Astron. Astrophys. 104*(1981), 173-176.

J. Christensen-Dalsgaard, *Mon. Not. R. Astro. Soc. 199*(1982), 735-761.

J. Christensen-Dalsgaard, T.L. Duvall, Jr., D.O. Gough, J.W. Harvey, and E.J. Rhodes, Jr., *Nature 315*,6018 (1985), 378-382.

J. Christensen-Dalsgaard, D.O. Gough, and J. Toomre, *Science 229*(1985), 923-931.

J. Christensen-Dalsgaard, in *Seismology of the Sun and the Distant Stars*, D.O. Gough (editor), D. Reidel Publishing Company, 1986, 23-53.

A. Claverie, G.R. Isaak, C.P. McLeod, H.B. van der Raay, and T. Roca Cortes, *Nature 282*(December 1979), 591-594.

A. Claverie, G.R. Isaak, C.P. McLeod, H.B. van der Raay, and T. Roca Cortes, *Astron. Astrophys.*, 1980, L9-L10.

A. Claverie, G.R. Isaak, C.P. McLeod, H.B. van der Raay, and T. Roca Cortes, *Nature 293*(October 8, 1981), 443-445.

W. Dappen, R.L. Gilliland, and J. Christensen-Dalsgaard, *Nature 321*, 229-231.

P. Delache and P.H. Scherrer, *Nature 306*,5944 (1983), 651-653.

P. Delache, F. Laclare, and H. Sadsaoud, *Nature 317*(1985), 416-418.

F.L. Deubner, *Astron. Astrophys. 44*(1975), 371.

F.L. Deubner and D.O. Gough, *Ann. Rev. Astr. Astrophys. 22*(1984), 593.

P.H. Dittmer, Thesis, Large-scale Periodic Solar Velocities: An Observational Study, Stanford University, Stanford Univ. Inst. for Plasma Res. 686., 1977.

T. Duvall, J. Harvey, K. Libbrecht, B. Popp, and M. Pomerantz, Frequencies of Solar P-Mode Oscillations, Caltech Astrophysics Preprint, Big Bear Solar Observatory, (in press), 1987.

T.L. Duvall, Jr. and J.W. Harvey, *Nature 302*(1983), 24.

T.L. Duvall, Jr. and J.W. Harvey, *Nature 310*(1984), 19.

T.L. Duvall, Jr., W.A. Dziembowski, P.R. Goode, D.O. Gough, J.W. Harvey, and J.W. Leibacher, *Nature 310*(1984), 22-25.

T.L. Duvall, Jr. and J.W. Harvey, in *Seismology of the Sun and the Distant Stars*, D.O. Gough (editor), D. Reidel, 1986.

J. Faulkner, D.O. Gough, and M.N. Vahia, *Nature 321*(1986), 226-229.

E. Fossat, B. Gelly, G. Grec, and M.A. Pomerantz, *Astron. Astrophys. 177*,1/2 (1987), L47-L48.

C. Frohlich, in *Proceedings of the IAU Symposium No. 123, Advances in Helio- and Asteroseismology*, (in press), 1987.

D.O. Gough, *Physics Bull. 34*(1983), 502.

G. Grec, E. Fossat, and M.A. Pomerantz, *Nature 288*,5791 (1980).

G. Grec, E. Fossat, and M.A. Pomerantz, *Sol. Phys. 82*(1983), 55.

H.M. Henning and P.H. Scherrer, in *Seismology of the Sun and the Distant Stars*, D.O. Gough (editor), D. Reidel, 1986.

H. Henning and P. Scherrer, in *Proceedings of the IAU Symposium No. 123, Advances in*

Helio- and Asteroseismology, (in press), 1987.

H.A. Hill, *Ap. J.*, (submitted), 1984.

H.A. Hill, *Ap. J. 290*(March 1985), 765-781.

H.A. Hill and W.M. Czarnowski, *Astron. Astrophys.*, (submitted), 1986.

J.T. Hoeksema and P.H. Scherrer, *Sol. Phys. 105*(1986), 205-211.

G.R. Isaak, H.B. van der Raay, P.L. Palle, T. Roca Cortes, and P. Delache, *Memorie della Societa Astronomica Italiana 55*,1-2 (June 1983), 91-97.

W. Jeffrey and R. Rosner, *Ap. J. 310*(November 1, 1986), 463-472.

A. Jimenez, P.L. Palle, C. Regulo, T. Roca Cortes, Y.P. Elsworth, G.R. Isaak, S.M. Jefferies, C.P. McLeod, R. New, and H.B. van der Raay, in *Proceedings of the IAU Symposium No. 123, Advances in Helio- and Asteroseismology*, (in press), 1987.

A. Jimenez, P.L. Palle, T. Roca Cortes, V. Domingo, and S. Korzennik, *Astron. Astrophys. 172*(1987), 323-326.

V.A. Kotov, A.B. Severny, and T.T. Tsap, *MNRAS 183*(1978), 61-78.

J.R. Kuhn, K.G. Libbrecht, and R.H. Dicke, *Nature 319*,6049 (January 1986), 128-131.

B.J. LaBonte and R.A. Howard, *Sol. Phys. 80*,2 (October 1982), 361-372.

H. Lamb, in *Proceedings of the London Mathematical Society No. 7, Series 2*, vol. 7 , 1908, 122.

J.W. Leibacher and R.F. Stein, *Astrophys. Lett. 7*(1971), 191.

J.W. Leibacher and R.F. Stein, in *The Sun as a Star*, S. Jordan (editor), NASA Sol. Phys.-450, 1981, 263-287.

R.B. Leighton, in *IAU Symposium No. 12; Suppl. Nuovo Cimento 22*, R.N. Thomas (editor), 1960, 321.

R.B. Leighton, R.W. Noyes, and G.W. Simon, *Ap. J. 135*(1962), 474.

K.G. Libbrecht, B.D. Popp, J.M. Kaufman, and M.J. Penn, Solar Oscillation Amplitudes, Preprint, Big Bear Solar Observatory #0260, 1986.

P.H. Scherrer, J.M. Wilcox, V.A. Kotov, A.B. Severny, and T.T. Tsap, *Nature 277*,5698

(1979), 635-637.

P.H. Scherrer, J.M. Wilcox, A.B. Severny, V.A. Kotov, and T.T. Tsap, *Ap. J. 237*,3 (1980), L97-L98.

P. Scherrer, J. Wilcox, J. Christensen-Dalsgaard, and D. Gough, *Nature 297*,5864 (May 27, 1982), 312-313.

P.H. Scherrer, J.M. Wilcox, J. Christensen-Dalsgaard, and D.O. Gough, *Sol. Phys. 82*(1983), 75-87.

P.H. Scherrer, in *Solar Seismology From Space, A Conference at Snowmass, Colorado*, R.K. Ulrich, J. Harvey, E.J. Rhodes, Jr., and J. Toomre (editor), NASA, December 15, 1984, 173-182.

M. Tassoul, *Ap. J. Supplement Series 43*(August 1980), 469-490.

R.K. Ulrich, *Ap. J. 162*(1970), 933.

M.F. Woodard and R.W. Noyes, *Nature 318*(1985), 449-450.